LIÈGE université
Sciences Appliquées

Aerospace and Mechanics department
Design of Turbomachine Group

von KARMAN INSTITUTE
FOR FLUID DYNAMICS

Aeronautic and Aerospace department

A Monolithic High-Order Multi-Domain Solver for Inductively Coupled Plasma

Nicolas Corthouts

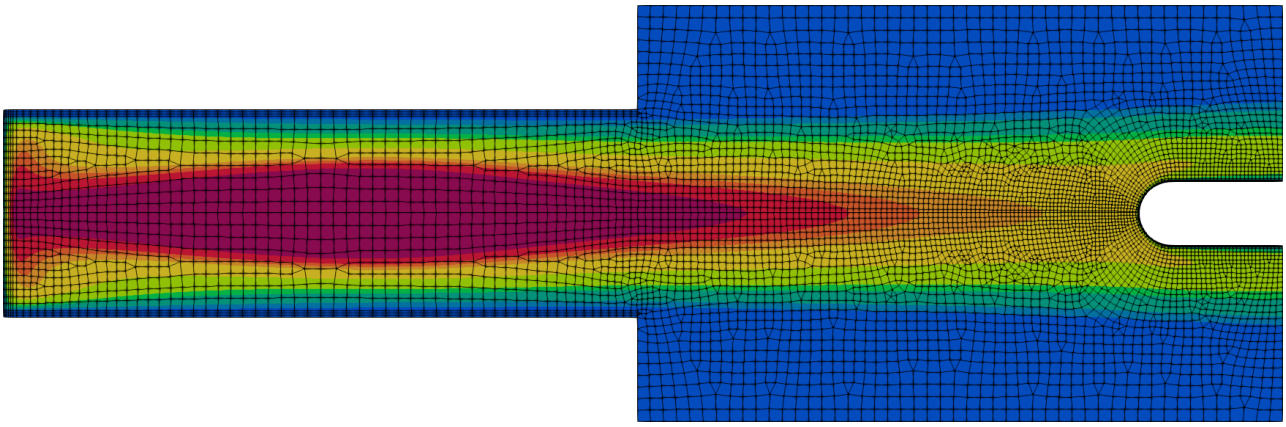

Supervisors Koen Hillewaert, *Université de Liège*
Thierry Magin, *Université Libre de Bruxelles*

Submitted in Partial Fullfillment of the Requirements for the Degree of
Doctor of Philosophy in **Aerospace Engineering** at the **University of Liège** in
September 2025

Pour Gilbert Corthouts, Elisa Digneff, et Francesca Marino.
Sans eux, ce travail n'aurait probablement pas eu lieu.

Abstract

Plasma have an important role in the field of aerospace, more specifically in atmospheric reentry of spacecraft. Indeed, when an object (re)enters an atmosphere at supersonic speed, a shock forms in front of it. This shock converts the kinetic energy of the reentering object by ionizing the gas composing the atmosphere (air on earth), creating a plasma. The latter interacts thermally and chemically with the material. Understanding plasma behaviour is thus of capital importance in the design of spacecraft material. For instance, space shuttles are protected during reentry by thermal protection systems. The latter must be sufficiently resistant for the spacecraft to survive the reentry. On the other hand, when a satellite is decommissioned, it should fall back on earth and completely disintegrate in order to keep a clean spatial environment. Inductively coupled plasma facilities have been created in order to study these interactions. They reproduce the atmospheric reentry by heating a plasma using electric induction. There has been an increasing interest in those facilities in the past decades due to the high purity of the flow they produce and the possibility to run long experimental campaigns. Over the years, the complexity of the experiments performed has also increased. For instance, nozzles are now placed at the exit of the ICP torch in order to study supersonic plasma. More complex geometries are investigated, such as semi-elliptical nozzles for the study of shear flows. Unsteady and turbulent behavior are also studied. New thermal protection systems involving electron transpiration cooling, *i.e.* the spontaneous emission of electrons from a surface carrying the heat away, are tested. Another example is the study of communication black-out during reentry, and the possible ways to mitigate this phenomenon.

Due to the wide variety of configurations encountered in ICP facilities and the possibility to perform measurements in specific locations only, it is difficult to predict the flow features beforehand. Flow prediction is very important before planning an ICP experimental campaign, as the plasma modes could damage the facility. Moreover, predicting the flow correctly saves not only preparation time, but also funds. In this context, numerical solvers have been developed to simulate the ICP flows. The legacy numerical solvers are based upon the finite volume method, demanding a high mesh quality, making this approach very cumbersome for complex geometries. Moreover, these solvers are only axisymmetric, most of them performing computations at local thermodynamic equilibrium and steady state, missing many important physical features of ICP flows. Moreover, they are not robust, as they are based on a staggered solution strategy, converging in thousands of iterations and sometimes requiring to be carefully monitored. In order to address all these issues, we develop in this work the first monolithic multi-domain high order solver for inductively coupled plasma

iii

using the hybridized discontinuous Galerkin method. The high-order aspect of the method brings accuracy and mesh flexibility, while the monolithic solution strategy brings robustness to the code.

In this thesis, we first discuss the various plasma models stemming from the kinetic theory of gas, each one representing a different degree of thermal and/or chemical non-equilibrium. Unfortunately, we are not able to explore all of them in this work, as the task is far too ambitious. The goal is to give an overview of the possible improvements to the relatively simple thermochemical model used in this thesis, which is the local thermodynamic equilibrium (LTE). Then, we particularize the LTE plasma equations to the axisymmetric approximation of inductively coupled plasma flows. In particular, we discuss hypotheses made on the electromagnetic field. We also present the boundary conditions, explicitly stating that, in steady numerical simulations, a coflow is introduced in the chamber in order to stabilize the flow. Then, we present the multi-domain hybridized discontinuous Galerkin solver, which is the first solver of its kind. We prove that the correct orders of convergence of the method are retrieved on a manufactured solution. We also study the impact of the coflow on the steady state result, and conclude that it does not have a significant influence on the flow features in the jet. We also show that the HDG code is able to produce the same result as a legacy FV solver, COOLFluiD, and that it is robust and converges in only a few Newton iterations. Finally, we study a realistic case and assess the impact of various experimental parameters on the flow features.

To summarize, we developed a robust and easy-to-use high order solver for inductively coupled plasma which easily adapts to complex geometries. This thesis marks a turning point in the field of ICP simulation, as it proves that high-order methods are well suited for this applications. Thanks to its robustness, precision, ease of use and flexibility, it opens the door to future developments in this field: supersonic flow simulations, instability and turbulence studies, or more complex thermochemical models.

Remerciements

Aucune thèse de doctorat ne peut être écrite en complète isolation, et ce manuscript ne serait sûrement pas entre vos mains si je n'avais pas été entouré de nombreuses personnes qui ont rendu cette recherche possible. A commencer par Koen, qui a été d'un indéfectible soutien. Le père numéricien du B52 aura tout au long du chemin éclairé ma lanterne dans les couloirs sombres et tortueux des méthodes numériques haut-ordre. Je remercie aussi Thierry, qui, non seulement pendant mon master de recherche à l'IVK, mais aussi durant ma thèse, ma donné de précieux conseils au sujet de la simulation des plasmas à induction. Son savoir encyclopédique dans le domaine m'aura sorti bien des fois de mauvais pas. Tous les deux ont été pour moi de véritables références, non seulement techniques, mais aussi lors des nombreux moments de doute durant ces quatres (longues) années de recherche.

Un remerciement tout particulier aux collègues du B52, sans qui la vie aurait été bien plus morose. La thèse aurait été bien plus difficile sans les cinés organisés avec Nyan et Thomas, les longues discussions sur l'avenir professionel et les potins avec Amaury, à ce super voyage en Floride avec Paul et aux temps de midi passés avec Max et tous les autres que j'ai oublié de citer. Une salutation particulière à Julien et à Bruno, mes camarades de bureau. Bruno, tu vas enfin pouvoir avoir mon bureau côté fenêtre! Salutations aussi à Giuseppe ("Joseph", pour les intimes), qui m'a d'abord soutenu en tant qu'advisor lors de mon master de rechercher, et avec qui j'ai continué de collaborer pendant ma thèse.

Un doctorat, ça se fait aussi en décompressant un bon coup. Un immense merci à la Confrérie! Les soirées, les vacances à Marseille, les sorties à Bruxelles, les barbecs, les festivals, ça permet de sortir la tête du guidon. Une légende raconte que les bières fraîches du Woodpecker dans le parc royal de Bruxelles ont fini par debugger plus de lignes de mon code que n'importe quel forum Stack Overflow... Un grand merci aussi à la Brique, avec qui j'ai pu créer un projet de théâtre et passer de chouettes moments. Ca m'a aussi permis de respirer et de prendre du recul bien nécessaire.

Je remercie énormément ma famille pour leur soutien inconditionnel. Malgré que les sciences ne soient pas du tout, mais alors pas du tout, un amour familial, je les remercie d'avoir cru et eu confiance en mes choix tout au long de mon parcours scolaire et académique. En particulier, merci à ma mère de m'avoir inculqué la ténacité face aux difficultés, qu'elles soient de nature scientifique ou dans la vie de tous les jours. A ma petite soeur, pour sa relecture de mon anglais parfois laborieux et approximatif tout au long de mes études, comme quoi, on a toujours besoin d'un plus petit que soi! A mon père, qui, assez ironiquement pour un littéraire et cinéphile convaincu, a motivé ma passion pour les mathématiques et la physique au

travers de la science-fiction et surtout, Star Wars. Enfin, un merci tout particulier à ma compagne Sarah. Mon phare dans la nuit, ma présence rassurante quand j'étais convaincu que rien n'allait! Nous sommes deux docteurs à présent: une qui soigne, et l'autre pas. Merci pour ta patience, ton écoute de mes complaintes, d'avoir supporté mes énervements sur d'interminables sessions de débuggage et mes nombreux questionnements sur mon avenir professionel. Tes précieux conseils ont été pour moi une véritable bouée de sauvetage dans cette mer agitée, et sans toi, c'est certain, je n'y serais pas arrivé!

A tout ceux cités ici, et aux autres que j'ai sûrement oubliés, que la Force soit avec vous! Ce travail est aussi, d'une manière indirecte, un peu le vôtre.

Contents

1 Introduction

1.1 Plasma

It is impossible to present our work on the development of a high-order numerical solver for inductively coupled plasma without describing the notion of plasma, and giving an overview of its wide range of applications. On earth, matter is mainly encountered in one of three states: solid, liquid or gas. However, what is usually called "the fourth state of matter", the plasma state, is estimated to compose about 90% of the visible matter in the universe. *De facto*, plasma are the ordinary state of visible matter in the universe. A definition of the plasma state is given by Chen [20] : "*A plasma is a quasi-neutral gas of charged and neutral particles which exhibits collective behaviour*". The collective aspect is due to the electric interaction between charged particles. In a classical gas, the particles interact only with their neighbours through *short-ranged* collisions. In plasma, the charged particles also "feel" the presence of others ions and electrons from a much longer distance due to the strong and wide range nature of the electric force. These are *long-ranged* interactions.

One may wonder where to place the limit between a gas and a plasma. Although this is not a definitive indicator, the ionization level can be used to estimate the plasma behaviour of a material. It is defined as the ratio of the number density of ionized n_i over neutral n_n particles and is governed by the well-known Saha's equation [99]. A fully ionized plasma typically has a large ionization parameter ($n_i/n_s \gg 1$), while a conventional gas will have a small one ($n_i/n_s \ll 1$). For partially ionized gas, the ionization parameter is close to unity. We have listed a series of material and typical values for their ionization parameter in Table 1.1.

Material	**Ionization parameter** n_i/n_n	**Plasma behaviour**
Air (Room conditions)	$\simeq 0$	Not a plasma
Laboratory nuclear fusion	$\simeq 10^{13}$	Fully ionized plasma
Sun core	$\simeq 1$	Partially ionized plasma
Sun corona	$\simeq 10^{18}$	Fully ionized plasma

Tab. 1.1.: Representative values of ionization parameters for various plasma. [48]

Although relatively rare on earth, plasma can be observed in our everyday life by looking at the sky: the sun is basically a giant ball of plasma. The northern lights,

product of the interaction between the charged solar winds and our atmosphere, are also a plasma. Finally, the electric arc occurring during lightning strikes ionizes the air on its path, producing a plasma (see Fig. 1.1).

Fig. 1.1.: The sun (left), an aurora borealis (center) and a lightning (right) are composed of plasma.

Nowadays, one of the first applications coming to our mind involving plasma is the energy production through nuclear fusion. In this context, a gas (*e.g.* a mixture of deuterium and tritium) is heated so that the kinetic energy of its nuclei is sufficient to overcome the repulsive electric forces. The nuclei then fuse into new elements (α particles and neutrons for the deuterium-tritium reaction), releasing a large amount of energy. For the process to be effective, the gas must be heated to temperatures of the order of 10^8K. In this regime, the charged particles move freely, and a plasma is formed. The core of the stars are also the siege of fusion reactions (although different from laboratory fusion). In fact, many stellar phenomena, such as the magnetic activity or stellar winds are described using plasma physics. Generally speaking, plasma are found in many fields of astrophysics, due to their large presence in the visible universe.

It would not be fair to restrict the plasma technological applications to nuclear fusion. In fact, plasma occur in a wide variety of fields. For instance, laser-generated plasma are broadly used. They are produced by directing a high-energy pulsed laser towards a surface. If the power of the laser is sufficiently large, the material is heated and ionized, creating a plasma. It is used for thin films deposition and ablation, elemental composition detection or spectroscopy. The plasma television screens are organized as arrays of pixels filled with a plasma reacting to electric fields. The excitation of these pixels give rise to the images. Plasma also have an important role in medical applications, such as in nanomaterial synthesis or aerosol processing. It is also present in biomaterials manufacturing. Plasma also allows the deposition and ablation of materials with a resolution of the order of the nanometer. These high-precision are required in the manufacturing of microprocessors, vital for computers. In this work, we will be mainly concerned with plasma in the field of aerospace. Whether it is in space propulsion (Hall thrusters) or the design of thermal protection systems and reentry material, plasma play a central role in the aerospatial industry and space exploration.

The definition of plasma state is relatively large, since it encompasses numerous physical systems. In order to ease their physical description, plasmas have been

categorized. Each category comes with a set of assumptions allowing to describe the dominating physics. For instance, reentry plasmas can be considered dense enough to have a fluid behaviour. On the other hand, sufficiently high in the atmosphere, the air is so rarefied that the continuum hypothesis collapses and the plasma must be seen from a statistical point of view. The highly ionized plasma in laboratory fusion cannot be described in the same manner as atmospheric reentry plasma, because the physics and chemistry are very different.

The exploration of all plasma types is far beyond the scope of this work. Instead, we are mainly interested in the so-called low-temperature plasma (LTP). LTP are generally produced using electrodes (in arc-jet facilities for instance, where a gas is heated using an electric arc) or coils (*e.g.* in inductively coupled plasma facilities, extensively discussed later). Basically, the generated electric field transmits kinetic energy to the electrons, which then collide with the heavies (*i.e.* ions and neutrals), resulting in chemical reactions, ionizations and the heating of the plasma. Because most of the electromagnetic energy is yielded to the electrons, they have a larger temperature (*i.e.* a larger kinetic energy) than the heavies, considered "low" temperature (thus the denomination "low-temperature" plasma). When this temperature disparity occurs, the plasma is said to be in *thermal non-equilibrium*, as opposed to a *thermal* plasma (or plasma in *thermal equilibrium*), where the electrons and heavies have the same temperature.

Although many LTP are in thermal non-equilibrium, this is not their defining feature, as LTP can be found in various pressures (from near vacuum to atmospheric pressures), temperatures (thermal equilibrium and non-equilibrium, for temperatures ranging from a few to tens of thousands kelvin) and ionization (from partially to fully ionized) conditions. In fact, the central characteristic of a LTP is its large chemical reactivity at low gas (*i.e.* low heavies) temperature compared to nuclear fusion plasma. The broad range of applications of LTP makes it an active field of research. The interested reader may refer to the 2022 low-temperature plasma roadmap [2] for a summary of the research and future development in this field. In this thesis, we only focus on the LTP produced for studying the demise of space debris and the design of thermal protection systems. In the following, we describe these applications in more detail, and give the framework of the thesis.

1.2 Plasma for atmospheric re-entry

Space vehicles reenter the atmosphere with velocities of around $10\,\mathrm{km\ s^{-1}}$. For instance, typical low-earth orbit re-entry happen at around $7.8\,\mathrm{km\ s^{-1}}$, which is the velocity required to keep a spacecraft in orbit. On the other hand, lunar return occur at around $11\,\mathrm{km\ s^{-1}}$. As the spacecraft enters the atmosphere, the flow is commonly regarded as hypersonic, with a re-entry Mach number $\mathrm{Ma} > 5$. Then it starts to decelerate, becoming successively supersonic ($\mathrm{Ma} > 1$), transonic ($\mathrm{Ma} \sim 1$) then subsonic ($\mathrm{Ma} < 1$) as the shuttle slows down and loses altitude. For $\mathrm{Ma} > 1$, a

reacting shock forms in front of the vehicle.

The cold and low density air surrounding the aircraft goes through the shock moving with a large velocity. After the shock, it is denser and has a higher temperature. Inside the shock, the kinetic energy of the air is converted into translational, rotational, vibrational and electronic energy. The large internal energies attained in this region (the temperature of the gas rises up to 10^4K) provoke molecular dissociation and ionization, effectively creating a plasma. The excitation and de-excitation of the bound electrons also produce radiation. These phenomena impose a huge heat load at the surface of the shuttle. These heat fluxes can be hazardous for the crew and material samples. For this reasons, thermal protection systems (TPS) have been designed. Generally composed of ceramics, reinforced carbon or composite materials, and organized in tiles covering the spacecraft, the purpose of TPS is to absorb the heat flux during reentry and being gradually ablated from the shuttle surface, preserving the latter. An example of a heat shield is given in Fig. 1.2).

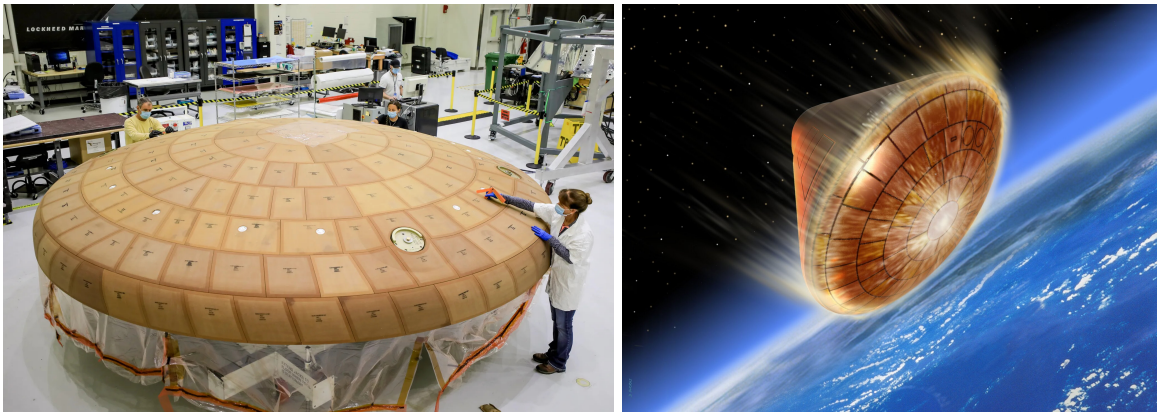

Fig. 1.2.: On the left, the Orion spacecraft TPS. It is composed of blocks of ablative material to protect its crew during reentry. Credit to NASA (Isaac Watson). On the right, a drawing of atmospheric reentry (credit to ESA).

Ideally, any decommissioned man-made object sent in orbit should fall back on earth at the end of its life cycle and disintegrate in the atmosphere. This way, the space surrounding the earth remains clean, both decreasing the risk of collisions with space debris and preventing damage caused by pieces of spacecraft falling back on earth. Another hazard is the cascade effect: due to their large velocity, two objects colliding may produce debris that will themselves collide other satellites with a large speed, leading to a catastrophic chain of destruction. Unfortunately, since the first launch of a man-made satellite, the number of decommissioned space objects in orbit has been increasing, making the cleaning of space a topic of capital importance (Fig. 1.3). In this context, NASA is developing the Active Debris Removal Vehicle, which is meant to deorbit space debris. In the same objective, the European Space Agency (ESA) has developed the ClearSpace-1 mission, supposed to be launched in 2025. These missions, categorized as "active space debris removal", consists in sending a space vehicle to deorbit the decommissioned objects. Unfortunately, these

projects are expensive and time consuming. One solution found by NASA and ESA to this problem is to take into account the safe disposal during the design of a satellite or any orbiting object. In fact, the design of TPS and demise of space debris are two sides of the same coin in the context of space reentry, as they consists in studying the behaviour of a material when it reenters the atmosphere. For TPS, the objective is to ensure its protective power during reentry, while space debris must disintegrate completely.

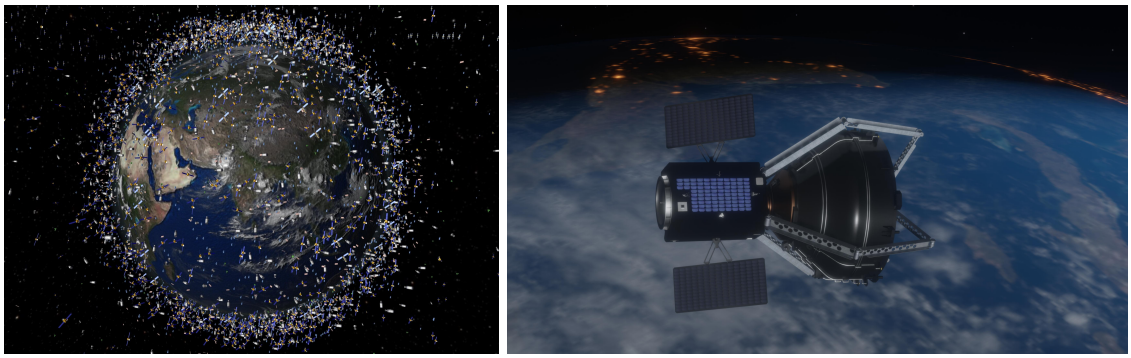

Fig. 1.3.: Vizualisation of the number of known objects orbiting around the earth in 2022 (on the left). They have been magnified to be distinguishable. On the right, a 3D model of the ClearSpace-1 with its mechanical arms around a space debris (Credits to ESA).

One of the main challenges in designing these thermal protection systems is to reproduce the *aerothermodynamic* features (i.e. the chemical reaction, heat transfers and aerodynamics) of the reentry plasma experimentally. This way, flight conditions can be reproduced on the ground and tested on sample material (TPS or space debris). Inductively coupled plasma facilities have been specifically designed for these studies. They are discussed later. But first, we give an overview of the characteristic scales of the reentry plasmas.

1.2.1 Scales of reentry LTP

We assume that the spacecraft has sufficiently reentered the atmosphere so that the air is not rarefied. This means that the Knudsen number is small ($\mathrm{Kn} \ll 1$). The Knudsen parameter is the ratio of the mean free path, *i.e.* the characteristic distance between inter-molecular collisions of the particles composing the plasma, over the characteristic length of the problem. The plasma thus behaves like a fluid in this regime, because the smaller the distance between the particle collisions, the denser the fluid.

Another important parameter of the plasma is the Damköhler parameter Dam, which assesses the degree of *chemical equilibrium* of a mixture. Dam is the ratio between the characteristic reaction time of the plasma (such as ionization or chemical

reactions) and the characteristic time of mass transport of the mixture. For $\mathrm{Dam} \gg 1$, the plasma is in chemical equilibrium and reaction rates are instantaneous. For $\mathrm{Dam} \simeq 1$, the plasma is in chemical non-equilibrium and finite reaction rate must be taken into account. Finally, for $\mathrm{Dam} \ll 1$, the reactions are so slow that chemistry is considered frozen. For typical LTP, $\mathrm{Dam} \geq 1$ and the flow is either in chemical equilibrium or non-equilibrium, depending on the flow conditions.

Another characteristic of the plasma is its magnetization, described by the hall parameter β. It is a measure of how the electrons are affected by magnetic fields. In plasma, ions and electrons tend to have a cyclotronic motion around the magnetic field, meaning that they move along the magnetic field line with a gyrating motion. If the plasma charged particles undergo sufficiently many collisions, these helicoidal trajectories are perturbed and the magnetic field has little effect on the plasma properties. β is the ratio of the cyclotron frequency, *i.e.* the frequency at which the charged particles gyrate around the field magnetic field lines, over the collision frequency of the plasma particles. If $\beta \gg 1$, the plasma is *magnetized* and it is influenced by the magnetic field. If $\beta \simeq 1$ then the plasma is *weakly magnetized*, and the magnetic field has a marginal effect on its behaviour. Finally, if $\beta \ll 1$, the plasma is *unmagnetized*. In the present application, the plasma is assumed weakly magnetized. Concerning the hydrodynamic characteristics of the plasma studied, the Reynolds number is low ($\simeq 100$), since the fluid has a large temperature and relatively low velocity. The Mach number is highly subsonic (≤ 0.01), since the plasma after the choc has a large speed of sound ($\simeq 2700\,\mathrm{m\,s^{-1}}$) and it has a relatively low velocity of close to the spacecraft surface. Finally, the plasma electrons temperature T_e is greater or equal to the heavies temperature T_h, meaning that the plasma can be either in thermal equilibrium or non-equilibrium. The departure from equilibrium strongly depends on the flow conditions. We have summarized the characteristics of the re-entry plasma in Table 1.2.

1.2.2 Inductively coupled plasma

We discussed earlier the importance of studying reentry plasma experimentally. *Inductively coupled plasma* (ICP) facilities have been designed to this end. An ICP facility is schematically presented in Fig. 1.4. A gas (such as air or argon) enters the torch through an annular injector, stabilizing the flow. It is heated by electric induction using an alternative high-frequency current flowing through coils surrounding the facility. Because the ions are more massive than the electrons (the protons and neutrons are approximatively 1800 times heavier than electrons), the free electrons are much more affected by the fast-varying electromagnetic field. They communicate their kinetic energy to the slow heavies by collisions, creating a low-temperature plasma (LTP). This is in fact a Joule effect, as the electric current (*i.e.* the free electron motion) heats a resistance (the collision with the heavies composing the plasma). The plasma reaches temperatures of about $10^4\mathrm{K}$ in the torch center. It is then released in

Non-dimensional parameter	Value	Plasma regime
Kn	$\ll 1$	Continuous medium
Re	100	Laminar
Ma	0.01	Subsonic
Dam	≥ 1	Chemical equilibrium and non-equilibrium flow
β	$\simeq 1$	Weakly magnetized
T_e/T_i	≥ 1	Thermal non-equilibrium and equilibrium

Tab. 1.2.: (Non exhaustive) list of re-entry plasma non dimensional parameters. Kn is the Knudsen number, Re is the Reynolds number, Ma is the Mach number, Dam is the Damköhler number, β is the hall parameter, T_e is the free electron temperature and T_i is the ion temperature. For each parameter, the corresponding physical plasma regime is given.

the test chamber. The walls of the facility are maintained at a constant temperature of a few hundred kelvins through a water-cooled cold-cage system.

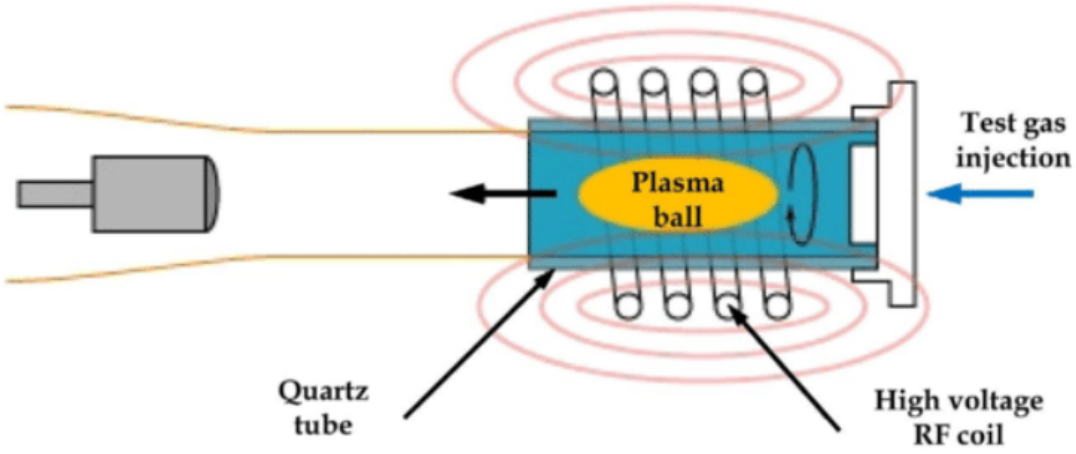

Fig. 1.4.: Schematic representation of an ICP facility. The torch is surrounded by high-voltage, radio frequency coils producing an alternative electromagnetic field. The gas is injected in an annular fashion in order to produce a stabilizing flow recirculation close to the inlet. Swirl can be added to further stabilize the torch. The test material is placed in the chamber, after the torch exit. The torch is surrounded by quartz. The magnetic field lines have been shown in pink lines. Image taken from [66]

The flow is subsonic ($Ma \simeq 0.01$) and laminar ($Re \simeq 100$) in the whole facility, but can be accelerated to supersonic speeds by placing a nozzle at the torch exit. In subsonic regions, the flow is incompressible and the pressure is almost constant.

Consequently, the large density variations that can be observed in an ICP facility are due to the temperature gradients. These gradients give rise to strong variations in the fluid transport properties, such as viscosity, thermal conductivity or electric conductivity. The fluid injection system is annular in order to create a stabilizing recirculating flow close to the inlet wall. Another stabilization technique consists in adding a swirl component to the inlet. However, a too large swirl might create a cold recirculation bubble at the torch exit. The degree of thermal and chemical departure from equilibrium of the generated low-temperature plasma depends on the operating conditions of the torch (frequency employed, power delivered by the coil in the plasma, pressure, etc...). These parameters dictate if the electrons have the time to *thermalize*, *i.e.* to reach the same temperature as the heavies through collisions, and the chemical reactions speeds.

ICP facilities allow to study the aerothermodynamics of spacecraft reentering the atmosphere. They produce a high purity plasma, as electric induction heating is a non-intrusive method. Consequently, the chemistry of the fluid is not altered, and the plasma chemical interaction and heat exchanges with a sample material can be studied thoroughly. While ICP produce a plasma similar to the one encountered in atmospheric reentry, they fail to match the exact reentry conditions. Indeed, ICP facilities are not able to recreate the bow shock in front of the aircraft. Fortunately, the experiments in ICP were proved to correctly recreate the flow conditions at the spacecraft stagnation point using the concept of local heat transfer simulation (LHTS). LHTS was introduced by Kolesnikov [62], who proved that the accurate simulation of the stagnation point flow conditions on a spacecraft during atmospheric reentry can be achieved if the gas has the same chemical composition as the studied atmosphere and the pressure, velocity gradient, and total enthalpy at the boundary layer edge are properly reproduced. This procedure allows to simulate the hypersonic conditions occurring during reentry using a subsonic facility. ICP are also able to reproduce atmospheres different from the earth. In Fig. 1.5, the Plasmatron ICP facility, which is the main focus of this work, is shown in operation and Table 1.3 gives an idea of its test envelope. The regimes listed in Table 1.3 can be easily reproduced and can be sustained for hours (even, days) by the facility, allowing large test campaign to be carried for weeks.

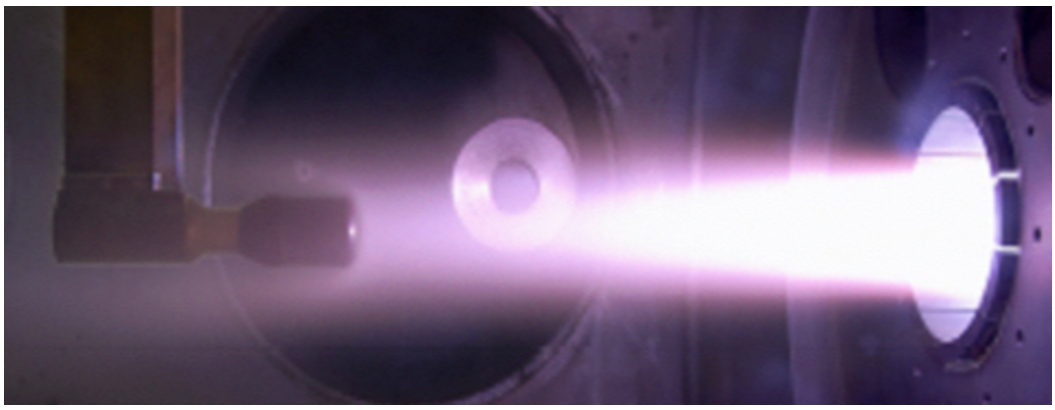

Fig. 1.5.: Water-cooled copper calorimeter in the plasma jet produced by the Plasmatron facility at the von Karman Institute for Fluid Dynamics.

Test gas	argon, air, nitrogen, any mix!
Pressure range	From 3 to 350 hPa
Electrical power	Up to 1.2 MW
Heat flux	15 $\mathrm{MW/m^2}$
Induction frequency	Up to 400 kHz
Inflow mass flux	8 g/s or 16 g/s
Torch diameter	16 cm
Chamber diameter	160 cm

Tab. 1.3.: Plasmatron operation ranges.

Of course, inductively coupled plasma are not the only tools for studying reentry. The plasma shock tube, which recreates the strong bow shock in front of the spacecraft by releasing a membrane between a high pressure, high temperature gas and cold air, can also be used to study the effect of the plasma on test materials. Although the shock tube conditions are closer to reentry (the plasma is produced in the strong shock), the test time is very short, making the results not easily reproducible and difficult to analyze compared to ICP. Another process is the use of arc-jet plasma facilities (Fig. 1.6). The plasma is produced by supplying two electrodes with a continuous current, creating an electric arc which ionizes and heats the gas. The main drawback of this method is that the electrodes evaporate in the process, effectively polluting the flow [111, 61, 104] and making the study of the chemical interaction with test materials difficult. However, the power reached in this type of facility can be greater than ICP.

Although very useful, the information provided by experiments in ICP facilities is

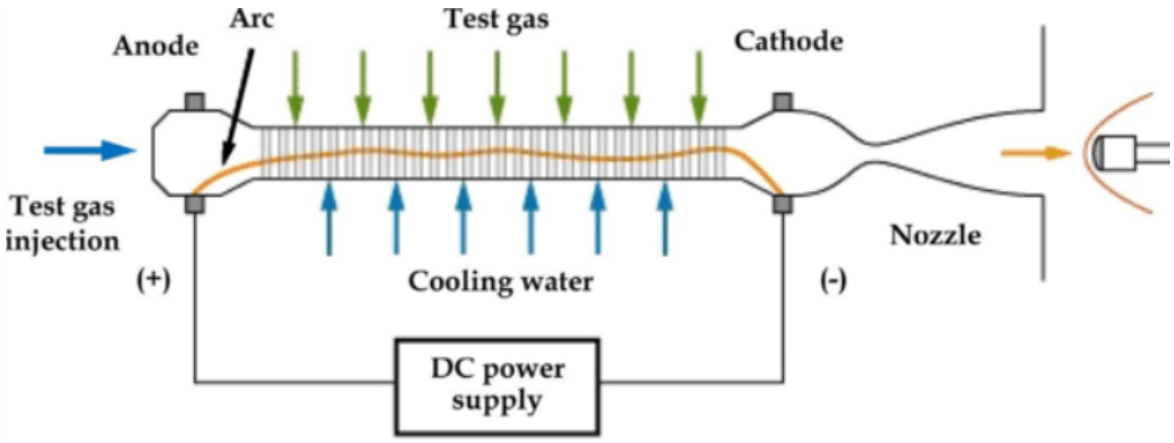

Fig. 1.6.: Schematic representation of an arc-jet generated plasma. The electrodes placed at both ends of the torch are supplied with continuous current, creating an electric arc (yellow line connecting the electrodes). The arc ionizes the gas, sustaining the plasma. Image taken from [66].

restrained by the measurement instruments, which usually allow for the acquisition of specific quantities at defined locations. Generally speaking, the experimenter has access to the temperature at specific locations in the plasma jet along the stagnation line using spectroscopy: from the radiation emitted by the plasma, it is possible to retrieve the temperature and plasma composition. The heat flux transmitted to a sample material is usually only measured at the tip of the test sample or probe. Also, it is very difficult to acquire data in the torch, although the flow inside the torch has an impact on the jet and should be well understood. Another drawback is the cost of running the facility. Predicting the viability of a test campaign is thus of capital importance, as it allows not only to save time, but also funds.

In order to better prepare the experiments in ICP facilities, numerical solvers are employed. They allow to predict flow characteristics, such as plasma modes sticking to the torch walls, temperature distributions and heat fluxes. Although they rely on a large set of assumptions (discussed later), they allow the virtual preparation of experiments in new conditions without running the risk of damaging the device. In this context, having an accurate ICP solver is an invaluable tool. Although several numerical approaches have been tried for simulating ICP flows, none of them is fully satisfying, as they imply too restrictive assumptions on the physics, geometry or on the chemical complexity of the flow. In the following, we present a state of the art of the ICP simulations and facilities, and identify the issues of existing solvers.

1.3 State of the art

1.3.1 ICP facilities

Since the first attempts by Babat in 1947 [5] to maintain inductively coupled plasma on a stream of gas, inductive plasmas have been intensively developed. The space race opposing the USA and the Soviet union taking place from the beginning of the sixties to the early seventies motivated the research for reentry plasma. The Soviet union was the first to commission ICP facilities for reentry at the Institute for Problems in Mechanics (IPM), with the series of Inductive Plasma Generators (IPG) extending from the late seventies to the late nineties [44, 49, 9, 14]. The facilities developed there were mainly used for the study of earth and, more recently, martian atmospheric reentry. The IRS (Institut für Raumfahrtsysteme of Stuttgart University) also developed its IPG facilities around the end of the eighties [4], until the development of the IPG-6 in 2012 [31]. This latter facility allows to study *dusty plasma* (*i.e.* plasma containing charged particles smaller than the millimeter), omnipresent in space but impossible to analyze in more traditional ICP facilities. In 1997, the most powerful ICP device in the world, the Plasmatron, was commissioned at the von Karman Institute for Fluid Dynamics (VKI) in Belgium [19]. The power reached by this facility is still unmatched for an ICP, allowing to study the effect of much larger heat transfers on sample material. The USA developed their first inductively coupled plasma torch for space reentry in 2010, in the university of Vermont [92, 91]. At the time, the only available aerothermal testing facilities in the US were arc-jets. Later, in 2016, the university of Austin [39] commissioned another ICP torch in order to match the increasing demand in aerothermal testing for the Orion and Space-X Dragon missions. In 2023, the university of Urbana-Champaign in Illinois presented its Plasmatron X wind tunnel [15]. It is to this day the largest in the USA, allowing for testing larger sample material. The list of ICP torches presented here is far from exhaustive, but it already shows the increasing interest in space exploration, and more specifically in the study of atmospheric reentry flows.

1.3.2 The VKI Plasmatron

In this work, we focus on the VKI Plasmatron facility. This wind tunnel was commissioned for the study of the thermal loading of the ESA Hermes space plane (Fig. 1.7). The Hermes project was initiated in the late 1980s. Unfortunately, it was abandoned in 1992, but the Plasmatron facility was nonetheless built, and is still extensively used up to this day.

Fig. 1.7.: Sketch of the Hermes space plane (taken from ESA).

Fifteen years ago, the thermal protection systems of the Intermediade eXperimental Vehicle (IXV) were characterized in the Plasmatron. IXV was a project to validate the atmospheric reentry technologies in flight conditions. It was part of the Future Launcher Prepararatory Program (FLPP), an ESA program to prepare the new generation of launchers [93, 110]. The IXV mission was successfully accomplished in February 2015. Around the same time, the Plasmatron was used in a large test campaign for characterizing a new lightweight ablative carbon composite thermal protection system [52]. It was also used to analyze the temperature and chemical reactions in the boundary layer of the ablative material using emission spectroscopy [53], which is a non-intrusive, line-of-sight technique based upon the analysis of the electromagnetic spectrum radiated by the plasma. The Plasmatron was also used to study the demise of space debris. In this context, Fagnani *et al.* [36] studied the ablation and transient thermal response of quartz during reentry. This research motivated the development of new measurement techniques in order to correctly assess the radiative emissivity of material in ICP facilities [1], as this property is critical in studying the response of reentry material. In the same spirit, the disintegration of meteoroid was also investigated [54], as this process is still not well understood. Another field of research is the study of the *communication black-out* phenomenon. The black-out occurs during reentry, when the ionized air perturbs the propagation of electromagnetic waves coming from an going to a spacecraft, preventing communications for a few minutes. The goal is to better understand the black-out causes and try to mitigate its effects [74]. Electron transpiration cooling (ETC) was also studied at VKI [18, 43]. It consists in reducing the heat load of on the thermal protection system by using the thermoionic electron emission phenomenon. Basically, material with low binding energy, when sufficiently heated, release electrons which carry away heat.

Another important topic is the characterization of the Plasmatron facility itself. For instance, it is important to predict (*i.e.* to characterize) the plasma chemical and thermal state for given experimental conditions. Basically, the characterization

procedure consists in, for several input parameters, analyzing the features of the resulting flow such as an instability, the temperature at a given point or the heat flux at a specific location. For instance, the free stream flow temperature has been characterized experimentally in several locations [37] using spectroscopy. During another characterization campaign, Cipullo *et al.* [22] found that the ripple component of the generator pulse rectifier is completely transmitted to the flow. This effect strongly depends on the operating pressure of the facility. It can be directly observed in the emission spectrum of the plasma, with alternating bright (when the ripple component transmits more energy to ionize the molecules further) and dark (when the ripple component is the lowest) bands (see Fig. 1.8). This phenomenon is not observed in real flight conditions, and can have a non negligible impact on the experiments. On the other hand, Demange *et al.* [28, 27, 29] developed numerical and analytical models to study the instability modes of the hot axisymmetric plasma jet released in the cold still air of the chamber. Depending on the experimental conditions, the ICP jet may destabilize the boundary layer of the sample material, which has an impact on heat tansfer and chemical interactions. This phenomenon can also be seen in Fig. 1.8. Predicting the occurrence, location and severity of those instabilities is of capital importance as they strongly impact the flow and may damage the facility. However, because the experimenter is limited by its instrumentation and the experimental device, the characterization can never be complete, and there will always be unknown and unexpected flow features.

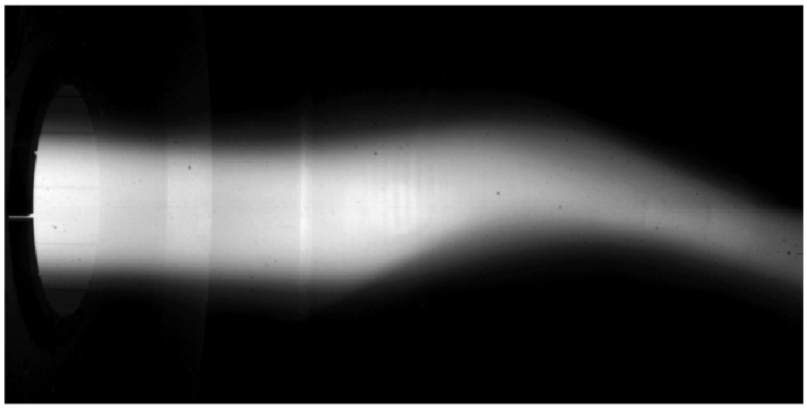

Fig. 1.8.: Camera picture of the plasma jet from the VKI Plasmatron showing both the unsteadiness and the ripple part of the current (alternance of dark and light bands in the jet) [21].

.

Focusing now on spatial modes, it was shown numerically [10] that, for any ICP flow, the coil configuration impacted the flow geometry inside the torch, subsequently breaking the axial symmetry of the jet (Fig. 1.9) Unfortunately, as the torch is not easily accessible, only numerical studies have been performed.

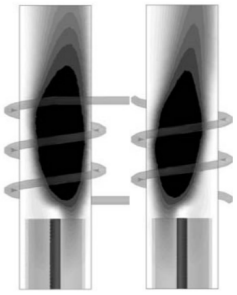

Fig. 1.9.: Effect of the coil configuration on the plasma flow in the torch (taken from Bernardi *et al.* [10]). The jet is not symmetric due to the coil geometry.

Three new nozzles were designed for the Plasmatron: two conical and a semi-elliptical one (see Fig. 1.10). They allow to reach supersonic speed (up to $\mathrm{Ma} \simeq 3$) and study the effect of a shock in front of the sample material. These conditions are closer to real flight circumstances as they reproduce a front shock. In addition, the semi-elliptical nozzle allows to study high-shear flat plate flow configurations. A characterization of the nozzles can be found in Capriati *et al.* [16] and Elrassi *et al.* [33].

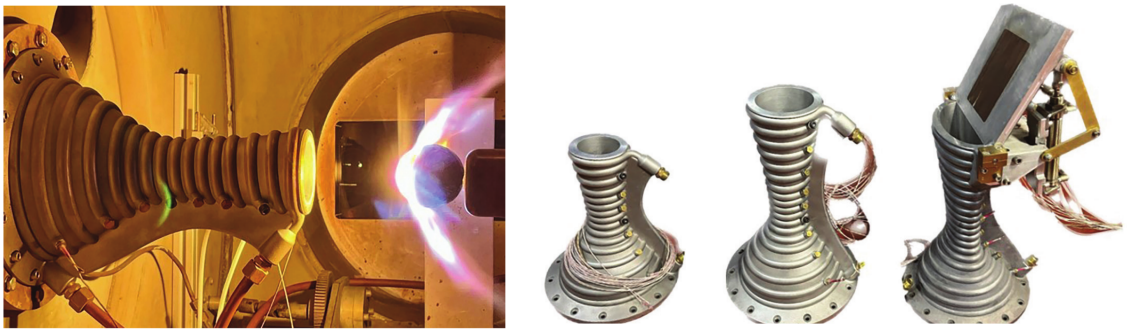

Fig. 1.10.: On the left, the VKI supersonic nozzle in operation. A shock is created in front of the sample material. On the right, the three new nozzles. Taken from [33]. (left).

Regarding the vast number of applications, the complexity of the flow and the difficulty to acquire data in some locations of ICP flows, numerical solvers have been developed to support experiment. Their main goal is to give sufficiently accurate predictions on flow features to better prepare the experiments, saving both time and funds. Moreover, these solvers may highlight physical phenomena that are not readily observed in the facility, opening the door to novel fields of research. In the following, we give an overview of the supporting codes of ICP facilities.

1.3.3 Legacy numerical solvers for ICP

The difficulty of running an ICP facility and performing measurements in several locations led to the development of dedicated numerical solvers to better prepare the experiments. The first numerical model of an ICP was developed by Boulos [12] in 1976 using a finite difference (FD) method, considering a 1D electric field. He realized that a constant power had to be maintained during the ICP simulation, otherwise the torch quenched. Further simulations were performed by the group of Proulx for monoatomic and molecular gases [40]. Various numerical solvers of increasing complexity based upon the finite volume (FV) method have also been proposed. Vanden Abeele [106] studied the physics of ICP using a two-temperature model of the plasma torch in non-equilibrium with a 2D electric field. Then, Magin [75] developed an axisymmetric code for equilibrium cases for the complete problem (torch and test chamber). Finally, inductively coupled plasma was implemented in the COOLFluiD solver [68, 67], and is still used to this day at VKI. More recently, the Center for Hypersonics and Entry Systems Studies (CHESS) at the University of Illinois at Urbana-Champaign developed a 3D, unsteady code for ICP [65], opening the path to capture 3D ICP modes and instabilities.

Although very useful, legacy solvers have a very limited range of applications. Most of them are based upon FV or FD second order total variation diminishing method, with relatively strict constraints on the mesh quality. This is a real obstacle in the simulation of plasma flows with more complex geometries. Moreover, these methods require a large number of elements in near isothermal walls, where large temperature gradients occur. An example of such mesh for FV method is given in Fig. 1.11. The element size in the near probe region is of the order of the micro-meter. When considering 3D configurations such as the semi-elliptic nozzle, the computational cost becomes prohibitive.

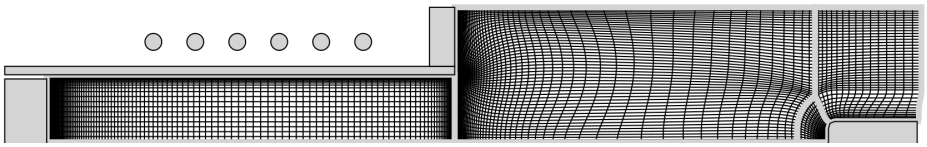

Fig. 1.11.: Mesh of a finite volume ICP solver (taken from Magin [75]).

Many of these codes are designed for steady-state computations, overlooking jet instabilities. In order to partially alleviate the problem, ICP solvers can be coupled to codes dedicated to the study of jet and boundary layer instabilities, such as VESTA [96]. This approach, although giving valuable information, requires to couple and master multiple codes (see Demange [26]). Moreover, these stability computations are based on the gradient of temperature, velocity and pressure. Since the finite volume solver do not give access to the gradient directly, they need to be reconstructed before the results can be used. For this reconstruction to be accurate, the mesh must be sufficiently refined, increasing the computational costs of the simulations. Another

underlying hypothesis of legacy ICP solvers is the quasi-steady assumption, meaning that the equations are averaged over one oscillation period of induction current. This prevents to model the effect of the ripple part of the power supply, missing physical phenomena linked to this issue. Most of the current ICP solvers are axisymmetric, making the simulation of 3D geometries, such as the semi-elliptical nozzle, impossible. A notable exception is the code developed at CHESS [85]. However, they solve for the 3D Navier-Stokes equations for the fluid, while solving for the electric field in the azimuthal direction only, preventing the study of any 3D electric field effect. The simulation of ablation phenomena can be performed, but at the cost of coupling two solvers. First, a simulation is performed using an ICP solver in the torch region. The temperature profile obtained at the torch exit is then input in an ablation solver. For instance, Schrooyen [101] developed an ablative solver in the high-order discontinuous Galerkin (DG) software Argo [55]. Once again, the simulation requires the use of at least two programs and a coupling procedure. Concerning local thermodynamic equilibrium, Rini [98] proved that *elemental de-mixing*, *i.e.* the diffusions of chemical elements, had an important effect on the plasma flow. None of the previous solvers takes this phenomenon into account. The molecular radiation is also completely overlooked in current ICP simulations, although it has an impact on the heat transfer. Another issue is the solution strategy of the ICP solvers. The electric field and hydrodynamic equations are solved in a decoupled manner. Basically, while the electric field is frozen, the hydrodynamic field is solved. Then, the solution of the hydrodynamic field is frozen while solving the electric field. This loop is continuously performed until convergence occur. This method, although simple to implement since the electric and hydrodynamic solvers can be constructed separately, has the disadvantage of converging slowly towards the solution and sometimes leads to solver instabilities [45, 109].

In regards of the numerous drawbacks of legacy ICP solvers, we aim to develop a framework that can adapt to the rapid evolution of experimental ICP facilities. This implies that the solver should be capable of reproducing unsteady phenomena, to be able to capture high spatial frequencies in order to correctly simulate instabilities, unsteady behaviours and spatial modes occurring in ICP flows. It should also work with unstructured grids to represent complex geometries, and easily extend to new physical and thermo-chemical features. For this reason, we decided to implement the very first *monolithic* (*i.e.* fully coupled) high-order ICP solver using the hybridized discontinuous Galerkin (HDG) method.

1.3.4 Hybridized discontinuous Galerkin method

The discontinuous Galerkin (DG) family of method was first introduced by Reed and Hill [97] for hyperbolic problems in the context of neutron transport. During the 1990s, DG methods were developed for convection-diffusion equations (see *e.g.* the work of Cockburn and Shu [24]). In 2002, Arnold and Brezzi [3] analyzed the

DG method applied to purely elliptic problems and improved its stability, adjoint consistency and convergence rate. Although they were never used for ICP, DG codes were employed in the case of high-enthalpy flows (*e.g.* Shrooyen et al. [101] in the framework of ablation). DG methods result in stable and accurate high-order discretization of the convective and diffusive operators on unstructured meshes of almost arbitrary quality. They allow for straightforward imposition of the boundary conditions (BC) and are very flexible to parallelization and adaptivity. Although the computational complexity of DG is higher than standard methods, its computational efficiency is increased and it requires less degrees of freedom. This is further improved in combination with mesh and order (h and p) adaptation for which the methods are particularly well suited.

In this work, we use a variant of DG, called the hybridized discontinuous Galerkin (HDG) method. HDG was developed with the purpose of reducing the large systems required when considering implicit DG methods. It was first presented by Cockburn [23] for elliptic problems. The main advantage of the method is its reduced number of globally coupled degrees of freedom (DOFs), obtained *via* static condensation using hybrid variables, leading to a non-negligible reduction of the computational costs and memory storage compared to DG as pointed out by Woopen [113]. The method was further developed for linear and nonlinear convection-diffusion problems by Nguyen et al. [88, 89, 90]. It was later applied to several physical configurations (*e.g.* see Fernandez [38] for turbulent flows or Modave [80] for Helmholtz equation). In this work, we use a HDG framework developed by Woopen, Balan and May [112] in order to solve the ICP problem. The framework has the advantage to be both user friendly and easy to modify. It is also already equipped with shock capturing techniques and h and p adaptation. One of the main disadvantage of this code is that it is not designed to support multi-physics problems, which is an issue regarding ICP equations, as both Maxwell and Navier-Stokes equations have to be solved.

1.4 Scope and overview of the thesis

Considering the increasing complexity of the experimental ICP facilities, and the drawbacks of the legacy ICP codes, we develop in this thesis a new numerical monolithic solver based upon the hybridized discontinuous Galerkin method. Within this framework, we hope to answer the following questions:

- **In addition of being precise, can a high-order solver be robust?** One of the major issues with the legacy codes is their robustness, since the code requires carefully designed mesh and a constant monitoring during the solution procedure. Moreover, the solver usually requires thousands of iterations to reach steady state. On the other hand, although high-order solvers are known to be more accurate than finite volume methods, they are also less stable in the vicinity of large gradients or shocks. Will the monolithic approach be sufficient to make a robust plasma solver? Or will it be necessary to carefully design a

numerical flux to stabilize the method near large gradients regions?

- **Is the developed solver user-friendly?** This is not the case with the legacy codes, as they require a lot of trial and error to make the ICP solver converge. Moreover, the careful design of the grid can be a barrier to the user. The CFL convergence procedure is also cumbersome as it requires a constant monitoring from the user. Finally, the convergence is slowed by the large number of required Newton iterations. Since high-order methods are less sensitive to mesh quality, we hope to make ICP simulations work on unstructured and automatically-generated grids. We also want to rework the CFL procedure, and hope that the monolithic solver developed will accelerate the convergence process. Ideally, we would like it to work on a simple laptop.
- **Can the new solver be easily adapted to the new experiments performed in ICP facilities?** We want the solver to be able to reproduce 3D modes, such as the effect of the coil geometry, jet instabilities and the simulation of the ripple part component of the generator and the general unsteady behavior of ICP facilities. We also want to explore more more detailed physics: non-equilibrium (both thermal and chemical), radiation and possibly the combination of LTE and elemental de-mixing. We also want to study more complex probe geometries, such as the probes used in the context of black out. Will the developed solver be able to withstand these applications?

With the goal of answering these questions, we have structured our work as follows:

Chapter 2 presents the equations governing a plasma in local thermodynamic equilibrium (LTE). Starting from a general form of the Boltzmann equation, we discuss the basic assumptions underlying the LTE model and give a short presentation of more general plasma descriptions, hinting at future developments. This Chapter does not contain any original scientific contribution, but sets the framework of the project.

Chapter 3 presents additional assumptions specific to ICP based on the LTE plasma equations derived in Chapter 2. In particular, we introduce hypotheses on the electric field, on the flow geometry and on the time averaging of the equations with respect to the induction current frequency.

Chapter 4 discusses the hybridized discontinuous Galerkin method applied to ICP. We present a new monolithic multi-domain solver valid for any conservation law, but particularized to ICP.

Chapter 5 presents a validation and verification of the ICP numerical simulation. We perform convergence studies using manufactured solution. We also study the dependence of the solution on the mesh size and on the order of the method, and compare our results with an existing code. We also discuss the convergence properties of our solver.

Chapter 6 We study the impact of the simulation parameters on the ICP torch. This can be especially helpful for the experimenter, as it helps predicting the facility behavior and thus better prepare the experiment. We have studied separately the effect of the frequency, power, mass flow rate, swirl and background pressure on the various flow fields.

2

Governing equations

This work considers only plasma in both thermal and chemical equilibrium. Consequently, the species composing the plasma have a common temperature and are implied in infinite rate chemical reactions. This relatively simple model misses many physical and chemical features of plasma flows. One of the possibilities to improve the predictions of this model is to consider elemental demixing, *i.e.* the diffusion of elements. It was proved by Rini [98] that, when a plasma is not too far from chemical equilibrium, considering an LTE model accounting for the elemental diffusion gave as accurate results as non-equilibrium models, with the advantage to have an easier set of equations to solve. However, we do not consider this topic here. Before presenting the LTE governing equations, we give a brief review of the wide variety of plasma thermo-chemical models that should be tested in future ICP simulations.

2.1 Review of plasma modeling

Plasma can be modeled using the kinetic theory of gas, representing it as a collection of a large number of charged particles interacting with each other and with a surrounding electromagnetic field. It consists in defining an equation for the velocity distribution function of each species constituting the plasma: the Boltzmann equation. The latter expresses the temporal evolution of this velocity distribution function by taking into account the short (collisions of a particle and a neutral one) and long (between charged particles, due to the electromagnetic force) range interactions between particles. Solving this equation is still a subject of research for rarefied plasma flow[42, 41, 30, 56, 84, 115], but is not the scope of this thesis. The plasma considered in this work is sufficiently dense to be considered as a fluid. We thus use an approach based on the moments of the Boltzmann equation to determine conservation laws for the species constituting the plasma.

The kinetic plasma theory produces equations describing plasma using statistical mechanics. The starting point of the kinetic theory is the Boltzmann equation for each particle composing the plasma. Besides the variety of particles, their energy levels and the way they collide with each other are also important in the description of the plasma flow. Generally speaking, the plasma model accuracy increases with the number of species taken into account and the level of accuracy of the modeling of collisions. However, a too detailed description leads to overly complex models with prohibitive computational costs. The simplest model, and the one used in this work, is

a mixture at *thermochemical equilibrium*, meaning that the excitation and deexcitation processes are in equilibrium, and the chemistry reaction occur much faster than the hydrodynamic timescale. It has been shown that, for sufficiently large pressure and low induction frequency, this assumption is reasonable for inductively coupled plasma [81, 82]. However, in this work, we do not always satisfy these conditions, but still consider the LTE model as a working approximation. Note also that models exists accounting for elemental demixing, but we do not discuss them here ([98]). A second model is the *thermal equilibrium* with finite rate chemistry. In this case, a continuity equation for each species has to be solved, accounting for the species production rate through chemical reactions. The advantage of such model is the relatively low computational cost, but assumes a single temperature for the whole mixture. To account for non-equilibrium phenomena, *multi-temperature* models, based on thermal and chemical approach rather than kinetic theory, have been introduced by Park [95] and Lee [70]. These models are still largely used today in aerospace applications. This model assumes that every internal energy mode, *i.e.* the electronic, vibrational and rotational energy modes of the molecules can be decoupled. Each mode represents a distinct thermal bath. While computationally efficient compared to more detailed models, its main disadvantage is the strong assumption of separability of the modes, making these models valid only for small departures from equilibrium. Coming back to the kinetic theory, *state-specific* models improves the validity of multi-temperature descriptions by considering some energy states as pseudo-species [76]. The energy of a molecular state is split into modes assumed to be far from equilibrium. Each mode is treated as a separate multi-temperature pseudo-species. In the same spirit, *state-to-state* models are the most rigorous energy partitioning models, treating all internal energy levels as pseudo-species [58, 59, 94]. However, they are computationally expensive due to the large number of energy levels far from equilibrium. Finally, the *coarse-grain* model [83, 79, 69, 86] groups close energy levels into bins, reducing the computational costs. Each bin is then treated as a pseudo-species, with its own temperature and continuity equation. It was shown that, with a limited number of bins, the non-equilibrium behavior of the plasma is retrieved [83].

The second challenge of kinetic theory is to compute the transport coefficients arising from the moments of Boltzmann's equation. They are determined using the transport theory, which consists in studying deviation from thermochemical equilibrium by developing the velocity distribution function in powers of a small parameter measuring that deviation. It then provides a relationship between the thermal quantities, based on the velocity fluctuations, and the gradient of the macroscopic quantities. Detailing the procedure for determining those coefficients is far beyond the scope of this thesis. The interested reader may refer to the work of Braginskii [13] or Balescu [7, 8] for an introduction to this exercise. The work of Chapman and Cowling [17] exposes early results of the kinetic theory, and the expansion procedure from the equilibrium configuration (the so-called Chapman-Enskog expansion). The plasma under investigation in this work are partially ionized, and have been broadly studied in the literature. To cite a few contributions, Kruger and Mitchner studied plasma out of equilibrium undergoing a magnetic field [64]. Kolesnikov [63] proposed the

first model self-consistent regarding diffusive phenomena. Magin developed models specifically designed for ICP applications [78, 77], with a simple Eucken correction for taking into account internal degrees of freedom of atoms and polyatomic molecules. Later, Graille *et. al* have derived a kinetic model for multi-component plasmas taking into account the electromagnetic field and thermal non-equilibrium influence [50]. Moreover, Nagnibeda and Kustova [87] developed a transport theory accounting for the internal energy and the non-equilibrium effects. In this work, the internal energy is ignored in the computation of the transport properties. However, a simple Eucken correction is applied to the heat flux.

Another important feature of plasma flows is the electromagnetic field. In plasma, the charged species evolve in an electromagnetic field that is partially originating from an external source (such as a coil) but also partially produced by themselves. The electric and magnetic fields can be described using the well-known Maxwell's equations. In the following, we will consider the specific case of un-magnetized plasma, *i.e.* the magnetic field is sufficiently small to have no impact on the transport properties. We will also consider the plasma as a linear, homogeneous and isotropic medium with respect to electromagnetic fields, with the vacuum electric permittivity and magnetic permeability.

2.2 Thermo-chemical equilibrium model for inductively coupled plasma

Starting from the Boltzmann equation, we give a general outline for the derivation of the plasma equations at thermal and chemical equilibrium. The developments presented here follow closely the notation proposed by Giovangigli [46].

2.2.1 The Boltzman equation

Let us consider a plasma composed of several species denoted by $i \in S$, with S the set of all species composing the plasma. Let $f_{i,I}(\mathbf{x}, \mathbf{c}_i, t)$ be the velocity distribution function of a particle i, with $\mathbf{x}$ the position, $\mathbf{c}_i$ the species velocity, t the time and $I \in Q_i$ its quantum energy state, Q_i being the set of admissible quantum energy state of species i. f_i is governed by the Boltzmann equation

$$\mathcal{D}_i(f_i) = \partial_t f_{i,I} + \mathbf{c}_{i,I} \cdot \nabla f_{i,I} + \frac{\mathbf{F}_i}{m_i} \cdot \partial_{\mathbf{c}_i} f_{i,I} = \mathcal{S}_i + \mathcal{C}_i, \quad \forall i \in S, \tag{2.1}$$

where $\mathcal{D}_i$ is the streaming differential operator, m_i is the species mass, $\mathbf{F}_i$ is the external force undergone by species i, ∇ is the gradient operator in spatial coordinates and $\partial_{\mathbf{c}_i}$ is the gradient operator in the velocity space. The only force acting on the

system is assumed to be the Lorentz force, given by

$$\mathbf{F}_i = q_i \left(\mathbf{E} + \mathbf{c}_i \times \mathbf{B} \right), \quad \forall i \in S, \tag{2.2}$$

where q_i is the charge of particle of species i, $\mathbf{E}$ and $\mathbf{B}$ are respectively the electric and magnetic fields. Note that the electromagnetic field results not only from external sources, but also from the particles composing the plasma themselves.

Another crucial concept in kinetic theory is *collisions*. Collisions are interactions between particles (of the same or different kind) sufficiently close to each other. There can be short ranges collisions (implying a neutral and another particle) or long range (implying two charged particles due to electromagnetic force). These collisions have an impact on the distribution function of the particle, and are taken into account as source terms on the right hand side of Eq. (2.1). Collisions can either be scattering, as represented by the operator $\mathcal{S}_i$, or chemically reacting, as represented by the operator $\mathcal{C}_i$. On the contrary of the former, the latter create and destroy species through a chemical reaction. Note that we do not consider nuclear plasma here, so the mass is always conserved.

Macroscopic quantities

Eq. (2.1) is not solved as such. Since the considered plasmas are dense enough to have a fluid behaviour, macroscopic densities can be defined. The species number density n_i represents the number of particles of species i per unit volume

$$n_i = \sum_{I \in Q_i} \int f_{i,I} d\mathbf{c}_i. \tag{2.3}$$

The density is then given by ρ_i,

$$\rho_i = m_i n_i. \tag{2.4}$$

We also define the mixture density ρ

$$\rho = \sum_{i \in S} \rho_i, \tag{2.5}$$

and the mixture hydrodynamic velocity $\mathbf{v}$ as

$$\rho \mathbf{v} = \sum_{i \in S} \sum_{I \in Q_i} \int m_i \mathbf{c}_i f_{i,I} d\mathbf{c}_i \tag{2.6}$$

The mixture total energy is given by

$$\frac{1}{2} \rho \mathbf{v} \cdot \mathbf{v} + e = \sum_{i \in S} \sum_{I \in Q_i} \int \left(\frac{1}{2} m_i \mathbf{c}_i \cdot \mathbf{c}_i + E_{iI} \right) f_i d\mathbf{c}_i \tag{2.7}$$

where E is the internal energy of the mixture and E_{iI} is the internal energy of species i in quantum state I. The species diffusion velocity is defined as

$$\mathbf{V}_i = \frac{1}{n_i} \sum_{I \in Q_i} \int \mathbf{C}_i f_{i,I} d\mathbf{c}_i, \tag{2.8}$$

with $\mathbf{C}_i$ the peculiar diffusion velocity, defined as

$$\mathbf{C}_i = \mathbf{c}_i - \mathbf{v}. \tag{2.9}$$

Collisional invariants

According to the laws of dynamics, and energy conservation principles, the mass, momentum and total (kinetic + internal) energy are conserved after a collision. These collisional invariants are functionals denoted ψ^l, $l \in [1; n+4]$, where n_s is the number of species composing the mixture, whose value summed over all species implicated in a collision does not change during that collision. For the scattering operator $\mathcal{S}$, they take the form of

$$\begin{cases} \psi_i^k & = \delta_{ki}, & k, i \in S, & \text{(Mass conservation)} \\ \psi_i^{n+\nu} & = m_i c_{\nu i}, & i \in S,\ \nu \in 1,2,3 & \text{(Momentum conservation)} \\ \psi_i^{n+4} & = \frac{1}{2} m_i \mathbf{c}_i \cdot \mathbf{c}_i + E_{iI} & i \in S,\ I \in Q_i & \text{(Energy conservation)} \end{cases} \tag{2.10}$$

where $c_{\nu i}$ is the component of $\mathbf{c}_i$ in the ν direction. These collisional invariants, once projected on the Boltzmann equation, give conservation equations. Let us define the following scalar product

$$(\xi, \zeta) = \sum_{i \in S} \sum_{I \in Q_i} \int \xi_i \zeta_i d\mathbf{c}_i. \tag{2.11}$$

One can show that the projection of the collisional invariants on the scattering collision operator $\mathcal{S}$ yields [46]

$$(\psi^l, \mathcal{S}) = 0. \tag{2.12}$$

Taking into account Eq. (2.12), one gets the general form of macroscopic equations associated to collisional invariant ψ^l:

$$\left(\psi^l, \mathcal{D}(f)\right) = \left(\psi^l, \mathcal{C}_i\right). \tag{2.13}$$

Enskog expansion

The macroscopic plasma equations are obtained from the Enskog expansion of the velocity distribution function as a function of a small parameter ϵ around the Maxwellian velocity distribution function f_i^0

$$f_i = f_i^0 (1 + \epsilon \phi_i + \mathcal{O}(\epsilon^2)). \tag{2.14}$$

The ϵ parameter is the Knudsen number, which is small in the fluid limit. Using ε, it is possible to rewrite Eq. (2.1) as

$$\mathcal{D}_i(f_i) = \frac{1}{\epsilon}\mathcal{S}_i + \epsilon^a \mathcal{C}_i, \quad \forall i \in S, \tag{2.15}$$

The parameter a represnts the collisional regime of the plasma. If $a = -1$, the plasma is in kinetic equilibrium, meaning that the scattering collision term is as important as the chemical one. If $a = 0$, we are in strong reaction regime, where reactive collisions are dominated by scattering collisions. Finally, $a = 1$ is the Maxwellian regime, where the scattering collisions are much more important than the chemical ones. In this work, we assume that $a = 1$. From there, the scattering collisionnal invariants ψ^l are projected on Eq. (2.15) and, considering Eq. (2.12), one gets

$$\Big(\psi^l, \mathcal{D}(f)\Big) = \epsilon \Big(\psi^l, \mathcal{C}\Big) \tag{2.16}$$

The expansion of Eq. (2.14) is then plugged in Eq. (2.16) and, after some algebra not detailed in this work, the macroscopic equations are retrieved.

2.2.2 Macroscopic equations for plasma in thermochemical equilibrium

The macroscopic equation governing the plasma flow in the Maxwellian collisional regime are given in their general form by

$$\begin{cases} \partial_t \rho_i + \nabla \cdot (\rho_i \mathbf{v}) + \nabla \cdot (\rho_i \mathbf{V}_i) & = \dot{\omega}_i, \forall i \in S \\ \partial_t (\rho \mathbf{v}) + \nabla \cdot (\rho \mathbf{v}\mathbf{v} + p\mathbb{I}) - \nabla \cdot \boldsymbol{\tau} & = \mathbf{j} \times \mathbf{B} \\ \partial_t \left(\frac{1}{2}\rho ||\mathbf{v}||^2 + \rho e\right) + \nabla \cdot (\rho H \mathbf{v}) + \nabla \cdot (\mathbf{q} - \boldsymbol{\tau} \cdot \mathbf{v}) & = \mathbf{j} \cdot \mathbf{E} \end{cases} \tag{2.17}$$

where $\mathbf{V}_i$ is the species diffusion velocity, $\dot{\omega}_i$ is the species production rate, $H = e + \frac{||\mathbf{v}^2||}{2} + \frac{p}{\rho}$ is the mixture total enthalpy, $\mathbf{E}$ is the electric field, $\mathbf{B}$ is the induced magnetic field, $\mathbf{j}$ is the diffusion current and q is the charge. Since we are not interested in length scales smaller than the Debye length, the plasma is considered quasi-neutral. Finally, $\boldsymbol{\tau}$ is the viscous stress tensor and $\mathbf{q}$ is the heat flux. In this work, we solve a simplified version of Eq. 2.17, using the property of mass conservation (no mass is produced)

$$\sum_{i \in S} \dot{\omega}_i = 0 \tag{2.18}$$

and the linear dependence of the diffusion fluxes

$$\sum_{i \in S} \rho_i \mathbf{V}_i = 0, \tag{2.19}$$

yielding a set of equations for the plasma mixture (also arising from mass conservation)

$$\begin{cases} \partial_t \rho + \nabla \cdot (\rho \mathbf{v}) & = 0 \\ \partial_t (\rho \mathbf{v}) + \nabla \cdot (\rho \mathbf{v}\mathbf{v} + p\mathbb{I}) - \nabla \cdot \boldsymbol{\tau} & = \mathbf{j} \times \mathbf{B} \\ \partial_t \left(\frac{1}{2} \rho ||\mathbf{v}||^2 + \rho e \right) + \nabla \cdot (\rho H \mathbf{v}) + \nabla \cdot (\mathbf{q} - \boldsymbol{\tau} \cdot \mathbf{v}) & = \mathbf{j} \cdot \mathbf{E} \end{cases} \tag{2.20}$$

On the right hand side of the momentum equation, the term $\mathbf{j} \times \mathbf{B}$ appears. In fact, the only external force acting on particle $i \in S$ is the Lorentz force, given by

$$\mathbf{F}_i = n_i q_i \mathbf{E} + n_i q_i \left(\mathbf{v} + \mathbf{V}_i \right) \times \mathbf{B} \tag{2.21}$$

Consequently, the total force exerted on the plasma is

$$\mathbf{F} = \sum_i \mathbf{F}_i = \sum_i n_i q_i \left(\mathbf{E} + \mathbf{v} \times \mathbf{B} \right) + n_i q_i \mathbf{V}_i \times \mathbf{B} \tag{2.22}$$

Because of the plasma quasi neutrality,

$$\sum_{i \in S} n_i q_i = 0, \tag{2.23}$$

the linear dependence of the diffusive flux (Eq. (2.19)) and defining the diffusion current

$$\mathbf{j} = \sum_i n_i q_i \mathbf{V}_i, \tag{2.24}$$

one gets

$$\mathbf{F} = \mathbf{j} \times \mathbf{B} \tag{2.25}$$

which is the force effectively felt by the particles. On the other hand, the power dissipated by the Lorentz force for each species is

$$P = \sum_i P_i = \sum_i \mathbf{F}_i \cdot \left(\mathbf{v} + \mathbf{V}_i \right). \tag{2.26}$$

Using once again the quasi neutral hypothesis and some algebra, one can prove that

$$P = \sum_i n_i q_i \mathbf{V}_i \cdot \mathbf{E} = \mathbf{j} \cdot \mathbf{E}, \tag{2.27}$$

giving the right hand side of the energy equation.

Transport fluxes in equilibrium plasma

The transport fluxes describe the rate at which particles, momentum or energy are transported by diffusion. They depend on parameters called transport coefficients, and discussed below. The viscous stress tensor $\boldsymbol{\tau}$, impacting the momentum and

energy transport fluxes, is given by

$$\boldsymbol{\tau} = \eta \left[\nabla \mathbf{v} + (\nabla \mathbf{v})^T - \frac{2}{3} (\nabla \cdot \mathbf{v}) \mathbb{I} \right] + \kappa (\nabla \cdot \mathbf{v}) \mathbb{I} \tag{2.28}$$

with κ and η respectively the bulk and dynamic viscosity. In this work, κ is neglected, although it can have a significant impact for large polyatomic gases (Giovangigli *et al.* [47]) and non-equilibrium flows. The heat flux q, intervening in the energy transport diffusion flux, is given by

$$\mathbf{q} = -\lambda \nabla T \tag{2.29}$$

where T is the plasma equilibrium temperature and λ is the thermal conductivity. We take a few steps away from the derivation of Giovangigli and use an approach that was employed by Scoggins [102]. We split λ into several contributions:

$$\lambda = \lambda_h + \lambda_e + \lambda_{int} + \lambda_R + \lambda_D \tag{2.30}$$

where

- λ_h is the heat diffusion coefficient associated to heavy particles translation.
- λ_e is the heat diffusion coefficient associated to electron translation. Its relative importance increases with temperature.
- λ_{int} is the heat diffusion coefficient associated to rotation and vibration of the species. Its relative importance also increases with temperature.
- λ_R is the reactive heat diffusion coefficient. It represents the heat transfer due to the energy of the chemical reaction and the diffusion of the species in the plasma.
- λ_D is the heat diffusion due to the Dufour effect, namely the heat transfer resulting from a concentration gradient of the species.

Note that the classic Fourier coefficient $\lambda_{Fourier}$ is only given by

$$\lambda_{Fourier} = \lambda_h + \lambda_{int}. \tag{2.31}$$

Finally, the diffusion current $\mathbf{j}$, defined as

$$\mathbf{j} = \sum_i n_i q_i \mathbf{V}_i \tag{2.32}$$

with q_i the charge, n_i the number density and $\mathbf{V}_i$ the diffusion velocity of species i. Using kinetic theory, it is possible to derive a general expression for $\mathbf{j}$ which depends on the electric field $\mathbf{E}$, the electric conductivity σ, the pressure p, the temperature gradients and the diffusion coefficients D_{ij}, representing the rate at which species i

diffuse within species j:

$$\mathbf{j} = \sigma\mathbf{E} - \sum_{i,j\in S} n_i q_i D_{ij} \left(\frac{\nabla p_j}{n k_B T_h} - \frac{y_j p}{n k_B T_h} \nabla \ln(p) + k^h_{T_j} \nabla \ln(T_h) + k^e_{T_j} \nabla \ln(T_e) \right) \quad (2.33)$$

where S is the set of all species constituting the plasma, T_e and T_h are the electrons and heavy temperatures, y_i is the species mass fraction, n is the plasma number density, n_i is species i number density, $\kappa^e_{T_i}$ and $\kappa^h_{T_i}$ are the thermal diffusivity of the electrons and heavies respectively, D_{ij} is the diffusion coefficient of species i in species j, p is the plasma pressure, p_i is species i partial pressure, q_i is the charge of species i, σ the plasma electric conductivity and k_B the Boltzmann constant. Eq. (2.33) is in fact a generalized Ohm's law. In the absence of spatial gradients, one can prove that the electrons diffuse much faster than the heavies. Consequently, only the electrons carry the diffusion currents and Eq. (2.33) becomes

$$\mathbf{j} \simeq \sigma_e \mathbf{E}, \quad (2.34)$$

with σ_e the electron electric conductivity.

Transport coefficients

The viscosity η, thermal conductivity λ and electrical conductivity σ_e are transport coefficients that can be determined using the kinetic theory. More specifically, the transport properties are computed using the Galerkin approximate solution of the linearized Boltzmann equation. In order to compute these coefficients, we use the Mutation++ library developed by Scoggins *et al.* [103]. In Fig. 2.1, we show the discrepancy between the Sutherland and LTE viscosity of a mixture of air with 11 species at a pressure of 1 atmosphere. The viscosity η_i of a fluid composed of particles of type $i \in S$ is basically proportional to the square root of the particle temperature T_i and conversely proportional to its effective collisional cross section σ_i, with σ_i a portion of space surrounding the particle where collisions occur

$$\eta_i \propto \frac{\sqrt{T_i}}{\sigma_i}. \quad (2.35)$$

For constant σ_i, viscosity is proportional to $\sqrt{T}$, which is in fact Sutherland's law. However, when increasing the temperature of the gas, the plasma starts to ionize. Ionization tends to diminish the mean free path of the particles. It means that they more frequently collide, and their cross-section increases accordingly. The viscosity evolution departs from Sutherland's law (around $2000\,\mathrm{K}$ for air). When the ionization becomes sufficiently large, viscosity starts to diminish again (around $11\,000\,\mathrm{K}$ for air).

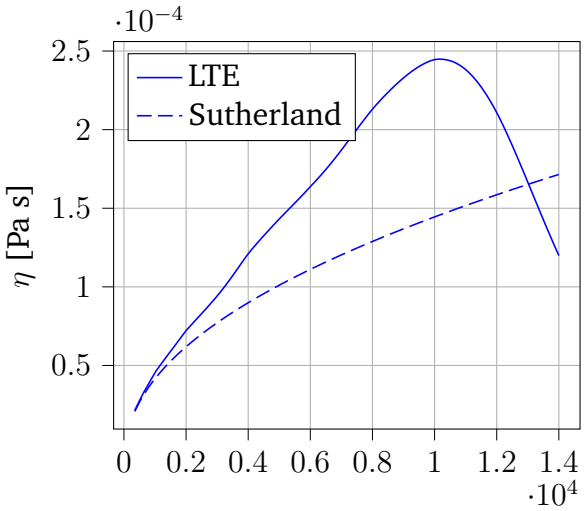

Fig. 2.1.: Comparison between the dynamic viscosity η obtained via Sutherland's law and using Mutation++ with a LTE model for a mixture of air with 11 species at $1\,\mathrm{atm}$. For low temperatures, both quantities are very similar, following a profile proportional to $\sqrt{T}$. When ionization becomes important, the effective collisional cross-section increases, and the Sutherland and LTE viscosities differ greatly.

In Fig. 2.2, we have compared the heat conductivity obtained *via* Fourier's law and using the LTE model. It can be shown that the reactive conductivity of each species $\lambda_{R,i}$, which is taken into account in LTE but not in the Fourier model, is proportional to the variation of the molar mass fraction with respect to temperature. When looking at the air molar fraction in Fig. 2.5, the peaks observed in Fig. 2.2 correspond to large variations of the molar fraction of the species. For instance, the peak in heat conductivity around $3000\,\mathrm{K}$ is explained by the dissociation of dioxygen O_2 in oxygen O. and the creation of nitrogen oxide NO. On the other hand, around $7000\,\mathrm{K}$, the dinitrogen N_2 dissociates in nitrogen N. Finally, around $10\,000\,\mathrm{K}$, the nitrogen and oxygen ionize, releasing electrons. The latter also participate in heat transfer and increase the heat conductivity of the mixture. It is represented by λ_e. These effects, not taken into account in the simple Fourier model, have an important impact on the plasma heat conductivity.

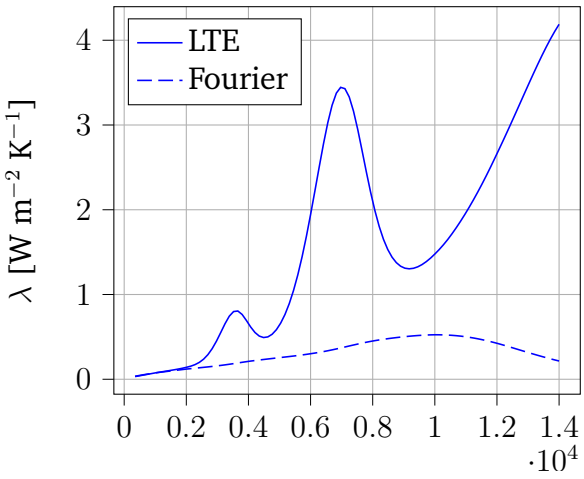

Fig. 2.2.: Comparison between the heat conductivity coefficient λ computed with Fourier's law and using Mutation++ with a LTE model for a mixture of air with 11 species at $1\,\mathrm{atm}$. For low temperatures, both quantities are very similar, but depart as the temperature is increased.

The heat capacity at constant pressure of the mixture (Fig. 2.3) has the same behaviour as the heat conductivity, with peaks at the same temperature. In fact, the heat capacity depends on the mass fractions Y_i variation of the species with respect to temperature (instead of the species molar fractions X_i). However, for air, both quantities behave similarly, giving qualitatively similar profiles.

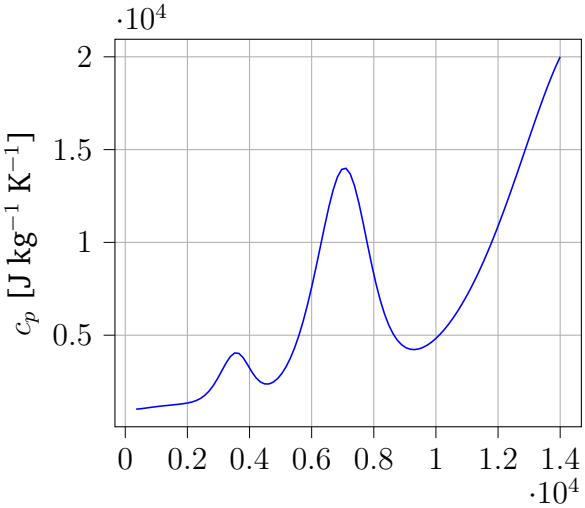

Fig. 2.3.: Heat capacity at constant pressure c_p of air mixture with 11 species at $1\,\mathrm{atm}$ as a function of temperature.

Finally, the electric conductivity increases with temperature (Fig. 2.4). Since the conductivity is increasing due to the electrons, it start increasing when the gas ionizes, close to $7000\,\mathrm{K}$.

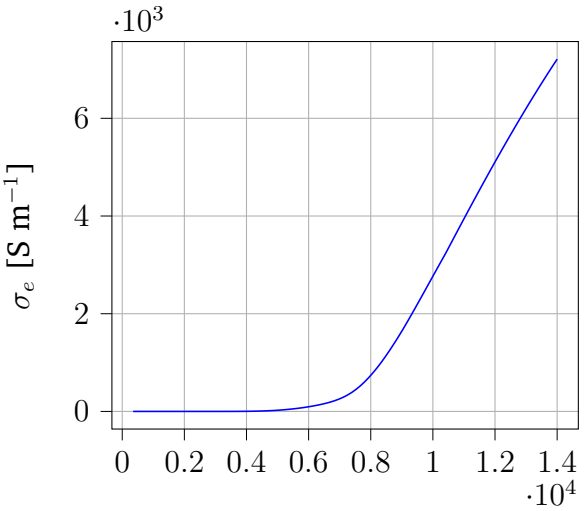

Fig. 2.4.: Electric conductivity σ_e of air mixture with 11 species at $1\,\mathrm{atm}$ as a function of temperature.

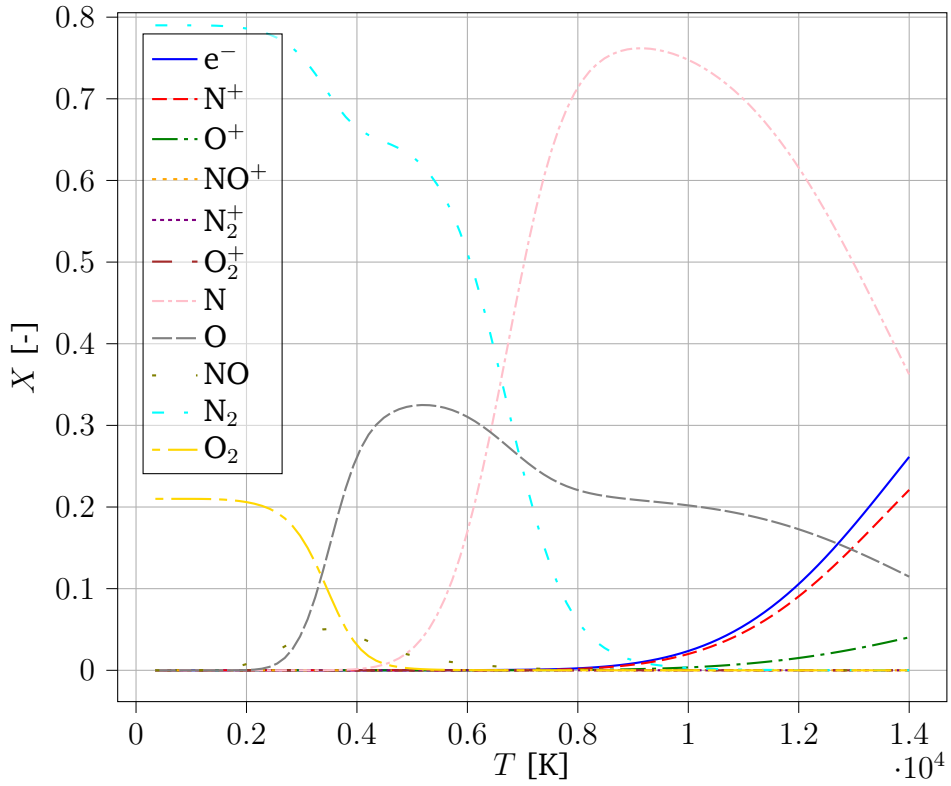

Fig. 2.5.: Species molar fractions X of a mixture of air with 11 species at $1\,\mathrm{atm}$.

2.3 Navier-Stokes and Maxwell's equation

The previous considerations lead to the following system of equations describing the plasma flow at thermochemical equilibrium

$$\begin{cases} \partial_t \rho + \nabla \cdot (\rho \mathbf{v}) & = 0 \\ \partial_t (\rho \mathbf{v}) + \nabla \cdot (\rho \mathbf{v}\mathbf{v} + p\mathbb{I}) - \nabla \cdot \boldsymbol{\tau} & = \mathbf{j} \times \mathbf{B} \\ \partial_t \left(\frac{1}{2}\rho ||\mathbf{v}||^2 + \rho e \right) + \nabla \cdot (\rho H \mathbf{v}) + \nabla \cdot (\mathbf{q} - \boldsymbol{\tau} \cdot \mathbf{v}) & = \mathbf{j} \cdot \mathbf{E} \end{cases} \tag{2.36}$$

where

$$\begin{aligned} H &= e + \frac{1}{2}||\mathbf{v}||^2 + \frac{p}{\rho} && \textit{(Total enthalpy)} \\ \tau &= \eta \left[\nabla \mathbf{v} + (\nabla \mathbf{v})^T \right] - \frac{2}{3}\eta \nabla \cdot \mathbf{v}\mathbb{I} && \textit{(Viscous stress tensor)} \\ \mathbf{q} &= -\lambda \nabla T && \textit{(Heat flux)} \end{aligned} \tag{2.37}$$

with all symbols keeping their previous meaning and $\mathbf{j}$ following Ohm's law Eq. (2.33). The transport properties of the plasma mixture are computed using the Mutation++ library according to the LTE model. The electromagnetic field is governed by Maxwell equations for un-magnetized and un-polarized media, given by (assuming the quasi-neutrality of the plasma)

$$\begin{aligned} \nabla \cdot \mathbf{E} &= 0 \\ \nabla \cdot \mathbf{B} &= 0 \\ \partial_t \mathbf{B} + \nabla \times \mathbf{E} &= \mathbf{0} \\ -\epsilon_0 \partial_t \mathbf{E} + \frac{1}{\mu_0} \nabla \times \mathbf{B} &= \mathbf{j} \end{aligned} \tag{2.38}$$

where $\epsilon_0 = 8.854 \times 10^{-12}$ F m^{-1} and $\mu_0 = 4\pi \times 10^{-7}$ N A^{-2} are respectively the vacuum electric permittivity and magnetic permeability.

Eq. (2.36) and (2.38) can be used for general quasi-neutral plasma in local thermodynamic equilibrium. In the next Chapter, we make additional simplifying assumptions to adapt them for the simulation of inductive plasma. Although these equations give satisfactory results for particular flow configurations, it should be noted that they fail for non-equilibrium regimes. The main focus of this work being the study of hybridized discontinuous Galerkin methods for ICP, the more detailed plasma models will not be explored.

2.4 Conclusions on the plasma governing equations

In this Chapter, we have presented the outline of the usual method to derive the plasma governing equations starting from the Boltzmann equation at thermochemical equilibrium. However, these equations still need to be particularized to the case of axisymmetric ICP, which is done in the next Chapter. Although the presented model has a restrained range of application, one must keep in mind that simulating the plasma flow of an ICP facility using a high order numerical solver is a challenging task. These assumptions are considered in order to ease the solver implementation. In the future, one should consider more detailed thermochemical models to extend the validity of the ICP numerical solver.

3

Model for inductively coupled plasma

We present the physcial model for the axisymmetric LTE inductively coupled plasma (ICP). It is similar to the one used in legacy ICP solver (see for instance Boulos [12], the group of Proulx [40], Vanden Abeele [106] or Magin [75]). It is based on an axisymmetric description of the hydrodynamic and electric fields, and the thermochemical equilibrium description of the plasma presented in Chapter 2. We first particularize Eq. (2.36) to the axisymmetric LTE ICP configuration. Then, we present the non-dimensional form of the ICP equations, and discuss the non-dimensional parameters.

3.1 Axisymmetric ICP equations

The general system of governing equations describing the flow of a quasi-neutral plasma at equilibrium has been presented in Chapter 2, in Eq. (2.36) and (2.38). We particularize them for the case of axisymmetric and LTE inductively coupled plasma following a series of additional assumptions listed below.

Collision-dominated and thermal plasma The plasma is dominated by intermolecular collisions. Consequently, the mean free path of the molecules is very small, and the continuity hypothesis applies. Moreover, the collisions are assumed to bring all species at a common equilibrium temperature. One must keep in mind that thermal non-equilibrium state has been observed in ICP for low pressure or high induction frequency (see *e.g.* [82, 81, 116]). Indeed, if the pressure is too low, the collisions between the particles are not sufficient for all species to thermalize. On the other hand, a too high induction frequency prevents the electrons to return to their equilibrium state. In the future, thermal non-equilibrium configurations should be investigated.

Quasi-neutrality The plasma characteristic length ℓ is assumed to be much larger than the Debye length λ_D, *i.e.* the length at which thermal fluctuations break charge neutrality,

$$\ell \gg \lambda_D = \sqrt{\frac{\epsilon_0 k_B T_e}{n_e q_e^2}}, \tag{3.1}$$

with ϵ_0 the air electric permittivity, k_B the Boltzmann constant, T_e the electronic

temperature, n_e the electron number density and q_e the electron charge. Consequently, the plasma is considered quasi-neutral, and $q \simeq 0$ to a high level of accuracy.

No displacement current The plasma oscillation frequency f_p is defined by

$$f_p = \frac{q_e}{2\pi}\sqrt{\frac{n_e}{\epsilon_0 m_e}} \tag{3.2}$$

where q_e, m_e and n_e are respectively the electron charge, mass and number density, and ϵ_0 is the vacuum electric permittivity. The coil induction current produces electromagnetic waves with characteristic wavelength

$$\lambda_{ELM} = \frac{1}{f\sqrt{\epsilon_0 \mu_0}} \tag{3.3}$$

with μ_0 the vacuum magnetic permeability and f the current frequency. The electromagnetic waves break charge neutrality and create oscillations of the electrons in the plasma with frequency f_p. In this work, we assume that $f \ll f_p$, which implies that the electron return sufficiently fast to equilibrium to neglect the effect of electromagnetic waves. On the other hand, the torch characteristic length L_C is much smaller than the electromagnetic wavelength λ_{ELM}. We thus fully neglect the displacement currents in Maxwell equations.

Axisymmetry Assuming axisymmetry excludes 3D plasma modes and coil-induced torch asymmetry [10]. Moreover, the coil is modeled as a series of infinitely thin parallel wires, although in experimental set-up, the coils are organized as slabs surrounding the torch. The electric field from these loops is determined analytically [57].

Non-radiative plasma No radiation is considered here, although radiation can have a significant impact on heat transfer and temperature profile caused by the medium itself at sufficiently high pressure [65, 60]. Having a reliable radiation model requires a relevant spectral database and expensive computations [105], but should definitely be included in future developments.

Neglected gravity It is assumed that gravity plays a negligible role in ICP flows.

No elemental de-mixing Elemental de-mixing is the separation of chemical elements by diffusion. This phenomenon is both present for equilibrium and non-equilibrium flows [98], but is ignored here.

Steady-state We assume the flow to be at steady-state. In general, ICP flows are unsteady due to possible the Kelvin-Helmholtz instabilities in the shear layer of the jet and the fast temporal variation of the different fields introduced by the high oscillation frequency of the induction current. However, we disregard these

effects, and average all variables over one oscillation period of the induction current. Then, in these time averaged equations, we find a steady solution ($\partial_t = 0$). Note that we show the temporal derivative in our developments to keep the argument general.

Local thermodynamic equilibrium The ICP computations are assumed to be at local thermodynamic equilibrium (LTE). The thermodynamic properties of the gas are computed using a linear interpolation in a thermodynamic table of states built using the Mutation++ library [103]. This table primary serves to retrieve the fluid density, internal energy, viscosity, thermal and electric conductivity. Note that the LTE assumption is reasonable for the jet exhausting the torch but questionable for the plasma in the torch (see for instance the work of Mostaghimi [82] or Zhang [116]).

Unmagnetized plasma Although plasma in ICP can be weakly magnetized, we assume that it is not the case in the model developed here. Consequently, the transport properties of the plasma are not affected by the magnetic field.

3.1.1 Hydrodynamic equations

Considering the previous hypotheses, the set of axisymmetric Navier-Stokes equations averaged over one oscillation period of the frequency is

$$\partial_t \mathbf{w} + \partial_z \left(\mathbf{F}_c^z - \mathbf{F}_v^z\right) + \partial_r \left(\mathbf{F}_c^r - r\mathbf{F}_v^r\right) = \mathbf{S} + \frac{\mathbf{F}_v^r - \mathbf{F}_c^r}{r} \tag{3.4}$$

where the vector of conservative variables is $\mathbf{w} = \left(\rho \quad \rho v_z \quad \rho v_r \quad \rho v_\theta \quad \rho e + \rho\frac{||\mathbf{v}||^2}{2}\right)^T$, the total flux is split in a convective and diffusive parts $\mathbf{F} = \mathbf{F}_c - \mathbf{F}_v$, the convective flux vector is given by

$$\begin{aligned} F_c^z &= \left(\rho v_z \quad \rho v_z^2 + p \quad \rho v_z v_r \quad \rho v_z v_\theta \quad \rho v_z H\right)^T, \\ F_c^r &= \left(\rho v_r \quad \rho v_r v_z \quad \rho v_r^2 + p \quad \rho v_r v_\theta \quad \rho v_r H\right)^T, \end{aligned} \tag{3.5}$$

the diffusive flux vector is given by

$$\begin{aligned} F_v^z &= \left(0 \quad \tau_{zz} \quad \tau_{zr} \quad \tau_{z\theta} \quad \textstyle\sum_j \tau_{zj} v_j - q_z\right)^T, \\ F_v^r &= \left(0 \quad \tau_{rz} \quad \tau_{rr} \quad \tau_{r\theta} \quad \textstyle\sum_j \tau_{rj} v_j - q_r\right)^T, \end{aligned} \tag{3.6}$$

and the source terms are given by

$$S = \left(0 \quad F_z^L \quad \frac{p+\rho v_\theta^2 - \tau_{\theta\theta}}{r} + F_r^L \quad \frac{-\rho v_r v_\theta + \tau_{r\theta}}{r} \quad P_J\right)^T. \tag{3.7}$$

with ρ the density, $\mathbf{v} = (v_z \ v_r \ v_\theta)$ the velocity vector, p the static pressure, $H = \rho e + \rho\frac{||\mathbf{v}||^2}{2} + p$ the specific total enthalpy and $q = -k\nabla T$ the heat flux, with T the temperature of the fluid. The components of the symmetric viscous stress tensor in cylindrical coordinates are given by

$$\begin{aligned}
\tau_{zz} &= 2\eta\left(\partial_z v_z - \frac{1}{3}\nabla\cdot\mathbf{v}\right) & \tau_{rr} &= 2\eta\left(\partial_r v_r - \frac{1}{3}\nabla\cdot\mathbf{v}\right)\\
\tau_{zr} &= \tau_{rz} = \eta\left(\partial_r v_z + \partial_z v_r\right) & \tau_{r\theta} &= \eta\left(\partial_r v_\theta - \frac{v_\theta}{r}\right)\\
\tau_{z\theta} &= \eta\partial_z v_\theta & \tau_{\theta\theta} &= 2\eta\left(\frac{v_r}{r} - \frac{1}{3}\nabla\cdot\mathbf{v}\right)
\end{aligned} \tag{3.8}$$

where η is the fluid dynamic viscosity and $\nabla\cdot\mathbf{v} = \partial_z v_z + \partial_r v_r + \frac{v_r}{r}$ is the divergence of the velocity field. Finally, the effective Lorentz force $\mathbf{F}^L$ and the power dissipated by joule heating P^J are linked to the real and imaginary parts (resp. E_I^{Im}, E_I^{Re}) of the induced electric field E_I (see Eq. (3.33))

$$\begin{aligned}
F_z^L &= \frac{\sigma_e}{4\pi f}\left[E_I^{Im}\partial_z E_I^{Re} - E_I^{Re}\partial_z E_I^{Im}\right],\\
F_r^L &= \frac{\sigma_e}{4\pi f}\left[E_I^{Im}\frac{1}{r}\partial_r(rE_I^{Re}) - E_I^{Re}\frac{1}{r}\partial_r(rE_I^{Im})\right],\\
P^J &= \frac{\sigma_e}{2}\left[(E_I^{Im})^2 + (E_I^{Re})^2\right]
\end{aligned} \tag{3.9}$$

where σ_e is the electron electric conductivity of the plasma and f is the frequency of the induction current. The electron electric conductivity σ_e is assumed to dominate the ionic electric conductivity and therefore is the only electric conductivity appearing in the equations. The transport properties at equilibrium are computed using Mutation++ [103]. The form of the effective Lorentz force and power dissipated by Joule effect is justified below, when discussing the electric field equation.

3.1.2 Electric field equations for axisymmetric ICP

We now simplify Maxwell equations in vacuum for quasi neutral plasma Eq. (2.38) for axisymmetric ICP. Neglecting the displacement currents, these equations become

$$\nabla\cdot\mathbf{E} = 0 \tag{3.10a}$$
$$\nabla\cdot\mathbf{B} = 0 \tag{3.10b}$$
$$\partial_t\mathbf{B} + \nabla\times\mathbf{E} = \mathbf{0} \tag{3.10c}$$
$$\frac{1}{\mu_0}\nabla\times\mathbf{B} = \mathbf{j}. \tag{3.10d}$$

The induced magnetic field being divergence-free, it is possible to write $\mathbf{B}$ as the rotational of a potential vector $\mathbf{A}$, effectively substituting Eq. (3.10b) by

$$\mathbf{B} = \nabla \times \mathbf{A}. \tag{3.11}$$

It is then possible to write Eq. (3.10c) as

$$\mathbf{E} = -\nabla\phi - \partial_t \mathbf{A}, \tag{3.12}$$

where ϕ is a scalar potential. Using Eq. (3.11) and (3.12), Ampere's law Eq. (3.10d) becomes

$$\frac{1}{\mu_0}\left[\nabla \times (\nabla \times \mathbf{A})\right] = \mathbf{j} \tag{3.13}$$

which can be expanded as

$$\frac{1}{\mu_0}\left[\nabla\left(\nabla \cdot \mathbf{A}\right) - \Delta\mathbf{A}\right] = \mathbf{j}. \tag{3.14}$$

The magnetic potential vector $\mathbf{A}$ and electric potential ϕ are not uniquely defined. In fact, the gradient of a scalar function can be added to $\mathbf{A}$ and ϕ without changing the magnetic and electric field. Indeed, it is easy to show that, if $\mathbf{A}'$ and ϕ' are defined as a function of the gradient of a scalar quantity Λ such that

$$\begin{aligned} \mathbf{A}' &= \mathbf{A} + \nabla\Lambda \\ \phi' &= \phi - \partial_t\Lambda \end{aligned} \tag{3.15}$$

then, the following equalities hold

$$\begin{aligned} \mathbf{B} &= \nabla \times \mathbf{A} = \nabla \times \mathbf{A}', \\ \mathbf{E} &= -\nabla\phi - \partial_t\mathbf{A} = -\nabla\phi' - \partial_t\mathbf{A}'. \end{aligned} \tag{3.16}$$

This indetermination is called gauge freedom. We can choose the gauge so the vectors $\mathbf{A}$ and ϕ obtain specific properties that simplify the equations. In this work, we use the Coulomb gauge, which is a gauge that has the property that $\mathbf{A}$ becomes divergence free

$$\nabla \cdot \mathbf{A} = 0, \tag{3.17}$$

Eq. (3.10d) becomes

$$\Delta\mathbf{A} = -\mu_0\mathbf{j}. \tag{3.18}$$

Finally, the Gauss law Eq. (3.10a) can be written as

$$\Delta\phi = -\partial_t\left(\nabla \cdot \mathbf{A}\right) = 0 \tag{3.19}$$

due to the Coulomb gauge. Consequently, the set of Maxwell's equations in vacuum for quasi-neutral plasma can be written using the magnetic potential vector $\mathbf{A}$ and

the electric potential ϕ (considering the Coulomb gauge $\nabla \cdot \mathbf{A} = 0$) as

$$\begin{aligned} \Delta\phi &= 0 \\ \mathbf{B} &= \nabla \times \mathbf{A} \\ \mathbf{E} &= -\nabla\phi - \partial_t \mathbf{A} \\ \Delta\mathbf{A} &= -\mu_0 \mathbf{j} \end{aligned} \tag{3.20}$$

The electric field $\mathbf{E}$ is then split into an electrostatic $\mathbf{E}_S$ part, due to the electromagnetic force between charged particles, and induced $\mathbf{E}_I$ part due to the response of the conductive plasma to the oscillating current generated by the coil

$$\mathbf{E} = \mathbf{E}_S + \mathbf{E}_I. \tag{3.21}$$

where

$$\begin{aligned} \mathbf{E}_I &= -\partial_t \mathbf{A} \\ \mathbf{E}_S &= -\nabla\phi \end{aligned} \tag{3.22}$$

Similarly, the current $\mathbf{j}$ is split into the current produced by the coil $\mathbf{j}_C$, which is known from the coil configuration, and the diffusion current produced in the plasma $\mathbf{j}_P$

$$\mathbf{j} = \mathbf{j}_P + \mathbf{j}_C \tag{3.23}$$

Deriving Eq. (3.14) with respect to time and taking into account the definition of the induced electric field and the generalized Ohm's law (we kept the same notations as in Eq. (2.33)), one gets the following set of equations for the electric field

$$\begin{aligned} &\Delta\mathbf{E}_I - \nabla\left(\nabla \cdot \mathbf{E}_I\right) = \mu_0\left(\mathbf{j}_C + \mathbf{j}_P\right) \\ &\mathbf{E}_S = -\nabla\phi \\ &\Delta\phi = 0 \\ &\mathbf{j}_P = \sigma\mathbf{E} - \mathbf{j}_\nabla \\ &\mathbf{j}_\nabla = \sum_{i,j\in S} n_i q_i D_{ij}\left(\frac{\nabla p_j}{n k_B T_h} - \frac{y_j p}{n k_B T_h}\nabla \ln p + k^h_{T_j}\nabla \ln T_h + k^e_{T_j}\nabla \ln T_e\right) \\ &\mathbf{E} = \mathbf{E}_S + \mathbf{E}_I \end{aligned} \tag{3.24}$$

One can reduce this system to solve an equation for the induced electric field and the Laplace equation for the electric potential, the other quantities being easy to reconstruct from the latter

$$\begin{aligned} &\Delta\mathbf{E}_I - \nabla\left(\nabla \cdot \mathbf{E}_I\right) = \mu_0\left[\sigma\left(\mathbf{E}_I - \nabla\phi\right) - \mathbf{j}_\nabla\right] \\ &\Delta\phi = 0 \end{aligned} \tag{3.25}$$

This equation has to be solved coupled to the Navier-Stokes equations, as σ and $\mathbf{j}_\nabla$ depend on hydrodynamic quantities such as pressure, temperature or diffusion velocities. Eq. (3.25) is relatively general, but has a high computational cost, as it

requires to solve the Laplace equation for ϕ and one equation for each electric field component in addition to the Navier-Stokes equations. Consequently, Eq. (3.25) is simplified for an axisymmetric configuration. Indeed, since $\partial_\theta \phi = 0$, the electrostatic field is located in the axisymmetric plane

$$\mathbf{E}_S = -\nabla\phi = -\partial_z\phi\ \mathbf{e}_z - \partial_r\phi\ \mathbf{e}_r \tag{3.26}$$

with r and z the radial and axial position. On the other hand, the induced electric field is in the azimuthal direction since the coil electric field is along $\mathbf{e}_\theta$

$$\mathbf{E}_I = E_I'\ \mathbf{e}_\theta \tag{3.27}$$

Because $\partial_\theta = 0$, the azimuthal component of $\mathbf{j}_\nabla$ is null. Ohm's law then becomes (recalling that, in the direction where no spatial gradient occur, the electric conductivity is mainly determined by the electrons, *i.e.* $\sigma \simeq \sigma_e$ as in Eq. (2.34))

$$\begin{aligned} j_{P,z} &= \sigma E_{S,z} - j_{\nabla,z} \\ j_{P,r} &= \sigma E_{S,r} - j_{\nabla,r} \\ j_{P,\theta} &= \sigma_e E_{I,\theta} \end{aligned} \tag{3.28}$$

with $\mathbf{j}_P = (j_{P,z}\ \ j_{P,r}\ \ j_{P,\theta})$, σ the plasma and σ_e the electron electric conductivity respectively. The Laplace equation for the electric potential should still be solved, subsequently determining the current in the plasma plane. However, to avoid solving for the Laplace equation, it is commonly assumed in axisymmetric ICP that the electrostatic field is *ambipolar*. The ambipolar assumption states that the electrostatic field $\mathbf{E}_S$ produced by the moving charges is such that no diffusion current occur in the axisymmetric plane

$$j_{P,z} = j_{P,r} = 0. \tag{3.29}$$

The electrostatic field can then be computed using the equations

$$\begin{aligned} \sigma E_{S,z} - j_{\nabla,z} &= 0 \\ \sigma E_{S,r} - j_{\nabla,r} &= 0. \end{aligned} \tag{3.30}$$

Because the induction current is sinusoidal, we use in this work the phasor notations. The coil being represented by a series of infinitely thin parallel wires, the current produced by the coil is given by

$$\mathbf{j}_C = I_C \exp(i2\pi f t) \sum_{l=1}^{N_{coil}} \delta(\mathbf{x} - \mathbf{x}_l)\mathbf{e}_\theta, \tag{3.31}$$

where I_C is the current magnitude, f the frequency, t the time, N_{coil} the coil number of turns, $\mathbf{x}$ the position vector, $\mathbf{x}_l$ the l^{th} coil position vector and i is the imaginary unit. The $\delta(\mathbf{x})$ function is 0 everywhere except when $\mathbf{x} = 0$, where $\delta = 1$. The induced

electric field also writes

$$E_I' = E_I \exp(i2\pi f t). \tag{3.32}$$

and the equation for the induced electric field Eq. (3.25) becomes

$$\partial_{zz}^2 E_I + \frac{1}{r}\partial_r \left(r\partial_r E_I\right) - \frac{E_I}{r^2} - i2\pi f \mu_0 \sigma_e E_I = i2\pi f \mu_0 r \sum_{k=1}^{N_{coil}} \delta(\mathbf{x} - \mathbf{x}_k) \tag{3.33}$$

The induced electric field can be split into a contribution from the plasma, E_P and the coil, E_C

$$E_I = E_C + E_P, \tag{3.34}$$

governed respectively by the equations

$$\partial_{zz}^2 E_C + \frac{1}{r}\partial_r(r\partial_r E_C) - \frac{E_C}{r^2} = 2i\pi f \mu_0 I_C \sum_{l=1}^{n_r} \delta(\mathbf{x} - \mathbf{x}_l) \tag{3.35}$$

and

$$\partial_{zz}^2 E_P + \frac{1}{r}\partial_r(r\partial_r E_P) - \frac{E_P}{r^2} = i2\pi f \mu_0 \sigma_e \left(E_C + E_P\right) \tag{3.36}$$

Eq. (3.35) has an analytical solution, which can be found for instance in Jang *et. al.*[57]

$$E_C = \sum_{l=1}^{N_{coil}} i f \mu_0 I_C \sqrt{\frac{r_0}{r}} \left[2\frac{E_2(k_l)}{k_l} - E_1(k_l)\left(\frac{2}{k_l} - k_l\right)\right] \tag{3.37}$$

where $E_1(k)$ and $E_2(k)$ are respectively the complete elliptic integrals of the first and second kind

$$\begin{aligned} E_1(k) &= \int_0^{\frac{\pi}{2}} \frac{d\theta}{\sqrt{1 - k^2 \sin^2(\theta)}} \\ E_2(k) &= \int_0^{\frac{\pi}{2}} \sqrt{1 - k^2 \sin^2(\theta)}\, d\theta, \end{aligned} \tag{3.38}$$

with k_l is defined as

$$k_l = \frac{4 r r_0}{(z - z_l)^2 + (r + r_0)^2}. \tag{3.39}$$

r_0 is the coil radius and z_l is the axial position of turn l. Eq. (3.52) is solved by using the expression for the coil current Eq. (3.37). In practice, the plasma and coil electric fields are split into a real and imaginary part, thus splitting Eq. (3.36) in a real and imaginary part as well. Note that Eq. (3.4) and (3.36) are solved monolithically using the HDG method. They are coupled through σ_e, which appears in the source term of both equations, and which depends on temperature and pressure.

We can now justify the fact that only $\mathbf{E}_I$, and not $\mathbf{E}_S$, appear in the source terms of the Navier-Stokes equations. Indeed, the average volume power dissipated by Joule

effect over one oscillation period is given by

$$\begin{aligned} P_J &= f\int_0^{1/f} \mathbf{j}\cdot\mathbf{E}dt \\ &= f\int_0^{1/f} j_\theta E_\theta dt \\ &= f\int_0^{1/f} \sigma_e \Re\{E_I \exp(2i\pi ft)\}dt \\ &= f\int_0^{1/f} \sigma_e \frac{1}{2}\left(|E_I|^2 + \Re\{E_I^2\exp(2i\pi ft)\}\right)dt \\ &= \frac{\sigma_e}{2}|E_I|^2 \end{aligned} \tag{3.40}$$

Following a similar rationale, by developing the time averaged Lorentz force

$$\mathbf{F}_L = f\int_0^{1/f} \mathbf{j}\times\mathbf{B}dt \tag{3.41}$$

one can show that the $\mathbf{F}_L$ has the form given in Eq. (3.4), only displaying the induced electric field. Although the electrostatic field does not explicitly appear in the Navier-Stokes system, it plays a role in the computations of the transport properties of the plasma. It is determined in the Mutation++ library, and is not explicitly solved in the developed code.

The electric field model presented here is very convenient for solving axisymmetric ICP equations, as it allows to avoid solving for the Laplace equation for the electric potential. However, when considering three dimensional flows, the complete system Eq. (3.25) should be solved.

3.2 Non-dimensional form of ICP equations

Due to the low-mach nature of ICP flows, the distinct eigenvalues λ_l of the projected convective operator of the Navier-Stokes equations in direction $\mathbf{n}$ have very different orders of magnitude

$$\lambda_1 = \mathbf{v}\cdot\mathbf{n} + c, \quad \lambda_2 = \mathbf{v}\cdot\mathbf{n}, \quad \lambda_3 = \mathbf{v}\cdot\mathbf{n} - c, \tag{3.42}$$

with $\mathbf{v}$ the velocity vector, c the speed of sound such that $c \gg \mathbf{v}\cdot\mathbf{n}$. A system of equation with a large disparity in its eigenvalues is badly conditioned. In order to mitigate this drawback, two solutions exists. First, the system can be non-dimensionalized using characteristic variables, reducing the eigenvalues discrepancy. Then, the numerical discretization can be adapted to improve the system conditioning. The latter will be discussed later.

3.2.1 Reference and dimensionless quantities

In order to make the ICP system of equation dimensionless, a set of reference quantities have to be defined. They are listed in Table 3.1. These quantities will serve to define the dimensionless numbers governing the equations. In the following, the dimensionless quantity corresponding to X is denoted with $\tilde{X}$. They are defined as $\tilde{X} = \frac{X}{X_0}$, where X_0 is the corresponding reference value.

Reference variable	**Description**	Value for $p_0 = 5 \times 10^3 \mathrm{Pa}$ $T_0 = 10^4 \mathrm{K}$	Value for $p_0 = 10^5 \mathrm{Pa}$ $T_0 = 10^4 \mathrm{K}$
L_0	Torch diameter.	1.6×10^{-1} m	1.6×10^{-1} m
ρ_0	Density	7.83×10^{-4} kg m^{-3}	1.72×10^{-2} kg m^{-3}
$\rho_{in}(T_{in}, p_0)$	Inlet density	4.96×10^{-2} kg m^{-3}	1.00 kg m^{-3}
A_{in}	Inlet area	2.435×10^{-3} m^2	2.435×10^{-3} m^2
Q	Mass flow rate	1.6×10^{-2} kg s^{-1}	1.6×10^{-2} kg s^{-1}
e_0	Internal energy	5.11×10^7 J kg^{-1}	4.22×10^7J kg^{-1}
k_0	Heat conductivity	2.34 W m^{-1}K^{-1}	1.47 W m^{-1}K^{-1}
η_0	Dynamic viscosity	1.80×10^{-4} Pa s	2.45×10^{-5} Pa s
σ_0	Electric conductivity	3.07×10^3 S m^{-1}	2.84×10^3 S m^{-1}
$u_0 = Q/(\rho_{in} A_{in})$	Velocity.	1.32×10^2 m s^{-1}	6.57 m s^{-1}
$t_0 = L_0/u_0$	Hydrodynamic time	1.21 s	2.44×10^{-2} s
E_0	Electric field	10^4 V m^{-1}	10^4 V m^{-1}
μ_0	Magnetic permeability	$4\pi \times 10^{-7}$ H m^{-1}	$4\pi 10^{-7} \times$ H m^{-1}

Tab. 3.1.: List of reference values for ICP flows used for dimensional analysis. Unless specifically marked, they are evaluated using the reference pressure p_0 and temperature T_0. The reference velocity is computed from the inlet flow rate Q, the inlet area A_{in} and the inlet density ρ_{in}. The value listed here reflects typical ICP cases in the Plasmatron ICP facility at VKI.

3.2.2 Hydrodynamic dimensionless equations

The hydrodynamic dimensionless equations are given in their vector form as

$$\begin{aligned}
&\partial_{\tilde{t}}\tilde{\rho} + \tilde{\nabla}\cdot(\tilde{\rho}\tilde{\mathbf{v}}) = 0 \\
&\partial_{\tilde{t}}(\tilde{\rho}\tilde{\mathbf{v}}) + \tilde{\nabla}\cdot(\tilde{\rho}\tilde{\mathbf{v}}\tilde{\mathbf{v}} + \mathrm{Eu}\,\tilde{p}) = \frac{1}{\mathrm{Re}}\tilde{\nabla}\cdot\tilde{\boldsymbol{\tau}} + \mathrm{Im}\,\tilde{\mathbf{F}}_L \\
&\partial_{\tilde{t}}\left(\tilde{\rho}\tilde{e} + \mathrm{Ek}\,\frac{1}{2}\tilde{\rho}||\tilde{\mathbf{v}}||^2\right) + \tilde{\nabla}\left(\tilde{\rho}\tilde{e}\tilde{\mathbf{v}} + \mathrm{Ek}\,\frac{1}{2}\tilde{\rho}||\tilde{\mathbf{v}}||^2\tilde{\mathbf{v}} - \mathrm{Eu}\,\mathrm{Ek}\,\tilde{p}\tilde{\mathbf{v}}\right) \\
&\quad = \frac{\mathrm{Ek}}{\mathrm{Re}}\tilde{\nabla}\cdot(\tilde{\boldsymbol{\tau}}\cdot\tilde{\mathbf{v}}) - \frac{1}{\mathrm{Re}\,\mathrm{Pr}}\tilde{\nabla}\cdot\left(\tilde{k}\tilde{\nabla}\tilde{T}\right) + \mathrm{Jn}\,\tilde{P}_J
\end{aligned} \tag{3.43}$$

Eq. (3.43) contains several dimensionless numbers, which are listed below.

Reynolds number The Reynolds number Re is the ratio of inertia over viscous forces:

$$\mathrm{Re} = \frac{\rho_0 u_0 L_0}{\eta_0}. \tag{3.44}$$

For an ICP facility, $\mathrm{Re} \sim 100$ and the flow is laminar.

Mach number The Mach number represents the ratio of the velocity u over the speed of sound c

$$\mathrm{Ma} = \frac{u}{c} \tag{3.45}$$

It is an indicator of the compressibility of the fluid, meaning the variation of density with respect to pressure. In the case of ICP, the Mach number is very low ($\mathrm{Ma} \sim 0.01$), and the flow can be considered incompressible, meaning that the density variation is only due to temperature effects.

Euler number The Euler number Eu is a comparison of the pressure force and inertia.

$$\mathrm{Eu} = \frac{\Delta p_0}{\rho_0 u_0^2} \tag{3.46}$$

where Δp_0 is a reference gauge pressure. The Euler number scales the pressure gradient term in the dimensionless momentum equation. However, in the case of ICP, pressure is almost constant everywhere, with $\Delta p_0 \simeq 50\,\mathrm{Pa}$, making pressure forces marginal compared to inertia.

Prandtl number the Prandtl number Pr assesses the ratio between the heat transferred due to momentum diffusivity and due to thermal diffusion

$$\mathrm{Pr} = \frac{\eta_0 e_0}{T_0 k_0}. \tag{3.47}$$

In this work, $\mathrm{Pr} \sim 0.4$, and ICP is dominated by thermal diffusive effects.

Eckert number the Eckert number Ek represents the ratio of kinetic energy over the internal energy

$$\mathrm{Ek} = \frac{u_0^2}{e_0} \tag{3.48}$$

In ICP, the thermal energy dominates the kinetic one, and $\mathrm{Ek} \ll 1$.

Magnetic interaction parameter The magnetic interaction parameter Im is evaluating the ratio of the effective Lorentz force over inertia. It is defined by

$$\mathrm{Im} = \frac{\sigma_0 E_0^2}{f \rho_0 u_0^2} \tag{3.49}$$

where f is the coil induction frequency. If f is sufficiently high, $\mathrm{Im} \ll 1$ and the effective Lorentz force can be neglected.

Joule number the Joule number Jn represents the ratio of the heat produced by Joule effect over the heat transported by convection.

$$\mathrm{Jn} = \frac{\sigma_0 E_0^2 L_0}{\rho_0 u_0^3} \tag{3.50}$$

In ICP, $\mathrm{Jn} \geq 1$ for the Joule heating to be effective. Otherwise, the torch is quenched.

Swirl angle Although it does not appear explicitly in the governing equation, the swirl angle S is the angle between the v_z and v_θ at the injection such that

$$\tan(S) = \frac{v_\theta}{v_z} \tag{3.51}$$

3.2.3 Electric dimensionless equation

The non-dimensional form of the plasma electric field equation Eq. (3.36) is given by

$$\tilde{\Delta} \tilde{E}_P - \frac{\tilde{E}_P}{\tilde{r}^2} i \, \mathrm{N_{ind}} \, \tilde{\sigma} \left(\tilde{E}_C + \tilde{E}_P \right) = 0 \tag{3.52}$$

where $\mathrm{N_{ind}}$ is the induction number, representing the ratio of the skin depth δ over the characteristic length L_0 of the ICP

$$\mathrm{N_{ind}} = 2\pi f \mu_0 \sigma_0 L_0^2 = \left(\frac{L_0}{\delta} \right)^2 \tag{3.53}$$

with

$$\delta = \sqrt{\frac{1}{2\pi f \mu_0 \sigma_0}}. \tag{3.54}$$

and is a measure of the penetration depth of the induced currents in the plasma.

3.3 Computational domain, boundary and initial conditions

The ICP configuration is a multi-domain problem as shown in Fig. 3.1. It contains two subdomains: the torch (ICP part), where Maxwell and Navier-Stokes equations are solved, and the outer region (electromagnetic part), governed by Maxwell equations. The computational domain is accompanied by a set of boundary and initial conditions listed below.

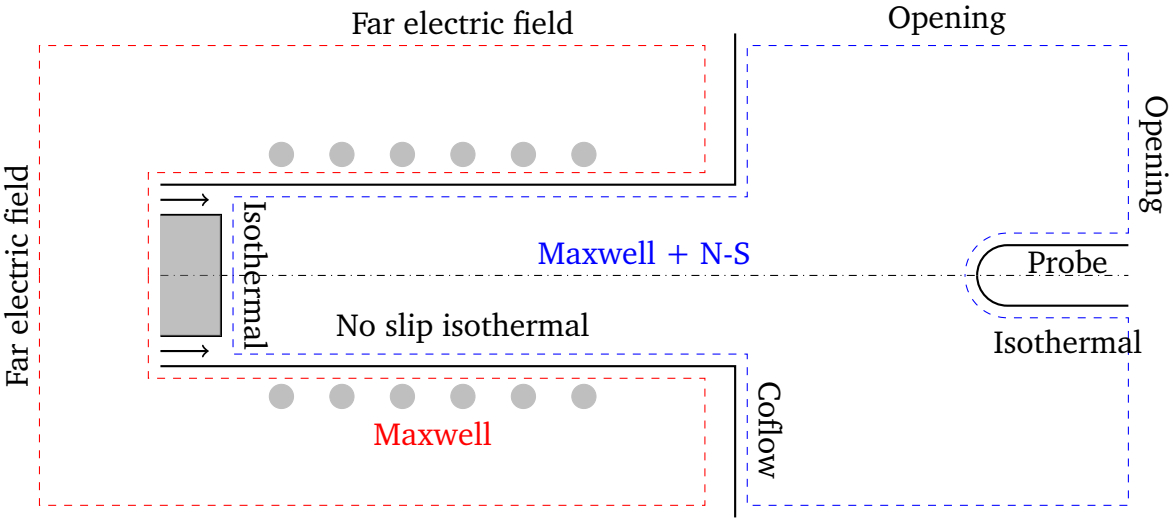

Fig. 3.1.: Schematic representation of the computational domain of an ICP. Conceptually, the Maxwell and Navier-Stokes equations are solved inside the torch (blue region), while only the Maxwell equations are solved outside (red region), making the ICP simulation a multi-domain problem. The boundary conditions have been marked.

The boundary conditions displayed in Fig. 3.1 are listed here.

Vanishing far electric field Since the electric field vanishes far away from the torch, the computational electric field has to be sufficiently extended. At the boundary of the outer region, $E_P = 0$.

Symmetry axis the center line is an axis of symmetry. $\partial_r p = 0$, $\partial_r u_z = 0$, $u_r = 0$, $\partial_r T = 0$ and $E_P = 0$.

Openings The chamber is cut to reduce the computational costs. Openings are placed on its boundaries (top and right end of the chamber domain). $p = p_0$

No-slip wall isothermal The wall below the annular injector and the torch upper walls are isothermal. $T = T_{wall}$ and $\mathbf{u} = \mathbf{0}$.

Inflow The inflow is annular, $u_z = U_{in}$, $u_r = 0$ and $T = T_{inlet}$.

Stabilizing co-flow A stabilizing coflow is blown from the chamber upper left wall. The purpose of this coflow is to remove the Kelvin-Helmholtz instabilities occurring in the shear layer of the jet in order to reach steady-state. This technique has been used in legacy codes [107, 75, 35]. $T = T_{wall}$, $\mathbf{u} = u_{coflow}\mathbf{e}_z$

ICP and Maxwell interface At the interface between Maxwell and ICP domains, the boundary conditions as shown in Fig. 3.1 are applied on the hydrodynamic fields. For the electric field, the normal electric field diffusive flux is conserved across the interface.

$$\begin{aligned} \nabla E_p^{Re,NS} \cdot \mathbf{n}^{NS} &= \nabla E_p^{Re,MAX} \cdot \mathbf{n}^{MAX} \\ \nabla E_p^{Im,NS} \cdot \mathbf{n}^{NS} &= \nabla E_p^{Im,MAX} \cdot \mathbf{n}^{MAX} \end{aligned} \tag{3.55}$$

where E_p^{Re} and E_p^{Im} represent the real and imaginary parts of the electric field, the superscripts NS and MAX label the Navier-Stokes and Maxwell domains, and $\mathbf{n}$ is the outward pointing normal with respect to a given subdomain.

The initialization of the flow does not have an impact on the steady solution. However, if the flow is not well initialized, the solver convergence may be slowed down or become impossible. We present now the initial solution used for every field in every ICP computations performed with the HDG code in this work.

Velocity field Uniform initial velocity $\mathbf{v} = U_{in}\mathbf{e}_z$.

Temperature field The temperature is initialized as follows:

- If $z > z_3$, or $r > R_{out}$, $T(z,r) = T_{wall}$.
- Else if $z \in [z_1; z_2]$, $T(z,r) = T_{12}(r) = T_{initial} + \frac{r^2}{R_{in}^2}(T_{wall} - T_{initial})$
- Else if $z < z_1$, $T(z,r) = \frac{T_{wall}-T_{12}(r)}{z_1^2}z^2 - 2\frac{T_{wall}-T_{12}(r)}{z_1}z + T_{wall}$
- Else if $z \in [z_2, z_3]$: $T(z,r) = T_{12}(r) + \frac{(z-z_2)^2}{(z_3-z_2)^2}(T_{wall} - T_{12}(r))$

The choice of z_1, z_2 and z_3 should be such that the initial data match the boundary conditions.

Pressure and electric field The pressure and electric fields are initialized as $E_P = 0 \quad p = p_0$. Note that the electric field is initialized the same way in both domains.

We would like to emphasize that the initial conditions on temperature have been specifically designed to match the boundary conditions. If this is not the case, the solution becomes oscillatory close to the boundary, resulting is non physical temperatures and the crash of the solver. Other configurations are possible, but the boundary conditions should be always respected by initial data.

3.4 Conclusions on the ICP model

We have presented the ICP model used in the subsequent simulations. Although the modeling is relatively simple, as many physical phenomena are disregarded, it gives a sufficiently complex framework to test the high-order numerical approach, especially for the capture of the large temperature gradients close to the facility isothermal walls. However, many of these assumptions should be dropped in the future. In particular, unsteady and 3D computations should be investigated in order to match the new experimental requirements (*e.g.* the semi-elliptical nozzle). The ambipolar assumption should also be removed and the Laplace equation for the electrostatic field should be solved. Finally, non-equilibrium chemistry should be investigated.

4

High-order discretization

We now present a new monolithic hybridized discontinuous Galerkin (HDG) method. We particularize it to the ICP case. This Chapter is divided in two parts. In the first one, we present the general discretization procedure for the HDG multi-domain method for any conservation law and link it to the ICP problem. This is one of the main contributions of this thesis, as this is the first time HDG has been used for a multi-domain solver. In addition, we present the numerical fluxes, compatibility conditions between subdomains and boundary conditions. Secondly, we discuss solution strategies for solving the multi-domain method at steady-state. We discuss the damped inexact Newton-Raphson procedure and the iterative algorithm for keeping the power constant in the facility. The developments presented here have been published by the author (see [25]).

4.1 Hybridized discontinuous Galerkin method for multi-domain problems

We present an extension of the classic HDG method to multi-domain problems, taking into account the conditions existing at the interface between physical subdomains. We first introduce the model problem. We then define the spatial discretization and the functional spaces. We discretize the weak formulation of the model problem using the multi-domain HDG method. This discretization procedure implies the definition of the local set of degrees of freedom (DOFs), containing the information about the solution $\mathbf{u}$ and its gradient $\mathbf{q}$ at the element level, and the global set of DOFs $\boldsymbol{\lambda}$ along the inter-element trace. Numerical fluxes at the element interface and compatibility conditions at the subdomain interfaces also have to be defined. The developments are structured similarly to the work of Nguyen *et al.* [88, 90] and Woopen *et al.* [114, 112]. At first, the physics of ICP is set aside, as the method is valid for any kind of conservation law. Then, we link the general formulation of the multi-domain HDG method to the case of ICP.

4.1.1 Multi-domain model problem statement

Multi-domain problems can be modeled as a collection of non-overlapping subdomains governed by their own physics. Consider a given subdomain $\Omega^l \subset \mathbb{R}^D$ of dimension D with boundary $\partial\Omega^l$. A set of conservation equations, boundary and initial conditions are defined over Ω^l as

$$
\begin{aligned}
&\partial_t \mathbf{w}^l(\mathbf{u}) + \nabla \cdot \left(\mathbf{F}_c^l(\mathbf{u}) - \mathbf{F}_v^l(\mathbf{u}, \nabla\mathbf{u})\right) = \mathbf{S}^l(\mathbf{u}, \nabla\mathbf{u}), && \mathbf{x} \in \Omega^l, && t > 0 \\
&\mathbf{u}^l = \mathbf{u}_{bc}^l, && \mathbf{x} \in \partial\Omega_d^l, && t > 0 \\
&\mathbf{F}_v^l \cdot \mathbf{n} = \mathbf{F}_{v,n,bc}^l, && \mathbf{x} \in \partial\Omega_n^l, && t > 0 \\
&\mathcal{F}^{l,l'}(\mathbf{u}^l, \nabla\mathbf{u}^l, \mathbf{u}^{l'}, \nabla\mathbf{u}^{l'}) = 0, && \mathbf{x} \in \gamma^{l,l'}, && t > 0,\ l \neq l' \\
&\mathbf{u}^l(t=0) = \mathbf{U}^l, && \mathbf{x} \in \Omega^l
\end{aligned}
\tag{4.1}
$$

where $\mathbf{u}^l$ is the vector of unknowns and $\mathbf{w}^l$ is the set of conservative variables. $\mathbf{F}_c$ and $\mathbf{F}_v$ are the convective and diffusive physical flux functions respectively and $\mathbf{S}$ represents the source terms. $\partial\Omega_d \subset \partial\Omega$ and $\partial\Omega_n \subset \partial\Omega$ are the part of the frontier where Dirichlet and Neumann boundary conditions apply respectively. $\mathbf{u}_{bc}$ and $\mathbf{F}_{v,n,bc}$ are boundary conditions on the solution and on the diffusive flux normal to the boundary respectively. $\mathbf{U}$ represents an initial field function. $\gamma^{l,l'} = \partial\Omega^l \cap \partial\Omega^{l'}$ is the common frontier to the subdomains l and l'. Finally, compatibility and conservation conditions are applied at the interface between the subdomains Ω^l and $\Omega^{l'}$. They are represented by the function $\mathcal{F}$.

We have illustrated Eq. (4.1) particularized to the ICP model in Fig. 4.1. This problem has been divided in two parts: one where the Maxwell and Navier-Stokes equations are solved, inside the torch and the chamber, and one where only Maxwell equations apply, outside the facility. We show the conservative $\mathbf{w}$ and unknown $\mathbf{u}$ vectors for each subdomain, and the conservativity condition $\mathcal{F}$ across their boundary. We also have listed in Table 4.1 the mapping of the symbols found in Eq. (4.1) and in the ICP problem. The boundary and initial conditions can be retrieved from Section 3.3. Note that, for the Navier-Stokes equations, we use the set of unknowns $\mathbf{u} = (p\ v_z\ v_r\ v_\theta\ T)$. This choice is mainly motivated by the use of an LTE table of state constructed using p and T. It is then easy to retrieve the usual conservative quantities $\mathbf{w} = (\rho\ \rho v_z\ \rho v_r\ \rho v_\theta\ e + \rho\frac{||\mathbf{v}||^2}{2})$ using the LTE table. Note also that, outside of the torch, the air is considered to be insulating, meaning that the right hand side of Eq. (3.36) vanishes in this region. Finally, E_C and E_P are split into a real and imaginary parts, and so is Eq. (3.36).

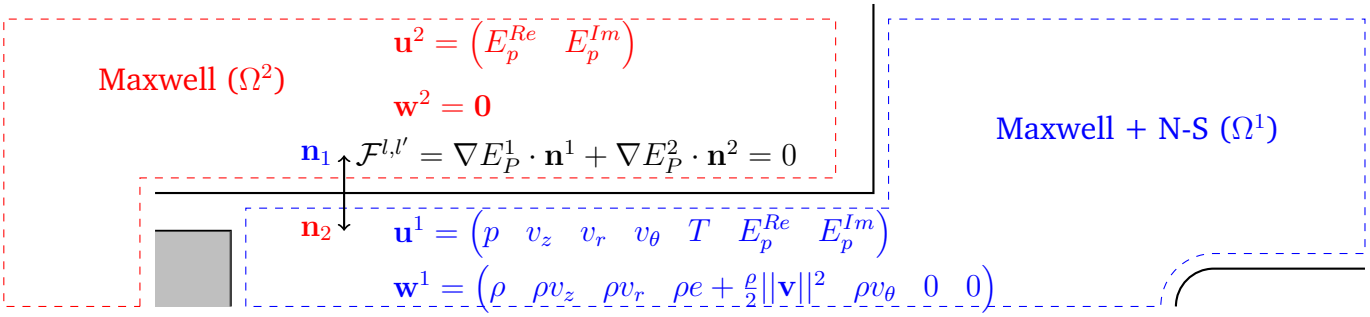

Fig. 4.1.: Schematic representation of an ICP as a multi-domain problem. Only half of the domain is represented. The two subdomains are Ω^1, the Navier-Stokes + Maxwell subdomain, and Ω^2 the Maxwell subdomain. The conservative variables $\mathbf{w}^l$ and $\mathbf{u}^l$ have been shown for each domain, with ρ the density of the fluid, v_z and v_r the radial and axial velocity components, T the temperature, e the internal energy, p the pressure, $E_P = E_P^{Re} + iE_P^{Im}$ the plasma electric field, with E_P^{Re} and E_P^{Im} its real and imaginary parts. The operator $\mathcal{F}$ has also been displayed, representing the conservation of the electric field diffusive flux across subdomains.

Eq. (4.1)	**NS + Maxwell** (Eq. (3.4) + Eq. (3.36))	**Maxwell** (Eq. (3.36))
$\mathbf{u}^l$	$\begin{pmatrix} p & v_z & v_r & v_\theta & T & E_P^{Re} & E_P^{Im} \end{pmatrix}^T$	$\begin{pmatrix} E_P^{Re} & E_P^{Im} \end{pmatrix}^T$
$\mathbf{w}^l$	$\begin{pmatrix} \rho & \rho v_z & \rho v_r & \rho v_\theta & \rho e + \rho\frac{\|\|\mathbf{v}\|\|^2}{2} & 0 & 0 \end{pmatrix}^T$	$\begin{pmatrix} 0 & 0 \end{pmatrix}^T$
$\mathbf{F}_c^l$	$(\mathbf{F}_c\ 0\ 0)^T$, $\mathbf{F}_c$ is given in Eq. (3.5)	/
$\mathbf{F}_v^l$	$\begin{pmatrix} \mathbf{F}_v & \nabla E_P^{Re} & \nabla E_P^{Im} \end{pmatrix}^T$, $\mathbf{F}_v$ is given in Eq. (3.6)	$\begin{pmatrix} \nabla E_P^{Re} & \nabla E_P^{Im} \end{pmatrix}^T$
$\mathbf{S}^l$	$\begin{pmatrix} r\mathbf{S} \\ 2\pi f\mu_0\sigma_e(E_C^{Im} + E_P^{Im}) - \frac{E_P^{Re}}{r} \\ -2\pi f\mu_0\sigma_e(E_C^{Re} + E_P^{Re}) - \frac{E_P^{Im}}{r^2} \end{pmatrix}$, $\mathbf{S}$ is given in Eq. (3.7)	$\begin{pmatrix} -\frac{E_P^{Re}}{r^2} \\ -\frac{E_P^{Im}}{r^2} \end{pmatrix}$
$\mathcal{F}^{l,l'}$	$\begin{pmatrix} \nabla E_P^{Re,NS} \cdot \mathbf{n}^{NS} + \nabla E_P^{Re,MAX} \cdot \mathbf{n}^{MAX} \\ \nabla E_P^{Im,NS} \cdot \mathbf{n}^{NS} + \nabla E_P^{Im,MAX} \cdot \mathbf{n}^{MAX} \end{pmatrix}$	
$\mathbf{u}_{bc}^l$	$\mathbf{u}$ evaluated using the boundary values in Section 3.3	
$\mathbf{F}_{v,n,bc}^l$	$\mathbf{F}_v \cdot \mathbf{n}$, evaluated using $\mathbf{u}_{bc}$ and the gradient boundary values in Section 3.3	
$\mathbf{U}^l$	$\mathbf{u}$, evaluated using the initial values as described in Section 3.3	

Tab. 4.1.: Mapping table between the notations of Eq. (4.1) and the notations of the ICP problem composed of the N-S + Maxwell subdomain (Eq. (3.4) + Eq. (3.36)) and the Maxwell subdomain (Eq. (3.36)). ρ is the density of the fluid, v_z, v_r and v_θ are the axial, radial and azimuthal velocity components respectively, T is the temperature, e is the internal energy, p is the pressure, E_P^{Re} and E_P^{Im} are the real and imaginary parts of the electric field respectively and r is the radial position. $\mathbf{n}$ represents the outward pointing normal to the boundary of a specific subdomain. The superscripts NS and MAX label the Maxwell + Navier-Stokes and the Maxwell domain respectively.

4.1.2 Spatial discretization

Let us consider a domain Ω composed of N_d non-overlapping sub-domains Ω^l:

$$\Omega = \bigcup_{l=1}^{N_d} \Omega^l. \tag{4.2}$$

Each sub-domain Ω^l is divided in a collection $\mathcal{T}^l$ of N_e^l non-overlapping elements. The tesselation $\mathcal{T}$ of the complete domain Ω is defined as

$$\mathcal{T} = \bigcup_{l=1}^{N_d} \mathcal{T}^l, \tag{4.3}$$

with boundary $\partial\mathcal{T}$. This tesselation forms the mesh of the problem. In this work, we employ only conformal mesh, meaning that any boundary face of an element can only be connected to a single other element. The subdomain mesh skeleton Γ^l is defined as

$$\Gamma^l = \{e : e = K_i \cap K_j; \forall K_i, K_j \in \mathcal{T}^l,\ K_i \neq K_j\}. \tag{4.4}$$

We also define the set of traces on the interface between sub-domains $\Gamma^{l,l'}$ as

$$\Gamma^{l,l'} = \{e : e = K \cap K'; K \in \mathcal{T}^l, K' \in \mathcal{T}^{l'},\ l \neq l'\} \tag{4.5}$$

In the following, we define Γ as the collection of all inter-element traces

$$\Gamma = \Gamma^l \cup \Gamma^{l,l'}, \forall l \neq l' \tag{4.6}$$

and by $\bar{\Gamma}$ the set containing all the traces located at the sub-domain interfaces

$$\bar{\Gamma} = \bigcup_{l,l'} \Gamma^{l,l'}, \forall l \neq l'. \tag{4.7}$$

4.1.3 Functional spaces

HDG searches an approximation of the solution $\mathbf{u}$ of Eq. (4.1) and its gradient $\mathbf{q} = \nabla\mathbf{u}$ on a functional subspace of the square integrable functions of the domain $L^2(\Omega)$. To do so, it also uses a set of hybrid degrees of freedom on the mesh skeleton, noted $\boldsymbol{\lambda}$ in the following. They represent the solution on the element interface. If $\mathcal{P}^p(K)$ represents the set of polynomials of degree at most p on K, we chose the

following sets to represent $\mathbf{u}$, $\mathbf{q}$ and $\boldsymbol{\lambda}$ respectively

$$\begin{aligned} W_h &= \left\{ w \in L^2(\Omega) : w|_K \in \mathcal{P}^p(K), \forall K \in \mathcal{T} \right\} \\ V_h &= \left\{ \mathbf{v} \in L^2(\Omega) : \mathbf{v}|_K \in \left(\mathcal{P}^p(K)\right)^D, \forall K \in \mathcal{T} \right\} \\ M_h &= \left\{ \mu \in L^2(\Gamma) : \mu|_e \in \mathcal{P}^p(e), \forall e \in \Gamma \right\} \end{aligned} \tag{4.8}$$

with D the spatial dimension of the problem. These functional sets contain all functions that are square integrable polynomial of degree at most p on each element or interface. In general, these functions are discontinuous across the element interface, which is very convenient for DG-like method. Indeed, it is possible to represent discontinuous solutions across the element interfaces. Moreover, this feature allows to use a different polynomial order on each element. This concept is not explored here, but could definitely be used in further improvements of ICP simulations. These sets being finite dimensional, it is possible to find a basis composed of a finite number of linearly independent functions. It is common practice in DG-like methods, such as HDG, to choose basis functions in the set of functions that have a compact support on the elements. This choice greatly simplifies subsequent developments. Consequently, let us define the set of functions belonging to W_h and V_h but have a compact support on a given element K and the set of functions belonging to M_h but that have a compact support on a given element e. We name these sets respectively $W_{K,h}$, $V_{K,h}$ and $M_{e,h}$

$$\begin{aligned} W_{K,h} &= \{ w(\mathbf{x}) \in W_h : \mathbf{x} \notin K \Rightarrow w(\mathbf{x}) = 0, \forall K \in \mathcal{T} \} \\ V_{K,h} &= \{ \mathbf{v}(\mathbf{x}) \in V_h : \mathbf{x} \notin K \Rightarrow \mathbf{v}(\mathbf{x}) = 0, \forall K \in \mathcal{T} \} \\ M_{e,h} &= \{ \mu(\mathbf{x}) \in M_h : \mathbf{x} \notin e \Rightarrow \mu(\mathbf{x}) = 0, \forall e \in \Gamma \} \end{aligned} \tag{4.9}$$

Because $W_{K,h}$, $V_{K,h}$ and $M_{e,h}$ are finite dimensional, one can find a basis of p linearly independent functions for each of these spaces. They will be denoted in the following by

$$\begin{aligned} &\varphi_{K,i} \in W_{K,h},\ i \in \{1, 2, ..., p\},\ \forall K \in \mathcal{T} \\ &\boldsymbol{\tau}_{K,i} \in V_{K,h},\ i \in \{1, 2, ..., p\},\ \forall K \in \mathcal{T} \\ &\mu_{e,i} \in M_{K,h},\ i \in \{1, 2, ..., p\},\ \forall e \in \Gamma \end{aligned} \tag{4.10}$$

By considering $\varphi_{K,i}$ and $\boldsymbol{\tau}_{K,i}$ for all $K \in \mathcal{T}$ and $\mu_{e,i}$ for all $e \in \Gamma$, it can be shown that a basis for V_h, W_h and M_h is retrieved respectively. An example of basis functions are the Lagrange polynomials of degree at most p. In this work, Dubiner's basis is used [32] for every set. Consequently, the solution $\mathbf{u}_h$, solution gradient $\mathbf{q}_h$ and the hybrid

variables $\boldsymbol{\lambda}_h$ are given by

$$\begin{aligned} \mathbf{u}_h &= \sum_{K\in\mathcal{T}}\sum_{i=1}^{p} \mathbf{u}_{K,i}\varphi_{K,i} \\ \mathbf{q}_h &= \sum_{K\in\mathcal{T}}\sum_{i=1}^{p} \mathbf{q}_{K,i}\boldsymbol{\tau}_{K,i} \\ \boldsymbol{\lambda}_h &= \sum_{e\in\Gamma}\sum_{i=1}^{p} \boldsymbol{\lambda}_{e,i}\mu_{e,i}. \end{aligned} \tag{4.11}$$

with $\mathbf{u}_{K,i}$, $\mathbf{q}_{K,i}$ and $\boldsymbol{\lambda}_{e,i}$ the solution, solution gradient and hybrid degrees of freedom at element K and facet e respectively. In HDG, or any other DG-like method, defining the global functional basis in terms of local functions allows to simplify the discrete system, as will be discussed in the following. An illustration of nodal DOFs for HDG is given in Fig. 4.2. In the following, we refer the DOFs associated to the elements ($\mathbf{u}$, $\mathbf{q}$) by the *local* DOFs, while the DOFs associated with the element trace ($\boldsymbol{\lambda}$) are the *hybrid* DOFs.

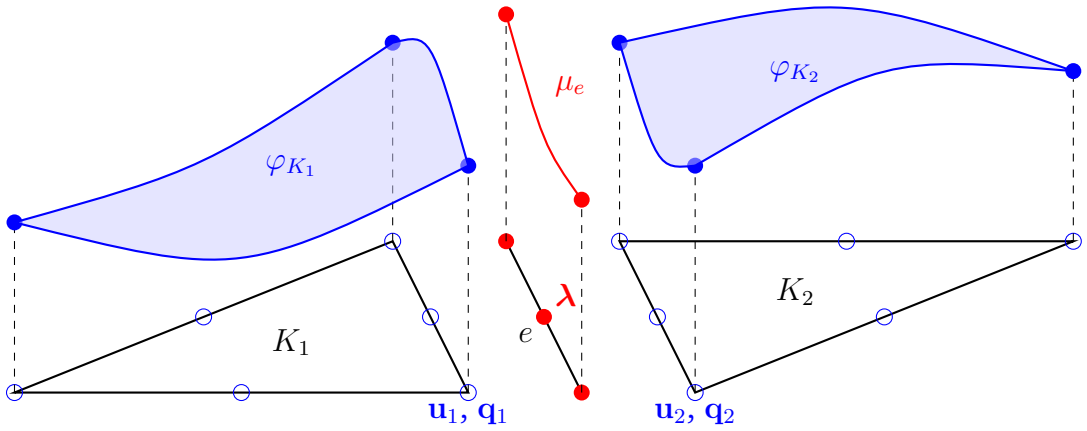

Fig. 4.2.: Illustration of the nodal degrees of freedom used in the HDG method for two triangular elements of order 2. Examples of basis functions are also shown. The nodes on the elements K_1 and K_2 (marked with ○) are associated with the local DOFs $\mathbf{u}$ and $\mathbf{q}$. At the interface e between elements, a set of hybrid DOFs $\boldsymbol{\lambda}$ (marked with ●), is defined. The purpose of the latter is to decouple the element DOFs ($\mathbf{u}$, $\mathbf{q}$), effectively reducing the number of globally coupled DOFs ($\boldsymbol{\lambda}$) compared to classic DG. Note also that the basis functions are not continuous across the elements (see φ_{K_1} and φ_{K_2}) and that the lement trace has its own functional space (μ_e).

Before presenting the discretization, some of the operators and symbols used in the following are defined. The jump operator at the interface between elements is

$$[[\mathbf{u}]] = \mathbf{u}_+ \cdot \mathbf{n}_+ + \mathbf{u}_- \cdot \mathbf{n}_-, \tag{4.12}$$

where the $+$ and $-$ label the two elements sharing the edge over which the jump is

computed, $\mathbf{n}$ represents the outward pointing normal to an element. We also define the following volume and surface integration operators respectively:

$$\begin{aligned}(a,b)_K &= \int_K ab\, dV,\\ \langle a,b\rangle_{\partial K} &= \int_{\partial K} ab\, dS.\end{aligned} \tag{4.13}$$

4.1.4 Discrete problem

The HDG method adapted to a multi-domain problem consists in, for each subdomain $\Omega^l \in \Omega$ tesselated using the set $\mathcal{T}^l \in \mathcal{T}$, finding an approximation to the solution of Eq. (4.1) by solving, for $(\mathbf{u}_h, \mathbf{q}_h, \boldsymbol{\lambda}_h) \in V_h \times W_h \times M_h$ and for any test function $(v, \boldsymbol{\tau}, \pi) \in V_h \times W_h \times M_h$, the following problem:

$$\begin{aligned}&\left(\partial_t \mathbf{w}_h^l - \mathbf{S}_h^l, v\right)_{\mathcal{T}^l} - \left(\mathbf{F}_{h,c}^l - \mathbf{F}_{h,v}^l, \nabla v\right)_{\mathcal{T}^l} + \sum_{K\in\mathcal{T}^l} \left\langle \boldsymbol{\mathcal{H}}^l, v\right\rangle_{\partial K} = 0\\ &\left(\mathbf{q}_h^l, \boldsymbol{\tau}\right)_{\mathcal{T}^l} - \left(\mathbf{u}_h^l, \nabla\boldsymbol{\tau}\right)_{\mathcal{T}^l} + \sum_{K\in\mathcal{T}^l} \left\langle \boldsymbol{\lambda}_h^l, \boldsymbol{\tau}\cdot\mathbf{n}\right\rangle_{\partial K\setminus\partial\Omega^l} + \left\langle \mathbf{u}_{bc}^l, \boldsymbol{\tau}\cdot\mathbf{n}\right\rangle_{\partial\Omega^l} = 0\\ &\left\langle [[\boldsymbol{\mathcal{H}}^l]], \pi\right\rangle_{\Gamma^l} + \sum_{\substack{l'=1\\ l'\neq l}}^{N_d} \langle \tilde{\mathcal{F}}^{l,l'}, \pi\rangle_{\Gamma^{l,l'}} = 0\end{aligned} \tag{4.14}$$

where the subscript h means that a quantity is evaluated using $\mathbf{u}_h$, $\mathbf{q}_h$ and $\boldsymbol{\lambda}_h$, the superscript l denotes the domain and N_d is the number of subdomains inside Ω. $\boldsymbol{\mathcal{H}}$ is the numerical flux function, *i.e.* an approximate consistent evaluation of the convective and diffusive physical fluxes at the interface used to stabilize the method. Eq. (4.14) is very similar to classic HDG. However, the third equation contains an additional term, which is the core of the multi-domain method presented in this work

$$\sum_{\substack{l'=1\\ l'\neq l}}^{N_d} \langle \tilde{\mathcal{F}}^{l,l'}, \mu\rangle_{\Gamma^{l,l'}} \tag{4.15}$$

The operator $\tilde{\mathcal{F}}$ is responsible for the exchange of information between subdomains Ω^l and $\Omega^{l'}$. In general, $\tilde{\mathcal{F}}$ is an approximation of $\mathcal{F}$, the actual compatibility or conservativity condition existing between the subdomains. Both the numerical flux functions $\boldsymbol{\mathcal{H}}$ and $\tilde{\mathcal{F}}$ are discussed more thoroughly in the following.

Because the sets V_h, W_h and M_h are finite dimensional, as long as Eq. (4.14) is verified for the basis functions, it is verified for all functions $(v, \boldsymbol{\tau}, \pi) \in V_h \times W_h \times M_h$. In DG methods, we use the local bases as described in Eq. (4.10). Due to their

compact domain, Eq. (4.14) becomes, for all $K \in \mathcal{T}$, $e \in \Gamma$ and $i \in \{1, 2, ..., p\}$

$$\begin{aligned}
&\left(\partial_t \mathbf{w}_h^K - \mathbf{S}_h^K, \varphi_{K,i}\right)_K - \left(\mathbf{F}_{h,c}^K - \mathbf{F}_{h,v}^K, \nabla\varphi_{K,i}\right)_K + \left\langle \boldsymbol{\mathcal{H}}^K, \varphi_{K,i}\right\rangle_{\partial K} = 0 \\
&\left(\mathbf{q}_h^K, \boldsymbol{\tau}_{K,i}\right)_K - \left(\mathbf{u}_h^K, \nabla\boldsymbol{\tau}_{K',i}\right)_K + \left\langle \boldsymbol{\lambda}_h^{\partial K}, \boldsymbol{\tau}_{K,i}\cdot\mathbf{n}\right\rangle_{\partial K_0} + \left\langle \mathbf{u}_{bc}, \boldsymbol{\tau}_{K,i}\cdot\mathbf{n}\right\rangle_{\partial K_{bc}} = 0 \\
&\langle [[\boldsymbol{\mathcal{H}}]], \mu_{e,i}\rangle_{e\setminus\bar{\Gamma}} + \langle \tilde{\mathcal{F}}^e, \mu_{e,i}\rangle_{e\cap\bar{\Gamma}} = 0
\end{aligned} \tag{4.16}$$

where the index K and e denote the restriction to element $K \in \mathcal{T}$ and $e \in \Gamma$ respectively. Note that the mapping given in Table 4.1 apply to Eq. (4.16). The frontier of each element is $\partial K = \partial K_0 \bigcup \partial K_{bc}$, where the boundary condition apply on ∂K_{bc} and the part of the element frontier connected to another element is ∂K_0. The numerical flux function is represented by $\boldsymbol{\mathcal{H}}^K$. They are both discussed in the following for the ICP case.

Numerical flux function

The numerical flux function $\boldsymbol{\mathcal{H}}$ is a cornerstone in high-order methods. The stability and accuracy of the method strongly depends on its definition. It is usually split into a convective $\boldsymbol{\mathcal{H}}_c$ and a diffusive part $\boldsymbol{\mathcal{H}}_v$

$$\boldsymbol{\mathcal{H}} = \boldsymbol{\mathcal{H}}_c - \boldsymbol{\mathcal{H}}_v. \tag{4.17}$$

In the case of classic implicit DG method, $\boldsymbol{\mathcal{H}}$ is a function of the local DOFs from neighboring elements, giving rise to a large globally coupled system. For HDG, it is a function of the local and the hybrid DOFs, effectively making the latter the only globally coupled DOFs. This results in a reduced system compared to DG. An illustration of the classic and hybridized DG method is given in Fig. 4.3.

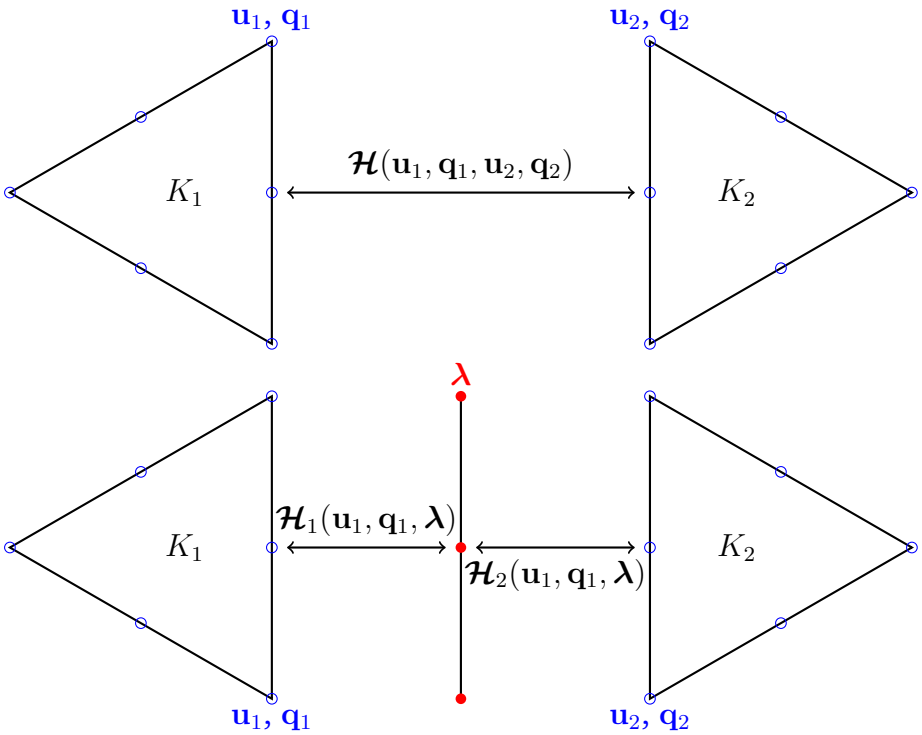

Fig. 4.3.: Illustration of the numerical fluxes in the classic (top) and hybridized (bottom) DG methods using two triangular elements of order 2. In the case of classic DG, the numerical flux function is computed once per interface, directly relating the local DOFs ($\mathbf{u}$ and $\mathbf{q}$). For hybridized DG, the numerical flux function relates the local DOFs and the hybrid ones $\boldsymbol{\lambda}$.

Convective numerical flux ICP flows are incompressible, since $Ma \simeq 0.01$. In these regimes, pressure cannot be updated easily [108], leading to a loss of accuracy and unstable solvers. We use here a convective numerical flux specifically designed for low-Mach regimes, belonging to the the Advection Upstream Splitting Method (AUSM) family. The AUSM scheme was first presented in the seminal work of Liou [73, 72, 71]. It is based on the splitting of the convective flux into a pressure part and an upwind convective part. The resulting flux is designed to be central in the low-mach number limit and upwind in the supersonic case. A simplified version of AUSM for $Ma \to 0$ has already been employed by Magin [75], where a pressure diffusion term is added to the momentum transport flux. We adapted this simplified version to the HDG method:

$$\boldsymbol{\mathcal{H}}_{c,n}(\mathbf{u}, \boldsymbol{\lambda}) = (\dot{m} + \dot{m}_p)\Psi_\lambda - |\dot{m}|(\Psi_\lambda - \Psi_U) + \mathbf{P}, \tag{4.18}$$

where

$$\boldsymbol{\Psi} = \begin{pmatrix} 1 & v^\perp & v^\parallel & v_\theta & e + \frac{1}{2}||\mathbf{v}||^2 + \frac{p}{\rho} \end{pmatrix}^T, \tag{4.19}$$

with the $\|$ and $\perp$ superscript respectively denoting the perpendicular and parallel components of a vector with respect to the normal direction to the facet, p is the pressure, ρ is the density, e is the internal energy and $\mathbf{v}$ is the velocity vector. The subscripts U and λ represent respectively the values in the element and on the facet, $\dot{m} = \rho_\lambda v_\lambda^\perp$ is the mass flow rate, while $m_p = \frac{p_U - p_\lambda}{V_p}$ is the pressure diffusion factor, with V_p a preconditioning velocity, chosen as a characteristic velocity of the flow (in our case, the inlet velocity). Finally, the pressure flux is defined as $\mathbf{P} = \begin{pmatrix} 0 & p_\lambda & 0 & 0 \end{pmatrix}^T$. In order to express the convective numerical flux in the axisymmetric frame of reference, one must multiply it by a rotation matrix

$$\boldsymbol{\mathcal{H}}_c = \begin{pmatrix} 1 & 0 & 0 & 0 & 0 \\ 0 & n_z & -n_r & 0 & 0 \\ 0 & n_r & n_z & 0 & 0 \\ 0 & 0 & 0 & 1 & 0 \\ 0 & 0 & 0 & 0 & 1 \end{pmatrix} \boldsymbol{\mathcal{H}}_{c,n} \tag{4.20}$$

with $\mathbf{n} = (n_z \; n_r \; 0)^T$ the normal to the facet.

The diffusive numerical flux is discretized as follows

$$\boldsymbol{\mathcal{H}}_v(\mathbf{u}, \lambda, \mathbf{q}) = \mathbf{F}_v(\boldsymbol{\lambda}, \mathbf{q}) \cdot \mathbf{n} + \gamma(h)(\boldsymbol{\lambda} - \mathbf{u}) \tag{4.21}$$

where the definition of $\mathbf{F}_v$ for both subdomains can be retrieved from Table 4.1. The penalization parameter γ depends on a local characteristic mesh size. γ has been widely studied for DG methods (see for instance [55, 51, 34]). Based on these results, we suggest a form of γ very close to the one proposed by Hillewaert [55]:

$$\gamma = C \max_{K \ni f} \left(\frac{1}{2\mathcal{V}} \sum_{f \in K} \mathcal{A} \right) \tag{4.22}$$

with f denoting the facet under consideration, K being an element sharing the facet, C a multiplicative constant proportional to the physical diffusion processes (such as viscosity, heat conductivity), $\mathcal{A}$ is the area of the facet (length in 2D), $\mathcal{V}$ is the volume of the element (surface in 2D).

Imposing boundary conditions The boundary conditions are weakly imposed through the numerical flux $\boldsymbol{\mathcal{H}}(\mathbf{u}, \mathbf{q}, \mathbf{u}_{bc}, \mathbf{q}_{bc})$, where $\mathbf{u}_{bc}$ and $\mathbf{q}_{bc}$ are respectively the boundary condition and boundary condition gradient given in Section 3.3. If no BC is applied, the value is copied from inside the domain ($\mathbf{u}_{bc} = \mathbf{u}$ and/or $\mathbf{q}_{bc} = \mathbf{q}$). An illustration is given in Fig. 4.4.

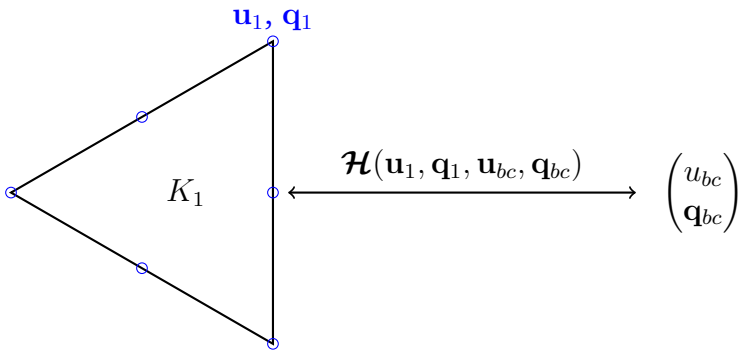

Fig. 4.4.: Illustration of the boundary conditions. The numerical flux is computed exactly like a bulk element, but it is evaluated using the various boundary conditions instead of the hybrid unknowns and local gradients.

Compatibility and conservativity conditions between subdomains

The compatibility and conservativity conditions between neighboring subdomains are treated in the third equation of the system given in Eq. (4.16). It contains an additional term compared to single domain HDG taking into account the discretization of the $\mathcal{F}$ operator, labeled here $\tilde{\mathcal{F}}$. This operator represents the conservation of a physical flux across the interface and/or a compatibility condition. These two cases are discussed below.

Conservative condition across sub-domains If $\mathcal{F}$ represents the conservativity of a flux across the interface, then the discretization $\tilde{\mathcal{F}}$ is the conservation of the associated numerical flux across that interface. In the case of ICP, the conservation of the normal diffusive electric flux gives:

$$\tilde{\mathcal{F}} = \begin{pmatrix} \mathcal{H}^{NS}_{v,E_p^{Re}} + \mathcal{H}^{MAX}_{v,E_p^{Re}} \\ \\ \mathcal{H}^{NS}_{v,E_p^{Im}} + \mathcal{H}^{MAX}_{v,E_p^{Im}} \end{pmatrix} \tag{4.23}$$

where $\mathcal{H}_{v,E_p^{Re}}$ and $\mathcal{H}_{v,E_p^{Im}}$ represents the diffusive numerical flux of the real and imaginary electric field respectively and the superscripts MAX and NS represent the Maxwell and the Maxwell + Navier-Stokes subdomains respectively. The complete expression of $\mathcal{H}_{v,E_p^{Re}}$ and $\mathcal{H}_{v,E_p^{Im}}$ can be found in Eq. (4.21).

Compatibility condition across sub-domains In other physical problem, $\mathcal{F}$ may represent a compatibility condition, such as a jump or the continuity of the solution across the interface. We give an example of the electric field normal to a wall E_n with surface charge σ_s. It is well known that the condition

$$\varepsilon E_n - \varepsilon' E'_n = \sigma_s \tag{4.24}$$

If these compatibility constraints are added to conservative conditions, the hybrid unknowns have to be doubled at the interface for the problem to be well-posed. In the case of ICP, if there is a normal component of the electric field at the interface between subdomains, $\tilde{\mathcal{F}}$ becomes

$$\tilde{\mathcal{F}} = \begin{pmatrix} \mathcal{H}^{NS}_{v,E_p^{Re}}(\boldsymbol{\lambda}^{NS}) + \mathcal{H}^{Max}_{v,E_p^{Re}}(\boldsymbol{\lambda}^{MAX}) \\ \mathcal{H}^{NS}_{v,E_p^{Im}}(\boldsymbol{\lambda}^{NS}) + \mathcal{H}^{Max}_{v,E_p^{Im}}(\boldsymbol{\lambda}^{MAX}) \\ \varepsilon^{NS} E_n^{NS}(\boldsymbol{\lambda}^{NS}) - \varepsilon^{MAX} E_n^{MAX}(\boldsymbol{\lambda}^{MAX}) - \sigma_s \end{pmatrix} \tag{4.25}$$

where the various symbols keep their definition from Eq. 4.23 and where we have emphasized the doubling of the hybrid unknown by associating half of them to each subdomain ($\boldsymbol{\lambda}^{NS}$ is associated to the Navier-Stokes + Maxwell domain, $\boldsymbol{\lambda}^{MAX}$ is associated to the Maxwell domain). We have illustrated this case in Fig. 4.5 for general conservation laws.

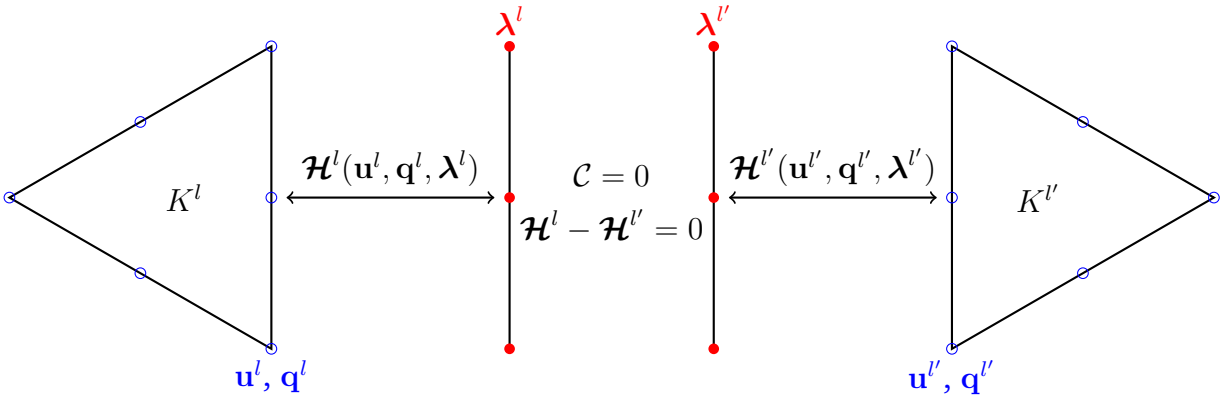

Fig. 4.5.: Illustration of conservativity and compatibility conditions. K^l and $K^{l'}$ are elements belonging to two separate domains Ω^l. When the numerical flux $\boldsymbol{\mathcal{H}}$ is conserved across the domains interface and there exists a compatibility condition $\mathcal{C} = 0$ between the variables of the two domains, the hybrid unknowns are doubled ($\boldsymbol{\lambda}^l$ and $\boldsymbol{\lambda}^{l'}$) in order to impose all interface conditions.

Note that, in the case of axisymmetric ICP, the azimuthal electric field is conserved across the interface between the Maxwell and ICP domains, but there is no compatibility condition.

4.2 Solution strategy

Eq. (4.16) is solved implicitly using Newton's method and eliminating the local variables in order to obtain a global system for the hybrid unknowns. The resulting hybrid solution $\boldsymbol{\lambda}$ is used to reconstruct the element-wise $(\mathbf{u}, \mathbf{q})$ solutions using direct

inversion of small local matrices. We discuss here in detail the solution procedure.

4.2.1 Steady-state solution strategy

Since we are interested in steady-state computations, a damped inexact Newton iteration is used in this work. It consists in adding a fictitious temporal term to the steady-state form of Eq. (4.16) ($\partial_t = 0$). The role of this pseudo-temporal term is to ease the convergence towards the steady-state, especially when the initial data are far from the steady solution. When the CFL is sufficiently large, this term becomes negligible, and the newton method is retrieved. This is translated in the first equation of Eq. (4.16) by replacing $\partial_t \mathbf{w}^K$ by a finite difference approximation, leaving the other systems unchanged

$$\begin{aligned}
&\left(\frac{\delta \mathbf{w}_h^K}{\tau_K} - \mathbf{S}_h^K, \varphi_{K,i}\right)_K - \left(\mathbf{F}_{h,c}^K - \mathbf{F}_{h,v}^K, \nabla\varphi_{K,i}\right)_K + \left\langle \boldsymbol{\mathcal{H}}^K, \varphi_{K,i}\right\rangle_{\partial K} = 0 \\
&(\mathbf{q}_K, \boldsymbol{\tau}_{K,i})_K - (\mathbf{u}_K, \nabla\boldsymbol{\tau}_{K',i})_K + \langle \boldsymbol{\lambda}_{\partial K}, \boldsymbol{\tau}_{K,i}\cdot\mathbf{n}\rangle_{\partial K_0} + \langle \mathbf{u}_{bc}, \boldsymbol{\tau}_{K,i}\cdot\mathbf{n}\rangle_{\partial K_{bc}} = 0 \\
&\langle [[\boldsymbol{\mathcal{H}}]], \mu_{e,i}\rangle_{e\setminus\bar{\Gamma}} + \langle \tilde{\mathcal{F}}^e, \mu_{e,i}\rangle_{e\cap\bar{\Gamma}} = 0
\end{aligned} \tag{4.26}$$

where all symbols have their definition in Eq. (4.16), $\tau_K = CFL \times h_K/v_K$ is a local time step associated to element K and $\mathbf{x}^k = \mathbf{x}^{k-1} + \delta\mathbf{x}$, where k denotes the current Newton iteration. It is defined *via* a global Courant-Friederichs-Lewy number, the characteristic size h_K and speed v_K of each element. In this work,

$$\frac{h_K}{v_K} = \frac{V_K}{\int_{\partial K}\lambda_{max} dS}, \tag{4.27}$$

where λ_{max} is the maximal eigenvalue of the hyperbolic operator and V_K is the volume (or area in 2D) of the element K. The choice of the CFL is based on the evolution of L_2 norm of the residual $\mathcal{R}$ of the system. It is given by

$$CFL^n = \min\left(CFL_0\left(\frac{||\mathcal{R}||_2^0}{||\mathcal{R}||_2^n}\right)^\alpha, CFL_{max}\right) \tag{4.28}$$

where the index 0 denotes the initial value of a quantity, and CFL_{max} is a CFL upper bound. α is an exponent factor governing the evolution of the CFL. Note that we did note take into account the eigenvalues of the diffusive operator. They could be considered in the computation of the CFL by choosing between the maximum value of the convective operator and the diffusive one. This approach has not been tested but could have a stabilizing effect on the solver.

Eq. (4.26) can be cast in a generic form using a nonlinear operator $\tilde{\mathcal{N}}$

$$\tilde{\mathcal{N}}_h(\mathbf{x}_h; \mathbf{y}_i) = 0 \tag{4.29}$$

where $\mathbf{x}_h = (\boldsymbol{\lambda}_h, \mathbf{u}_h, \mathbf{q}_h)$ is the vector of unknowns and $\mathbf{y}_i = (\varphi_i, \boldsymbol{\tau}_i, \mu_i)$ is the vector containing the basis functions of the approximate functional spaces. We then linearize Eq. (4.29) and solve it

$$\tilde{\mathcal{N}}_h'(\mathbf{x}_h^k; \mathbf{y}_i)\delta\mathbf{x}_h^k = -\tilde{\mathcal{N}}_h(\mathbf{x}_h^k; \mathbf{y}_i), \tag{4.30}$$

where the $\tilde{\mathcal{N}}'$ is the Jacobian matrix. Although solving Eq. (4.30) is similar to the Newton method, it is not, since it contains a damping term. In the limit of $\tau_K \to \infty$, the Newton method is retrieved

$$\mathcal{N}_h'(\mathbf{x}_h^k; \mathbf{y}_i)\delta\mathbf{x}_h^k = -\mathcal{N}_h(\mathbf{x}_h^k; \mathbf{y}_i), \tag{4.31}$$

where now $\mathcal{N}$ and $\mathcal{N}_h'$ are respectively the residual and the Jacobian matrix of Eq. (4.16) at steady state without the damping term. The iterative procedure is started from an initial guess of the solution $\mathbf{x}_h^0$. From there, the solutions $\mathbf{x}^{k+1}$ are computed by solving successively Eq. (4.30) using $\mathbf{x}^k$ as an initial guess: $\mathbf{x}^{k+1} = \mathbf{x}^k + \delta\mathbf{x}^k$. The algorithm is stopped when the norm of the residual is sufficiently low. In order to further stabilize the solver, the update is limited such that

$$\mathbf{x}^{k+1} = \mathbf{x}^k + \beta\delta\mathbf{x}^k, \ \beta \in]0, 1] \tag{4.32}$$

In practice, $\beta = 0.8$ is sufficient to have a stable and relatively fast solver.

Following this procedure, Eq. (4.30) can be written for HDG as:

$$\underbrace{\begin{pmatrix} A & B & R \\ C & D & S \\ L & M & N \end{pmatrix}}_{\tilde{\mathcal{N}}_h'(\mathbf{x}_h^k;\mathbf{y}_i)} \overbrace{\begin{pmatrix} \delta Q \\ \delta U \\ \delta\Lambda \end{pmatrix}}^{\delta\mathbf{x}_h^k} = \underbrace{\begin{pmatrix} F \\ G \\ H \end{pmatrix}}_{-\tilde{\mathcal{N}}_h(\mathbf{x}_h^k;\mathbf{y}_i)}, \tag{4.33}$$

Eq. (4.33) can be rewritten in two sets of equations:

$$\Sigma \begin{pmatrix} \delta Q \\ \delta U \end{pmatrix} = \begin{pmatrix} F \\ G \end{pmatrix} - \begin{pmatrix} R \\ S \end{pmatrix} \delta\Lambda, \text{ with } \Sigma = \begin{pmatrix} A & B \\ C & D \end{pmatrix} \tag{4.34}$$

and

$$\begin{pmatrix} L & M \end{pmatrix} \begin{pmatrix} \delta Q \\ \delta U \end{pmatrix} + N\delta\Lambda = H \tag{4.35}$$

Eq. (4.34) is called the local system, because Σ is block diagonal, with each block associated to an element. Therefore, it is possible to eliminate the local variables from Eq. (4.35) by directly inverting Σ, leading to a global system for the hybrid unknowns:

$$\left(N - \begin{pmatrix} L & M \end{pmatrix} \Sigma^{-1} \begin{pmatrix} R \\ S \end{pmatrix} \right) \delta\Lambda = H - \begin{pmatrix} L & M \end{pmatrix} \Sigma^{-1} \begin{pmatrix} F \\ G \end{pmatrix} \tag{4.36}$$

Then, the linear system given in Eq. (4.36) is solved with the PETSc library [6]. A GMRES method is employed with at most 50 basis vectors. An ILU preconditioner with 4 levels of fill-in is used. The solution algorithm to solve the full HDG system is given in Algorithm 1. An interesting feature of the multi-domain solver is that it can be solved in exactly the same manner as single-domain HDG. The only difference lies in the assembly of the system. Even there, the only real difference is due to the coupling term between subdomains.

4.2.2 Newton-Raphson method and global power strategy

In ICP facilities, part of the power supplied to the generator is dissipated in the form of Joule heating in the plasma. Let us call this part P_{target}. There is no straightforward relation linking the current I_C to be imposed in the coil and P_{target} in the experimental facility. It is also not possible to know beforehand the current to be imposed in the ICP simulation at the coil in order to dissipate P_{target}. However, if P_{target} is not maintained during the computations, the torch is quenched [12]. To avoid this, an iterative procedure for maintaining a constant power in the facility inspired by legacy ICP solvers [107, 106] is described here.

Instead of solving the Navier-Stokes equations given in Eq. (3.5), we solve for a slightly different formulation of the problem

$$\begin{aligned}
&\partial_t \rho + \nabla \cdot (\rho \mathbf{v}) = 0 \\
&\partial_t (\rho \mathbf{v}) + \nabla \cdot (\rho \mathbf{v}\mathbf{v}) + \nabla p - \nabla \cdot \boldsymbol{\tau} = \gamma \, \mathbf{F}^L\big|_{I_c=1\,\mathrm{A}} \\
&\partial_t \left(\rho e + \frac{1}{2}\rho ||\mathbf{v}||^2\right) + \nabla \cdot \left(\rho e \mathbf{v} + \frac{1}{2}\rho ||\mathbf{v}||^2 \mathbf{v} + p\mathbf{v} - \boldsymbol{\tau} \cdot \mathbf{v} - \mathbf{q}\right) = \gamma \, P_J|_{I_c=1\,\mathrm{A}}
\end{aligned} \tag{4.37}$$

On the other hand, the electric field equation solved is

$$\Delta \, E_P|_{I_c=1\,\mathrm{A}} = \frac{E_P|_{I_c=1\,\mathrm{A}}}{r^2} + i2\pi f \mu_0 \sigma_e \left(E_C|_{I_c=1\,\mathrm{A}} + E_P|_{I_c=1\,\mathrm{A}}\right) \tag{4.38}$$

In these systems, the subscript $I_C = 1\,\mathrm{A}$ means that a quantity is evaluated for an induction current $I_C = 1\,\mathrm{A}$. Consequently, the computed electric field $E_P|_{I_c=1\,\mathrm{A}}$ is the electric field in the plasma when E_C is produced by $I_C = 1\,\mathrm{A}$. In order to match the desired power dissipated in the facility P_{target}, the scaling factor γ is introduced. If the power dissipated in the facility when $I_c = 1\,\mathrm{A}$ is defined by

$$P|_{I_c=1\,\mathrm{A}} = \int_{NS} \frac{\sigma_e}{2} || \, E_C|_{I_c=1\,\mathrm{A}} + E_P|_{I_c=1\,\mathrm{A}} \, ||^2 dV \tag{4.39}$$

then we define γ as

$$\gamma = \frac{P_{target}}{P_{tot}}, \tag{4.40}$$

meaning that

$$P_{target} = \gamma\, P|_{I_c=1\,\mathrm{A}} = \int_{NS} \gamma \frac{\sigma_e}{2} || \, E_C|_{I_c=1\,\mathrm{A}} + E_P|_{I_c=1\,\mathrm{A}} \, ||^2 dV \tag{4.41}$$

Reaching the target power is thus equivalent to multiply $E_P|_{I_c=1\,\mathrm{A}}$ and $E_C|_{I_c=1\,\mathrm{A}}$ by $\sqrt{\gamma}$ in the Navier-Stokes equations. This is translated in Eq. (4.37) by the multiplication of the effective Lorentz force $\mathbf{F}^L$ and joule dissipation P_J terms by γ. Consequently, the procedure for maintaining the power at P_{target} in the facility is the following:

1. Compute the coil electric field $E_C|_{I_c=1\,\mathrm{A}}$ for $I_C = 1\,\mathrm{A}$.
2. Compute γ for the initial solution using Eq. (4.40).
3. Solve for one Newton iteration for $I_C = 1\,\mathrm{A}$ and by multiplying $\mathbf{F}^L\Big|_{I_c=1\,\mathrm{A}}$ and $P_J|_{I_c=1\,\mathrm{A}}$ by the value of γ obtained previously.
4. At the end of the Newton iteration, $P|_{I_c=1\,\mathrm{A}}$ is evaluated using the solution and another γ is computed using Eq. (4.40).
5. Return to step 3 until convergence occur.
6. Once the system has converged, the true E_C and E_P can be retrieved with

$$\begin{aligned} E_C &= \sqrt{\gamma}\, E_C|_{I_c=1\,\mathrm{A}} \\ E_P &= \sqrt{\gamma}\, E_P|_{I_c=1\,\mathrm{A}} \end{aligned} \tag{4.42}$$

This procedure is integrated in Algorithm 1.

4.2.3 Comparison with previous solution procedure and algorithm

The solution procedure employed with the HDG code (Fig. 4.6) is quite different from the previous solvers such as COOLFluiD (Fig. 4.7). In the HDG code, the system of equation (ICP + Maxwell) is solved in a fully coupled manner. On the other hand, the FV solver decouples the solutions of Maxwell and Navier-Stokes equations, solving them separately by assuming that all hydrodynamic quantities are frozen while solving the electric field, and *vice-versa*. While the latter procedure is easier to implement, it takes more Newton iterations to converge (on the order of thousand of iterations) than the monolithic solver (on the order of 10-100 iterations).

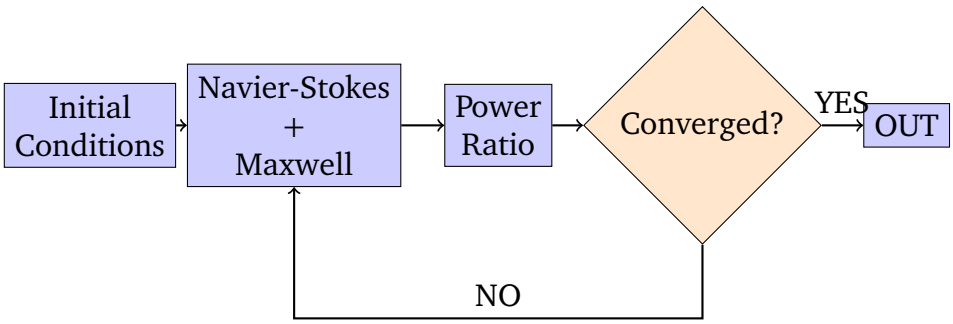

Fig. 4.6.: Diagram of the solution procedure of ICP simulations using the HDG method. The Navier-Stokes and Maxwell equations are solved in a fully coupled manner.

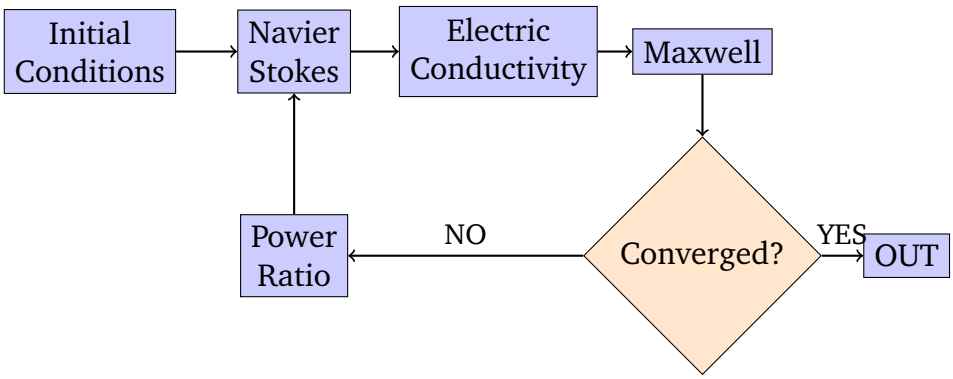

Fig. 4.7.: Diagram of the solution procedure of ICP simulations using the COOLFluiD FV solver. The system is solved in a decoupled manner: one system is frozen while the other is solved. The process is repeated until convergence occurs. This diagram was inspired by [100]

Finally, the complete solution procedure for the HDG method is given in pseudo-code form in Algorithm 1.

Algorithm 1 Solution procedure for multi-domain HDG

Set all simulation parameters
Initialize $\boldsymbol{\lambda}_h$, $\mathbf{w}_h$, $\mathbf{q}_h$;
Compute $E_C|_{I_c=1\,\mathrm{A}}$ using Eq. (3.37) and $I_C = 1\,\mathrm{A}$.
Compute $P|_{I_c=1\,\mathrm{A}}$ and γ using Eq. (4.39) and Eq. (4.40);
while $||Residual||_2 >$ Tolerance **do**
  for l = 1, ..., N_d **do**
    for i = 1,..., N_e **do**
      Assemble local system (Eq. (4.34)) of subdomain l;
      - Navier-Stokes and Maxwell subdomain: Eq. (4.37) and Eq. (4.38).
      - Maxwell subdomain: Eq. (4.38).
      Solve local system of subdomain l;
      Store local solution of subdomain l;
      Assemble global system (Eq. (4.36));
    end for
  end for
  Solve global system;
  Update $\boldsymbol{\lambda}_h$, $\mathbf{w}_h$, $\mathbf{q}_h$;
  Compute $P|_{I_c=1\,\mathrm{A}}$ and γ using Eq. (4.39) and Eq. (4.40);
end while
Multiply $E_C|_{I_c=1\,\mathrm{A}}$ and $E_P|_{I_c=1\,\mathrm{A}}$ by $\sqrt{\gamma}$ to obtain E_C and E_P;

4.3 Conclusions of the multi-domain HDG monolithic solver development

In this Chapter, we developed a new monolithic HDG solver and applied it to the ICP problem. It appears that the HDG method is well suited for this task, as it inherently possess a conservation condition for determining the hybrid variables. These conservation conditions can be modified at the boundary between subdomains to account for the relationship linking the two physics. In the same way, compatibility conditions can also be imposed. The key concept is to have as many hybrid unknowns as there is compatibility and conservativity conditions. This concept is of capital importance for the problem to be well-posed. Finally, although we restricted this new method to ICP applications, it can be easily applied to any system of conservation laws. The idea is to adapt the governing equations, numerical fluxes, conservation and compatibility conditions according to the physics at play.

5 Verification and validation

We present a numerical study of the ICP simulations. We first perform a convergence study using a manufactured solution. Next, we study the dependence of the solution on the mesh refinement and on the order of the HDG method. This analysis allows to find a mesh that is accurate while keeping a reasonable computational costs. We then study the impact of the coflow stabilizing the plasma jet. The HDG code is also compared to previous ICP computations performed using a finite volume solver (COOLFluiD). Finally, the convergence towards steady state using the Newton monolithic solver is discussed.

This Chapter is an important contribution of this thesis, as the various numerical studies performed here were never formally reported in the case of ICP, and in particular in the case of high-order methods. With this analysis, we want to prove that the HDG high-order code is reliable for ICP simulations. The comparison with COOLFluiD and the convergence study have been published by the author [25].

5.1 Convergence study

Finding an analytical solution for the complete ICP problem in order to perform a convergence study is challenging. Consequently, we use the method of manufactured solutions, which we describe in the following. Let us consider a non-linear equation that can be written in the form

$$\mathcal{F}(\mathbf{u}) = 0 \tag{5.1}$$

Manufacturing a solution is to modify Eq. (5.1) so that it is solved for a given solution $\mathbf{u}^*$. The modified problem is

$$\mathcal{F}(\mathbf{u}) = \mathcal{F}(\mathbf{u}^*). \tag{5.2}$$

$\mathcal{F}(\mathbf{u}^*)$ is then used as an additional source term in the equation. In our case, the equation

$$\mathcal{F}(\mathbf{u}) = \partial_t \mathbf{w}(\mathbf{u}) + \nabla \cdot \mathbf{F}(\mathbf{u}, \nabla \mathbf{u}) - \mathbf{S}(\mathbf{u}, \nabla \mathbf{u}) = \mathcal{F}(\mathbf{u}^*) \tag{5.3}$$

is solved. With this method, it is possible to verify a code implementation on any test solution, at the price of an additional source term, $\mathcal{F}(\mathbf{u}^*)$.

The manufactured solution for ICP equation is tested on an axisymmetric domain delimited by two concentric cylinders of radii $R_1 = 0.486\,\mathrm{m}$ and $R_2 = 0.972\,\mathrm{m}$ respectively and length $L = 0.486\,\mathrm{m}$. The region inside the first cylinder is governed by the full ICP equations (Maxwell and Navier-Stokes). The region delimited by the

radii R_1 and R_2 are ruled by Maxwell's equations only (Fig. 5.1).

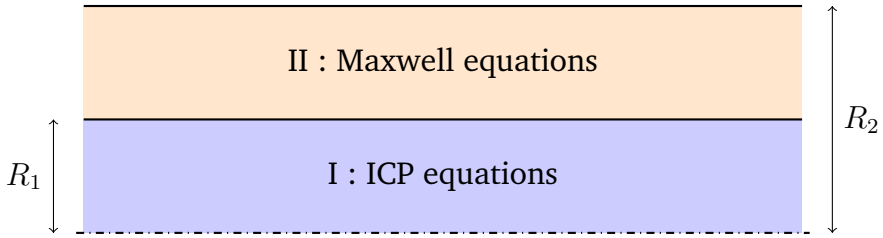

Fig. 5.1.: Illustration of the manufactured solution problem: the central cylinder is governed by Navier-Stokes and Maxwell equations, while the outer cylinder is governed by Maxwell equations.

The solutions chosen for the various fields are:

$$\begin{aligned} p &= \Delta p_0 f(z,r) + p_0 & T &= T_{min} + (T_{max} - T_{min})\, f(z,r) \\ v_z &= u_0 f(z,r) & E_p &= E_0 f(z,r)(1-i) \\ v_r &= u_0 f(z,r) & v_\theta &= u_0 f(z,r) \end{aligned} \tag{5.4}$$

with $p_0 = 5000\,\mathrm{Pa}$, $\Delta p = -10\,\mathrm{Pa}$, $u_0 = 100\,\mathrm{m\ s^{-1}}$, $T_{min} = 350\,\mathrm{K}$, $E_0 = 1\,\mathrm{V\ m^{-1}}$ and

$$f(z,r) = \left(\frac{rz}{RL}\right)^2 \exp\left(-\frac{z}{L} - \frac{r}{R_1}\right) \tag{5.5}$$

We consider an ideal gas, with specific gas constant $\mathcal{R} = 287\,\mathrm{J\ kg^{-1}\ K^{-1}}$. The heat conductivity is $k = 3.54\,\mathrm{W\ m^{-1}\ K^{-1}}$, the dynamic viscosity is $\mu = 1.25 \times 10^{-4}\mathrm{Pa\ s}$ and the heat capacity ratio is $\gamma = 1.46$. The electric field produced by the coil has been turned off ($E_C = 0$). The electric conductivity of the air is supposed constant in the ICP domain ($\sigma = 3804.7\,\mathrm{S\ m^{-1}}$), but null in the Maxwell domain. The induction frequency $f = 0.37\,\mathrm{MHz}$. Note that the chosen manufactured solution cannot be represented by a polynomial basis. This way, a convergence study with arbitrary order can be performed.

High-order methods using polynomial degree p converge in the L_2 norm to the analytical solution $\mathbf{u}^*$ of the problem with order $p+1$, meaning that

$$L_2(\mathbf{u} - \mathbf{u}^*) = \left[\int_V (\mathbf{u} - \mathbf{u}^*)^2 d\mathbf{x}\right]^{\frac{1}{2}} = \mathcal{O}\left(h^{p+1}\right) \tag{5.6}$$

where h is the characteristic mesh size. In Fig. 5.2 and in Fig. 5.3 the convergence order is retrieved for the solution in both domains. Note that the mesh used is quadrangular and structured. For sufficiently high polynomial order and number of elements, the round-off errors dominate and the convergence stalls.

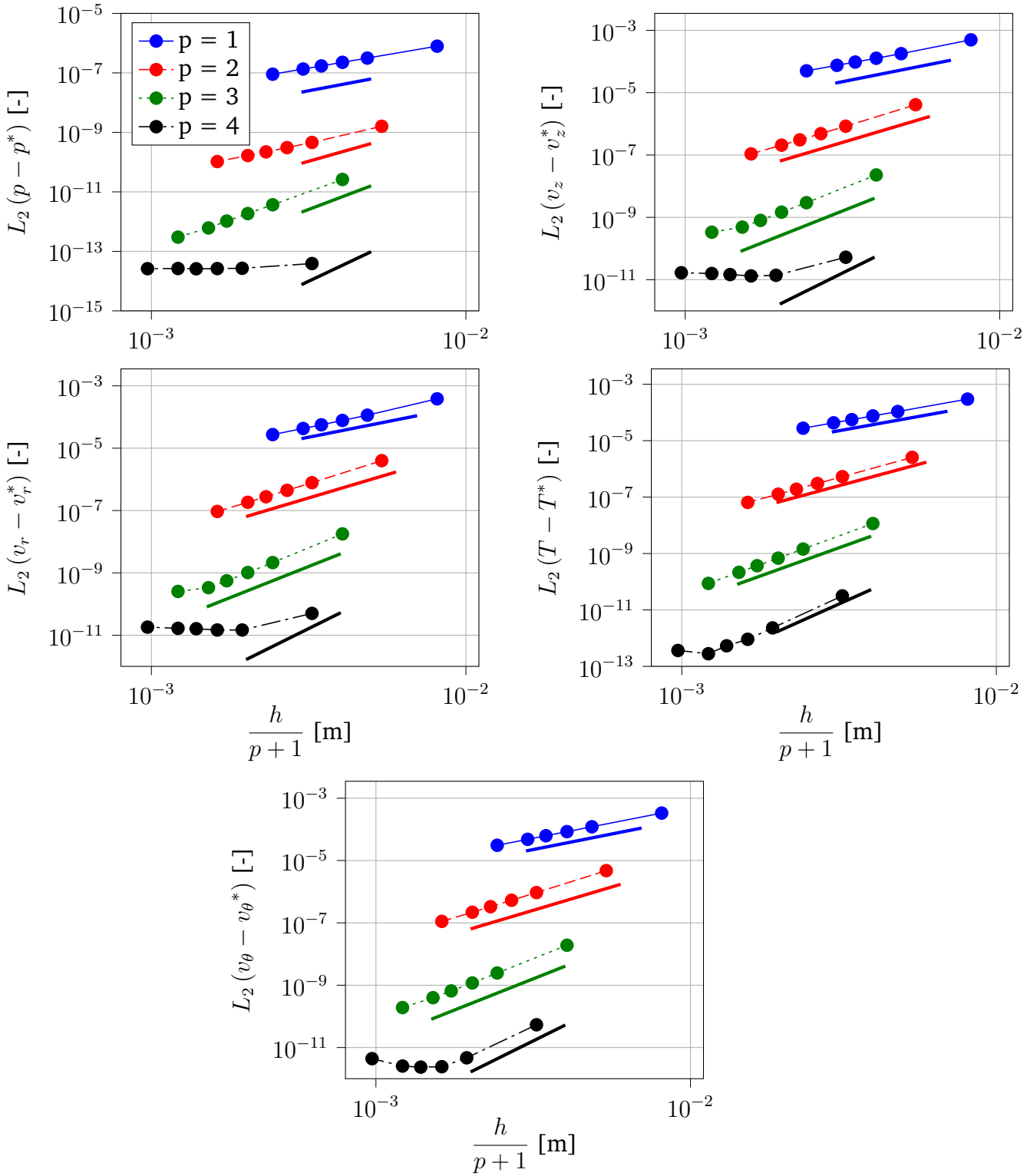

Fig. 5.2.: Convergence of the L_2 norm of the error on the pressure p, velocities v_z, v_r, temperature T and azimuthal velocity v_θ in the ICP domain as a function of the mesh size h. The quantities have been made dimensionless using their characteristic values. The thick lines have a slope $p+1$ and serve as comparison with the expected order of convergence.

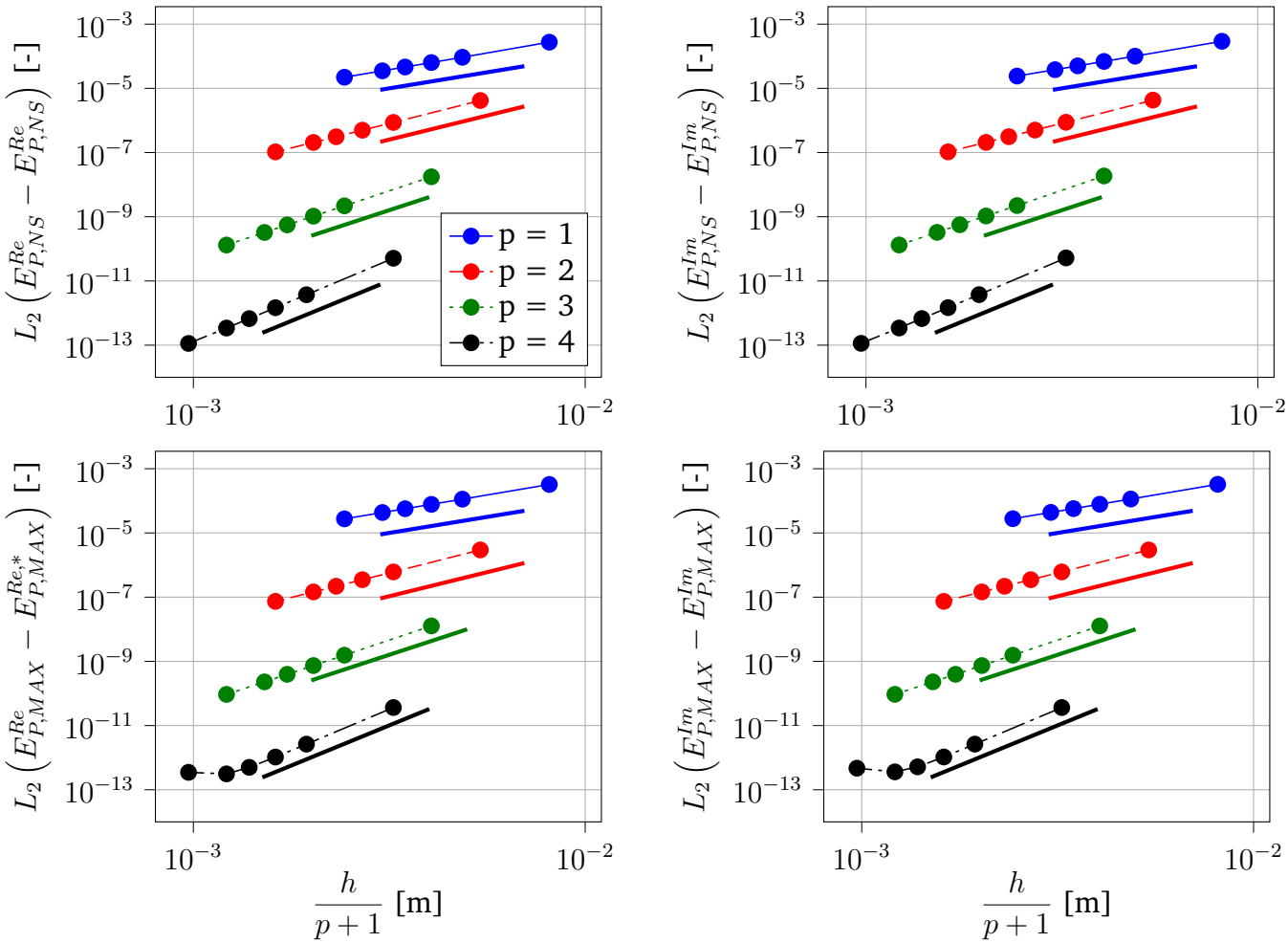

Fig. 5.3.: Convergence of the real and imaginary parts of the plasma electric field E_P^{Re}, E_P^{Im} fields respectively in the Maxwell + Navier-Stokes (NS) and Maxwell (MAX) domains as a function of the mesh size h. The quantities have been made dimensionless using their characteristic values. The thick lines are of slope $p+1$ and serve as comparison with the expected order of convergence.

5.2 Mesh and order dependence study

We consider an ICP flow with the following characteristics

- $P = 100\,\mathrm{kW}$ (power dissipated in the facility)
- $p_0 = 10\,000\,\mathrm{Pa}$ (background pressure)
- $f = 0.37\,\mathrm{MHz}$ (induction frequency)
- $Q = 16\,\mathrm{g\ s^{-1}}$ (mass flow rate)

- $S = 20°$ (swirl angle)
- air mixture with 11 species

and with a geometry given in Fig. 5.4.

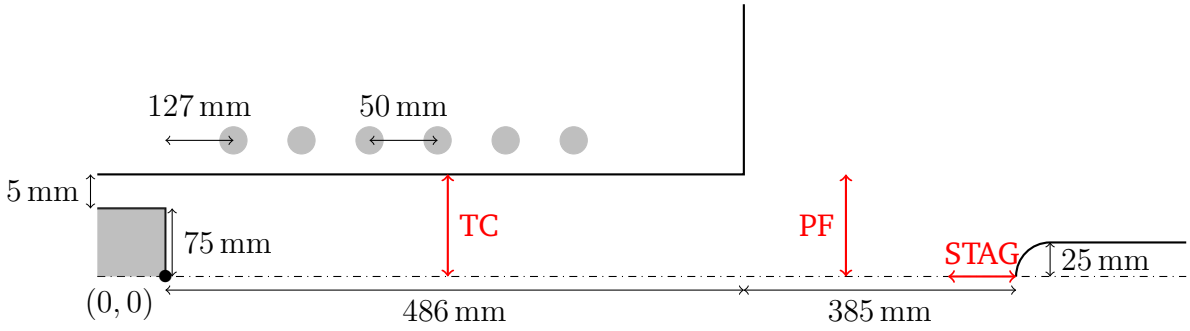

Fig. 5.4.: Geometry of the ICP torch. The red lines represent the locations where the mesh and order independence studies are performed. TC is for "torch center", STAG is for "stagnation line" and PF stands for "in front of the probe".

We have conducted the mesh and order dependence studies on various fields at specific locations (red lines in Fig. 5.4) on two realistic cases representative of actual ICP flows in Appendix A, where the reader will find the complete analysis. In this Section, we give only the main conclusions. These cases have the same input parameters, representative of actual ICP flows. However, one has a probe in the chamber, the other is in freestream conditions. The polynomial dependence was performed on three meshes, from coarse to refined, using polynomial order from 1 to 4. As a general rule, the solution becomes order independent for $p \geq 3$ for every mesh, although some profiles are very well captured by polynomials of second degree (even $p = 1$). From there, we performed the mesh dependence study on $p = 3$ and $p = 4$. The conclusion is univocal: mesh independence is reached for $p = 3$, no matter the level of refinement. With the objective of saving computational resources, a natural choice is to use $p = 3$ with the coarsest mesh. However, before choosing the mesh, two important quantities need to be assessed: the convergence of the probe total heat flux and the power ratio in the facility.

The effect of the mesh refinement and polynomial order on the power ratio γ, which is the square of the scaling factor of the electric field, in the ICP facility is given in Fig. 5.5. The results obtained at $p = 3$ and $p = 4$ are similar. Moreover, at these orders, γ is almost mesh independent.

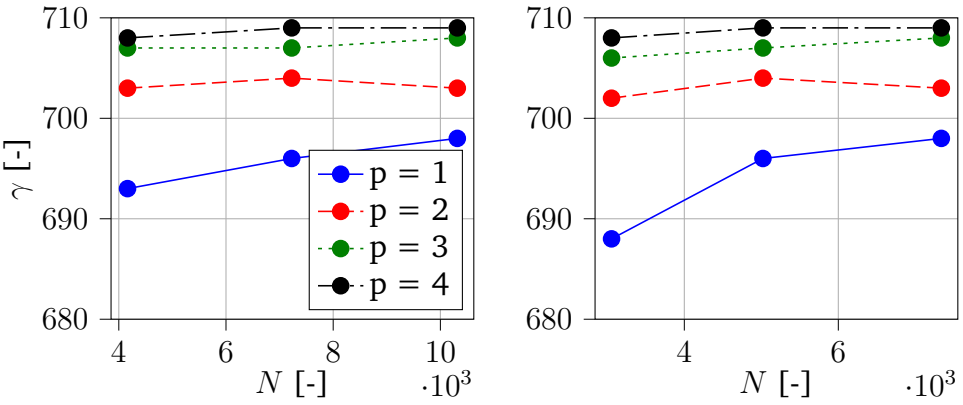

Fig. 5.5.: Evolution of the power ratio γ as a function of the mesh element number N for different polynomial orders p for the probe (left) and freestream cases (right).

On the other hand, the mesh and order dependence study of the probe heat flux is given in Fig. 5.6. The heat flux is the most accurate for order 4 polynomials, where it does not change anymore with respect to mesh refinement.

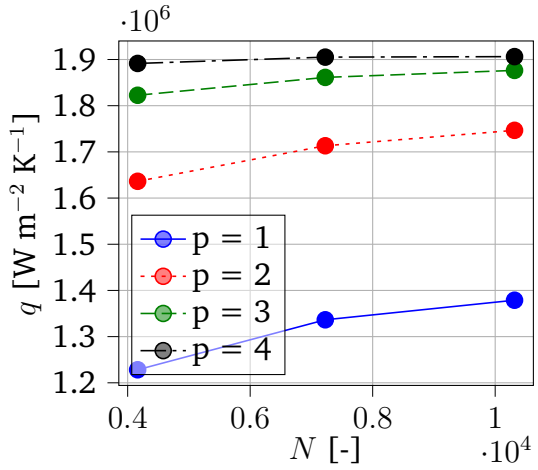

Fig. 5.6.: Normal heat flux q measured at the tip of the probe as a function of the number of elements N.

In light of all the previous discussions, we chose the coarse meshes given in Fig. 5.7 for the subsequent simulations with polynomial reconstruction of degree 4. On the contrary of legacy finite volume solvers, the mesh is fully unstructured and requires few elements. It is only structured near the boundary layer regions, where the velocity and temperature gradients are the steepest. The mesh size in the boundary layer near the probe is of the order of $10\,\mu\text{m}$, which is more or less 10 times greater than what is used with finite volumes. We tried coarser boundary mesh without success. However, this increased mesh size near the wall is non negligible, especially when considering 3D computations. A solution would be to increase the order of the solution next to

the boundary layer, while keeping a lower order on the rest of the domain. However, we leave these investigations for future work.

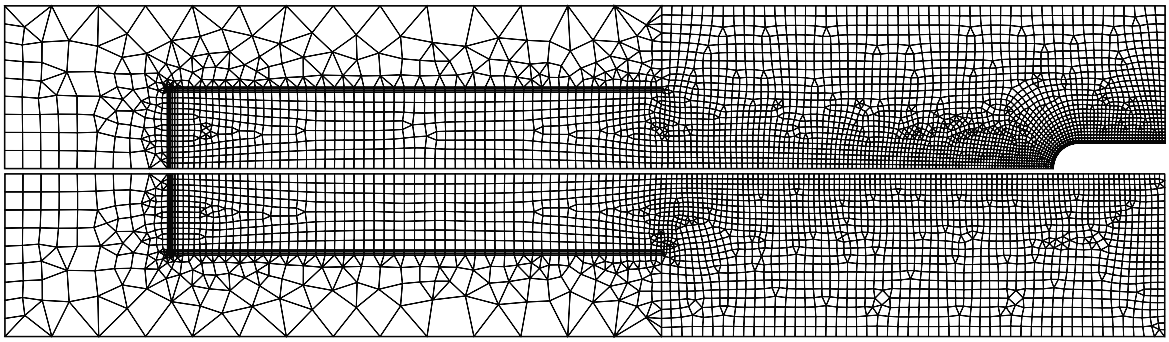

Fig. 5.7.: Mesh used in the simulations. It contains is an unstructured mix of quads and triangles at $p = 4$. The probe case has only 4013 elements (top) while the freestream case has 3055 elements (bottom).

5.3 Impact of the coflow in steady simulations

Previously, we introduced the stabilizing coflow in the chamber. However, this coflow is not present in experimental ICP. It is only added in numerical simulations to remove the Kelvin-Helmholtz instabilities or other unsteady behaviour at the torch exit for the steady solver to converge. It is important to note that, from our experience, it was impossible to obtain a steady solution with our high-order ICP simulations if the coflow was not applied. Although not rigorously physical, steady-state computations are computationally cheaper than their unsteady counter part, and already give an overview of the ICP flow features. However, the coflow may have a significant impact on the hydrodynamic fields. Consequently, we assess its influence on the probe and freestream ICP cases (see Section 5.2).

The formal definition of the coflow χ is

$$\chi = \frac{U_{blow}}{U_{in}} \tag{5.7}$$

where U_{in} is the inlet average velocity and U_{blow} is the velocity of the gas blown in the chamber at the inlet temperature. We found that, below $\chi = 0.16$, no steady solution could be found using the steady solver employed. The mesh used is the one determined during the mesh and grid independence study, with polynomial order 4. We also turned off the swirl component of the velocity.

5.3.1 Impact of the coflow in the probe case

The hydrodynamic fields along the stagnation line in front of the probe are not affected by the coflow (Fig. 5.8). The pressure is mildly affected, but it has no significant impact on the flow.

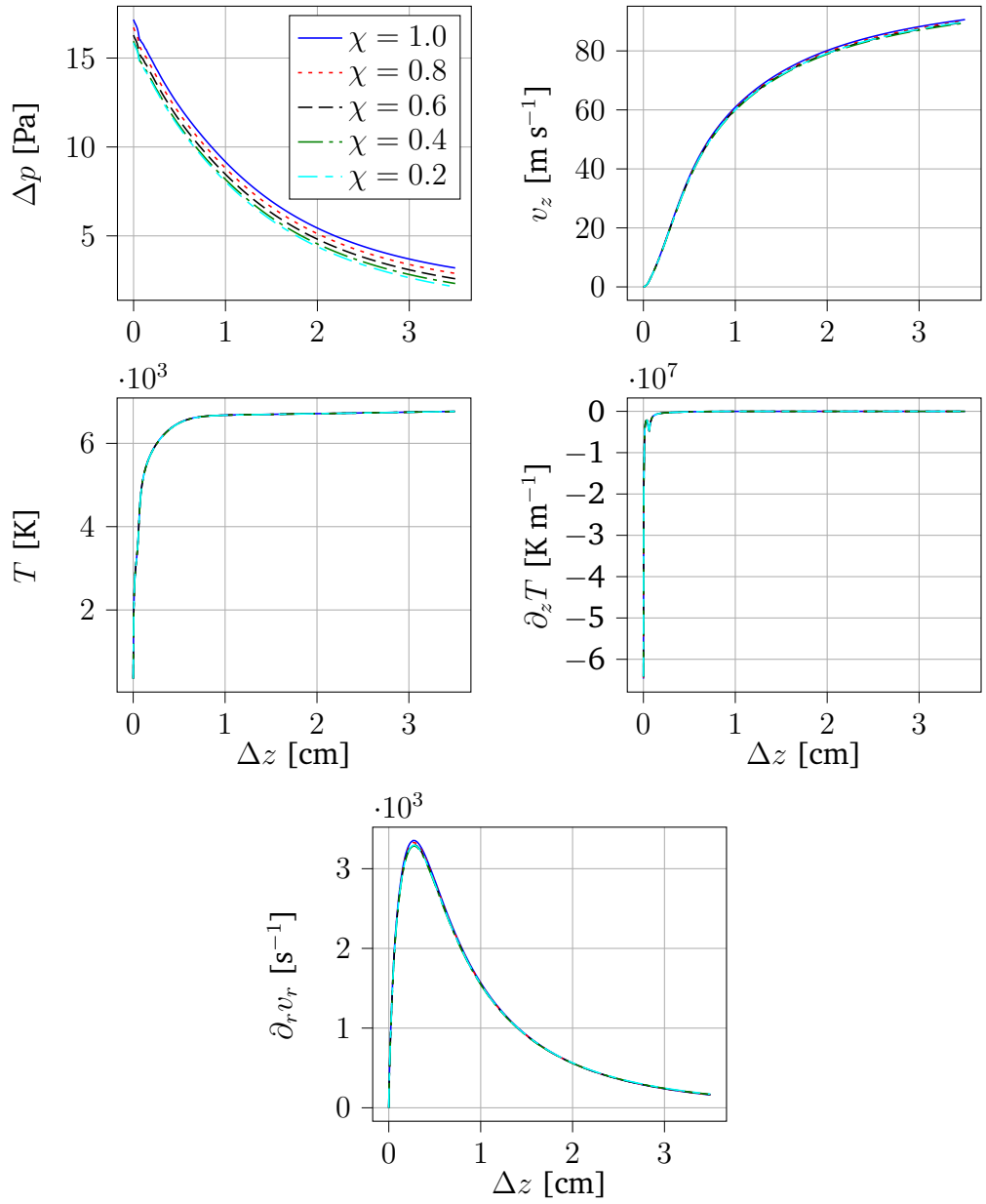

Fig. 5.8.: Variation of the pressure difference Δp, axial velocity component v_z, temperature T and radial gradient of the radial velocity $\partial_r v_r$ profiles along the stagnation line for the probe case with respect to the coflow χ. Δz represents the distance from the probe tip. The mesh used is given in Fig. 5.7, with $p = 4$.

The radial profiles in the torch were investigated and were found to be unaffected by the coflow. Indeed, the coflow being injected inside the chamber, it has a very limited impact upstream from its injection zone. On the other hand, discrepancies in the pressure and velocity profiles occur on the radial profile in the jet (Fig. 5.9). Since the characteristic gauge pressure ($\Delta p \simeq 3\,\mathrm{Pa}$) is very small compared to the background pressure of the facility ($10\,000\,\mathrm{Pa}$), and the temperature profile is not affected, the transport properties of the plasma are not altered by the numerical coflow. On the other hand, the large discrepancies in the axial velocity profile have an impact only above the torch radius ($r = 8\,\mathrm{cm}$), which is not a region of interest for experimental measurements. The radial velocity profile is the most affected. However, the magnitude of the radial velocity is so small compared to the axial one that it does not really impact the hydrodynamics. The gauge pressure profiles presents oscillations at large coflow at a radial distance $r = 8\,\mathrm{cm}$. It maybe a resolution problem in the shear layer. However, it has a limited impact on the flow due to the very small gauge pressure.

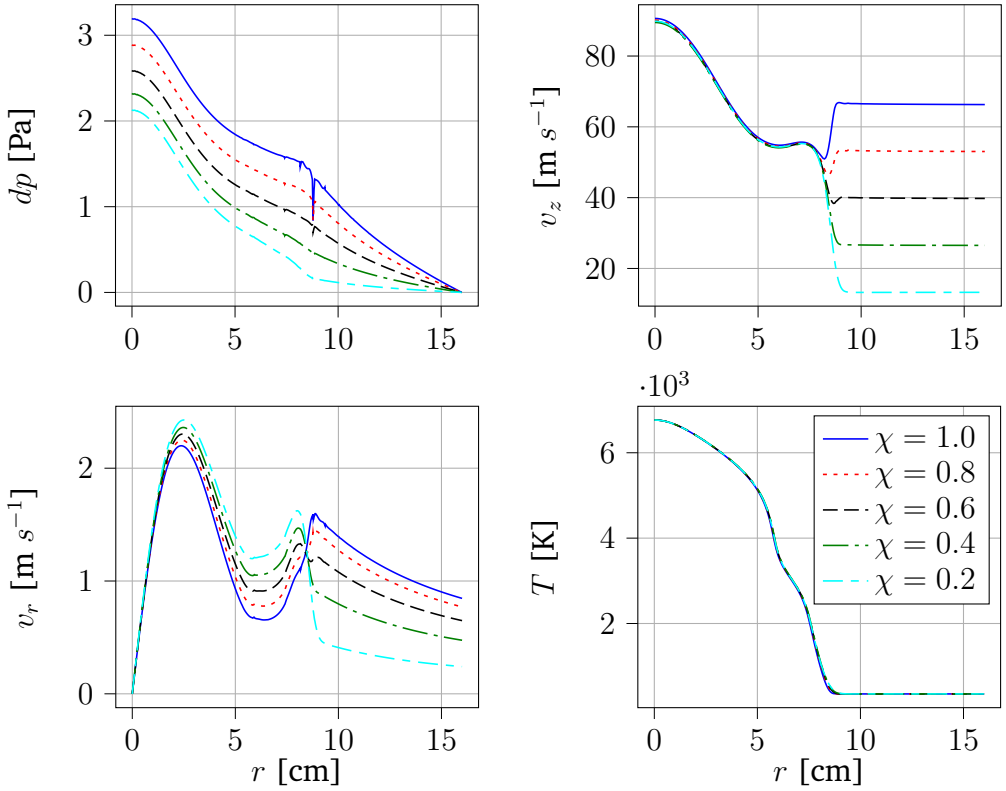

Fig. 5.9.: Variation of the pressure difference Δp, axial velocity component v_z, temperature T and radial gradient of the radial velocity $\partial_r v_r$ profiles along the radial direction r at $35\,\mathrm{mm}$ from the probe front for the probe case with respect to the coflow χ. The radial profile extends from the centerline (axis of symmetry) to twice the radius of the torch $2R = 16\,\mathrm{cm}$. The mesh used is given in Fig. 5.7, with $p = 4$.

The heat flux at the tip of the probe is almost not impacted by χ, with a variation

of at most $\simeq 2\%$ (Fig. 5.10).

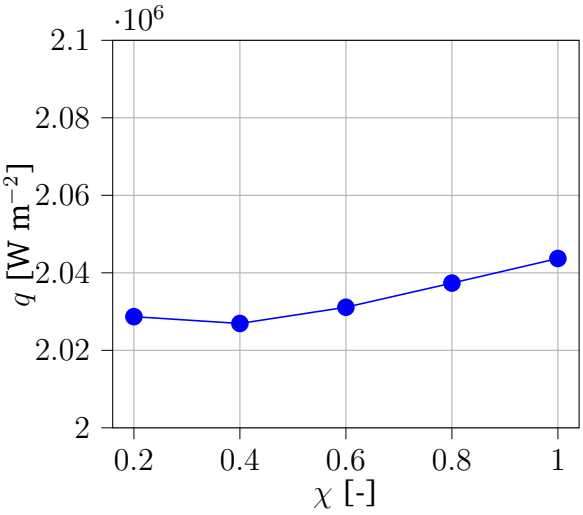

Fig. 5.10.: Heat flux at the tip of the probe q as a function of the coflow used χ. The mesh used is the coarse one given in Fig. 5.7, with $p = 4$.

5.3.2 Impact of the coflow in the freestream case

In the freestream case, as in the probe case, the flow inside the torch is unaffected by the coflow. The impact on the radial profiles in the jet is given in Fig. 5.11. The conclusions are the same as for the probe case. Pressure oscillations occur in the shear layer, around $r = 8\,\mathrm{cm}$. However, the gauge pressure is so low that it has practically no impact on the transport properties and the flow field. The strongest influence of the coflow is once again on the velocity profiles. Since the discrepancies mainly occur in the region outside of the torch radius, it has no real impact on the region where experimental measures are performed. Just like for the probe case, the radial velocity profile is the most impacted.

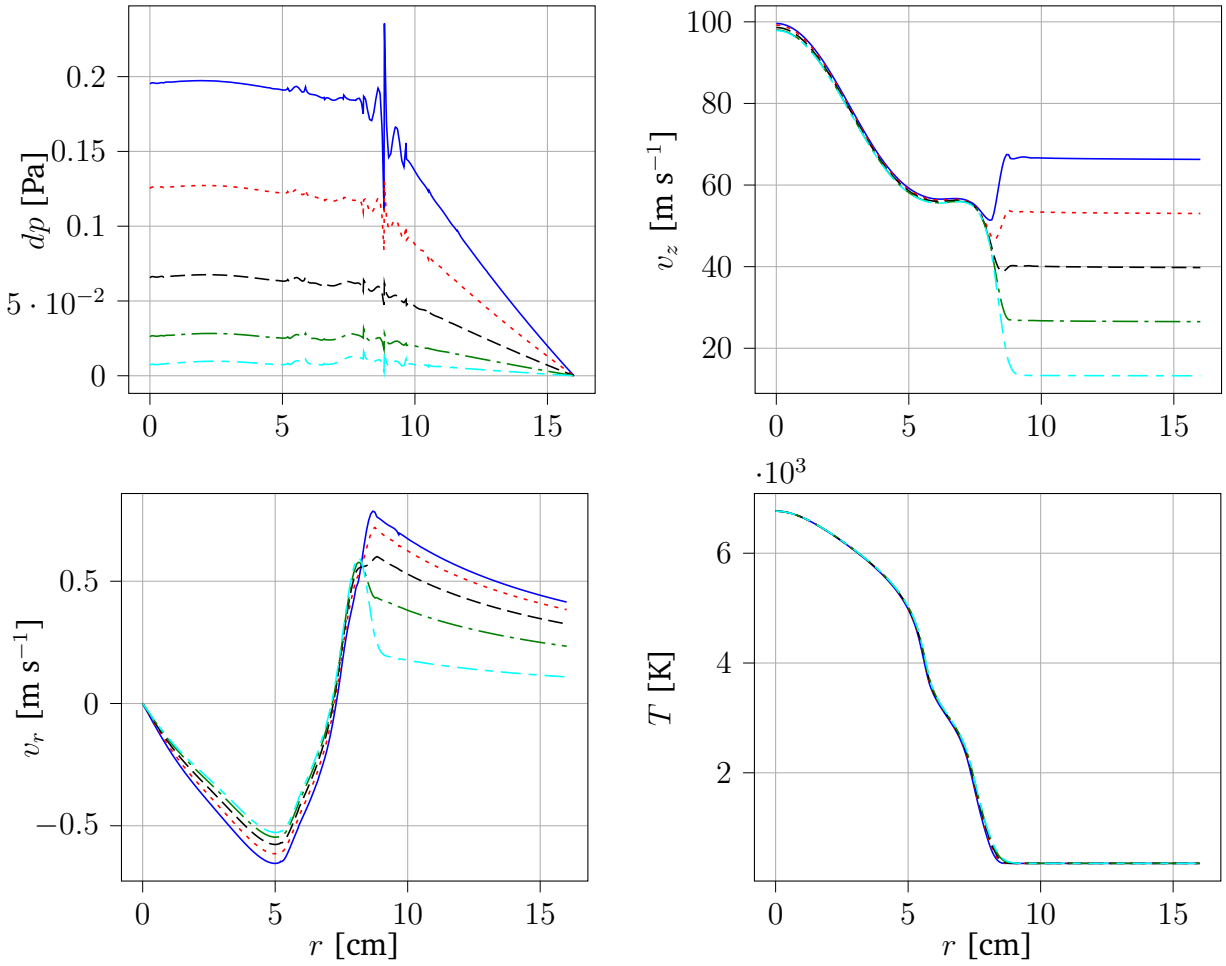

Fig. 5.11.: Variation of the pressure difference Δp, axial velocity component v_z, temperature T and radial gradient of the radial velocity $\partial_r v_r$ profiles along the radial direction r at $35\,\mathrm{mm}$ from the probe front for the freestream case with respect to the coflow χ. The radial profile extends from the centerline (axis of symmetry) to twice the radius of the torch $2R = 16\,\mathrm{cm}$. The mesh used is the coarse one given in Fig. 5.7, with polynomials of order 4.

5.3.3 Concluding remarks

We studied the impact of the coflow on the steady state simulation of ICP flows. We first realized that our steady state solver does not converge if a coflow χ of at least 0.16 is applied in the chamber. However, the coflow does not have a significant impact on the axial profiles along the stagnation line nor on the radial profile below the torch radius. The heat flux at the tip of the probe is also little affected. However, we suspect that the abscence of the coflow brings back unsteady behaviour in the jet and the flow becomes unsteady, potentially impacting the hydrodynamic fields. These considerations are left for future work, but the unsteady nature of ICP flows

should be investigated.

5.4 Comparison of HDG and COOLfluiD codes for ICP simulations

We now compare our HDG ICP code and the COOLFluiD finite volume solver. COOLFluiD was created at the von Karman Institute for Fluid Dynamics by Lani [67]. It allows, among other features, to perform ICP simulations on multiple processors. However, it is not a monolithic solver, the Maxwell and Navier-Stokes equations are solved successively until convergence occur.

Another notable difference is the handling of the electric field boundary condition. In HDG, the electric field domain is extended and canceled sufficiently far from the torch. For COOLFluiD, the domain is restricted to the torch and chamber and the integral boundary value for the electric field is used. It basically means that every cell of the domain is considered as a current loop. The combined effect of those loops dictates the electric field on the frontier of the domain. The advantage of the method is a reduction of the computational domain, but it also greatly fills the jacobian of the system, as the boundary condition depends on the electric field everywhere inside the torch. We compare our code and COOLFluiD from on a test case representative of the Plasmatron conditions with the following characteristics:

- $p_0 = 5000\,\mathrm{Pa}$ is the facility operating pressure,
- $Q = 16\,\mathrm{g\ s^{-1}}$ is the mass flow rate,
- $T_{wall} = 350\,\mathrm{K}$ is the temperature of the incoming air and the temperature of the walls of the facility,
- $P = 100\,\mathrm{kW}$ is the power dissipated in the facility,
- $f = 0.37\,\mathrm{MHz}$ is the coil induction frequency,
- air mixture with 11 species.
- No swirl angle.
- The coflow applied for HDG is $\chi_{HDG} = 0.2$.

The dimensions of the torch are given in Fig. 5.4. A hemispherical ($50\,\mathrm{mm}$ diameter) probe is placed in the chamber along the torch axis for the probe case. The freestream case is also investigated. We lowered the coflow to the minimum required for obtaining stable simulations, but could not match the one from COOLFluiD, which is $\chi_{CF} = 0.1$ for the probe case and $\chi_{CF} = 0$ for the freestream case.

5.4.1 Probe case

We compare the results of the COOLFluiD and HDG codes along the stagnation line, in front of the probe and in the torch center for the case with the probe.

Stagnation line

The pressure, temperature and axial velocity profiles obtained using HDG at order 4 and COOLFluiD on the stagnation line in front of the probe are given in Fig. 5.12. They show a very good agreement between the two simulations.

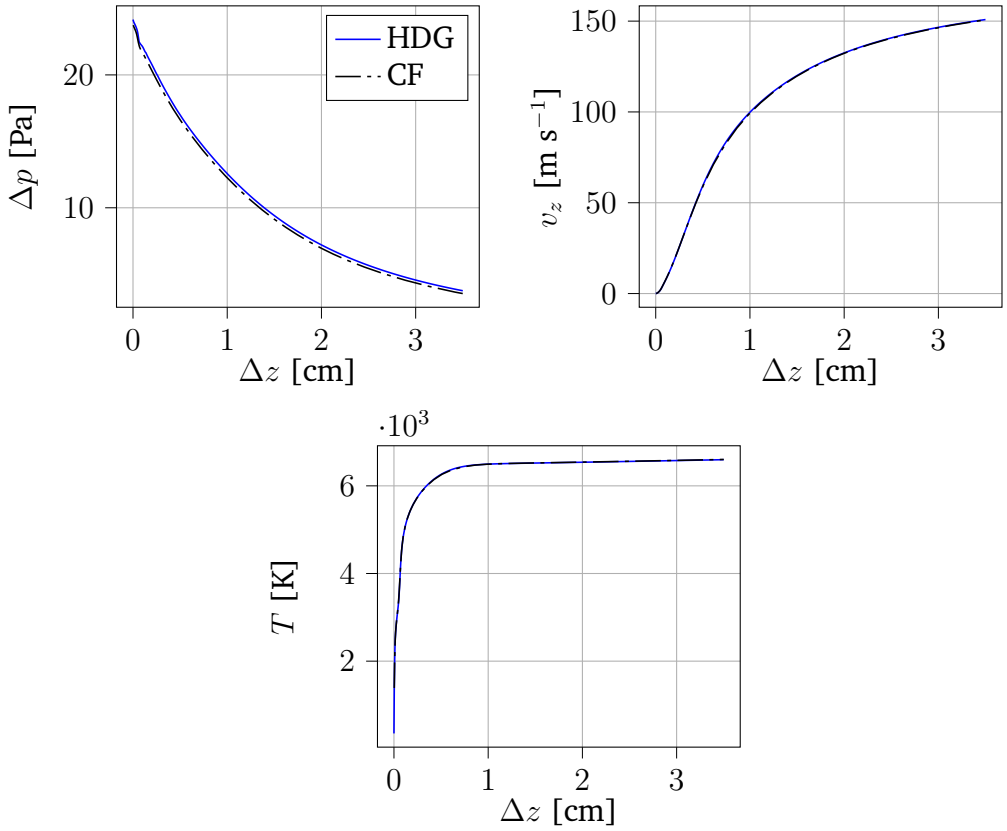

Fig. 5.12.: Comparisons of the axial velocity profile v_z, the pressure difference Δp and temperature profile T along the stagnation line in front of the probe in the Plasmatron for the HDG and COOLFluiD codes in the probe case. The stagnation line extends from the probe tip to $\Delta z = 35\,\mathrm{mm}$.

Probe front

The pressure, temperature and axial and radial velocity profiles obtained using HDG at order 4 and COOLFluiD on the stagnation line in front of the probe are given in

Fig. 5.13. There are some discrepancies in the pressure and velocity profiles, but they are negligible. They may arise from the different coflows employed for the simulations.

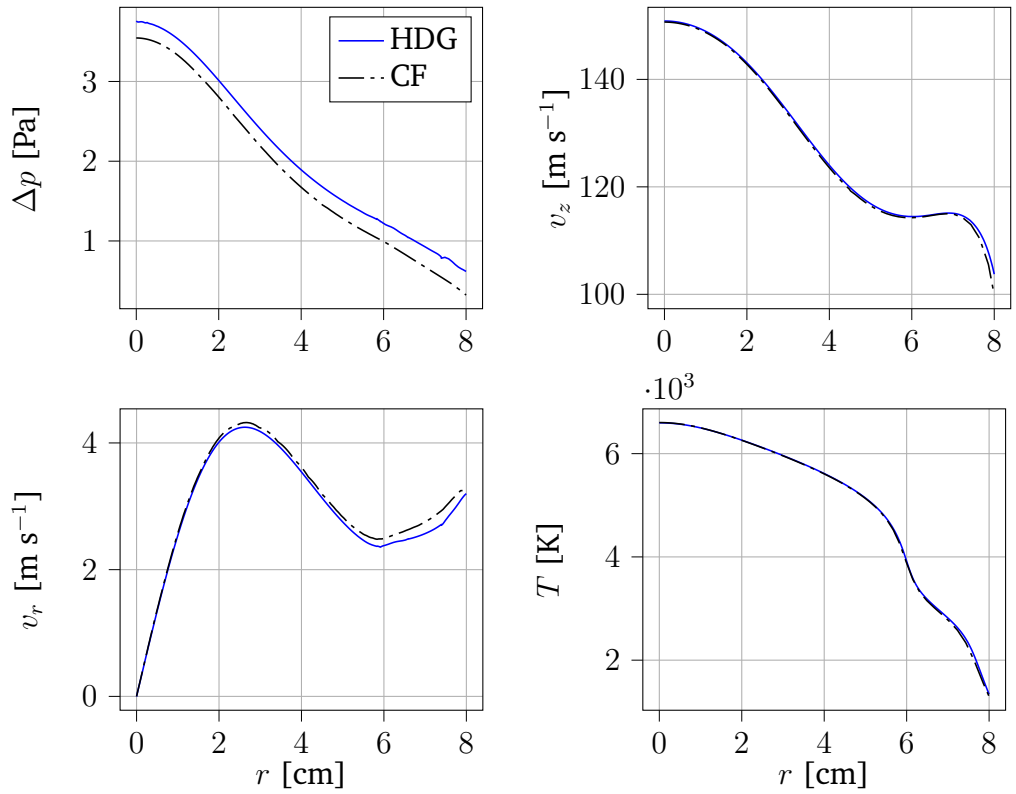

Fig. 5.13.: Comparisons of the axial v_z and radial v_r velocity profiles, the pressure difference Δp and temperature profile T along the radial direction at $\Delta z = 35\,\mathrm{mm}$ from the probe front.

Torch center

The pressure, temperature, axial and radial velocity profiles and the electric field obtained using HDG at order 4 and COOLFluiD on the stagnation line in front of the probe are given in Fig. 5.14. The only remarkable difference lies withing the electric field profiles.

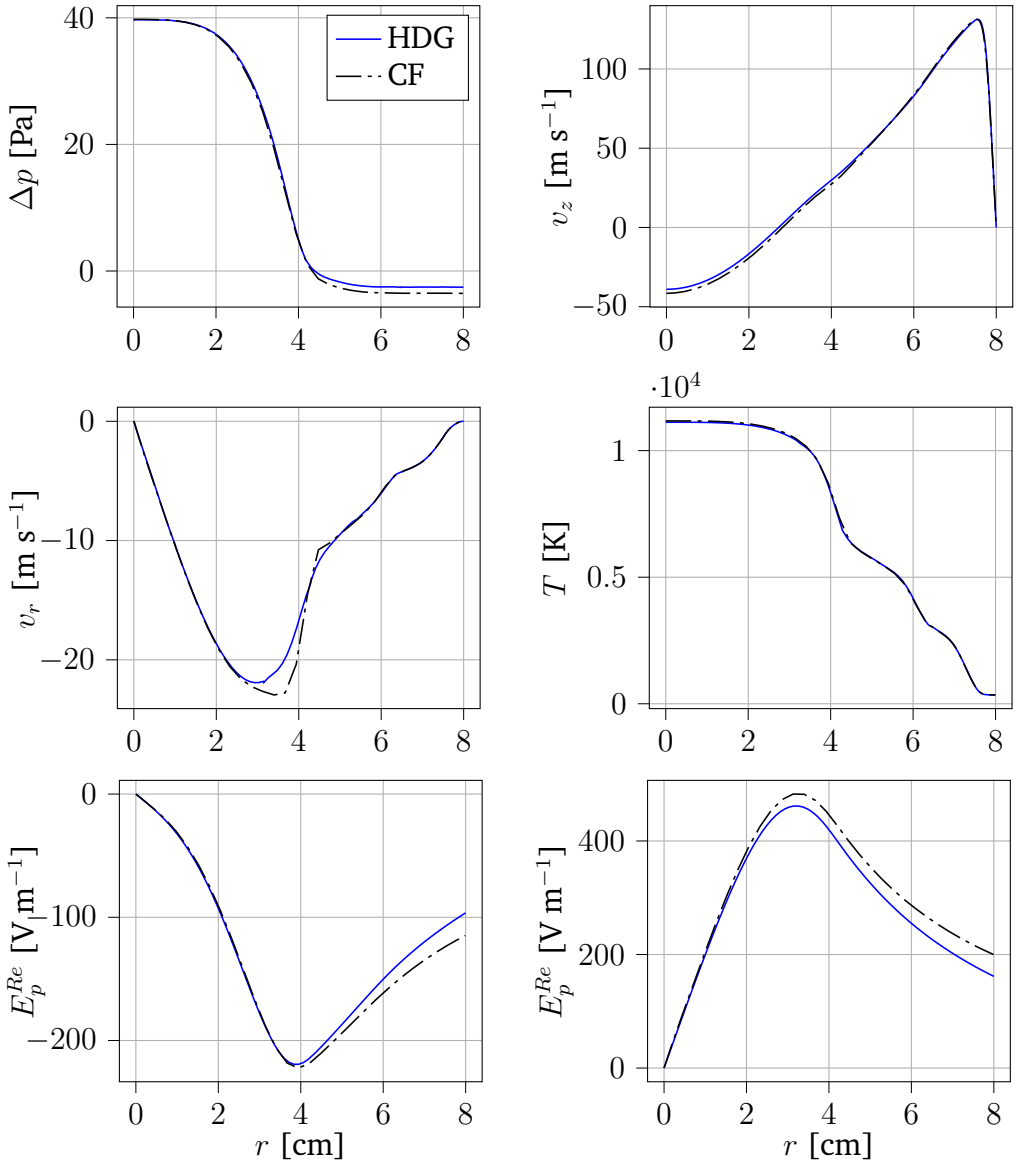

Fig. 5.14.: Comparisons of the axial v_z and radial v_r velocity profiles, the pressure difference Δp, temperature profile T and real E_p^{Re} and imaginary E_p^{Im} parts of the electric field along the radial direction at the torch center, at $24.3\,\mathrm{cm}$ from the torch inlet for the probe case.

They match close to the centerline but discrepancies appear close to the torch upper wall. The origin of this discrepancy is not well understood, but we can give potential causes. First, the imposition of the boundary condition for the electric field is very different in HDG, where the electric domain is extended, and in COOLFluiD, where the electric field is computed using integral boundary values. Second, the solution procedure is not the same. For HDG, the electric field is computed in a fully coupled way, while in COOLFluiD the electric and Navier Stokes solvers are

segregated. These possible causes are not explored here, but the difference in electric field has no substantial impact on the hydrodynamic field.

5.4.2 Freestream case

We compare the results of the COOLFluiD and HDG codes in the jet and in the torch center for the freestream case.

In the jet

The pressure, temperature and axial and radial velocity profiles obtained using HDG at order 4 and COOLFluiD on the stagnation line in front of the probe are given in Fig. 5.15.

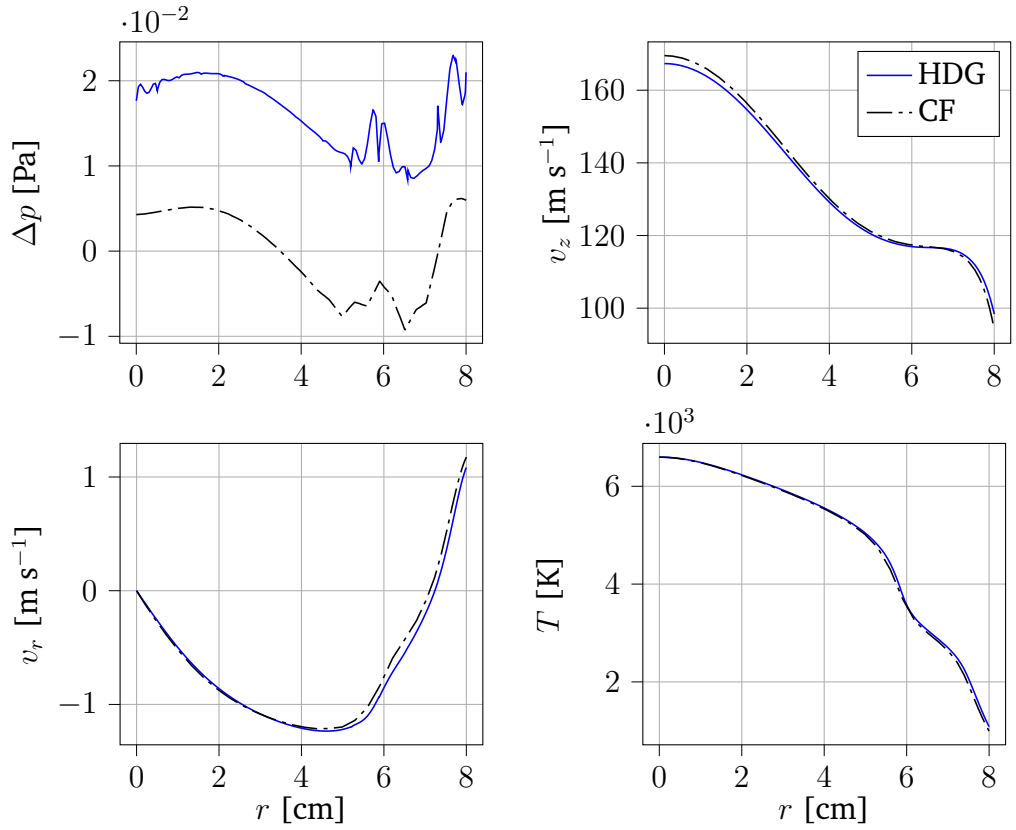

Fig. 5.15.: Comparisons of the axial v_z and radial v_r velocity profiles, the pressure difference Δp and temperature profile T along the radial direction in the freestream jet at $83.6\,\mathrm{cm}$ from the torch inlet.

The gauge pressure is very close to the background pressure p_0, so the oscillations are not an issue. All other fields are matching very well. The maximal axial velocity is not exactly the same. This might be due to the difference in coflows.

Torch center

The pressure, temperature, axial and radial velocity profiles and the electric field obtained using HDG at order 4 and COOLFluiD on the stagnation line in front of the probe are given in Fig. 5.16. The same observations about the hydrodynamic and electric fields as for the probe case can be made.

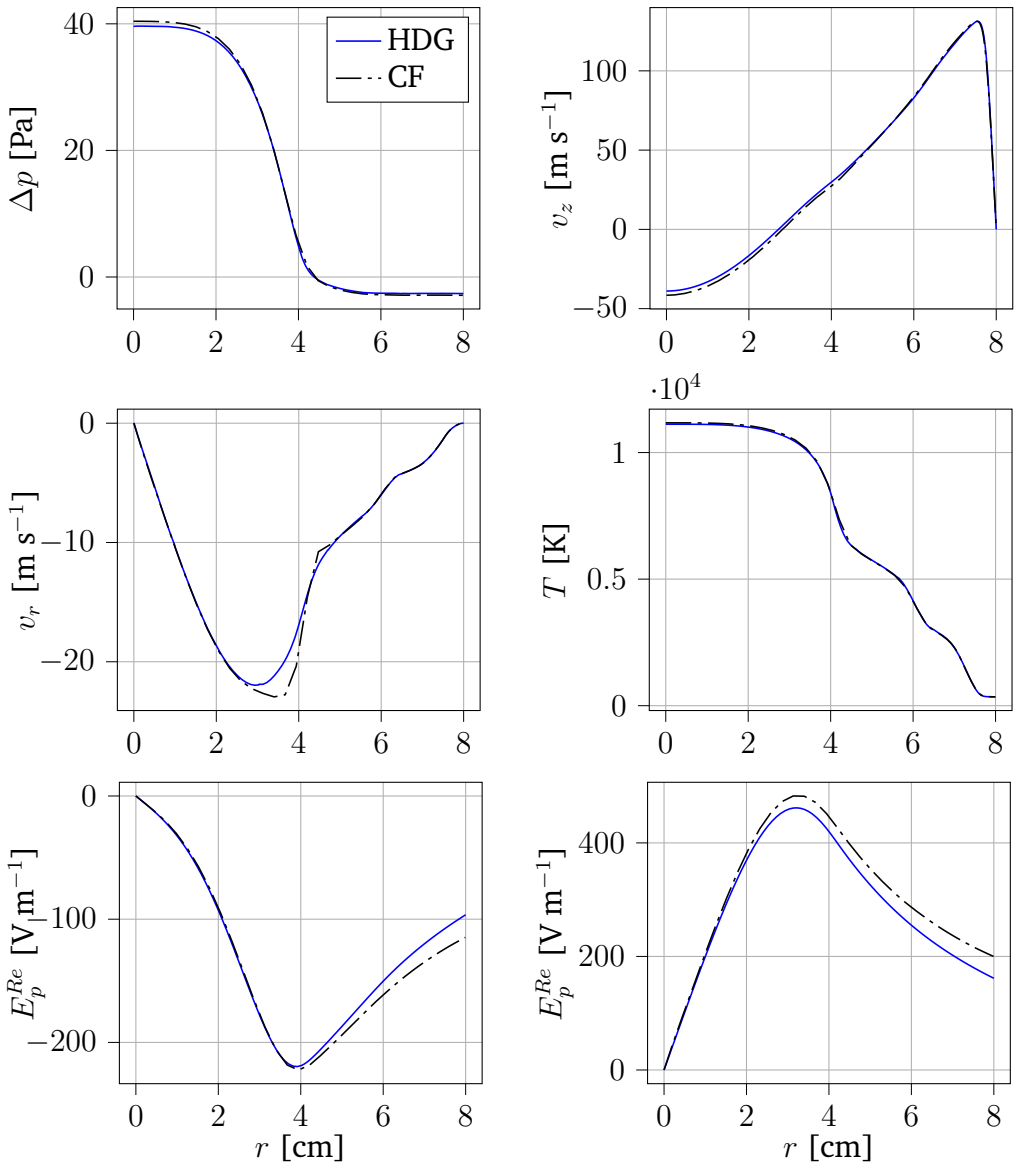

Fig. 5.16.: Comparisons of the axial v_z and radial v_r velocity profiles, the pressure difference Δp, temperature profile T and real E_p^{Re} and imaginary E_p^{Im} parts of the electric field along the radial direction at the torch center, at $24.3\,\mathrm{cm}$ from the torch inlet for the freestream case.

We were able to reproduce the results of a previous finite volume solver - COOLFluiD

- using the HDG method. On the contrary of finite volumes, high-order method allow to use a coarse, unstructured meshes, easing the use of the code.

5.5 Convergence history of the steady state

One important aspect of the ICP simulation is the convergence of the Newton solver. Previous segregated algorithms required thousands of iterations to converge to steady-state. In our case, with a monolithic approach, the L_2 norm of the residual for the freestream case described in Section 5.4 converges within 50 iterations (see Fig. 5.17).

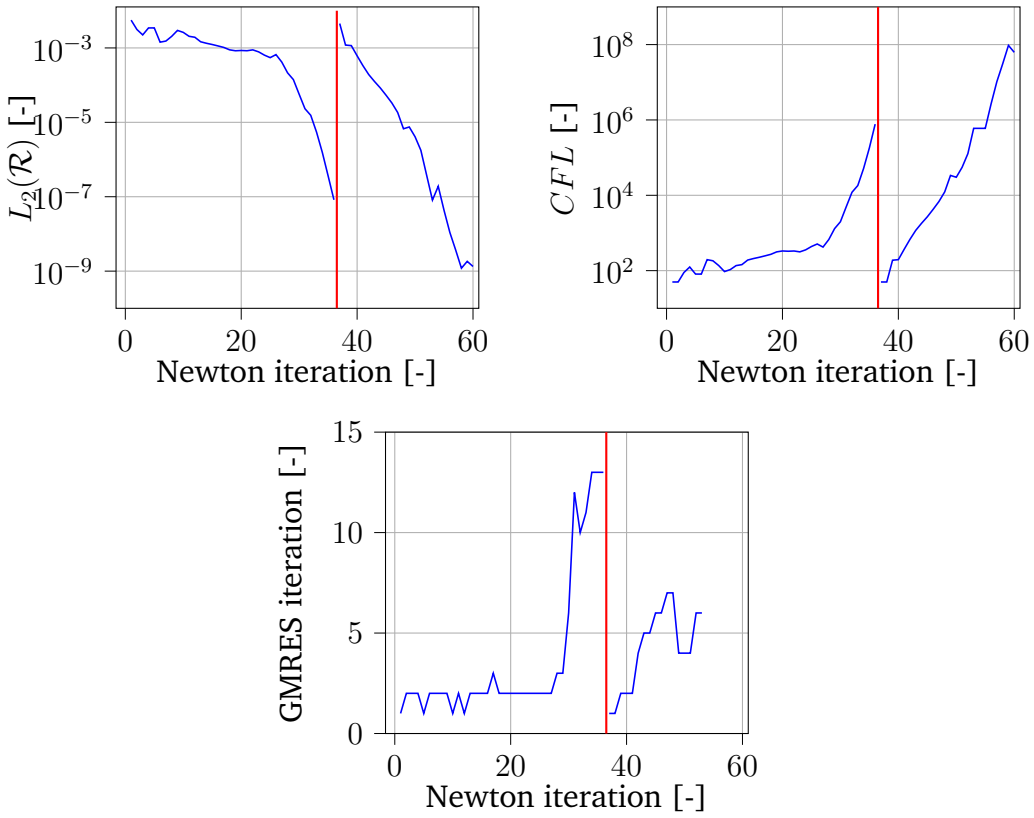

Fig. 5.17.: Convergence history of the L_2 norm of the residual $\mathcal{R}$ of the system. The CFL and GMRES vectors per Newton iteration have also been displayed. The red line shows the separation between the order 1 and order 4 simulations.

The solution strategy was the following: first, an order 1 simulation is run. Then, starting from the obtained results, we simulate the ICP flow at order 4. This procedure allows to reduce the number of high-order iterations, which are more expensive, while making the solver more stable. We also displayed the number of GMRES vectors per newton iteration and the evolution of the CFL number. The number of GMRES vectors generally increases with the CFL, but is far from prohibitive (at most 13

vectors).

The conclusion of this analysis is that the fully coupled solver is very advantageous compared to the staggered one in terms of newton iterations. We were able to perform order 4 ICP simulations on a laptop with single processor within more or less 60 newton iterations. This feature allows the HDG code to vastly outperform previous solvers, which required thousands of Newton iterations to converge. A parallelization strategy has to be considered in the future to fully take advantage of the HDG method and further improve the computational performance.

Finally, one of the main drawbacks of the HDG solver is the filling requirements of the ILU preconditioner. It demands 3 to 4 factor levels to be stable. The reason for this is not totally clear, but we suspect that the combination of high-order methods and stiff physics maybe the cause. To improve this problem, one may redesign of the non dimensional form of the equations or to use a preconditioner better suited for this application. These considerations are left for future work.

5.6 Conclusions

In this Chapter, we have performed numerical studies of ICP simulations. The convergence study based upon a manufactured solution proved that the multi-domain HDG method recovers the expected convergence orders. Then, for actual ICP cases, one with a probe, one in freestream conditions, we studied the mesh and order dependence of the solution. We concluded that, using a relatively coarse unstructured mesh with polynomial order 4, the solution was mesh and order independent. However, the mesh still needs to be structured in the vicinity of the boundary layer, with a mesh size of $10\,\mu\mathrm{m}$ at the wall compared to $1\,\mu\mathrm{m}$ in the case of finite volume. This difference may seem small, but if 3D cases are considered, it results in great economy of degrees of freedom. We also studied the impact of the coflow on the hydrodynamic fields and observed that it has practically no effect in regions of interest. Then, we compared our results to the ones obtained *via* the COOLFluiD finite volume solver. We concluded that the results for both simulations were matching, except for the electric field in the torch. This difference maybe due to the way boundary conditions are imposed in the two codes and the solution procedure. Finally, we analyzed the convergence of the L_2 norm of the residual for the HDG code, and highlighted that the number of iterations for the HDG solver were low and the computational time was fast, making the monolithic HDG code better suited than finite volume, segregated solvers.

6

Physical simulations of ICP flows

This Chapter deals with the simulation of actual ICP cases. First, we present the fields in the facility for the case described in Section 5.4. This gives an overview of the general characteristics of the flow in an ICP with and without a probe. Next, we give a parametric study of the test case with the probe. In particular, we analyze the impact on the distribution of the power dissipated in the facility, on the total enthalpy at the torch exit and along the stagnation line, and on the heat flux and boundary layer thickness at the level of the probe.

Note that the stabilizing coflow velocity is the inlet velocity. This helps the solver to converge faster towards steady-state without significantly perturbing the solution in the torch and the jet, as shown in Section 5.3.

6.1 Fields in the torch at steady state

We now present an overview of the various fields in the torch for the freestream and probe cases given in Section 5.4. The geometry of the simulation is given in Fig. 5.4. We show the gauge pressure (the reason behind the display of the gauge instead of the static pressure is discussed below), the temperature, the density, the velocity, the volume power dissipated by Joule effect, the electric field and the Lorentz force. The magnitude of the effective Lorentz force is displayed, and the streamline and Mach number are also analyzed. For each picture, we have represented the position of the coils with black disks. When possible, they have been represented for both the probe and freestream cases. If not displayed, they are located at the same positions in both cases.

Since pressure p is very close to the background pressure p_0, the gauge pressure $\Delta p = p - p_0$ is shown in Fig. 6.1. Considering a background pressure $p_0 = 5000\,\mathrm{Pa}$, the steady solver predicts change in pressure of at most 1%. The flow is thus incompressible in the sense that the density variation are not caused by pressure variation. However, density, as seen below, varies due to the large temperature gradients. Note also that a small increase in pressure is observed near the probe stagnation point.

87

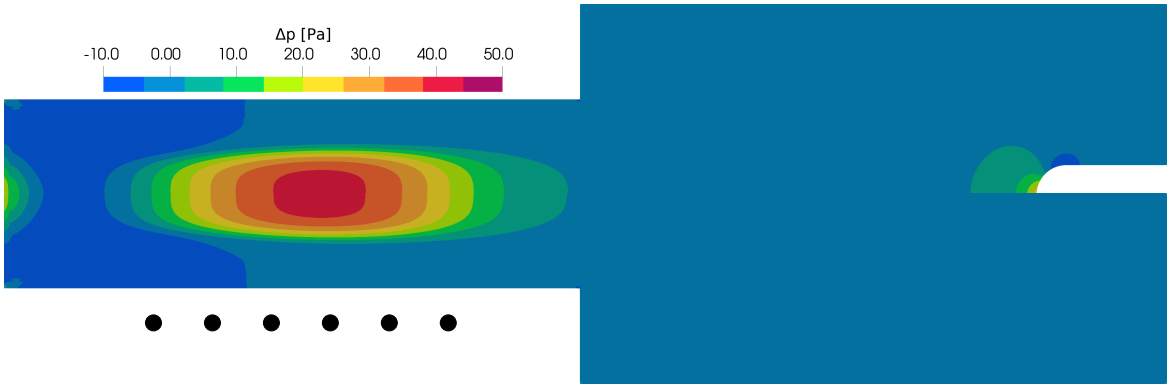

Fig. 6.1.: Gauge pressure field Δp for the case with a probe (top) and without a probe (bottom) in the Plasmatron facility. The coils surrounding the facility are represented by the black dots. The exact simulation parameters are shown in Section 5.4.

The temperature T varies greatly in the facility (Fig. 6.2), with large temperature gradients occurring close to the isothermal wall boundaries (probe and the torch walls). The largest temperatures are reached close to the axis of symmetry.

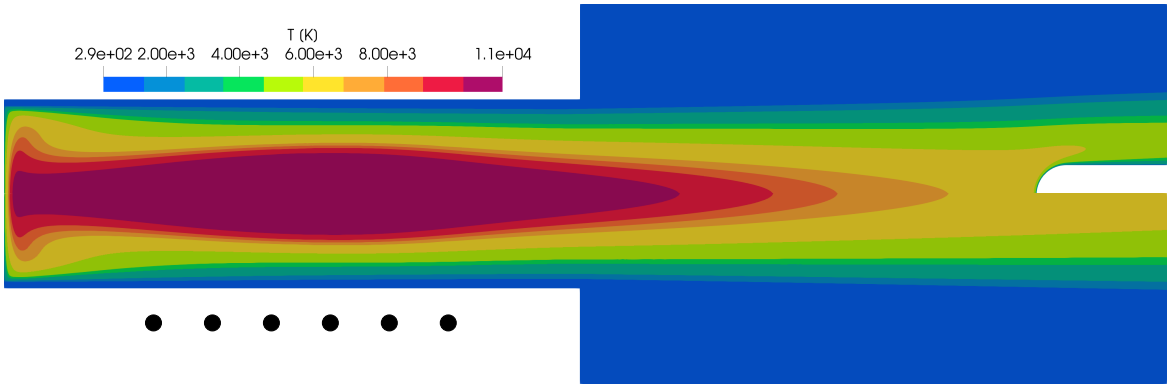

Fig. 6.2.: Temperature field T for the case with a probe (top) and without a probe (bottom) in the Plasmatron facility. The coils surrounding the facility are represented by the black dots. The exact simulation parameters are shown in Section 5.4.

ICP flows are subsonic and considered incompressible. The pressure, which is constant almost everywhere in the facility, does not play a role in the density (noted ρ) variation. However, ρ is not constant over the domain because of the large temperature gradients (see Fig. 6.3). The largest density gradients occur near the upper wall of the facility and in the shear layer.

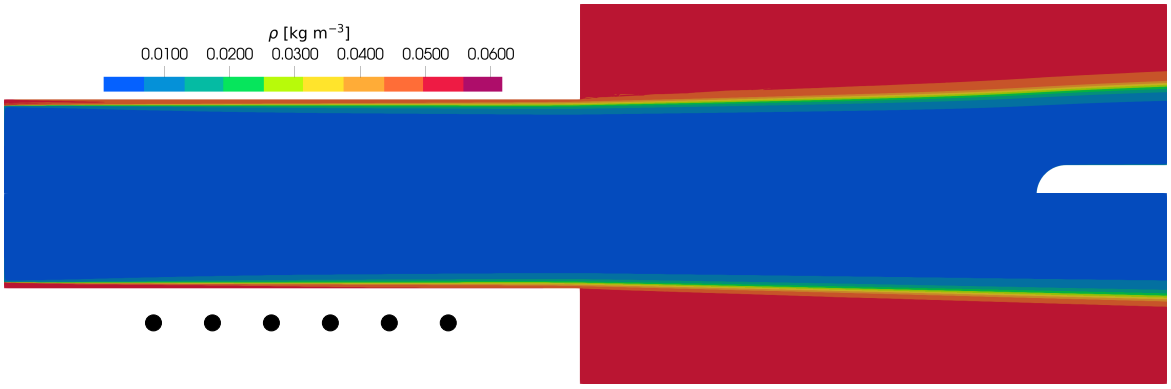

Fig. 6.3.: Density field ρ for the case with a probe (top) and without a probe (bottom) in the Plasmatron facility. The coils surrounding the facility are represented by the black dots. The exact simulation parameters are shown in Section 5.4.

The annular injection creates a fluid recirculation close to the inlet (Fig. 6.4). The latter brings back a portion of the heated fluid towards the injector, stabilizing the torch but also giving rise to large temperature gradients close to the left wall. The other part of the heated fluid is convected in the chamber. In addition, the streamlines are closed, meaning the behaviour of the fluid is quasi incompressible. Concerning the Mach number (Fig. 6.5), the flow is subsonic everywhere in the facility, especially in regions of high temperature. It is the highest close to the injection, the top wall and in the shear layer, since it is the region where the flow is the coldest.

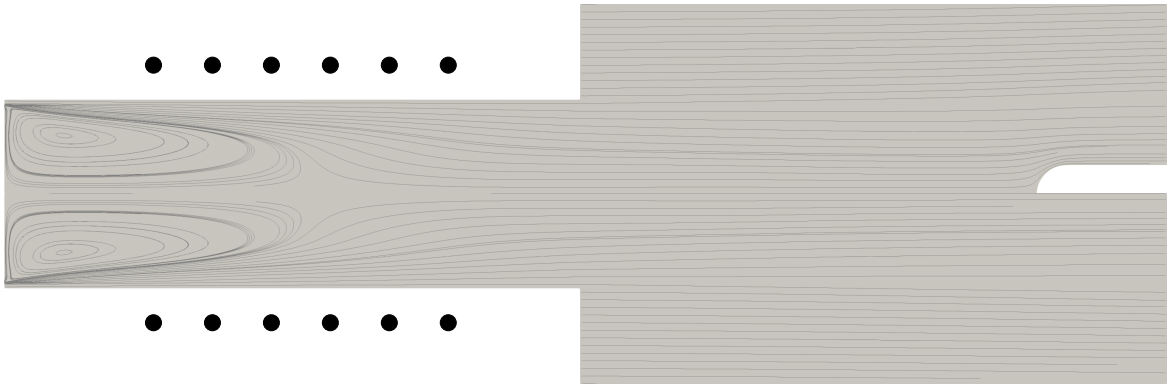

Fig. 6.4.: Streamlines for the case with a probe (top) and without a probe (bottom) in the Plasmatron facility. The coils surrounding the facility are represented by the black dots. The exact simulation parameters are shown in Section 5.4.

The axial velocity shows an acceleration of the fluid after the heating. This is due to the thermal expansion: the hot air is less dense than the cold one, and the flow is accelerated after being heated in order to conserve the mass flux in the torch.

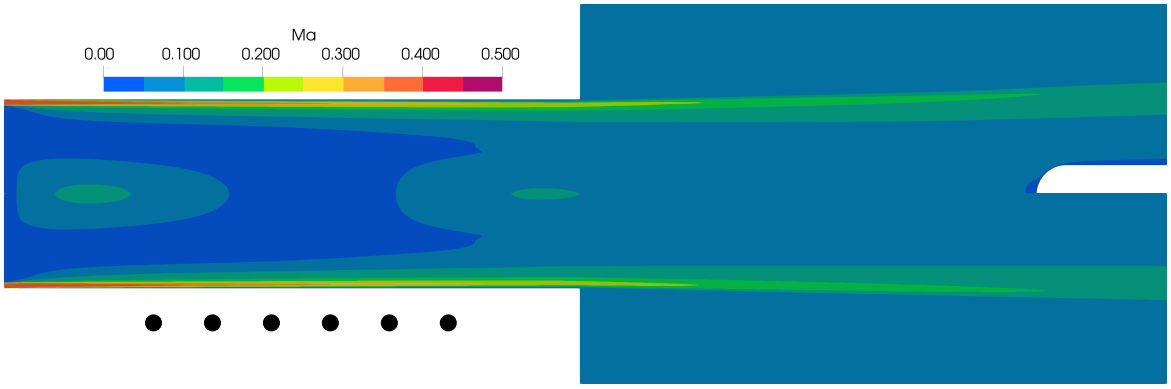

Fig. 6.5.: Mach number Ma for the case with a probe (top) and without a probe (bottom) in the Plasmatron facility. The coils surrounding the facility are represented by the black dots. The exact simulation parameters are shown in Section 5.4.

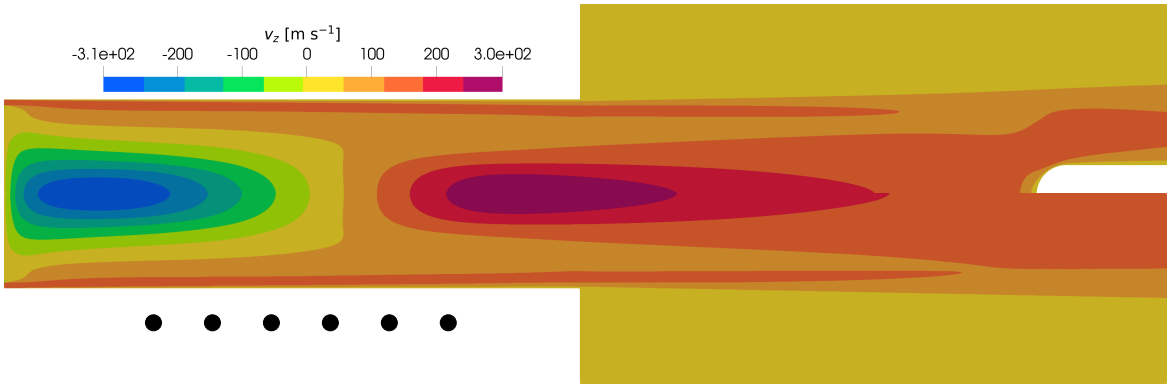

Fig. 6.6.: Axial velocity field v_z for the case with a probe (top) and without a probe (bottom) in the Plasmatron facility. The coils surrounding the facility are represented by the black dots. The exact simulation parameters are shown in Section 5.4.

The volume power dissipated *via* Joule heating in the facility P is shown in Fig. 6.7. The greatest volume power dissipation is located at equal distance from the torch upper wall and the axis of symmetry. It corresponds to the region where the product of the total electric field norm squared E_{tot}^2 and the electron electric conductivity σ_e is maximal, *i.e.* where the coupling of the plasma and the electric field is maximal.

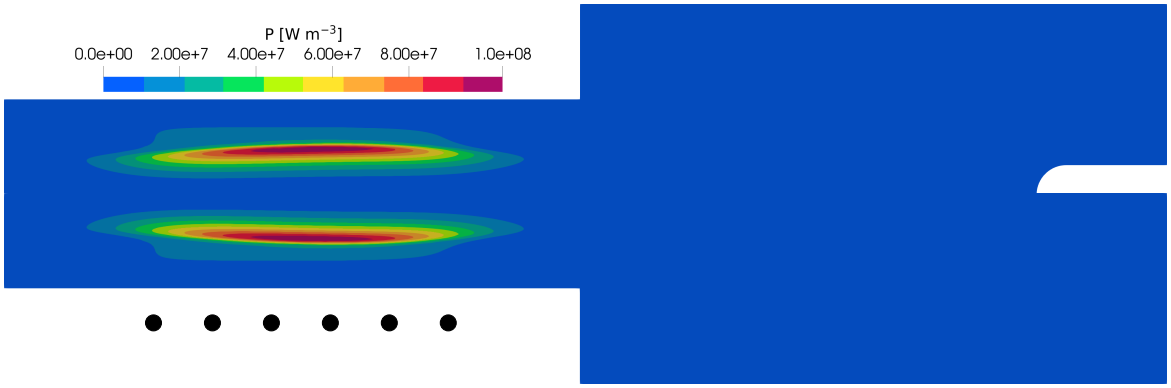

Fig. 6.7.: Power field P for the case with a probe (top) and without a probe (bottom) in the Plasmatron facility. The coils surrounding the facility are represented by the black dots. The exact simulation parameters are shown in Section 5.4.

The norm of the total electric field, which is purely azimuthal in our case, is defined as

$$E_{tot} = \sqrt{(E_I^{Re})^2 + (E_I^{Im})^2} \tag{6.1}$$

with E_I the induced electric field, sum of the plasma and the coil electric field contributions. E_{tot} is represented in Fig. 6.8. It is maximal close to the coil and decays towards the axis of symmetry (where it cancels). When looking at the spatial repartition of the electric conductivity (Fig. 6.9), it is no surprise the power is maximal at mid distance from the wall and the centerline, as it is the region where the product of σ_e and E_{tot}^2 is maximal. We also see that the σ_e profile closely follows the temperature profile, as the conductivity is manly dependent on temperature, and the pressure is constant almost everywhere.

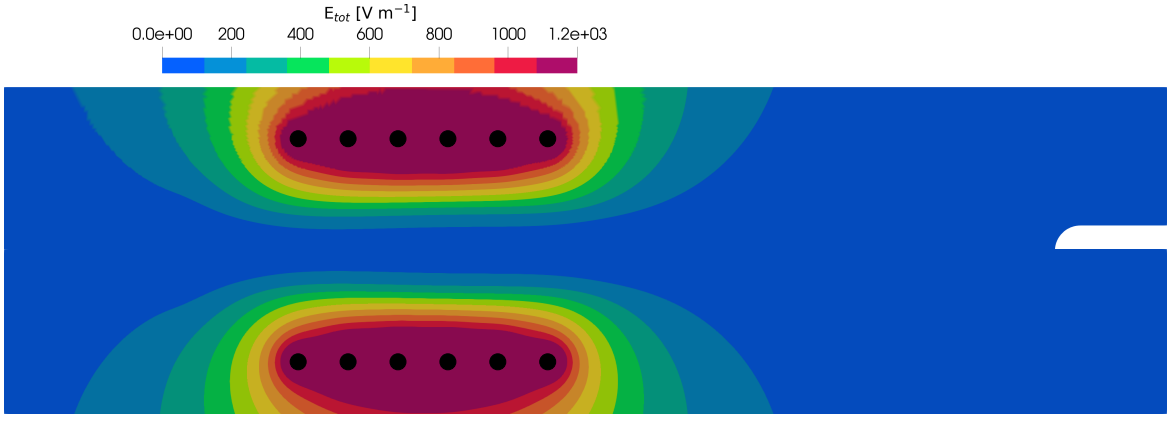

Fig. 6.8.: Total electric field magnitude $||E_{tot}||$ for the case with a probe (top) and without a probe (bottom) in the Plasmatron facility. The coils surrounding the facility are represented by the black dots. The exact simulation parameters are shown in Section 5.4.

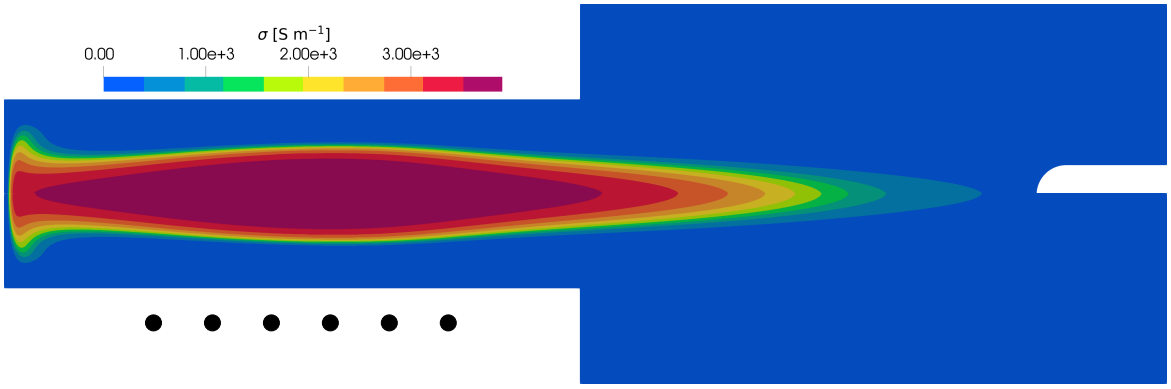

Fig. 6.9.: Electron electric conductivity σ for the case with a probe (top) and without a probe (bottom) in the Plasmatron facility. The coils surrounding the facility are represented by the black dots. The exact simulation parameters are shown in Section 5.4.

The effective Lorentz force magnitude and the electric force field lines have been displayed in Fig. 6.10. The effective Lorentz force is maximal close to the first and last coils.

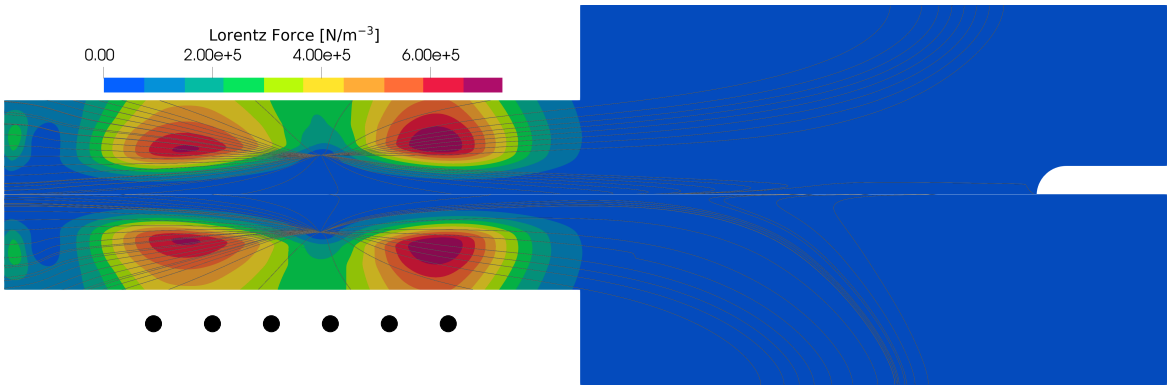

Fig. 6.10.: Magnitude of the effective Lorentz Force for the case with a probe (top) and without a probe (bottom) in the Plasmatron facility. The coils surrounding the facility are represented by the black dots. The exact simulation parameters are shown in Section 5.4.

6.2 ICP parametric study

In ICP facility, the experimenter has control over certain parameters, namely the inlet mass flow rate Q and swirl angle S, the power injected in the coil (controlled with P_{tot} in the simulation), the induction frequency f and the background pressure p_0. Predicting the impact of each of these parameters on the various fields is not

easy, but is crucial for the preparation of actual experiments. We analyze the impact of the previously mentioned parameters on the Plasmatron probe case described in Section 5.4, with geometry given in Fig. 5.4. They are discussed separately, meaning that all parameters of the simulation (boundary conditions, etc...) remain constant except for the one under investigation. Note that only steady-state computations are considered.

We first assess the impact on the streamlines in the facility for the smallest and largest value of each parameter respectively. Then, we study the profiles inside the torch (see TC line in Fig. 5.4). In particular, we analyze the temperature T, volume power P, electric conductivity σ_e, total electric field magnitude E_{tot}, gauge pressure Δp and axial velocity v_z. Then, we analyze the evolution of the total enthalpy radial profile H at the exit of the jet, at $48.6\,\mathrm{cm}$ from the torch inlet. The total volume enthalpy H is defined as

$$H = \rho e + \frac{1}{2}\rho||\mathbf{v}||^2 + p \tag{6.2}$$

with e the internal energy, ρ the density and p the static pressure.

Finally, we discuss the variation of the profiles along the stagnation line (H, T, v_z, $\partial_r v_r$, $\partial_z T$, with v_r the radial velocity component) as a function of each parameter (see the STAG line in Fig. 5.4). The axial inflection point of $\partial_r v_r$ gives an estimate of the boundary layer thickness close to the probe tip. The latter is displayed on the corresponding graphs. The normal heat flux at the probe tip variation is also discussed. The outlet pressure and wall temperature are set for all following simulations to the background pressure p_0 and $T_{wall} = 350\,\mathrm{K}$ respectively.

6.2.1 Impact of the mass flow rate

We studied flow rates from $8\,\mathrm{g\,s^{-1}}$ to $16\,\mathrm{g\,s^{-1}}$, with steps of $2\,\mathrm{g\,s^{-1}}$, as they are representative of flow rates in the Plasmatron facility.

Impact on the streamlines and speed

The impact of the mass flow rate Q on the streamlines and the velocity magnitude is shown in Fig. 6.11 for $Q = 8\,\mathrm{g\,s^{-1}}$ and $Q = 16\,\mathrm{g\,s^{-1}}$. While the velocity norm is greater in the recirculation region for larger Q, the opposite is true in the part of the torch after the flow has been heated. In fact, the slower incoming fluid has more time to be heated in the torch, decreasing its density compared to faster inlet flow. Because Q is conserved, the slower fluid undergoes a greater acceleration after being heated.

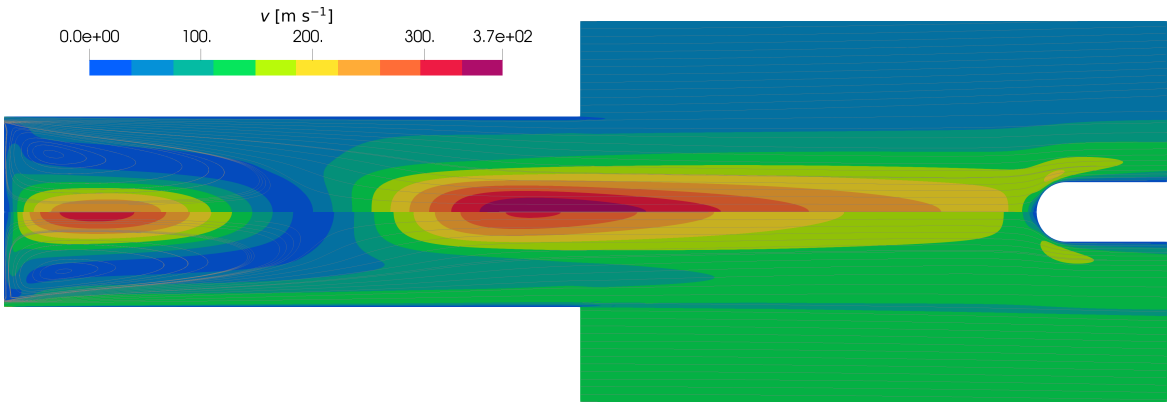

Fig. 6.11.: Streamlines and velocity magnitude v for a mass flow rate of $Q = 8\,\mathrm{g\,s^{-1}}$ (top) and $Q = 16\,\mathrm{g\,s^{-1}}$. The exact simulation parameters are shown in Section 5.4.

In the torch

In the torch center, the flow rate has a negligible impact on the electric and temperature fields, and consequently on the power and electric conductivity (Fig. 6.12 and Fig. 6.13).

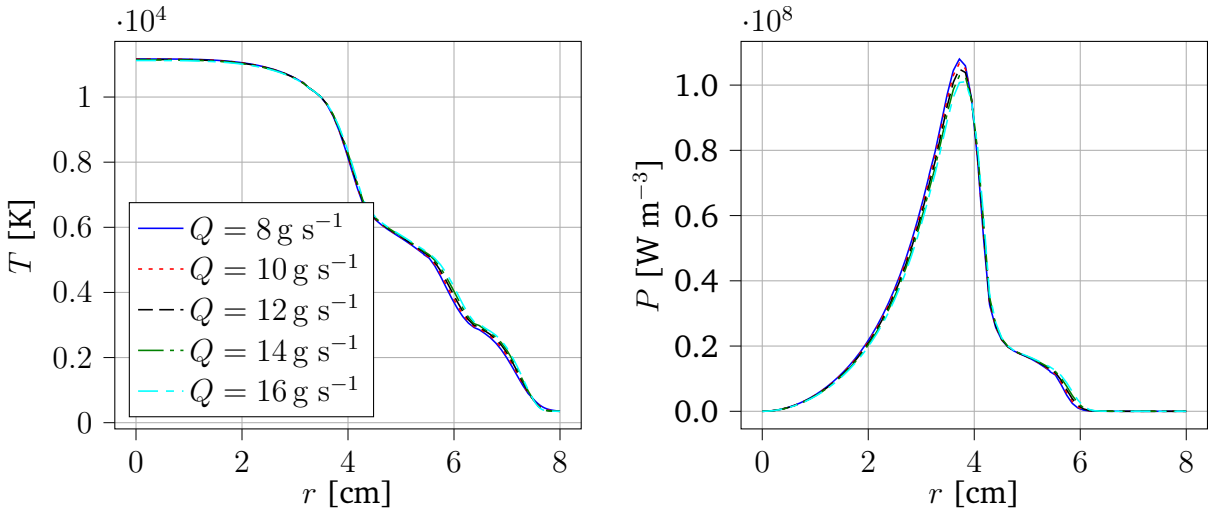

Fig. 6.12.: Temperature T and Joule heating volume power P profiles in the torch center as a function of the mass flow rate Q. r is the radial position from the symmetry axis. The exact simulation parameters are shown in Section 5.4.

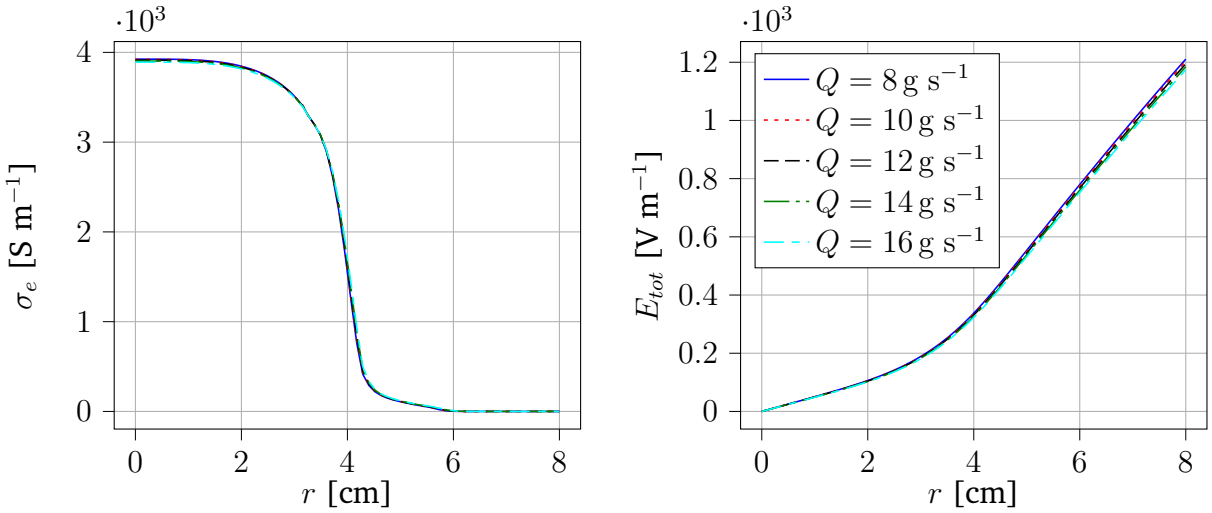

Fig. 6.13.: Total electric field norm E_{tot} and electron electric conductivity σ_e profiles in the torch center as a function of the mass flow rate Q. r is the radial position from the symmetry axis. The exact simulation parameters are shown in Section 5.4.

However, it has an influence on the gauge pressure Δp and the axial velocity v_z (Fig. 6.14). On the other hand, the v_z profile is significantly impacted, with increasing centerline velocity.

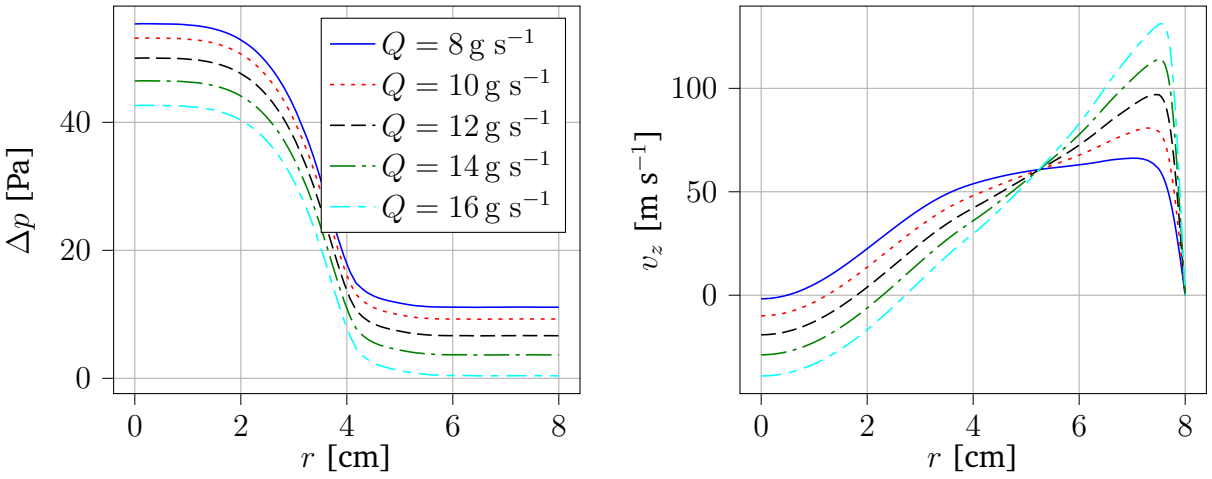

Fig. 6.14.: Gauge pressure Δp and axial velocity profile v_z in the torch center as a function of the mass flow rate Q. r is the radial position from the symmetry axis.

At the torch exit

At the torch exit, the total enthalpy of the system H is almost unchanged (Fig. 6.15). Following the previous discussion, the mass flow rate Q has a marginal impact on

the temperature profile, but acts mainly on the hydrodynamic fields. Since for ICP flows, H is mainly dominated by the internal energy, and the velocity changes are not sufficient to make kinetic energy dominant.

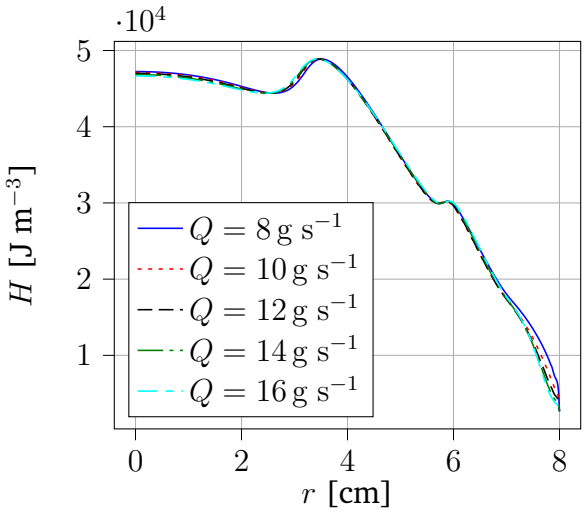

Fig. 6.15.: Total enthalpy H profile at the torch exit as a function of the mass flow rate Q. r is the radial position from the symmetry axis. The exact simulation parameters are shown in Section 5.4.

Along the stagnation line

Along the stagnation line, Q has almost no impact on the enthalpy profile. However, it influences the temperature of the incoming fluid, which decreases with increasing Q (Fig 6.16).

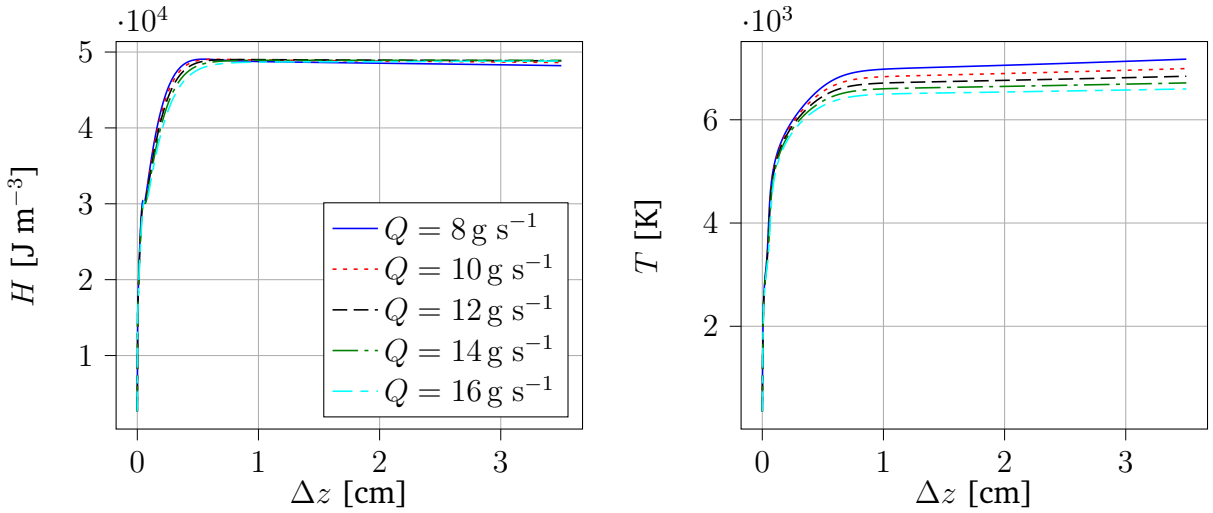

Fig. 6.16.: Total enthalpy H and temperature profile T along the stagnation line as a function of the mass flow rate Q. Δz is the axial position from the probe tip. The exact simulation parameters are shown in Section 5.4.

On the other hand, the axial velocity field v_z and the radial gradient of the radial velocity profile are significantly affected by Q (Fig. 6.17). The boundary layer thickness, dictated by the inflection point of $\partial_r v_r$, increases slightly with increasing Q.

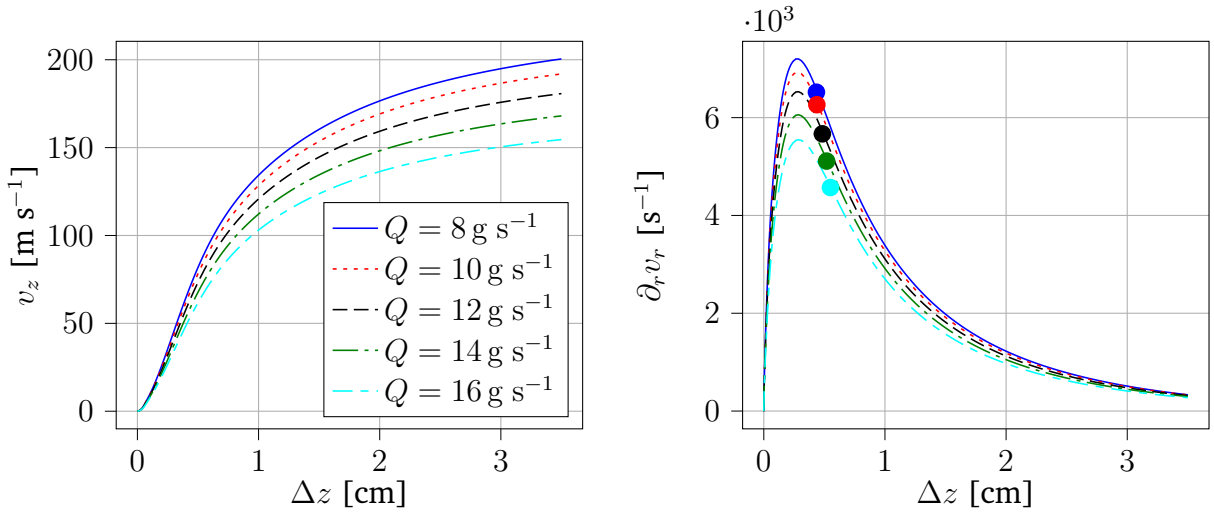

Fig. 6.17.: Axial velocity v_z and radial gradient of the radial velocity $\partial_r v_r$ profiles along the stagnation line as a function of the mass flow rate Q. Δz is the axial position from the probe tip. The inflexion point of $\partial_r v_r$ has been marked for each regime. The exact simulation parameters are shown in Section 5.4.

The temperature gradient decreases with increasing Q at the wall, while it remains constant everywhere else on the stagnation line. On the other hand, the normal heat

flux q at the tip of the probe is also decreasing (Fig. 6.18). This is explained by the lowering of the temperature of the fluid impinging on the probe with increasing Q.

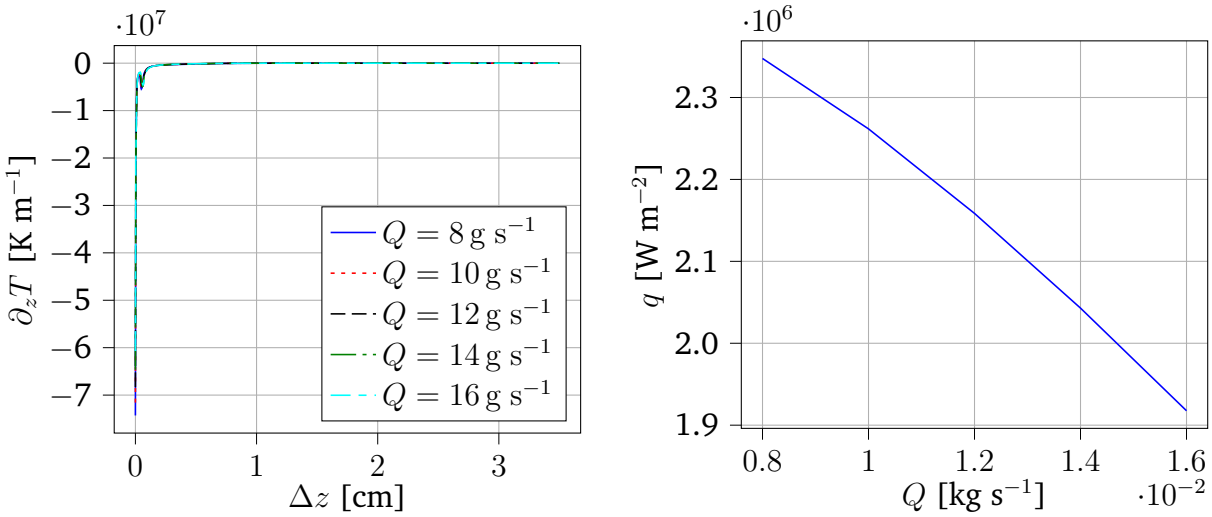

Fig. 6.18.: Axial temperature gradient $\partial_z T$ along the stagnation line and normal heat flux q at the tip of the probe as a function of the mass flow rate Q. Δz is the axial position from the probe tip. The exact simulation parameters are shown in Section 5.4.

Impact on the magnetic interaction parameter

The impact of Q on the local interaction parameter Im for $Q = 8\,\mathrm{g\,s^{-1}}$ and $Q = 16\,\mathrm{g\,s^{-1}}$ is given in Fig. 6.19. An increased mass flow slightly shifts the region of strong influence of the Lorentz force to the right.

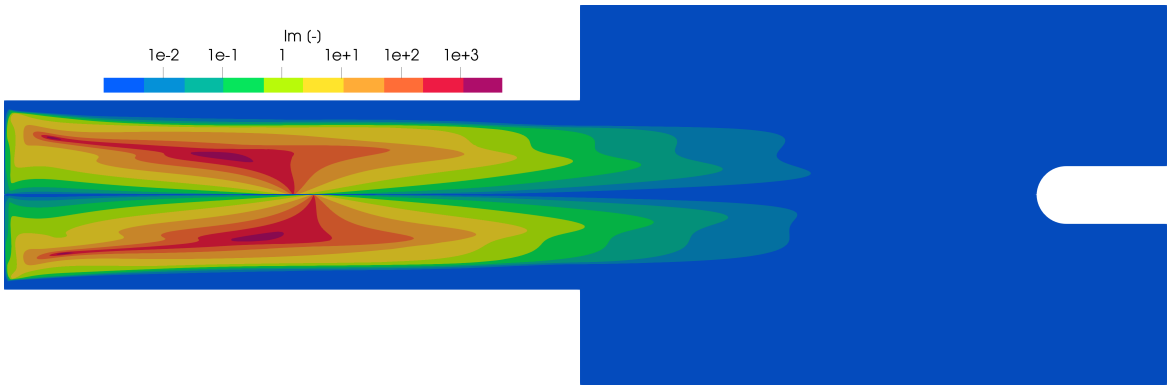

Fig. 6.19.: Magnetic interaction parameter Im for a mass flow rate of $Q = 8\,\mathrm{g\,s^{-1}}$ (top) and $Q = 16\,\mathrm{g\,s^{-1}}$. The exact simulation parameters are shown in Section 5.4.

6.2.2 Impact of the background pressure

We studied background pressures ranging from $5000\,\mathrm{Pa}$ to $20\,000\,\mathrm{Pa}$, with a step of $5000\,\mathrm{Pa}$. We chose this range because, below $5000\,\mathrm{Pa}$, the local thermodynamic equilibrium hypothesis completely breaks. On the other hand, above $20\,000\,\mathrm{Pa}$, it was found that the steady solver fails. The causes of this failure are still uncleared, but it could be due to unsteady behaviour of the fluid at these pressures. Nonetheless, these values represent plausible operating conditions of ICP facilities.

Impact on the streamlines and speed

The impact of the background pressure p_0 on the streamlines and the velocity magnitude is shown in Fig. 6.20 for $p_0 = 5000\,\mathrm{Pa}$ and $p_0 = 20\,000\,\mathrm{Pa}$. The entrance recirculation bubble length recedes a little, but the fluid recirculates faster for lower background pressure. The velocity norm is smaller for higher pressure, due to the higher density and conservation of the mass flow rate.

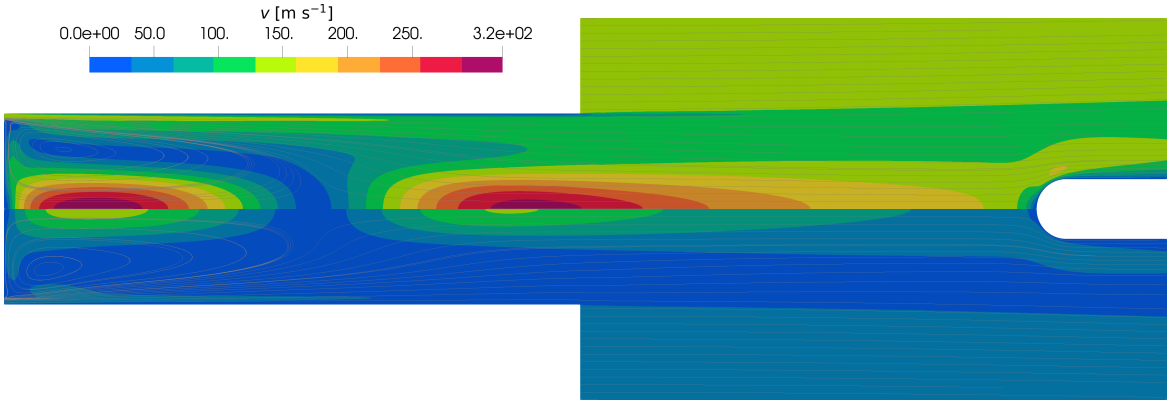

Fig. 6.20.: Streamlines and velocity magnitude v for a background pressure of $p_0 = 5000\,\mathrm{Pa}$ (top) and $p_0 = 20\,000\,\mathrm{Pa}$. The exact simulation parameters are shown in Section 5.4.

In the torch

In the torch, increasing the pressure does not affect significantly the maximal temperature of the ICP facility. However, it tightens the temperature profile around the center line and shifts the volume power peak towards the symmetry axis (Fig. 6.21). The modification of the temperature profile is explained by two phenomena. First, for these range of pressures, the fluid heat conductivity decreases with increasing pressure, concentrating the region of greater temperature close to the centerline. Second, the recirculation is weakened with increasing pressure, transporting less heat in the bulk of the torch.

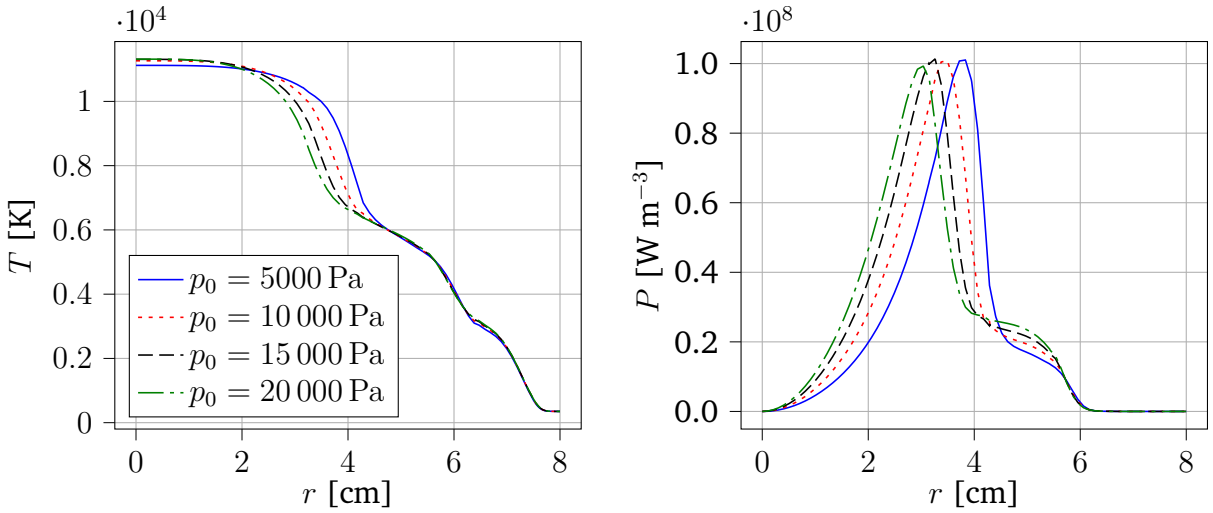

Fig. 6.21.: Temperature T and Joule heating power P profiles in the torch center as a function of the background pressure p_0. r is the radial position from the symmetry axis. The exact simulation parameters are shown in Section 5.4.

The electric conductivity profile tightens and increases around the center line. The general shape of the total electric field being almost unaffected by pressure (Fig. 6.22), the volume power peak shifts towards the center line accordingly.

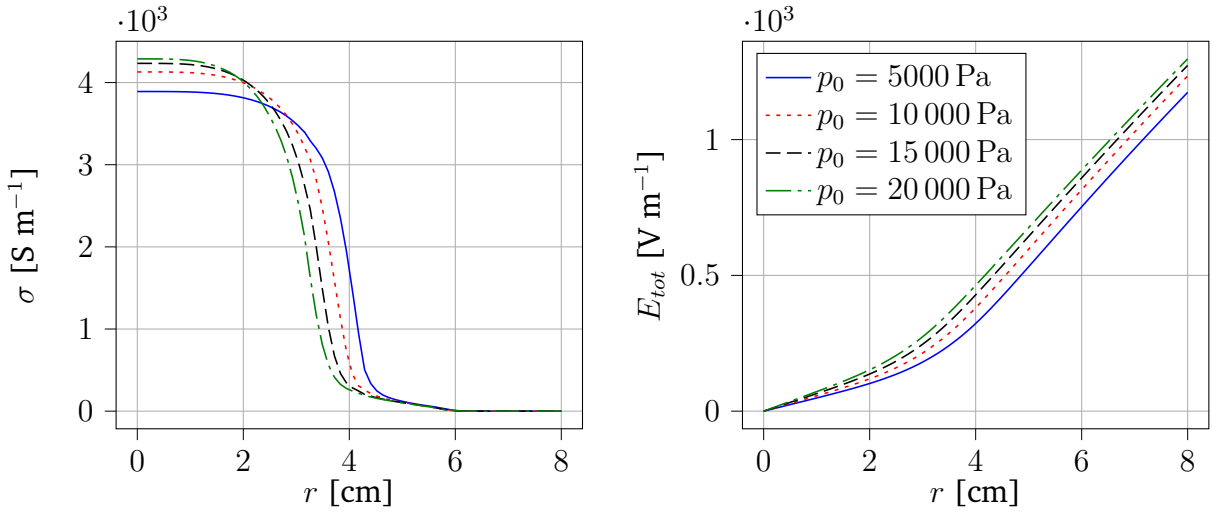

Fig. 6.22.: Total electric field norm E_{tot} and electron electric conductivity σ_e profiles in the torch center as a function of the background pressure p_0. r is the radial position from the symmetry axis. The exact simulation parameters are shown in Section 5.4.

Finally, the gauge pressure decreases with increasing background pressure. On the other hand, the axial velocity profile is modified (Fig. 6.23). It adapts to the density increase by lowering the axial velocity magnitude in order to keep a constant flow

rate. The axial velocity along the stagnation line increases.

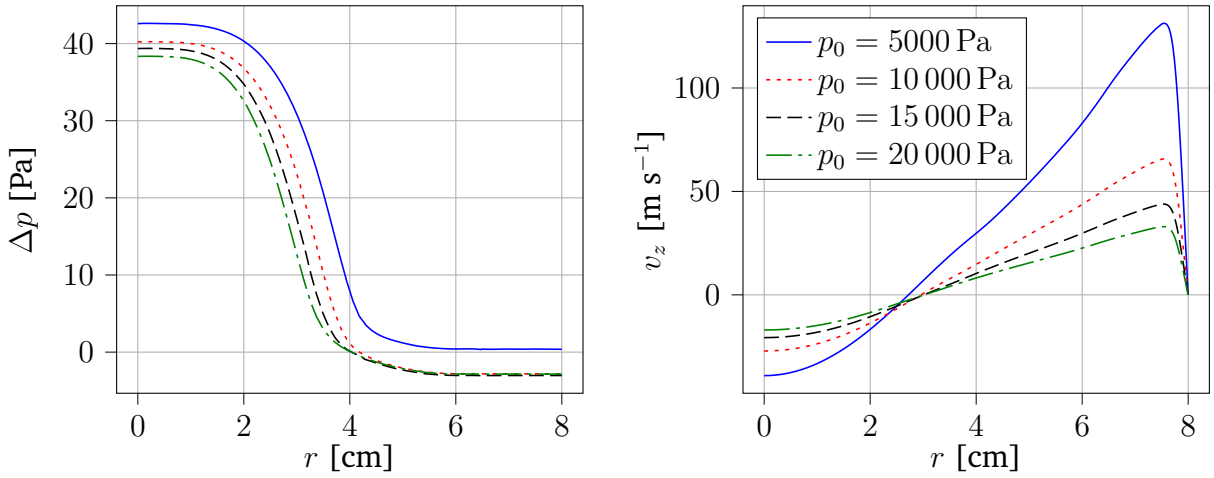

Fig. 6.23.: Gauge pressure Δp and axial velocity profile v_z in the torch center as a function of the background pressure p_0. r is the radial position from the symmetry axis. The exact simulation parameters are shown in Section 5.4.

At the torch exit

At the torch exit, the total enthalpy H of the system increases significantly with increasing pressure (Fig. 6.24). It is no surprise as increasing the pressure also increases the fluid density and internal energy, leading to an augmentation of H.

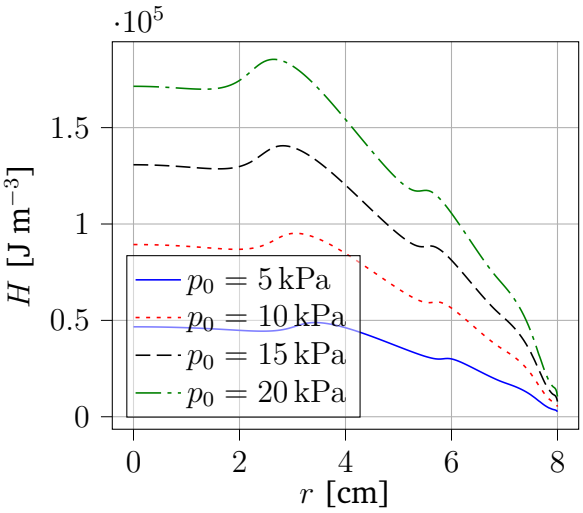

Fig. 6.24.: Total enthalpy H profile at the torch exit as a function of the background pressure p_0. r is the radial position from the symmetry axis. The exact simulation parameters are shown in Section 5.4.

Along the stagnation line

Along the stagnation line, the temperature is strongly affected by pressure variations around $p_0 = 5000\,\mathrm{Pa}$. Then, as pressure is increased, the temperature profile is less sensitive to the variation of this parameter. On the other hand, pressure has a significant effect on the total enthalpy profile (Fig 6.25).

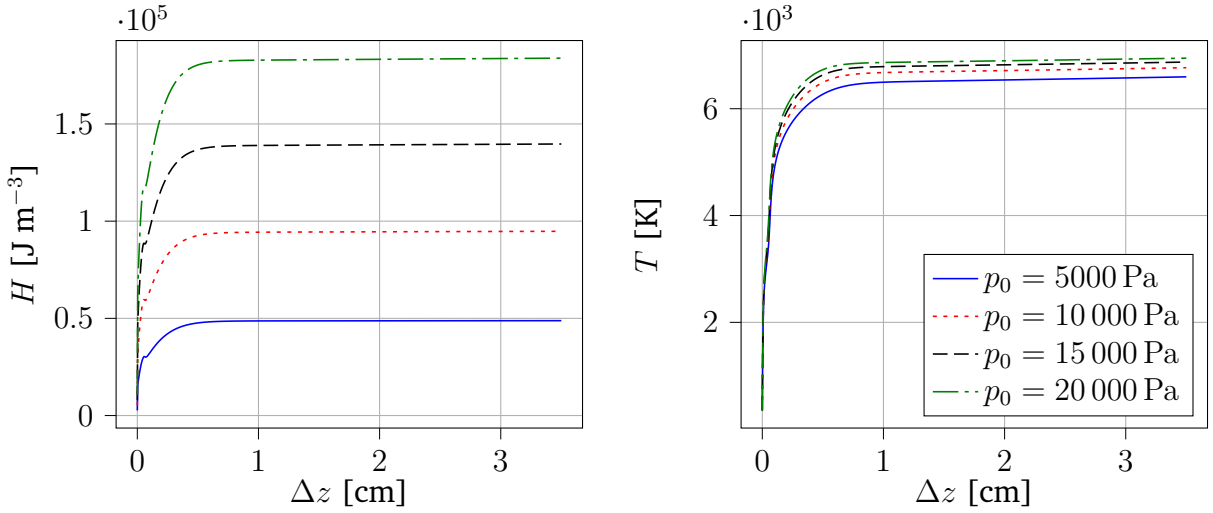

Fig. 6.25.: Total enthalpy H and temperature profile T along the stagnation line as a function of the background pressure p_0. Δz is the axial position from the probe tip. The exact simulation parameters are shown in Section 5.4.

The axial velocity field v_z and the radial gradient of the radial velocity profile are significantly affected by p_0 (Fig. 6.26), both decreasing with increasing background pressure. The boundary layer thickness is affected by pressure for p_0 around $5000\,\mathrm{Pa}$. However, it becomes pressure independent for background pressure above this value.

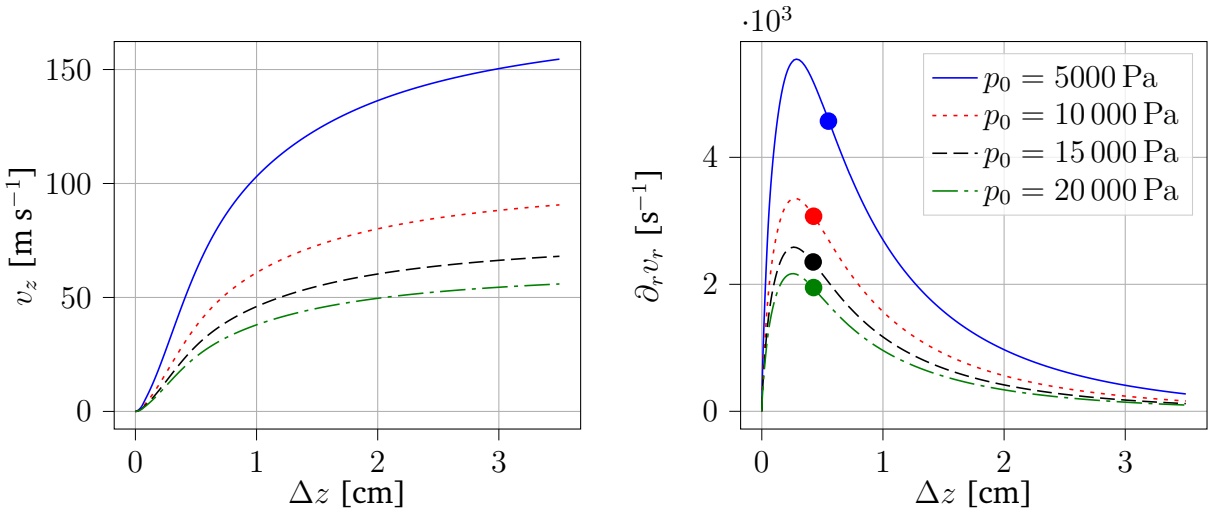

Fig. 6.26.: Axial velocity v_z and radial gradient of the radial velocity $\partial_r v_r$ profiles along the stagnation line as a function of the mass flow rate Q. Δz is the axial position from the probe tip. The inflexion point of $\partial_r v_r$ has been marked for each regime. The exact simulation parameters are shown in Section 5.4.

The temperature gradient becomes steeper with increasing p_0 at the probe tip, while it remains constant everywhere else on the stagnation line. On the other hand, the normal heat flux q at the tip of the probe is also increasing (Fig. 6.27). This is explained by the increase of temperature impinging on the probe with increasing p_0.

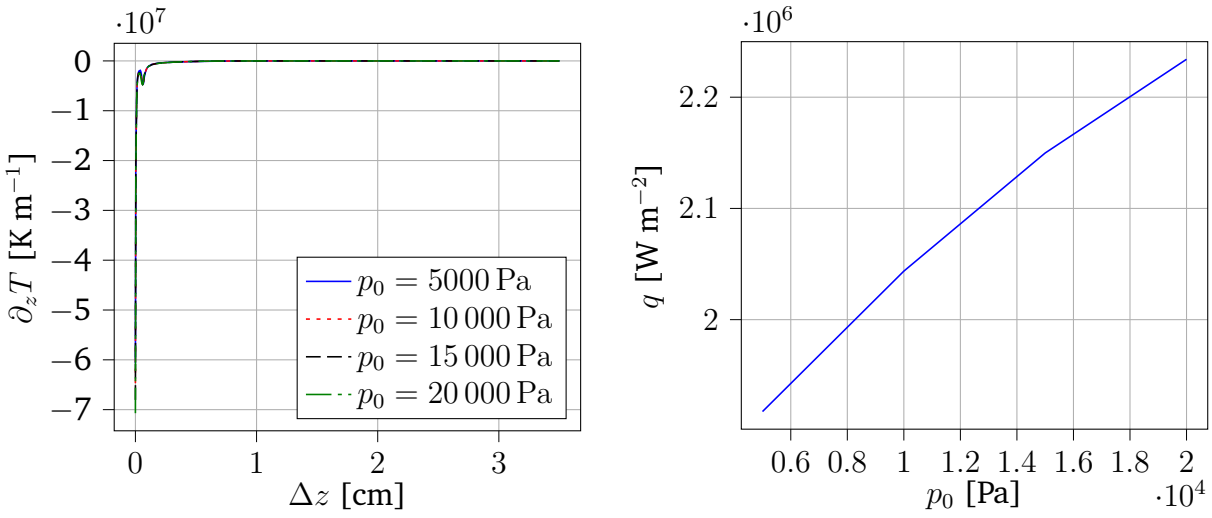

Fig. 6.27.: Axial temperature gradient $\partial_z T$ along the stagnation line and normal heat flux q at the tip of the probe as a function of the mass flow rate Q. Δz is the axial position from the probe tip. The exact simulation parameters are shown in Section 5.4.

Impact on the non-dimensional numbers

The impact of p_0 on the local interaction parameter Im for $p_0 = 5000\,\mathrm{Pa}$ and $p_0 = 20\,000\,\mathrm{Pa}$ is given in Fig. 6.28. An increase in pressure leads to an increase in Im, giving more importance to the effective Lorentz force both in the torch, but also in the chamber, where the effect of the Lorentz force is felt further down the jet.

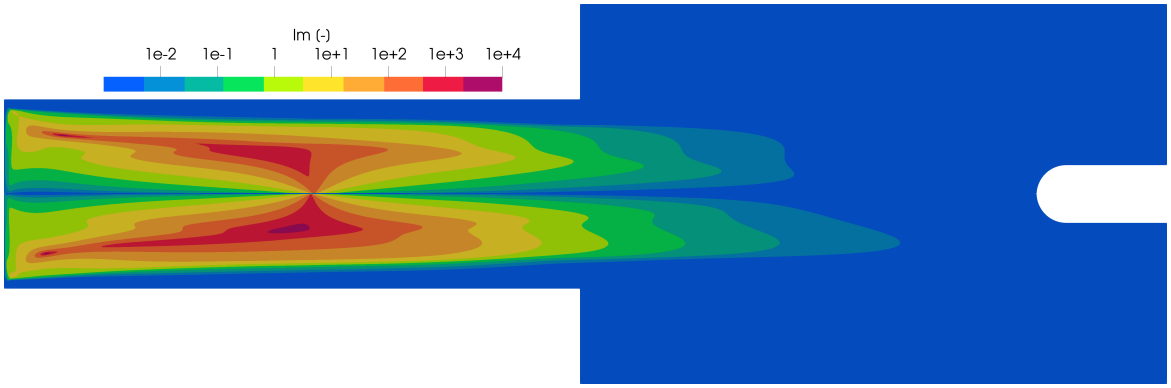

Fig. 6.28.: Magnetic interaction parameter Im for a background pressure of $p_0 = 5000\,\mathrm{Pa}$ (top) and $p_0 = 20\,000\,\mathrm{Pa}$ (bottom). The exact simulation parameters are shown in Section 5.4.

The impact of p_0 on the Joule and induction numbers is given in Table. 6.1. The Joule number Jn and induction number $\mathrm{N_{ind}}$ increase with pressure, meaning that the heating of the flow is more efficient and the induction current are located closer to the torch wall.

p_0	Jn	$\mathrm{N_{ind}}$
$p_0 = 5000\,\mathrm{Pa}$	118	284
$p_0 = 20\,000\,\mathrm{Pa}$	1866	344

Tab. 6.1.: Table reporting the Joule Jn and induction $\mathrm{N_{ind}}$ numbers for background pressure p_0 of $5000\,\mathrm{Pa}$ and $20\,000\,\mathrm{Pa}$.

6.2.3 Impact of the power

We studied the effect of the total power P_{tot} dissipated in the facility, in the range $50\,\mathrm{kW}$ to $200\,\mathrm{kW}$ with steps of $50\,\mathrm{kW}$, which are powers representative of ICP computations. Too low power would lead to a quenching of the torch.

Impact on the streamlines and speed

The impact of the total power P_{tot} dissipated in the facility on the streamlines and the velocity magnitude is shown in Fig. 6.29 for $p_0 = 5000\,\mathrm{Pa}$ and $p_0 = 20\,000\,\mathrm{Pa}$. The recirculation length is increased for lower power P_{tot}. On the other hand, the velocity magnitude increases dramatically in the whole facility with P_{tot}. Indeed, due to the greater heating, the fluid has a lower density, and the velocity increases due to the constant mass flux Q.

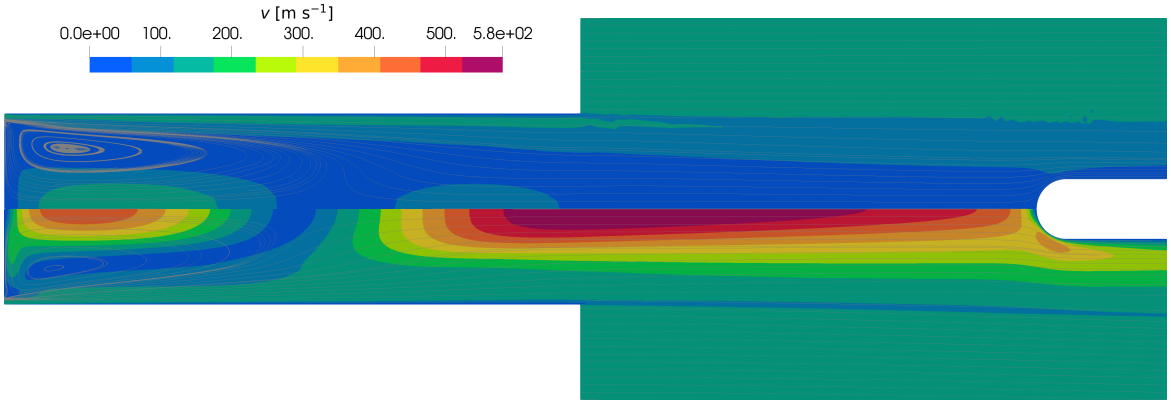

Fig. 6.29.: Streamlines and velocity magnitude v for a power of $P_{tot} = 50\,\mathrm{kW}$ (top) and $P_{tot} = 200\,\mathrm{kW}$. The exact simulation parameters are shown in Section 5.4.

In the torch

In the torch, the impact of the total power P_{tot} on the temperature profile is twofold. At first, the maximal temperature increases significantly with the rising power. Then, as P_{tot} increases, the temperature profiles broadens, but the maximal temperature stalls. The heat is spread more evenly in the torch since, for these temperature ranges, the heat conductivity of the air increases with temperature, easing the heat transferred from the torch center towards the wall. Moreover, the increase in power strengthen the recirculation bubble, which contributes to the distribution of heat. Secondly, increasing P_{tot} shifts the volume power peak further away from the center line in the facility, while increasing its magnitude. Although the volume power becomes more localized around the peak with increasing P_{tot}, its magnitude increases everywhere in the torch. Both temperature and volume power profiles are displayed in Fig. 6.30.

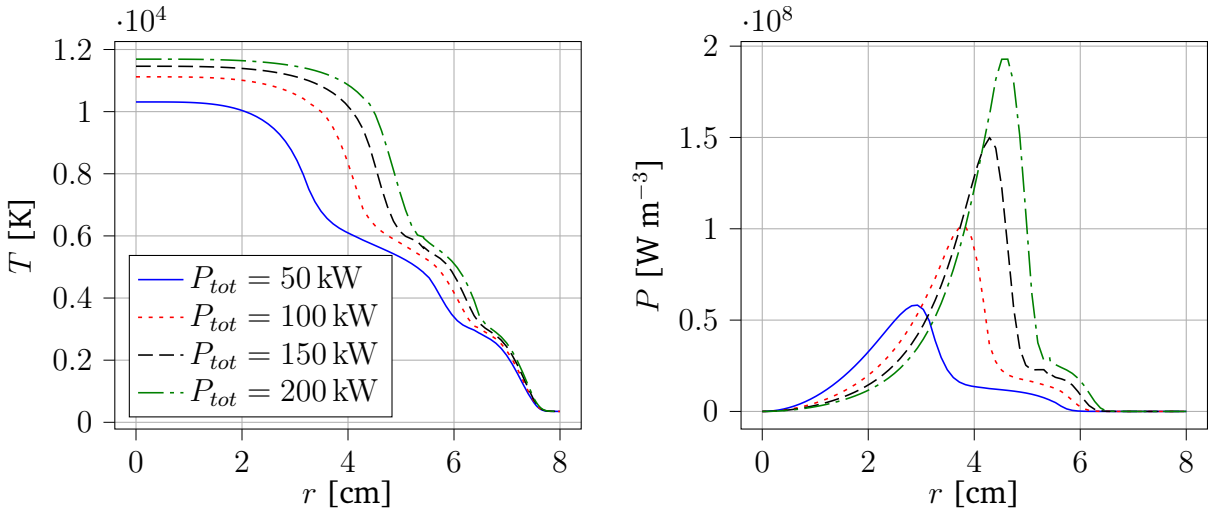

Fig. 6.30.: Temperature T and Joule heating power P profiles in the torch center as a function of the total power dissipated in the facility P_{tot}. r is the radial position from the symmetry axis. The exact simulation parameters are shown in Section 5.4.

The electric field and electric conductivity in the torch center are also affected by an increasing P_{tot}. The former decreases closer to the center line and increases towards the wall. The latter broadens and increases along the radial profile (Fig. 6.31).

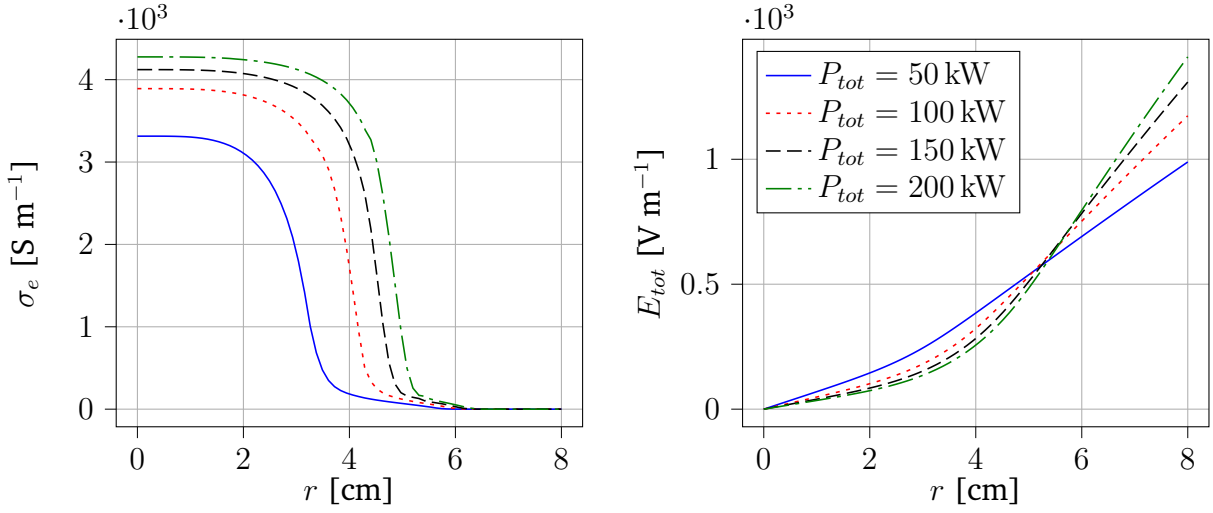

Fig. 6.31.: Total electric field norm E_{tot} and electron electric conductivity σ_e profiles in the torch center as a function of the total power dissipated in the facility P_{tot}. r is the radial position from the symmetry axis. The exact simulation parameters are shown in Section 5.4.

P_{tot} also has a significant effect on the gauge pressure Δp and velocity profiles (Fig 6.32). Δp is increased with growing P_{tot}, while v_z magnitude is reduced along the centerline.

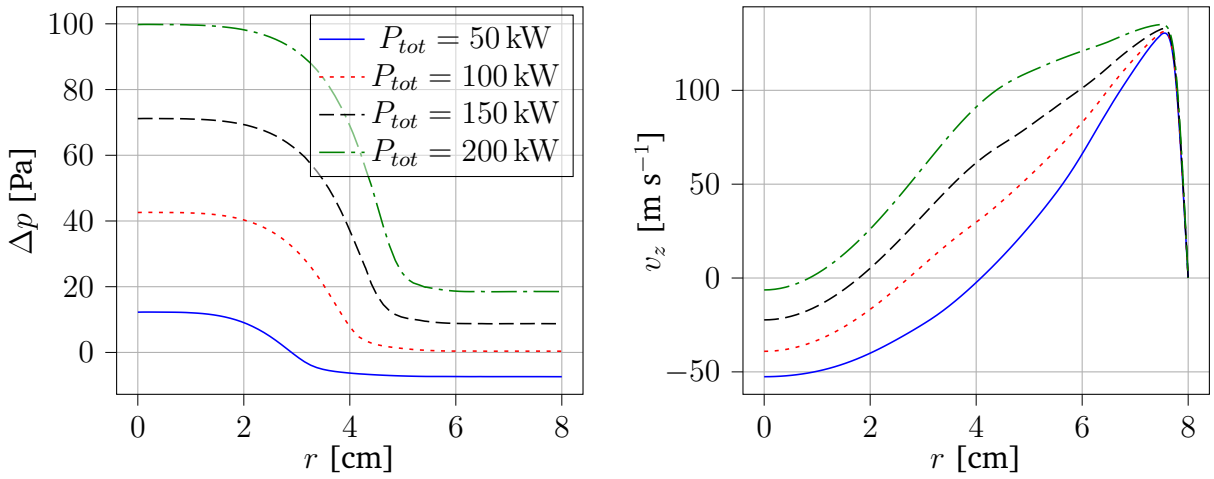

Fig. 6.32.: Gauge pressure Δp and axial velocity profile v_z in the torch center as a function of the total power dissipated in the facility P_{tot}. r is the radial position from the symmetry axis. The exact simulation parameters are shown in Section 5.4.

At the torch exit

At the torch exit, the maximal value of the total enthalpy H profile is almost not affected by increasing P_{tot} (Fig. 6.33). The profile is mainly broadened.

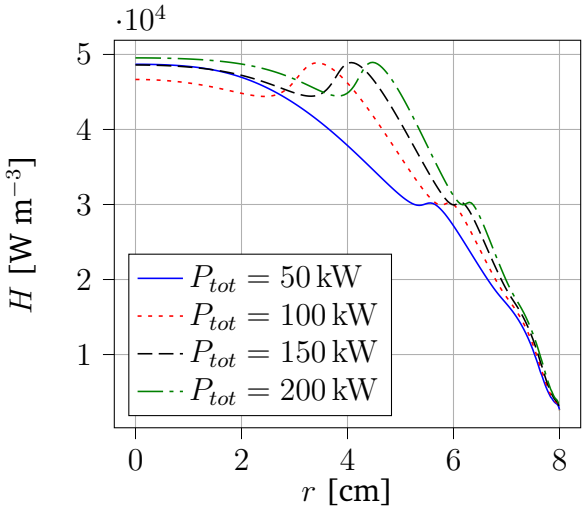

Fig. 6.33.: Total enthalpy H profile at the torch exit as a function of the total power dissipated in the facility P_{tot}. r is the radial position from the symmetry axis. The exact simulation parameters are shown in Section 5.4.

Along the stagnation line

P_{tot} has a significant impact on the temperature profile along the stagnation line, which increases with increasing power. The total enthalpy is influenced in the same manner.

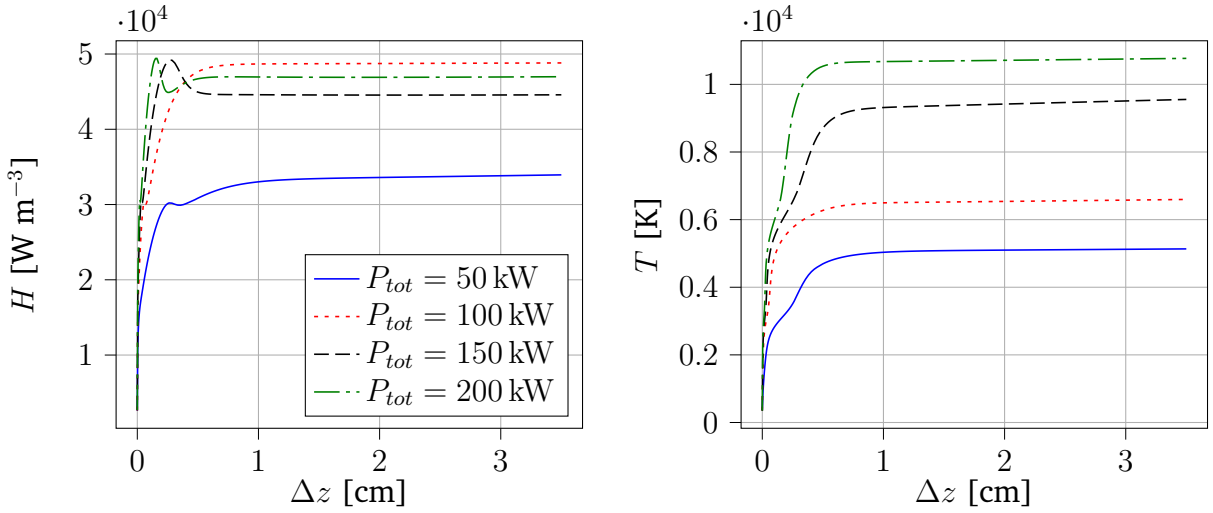

Fig. 6.34.: Total enthalpy H and temperature profile T along the stagnation line as a function of the total power dissipated in the facility P_{tot}. Δz is the axial position from the probe tip. The exact simulation parameters are shown in Section 5.4.

The axial velocity field v_z and the radial gradient of the radial velocity profile are significantly increased with an increasing P_{tot} (Fig. 6.35). The boundary layer thickness first decreases with power, then starts to increase again above $P_{tot} = 100\,\mathrm{kW}$.

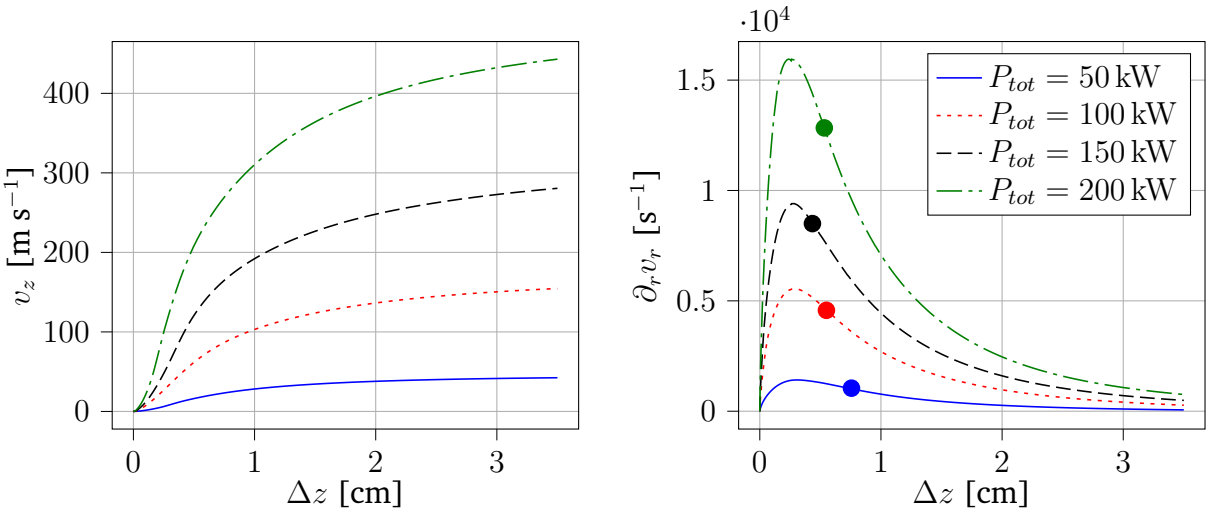

Fig. 6.35.: Axial velocity v_z and radial gradient of the radial velocity $\partial_r v_r$ profiles along the stagnation line as a function of the total power dissipated in the facility P_{tot}. Δz is the axial position from the probe tip. The inflexion point of $\partial_r v_r$ has been marked for each regime. The exact simulation parameters are shown in Section 5.4.

Because the temperature coming from the jet is greatly increased with an increasing P_{tot}, the temperature gradient magnitude also increases at the probe tip, while it remains constant everywhere else on the stagnation line. On the other hand, the normal heat flux q at the tip of the probe is also increasing (Fig. 6.36).

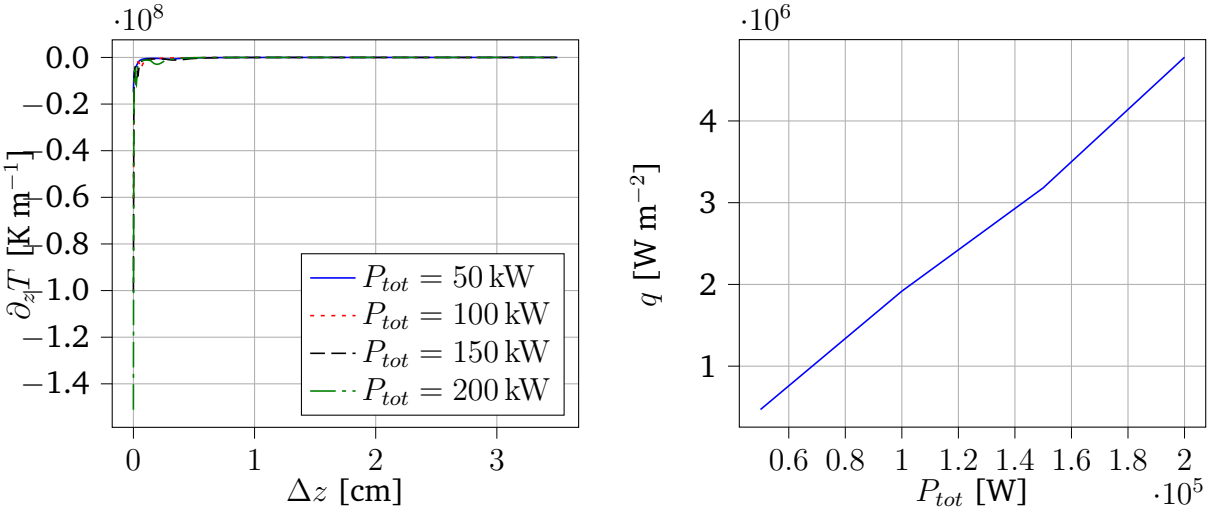

Fig. 6.36.: Axial temperature gradient $\partial_z T$ along the stagnation line and normal heat flux q at the tip of the probe as a function of the mass flow rate Q. Δz is the axial position from the probe tip. The exact simulation parameters are shown in Section 5.4.

Impact on the non-dimensional numbers

The impact of P_{tot} on the local interaction parameter Im is shown in Fig. 6.28. Increasing the power actually diminishes the importance of the Lorentz force, but does not have a significant impact on its area of effect.

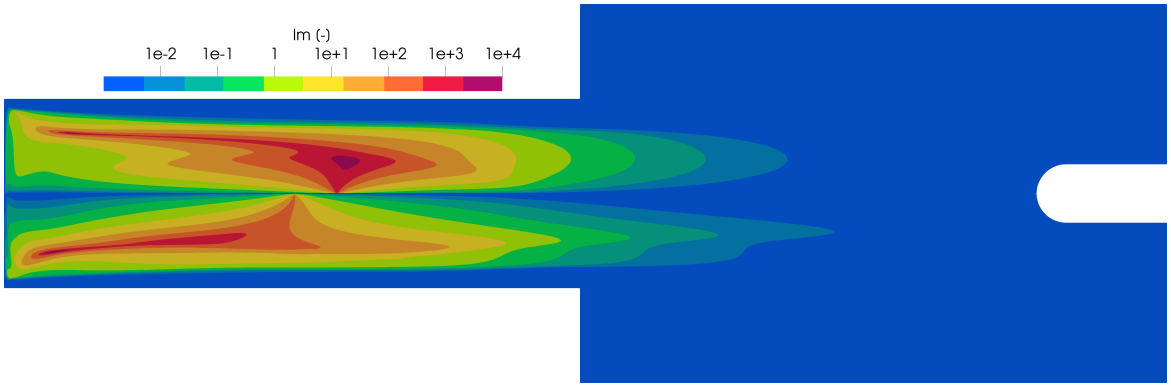

Fig. 6.37.: Magnetic interaction parameter Im for a power dissipated in the facility P_{tot} of $P_{tot} = 50\,\mathrm{kW}$ (top) and $P_{tot} = 200\,\mathrm{kW}$ (bottom). The exact simulation parameters are shown in Section 5.4.

The impact of P_{tot} on the Joule and induction numbers is given in Table. 6.2. The Joule number Jn increases, meaning that the heating of the flow is more efficient. On the other hand, the induction number $\mathrm{N_{ind}}$ remains the same, and the skin depth is more or less unchanged.

P_{tot}	Jn	$\mathrm{N_{ind}}$
$50\,\mathrm{kW}$	50	284
$200\,\mathrm{kW}$	236	284

Tab. 6.2.: Table reporting the Joule Jn and induction $\mathrm{N_{ind}}$ numbers for power P_{tot} of $50\,\mathrm{kW}$ and $200\,\mathrm{kW}$

6.2.4 Impact of the frequency

We studied frequencies f of $10\,\mathrm{kHz}$, $80\,\mathrm{kHz}$, $300\,\mathrm{kHz}$, $500\,\mathrm{kHz}$ and $1\,\mathrm{MHz}$. A too low frequency increases the impact of the effective Lorentz force and destabilizes the flow, and the steady-state solver fails. On the other hand, if f is too large, it becomes comparable or greater to the plasma electron oscillation frequency, and the local thermodynamic equilibrium hypothesis breaks. Moreover, at large frequencies, displacement current must be taken into account.

Impact on the streamlines and speed

The impact of the induction frequency f on the streamlines and the velocity magnitude is shown in Fig. 6.38 for $f = 10\,\mathrm{kHz}$ and $f = 1\,\mathrm{MHz}$. Increasing f has for effect to decrease the velocity magnitude in the facility and slightly decreases the recirculation bubble length.

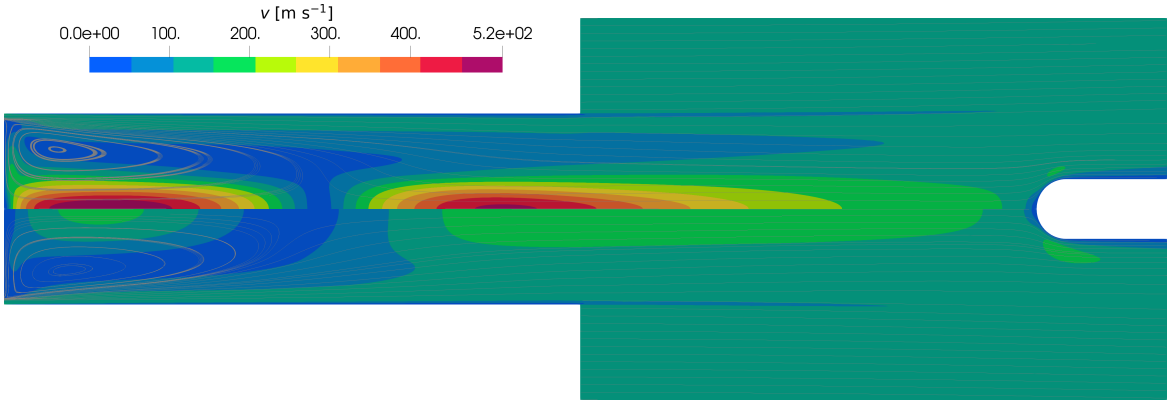

Fig. 6.38.: Streamlines and velocity magnitude v for an induction frequency of $f = 10\,\mathrm{kHz}$ (top) and $f = 1\,\mathrm{MHz}$. The exact simulation parameters are shown in Section 5.4.

In the torch

In the torch, the frequency f has an impact on the maximal temperature reached in the facility, but the width of the profile remains the same. On the other hand, the maximal volume power dissipated in the facility is reduced with increasing frequency. A shift in the power peak towards the wall is also observed, with a broadening of the profile (Fig. 6.39). Both maximal temperature and volume power decrease with increasing frequency.

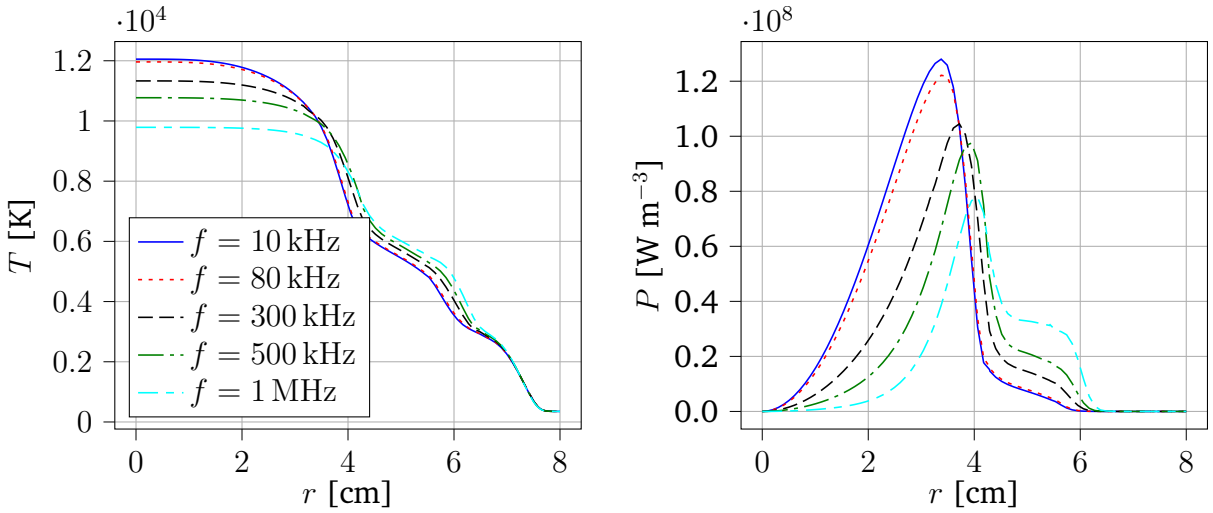

Fig. 6.39.: Temperature T and Joule heating power P profiles in the torch center as a function of the induction frequency f. r is the radial position from the symmetry axis. The exact simulation parameters are shown in Section 5.4.

f also has an impact on the total electric field and the electron electric conductivity profile σ_e. The effect on the former is qualitatively comparable to the impact of an increase in total power P_{tot}. On the other hand, σ_e decreases in magnitude. Consequently, the decrease in the power peak is due to the decrease in σ_e, and the power shift is mainly due to the increase of the electric field closer to the torch walls. Note that the frequency has a huge impact on E_{tot} magnitude close to the torch wall, while it is less important close to the center line.

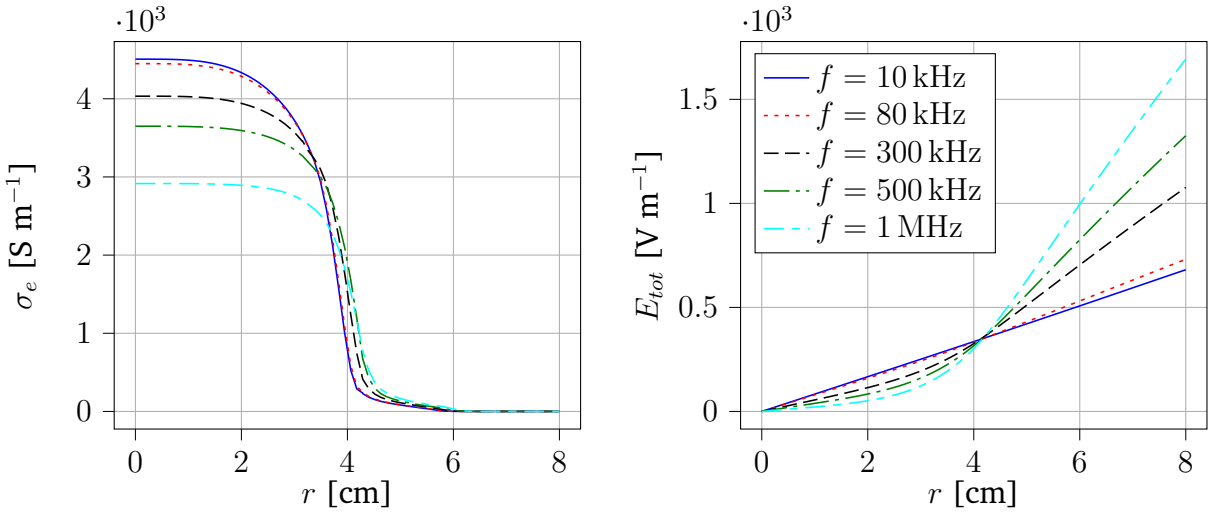

Fig. 6.40.: Total electric field norm E_{tot} and electron electric conductivity σ_e profiles in the torch center as a function of the induction frequency f. r is the radial position from the symmetry axis. The exact simulation parameters are shown in Section 5.4.

The axial velocity and gauge pressure profiles in the torch center (Fig. 6.41) are also influenced by f. The pressure increases closer to the center line but decreases closer to the torch wall. On the other hand, the magnitude of v_z decreases towards the center of the torch.

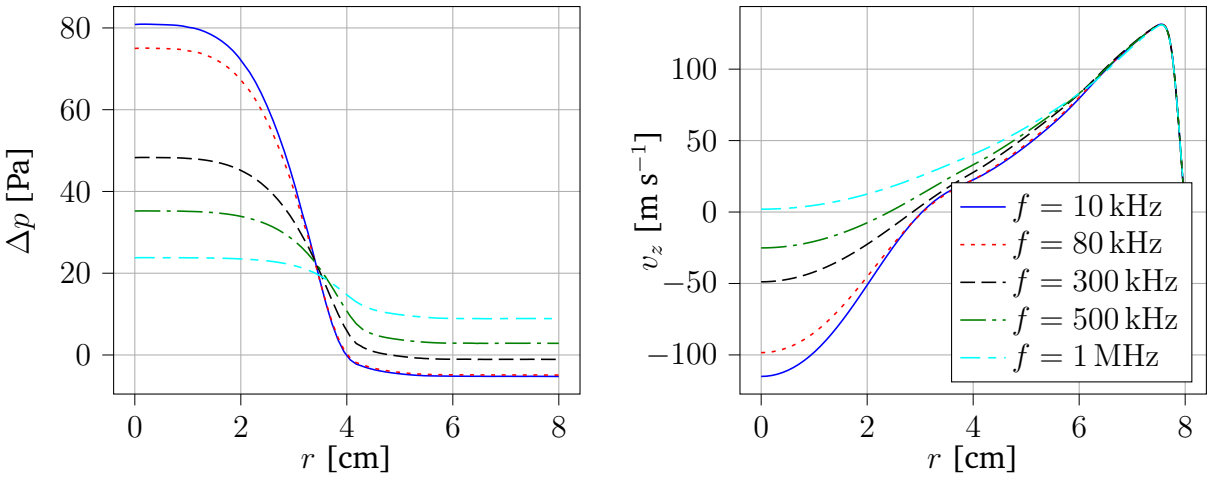

Fig. 6.41.: Gauge pressure Δp and axial velocity profile v_z in the torch center as a function of the induction frequency f. r is the radial position from the symmetry axis. The exact simulation parameters are shown in Section 5.4.

At the torch exit

At the torch exit, the total enthalpy H of the system is little influenced by the frequency (Fig. 6.42). The only region of influence is close to the center line, where the temperature varies the most.

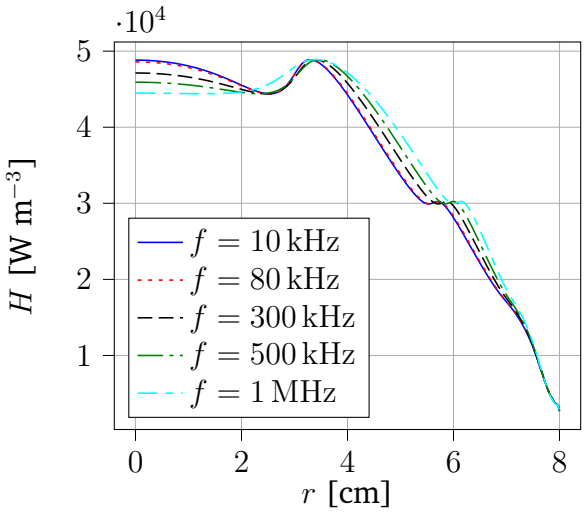

Fig. 6.42.: Total enthalpy H profile at the torch exit as a function of the induction frequency f. r is the radial position from the symmetry axis. The exact simulation parameters are shown in Section 5.4.

Along the stagnation line

The induction frequency does not really impact the enthalpy nor the temperature profile along the stagnation line, nor the axial velocity field v_z and the radial gradient of the radial velocity profile (Fig. 6.44). Moreover, the boundary layer thickness is independent of f.

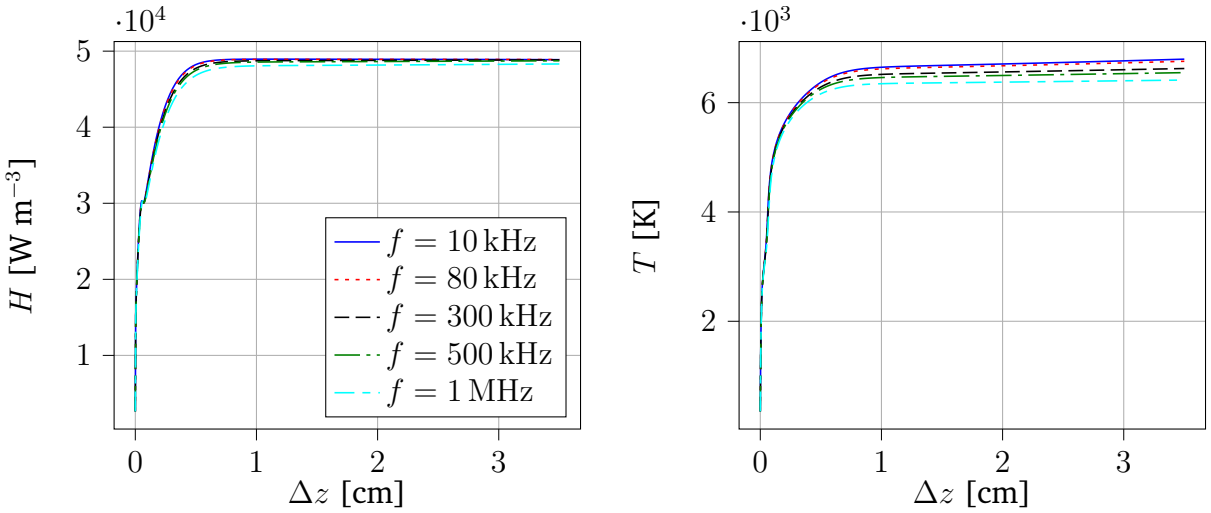

Fig. 6.43.: Total enthalpy H and temperature profile T along the stagnation line as a function of the induction frequency f. Δz is the axial position from the probe tip. The exact simulation parameters are shown in Section 5.4.

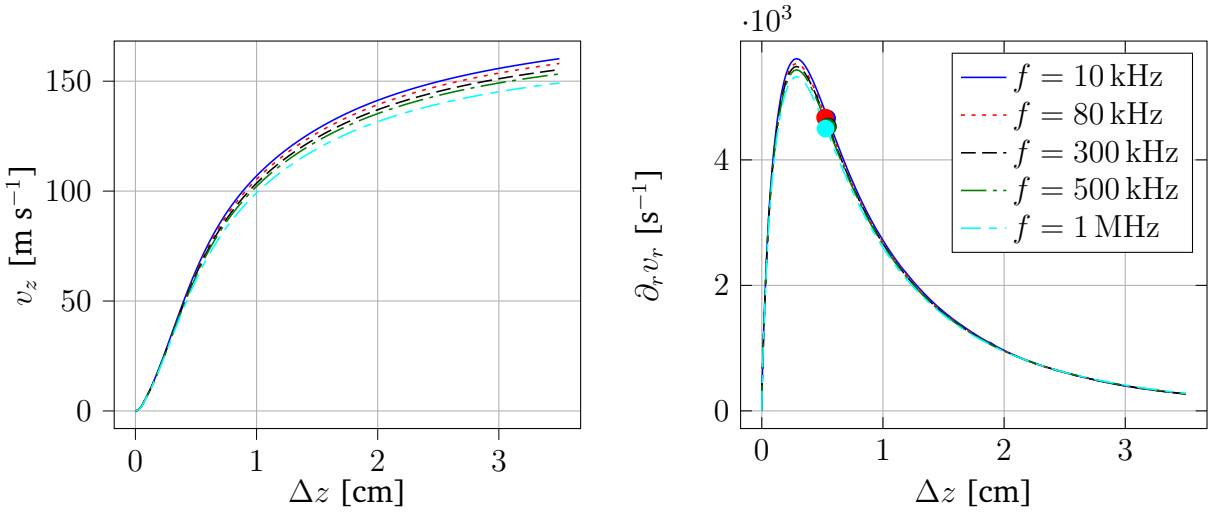

Fig. 6.44.: Axial velocity v_z and radial gradient of the radial velocity $\partial_r v_r$ profiles along the stagnation line as a function of the induction frequency f. Δz is the axial position from the probe tip. The inflexion point of $\partial_r v_r$ has been marked for each regime. The exact simulation parameters are shown in Section 5.4.

Because the temperature coming from the jet is not significantly impacted by f, the temperature gradient and the normal heat flux q at the tip of the probe are not affected as well (Fig. 6.45).

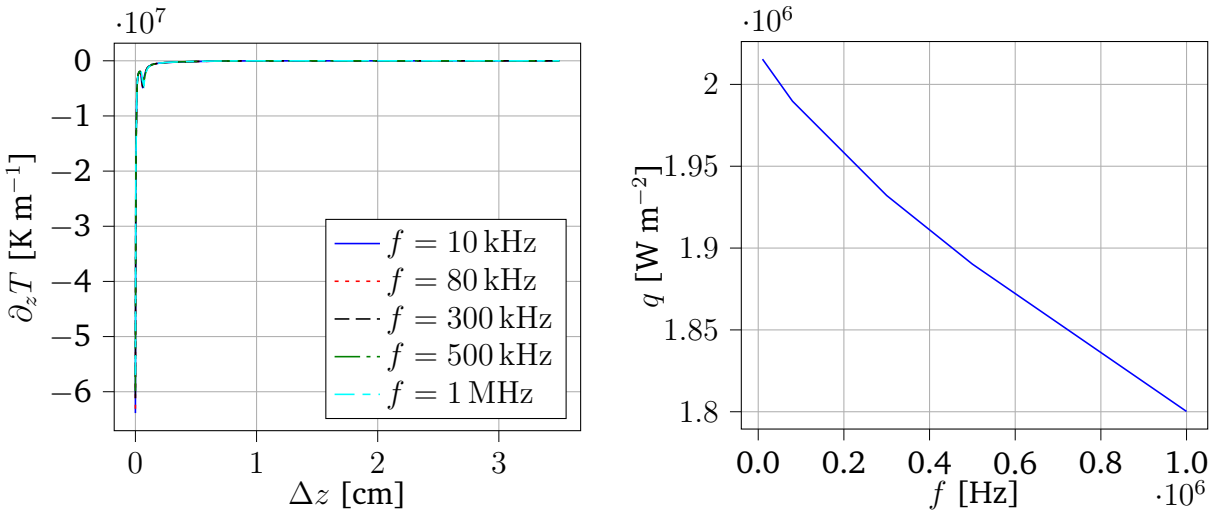

Fig. 6.45.: Axial temperature gradient $\partial_z T$ along the stagnation line and normal heat flux q at the tip of the probe as a function of the induction frequency f. Δz is the axial position from the probe tip. The exact simulation parameters are shown in Section 5.4.

Impact on the non-dimensional numbers

The impact of f on the local interaction parameter Im is shown in Fig. 6.46. Increasing the induction frequency decreases dramatically the importance of the Lorentz force. Its magnitude is decreased everywhere, and it almost has no impact on the jet.

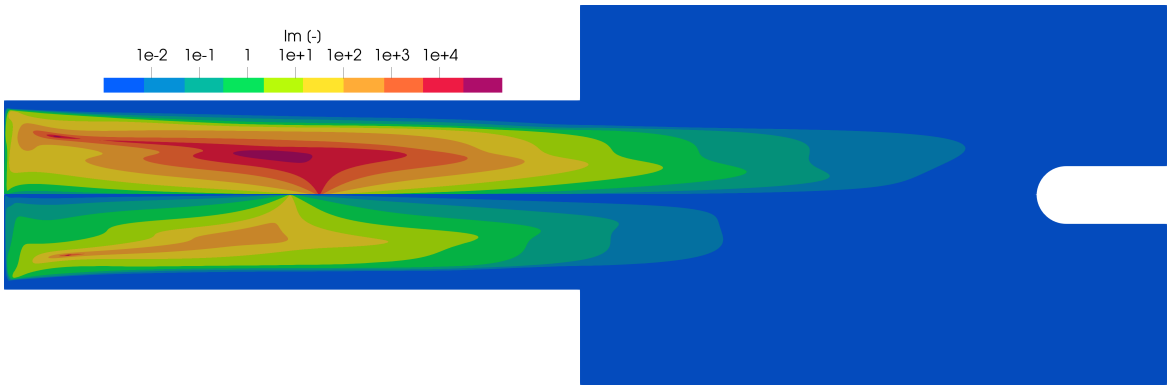

Fig. 6.46.: Magnetic interaction parameter Im for an induction frequency f of $f = 10\,\mathrm{kHz}$ (top) and $f = 1\,\mathrm{MHz}$ (bottom). The exact simulation parameters are shown in Section 5.4.

The impact of f on the Joule and induction numbers is given in Table. 6.3. The Joule number remains constant meaning that the heating of the flow is the same. On the other hand, the induction number $\mathrm{N_{ind}}$ increases proportionally to f. The skin depth decreases.

f	Jn	N_{ind}
10 kHz	118	6.23
1 MHz	118	623

Tab. 6.3.: Table reporting the Joule Jn and induction N_{ind} numbers for induction frequencies of 10 kHz and 1 MHz

6.2.5 Impact of the swirl

Swirl can be added at the inlet in order to further stabilize the torch. The main impact of the swirl is its influence on the probe velocity boundary layer. Also, the swirl creates a pressure drop at the exit of the torch. If the swirl is too large, the pressure defect becomes so strong that it creates a cold recirculation bubble at the torch exit. Predicting this phenomenon is crucial, since it has a significant impact on heat flux and velocity experimental measurements. We have shown in Fig. 6.47 the evolution of the pressure at the torch exit and the boundary layer thickness for swirl angles S ranging from $0°$ to $20°$ with a step of $5°$.

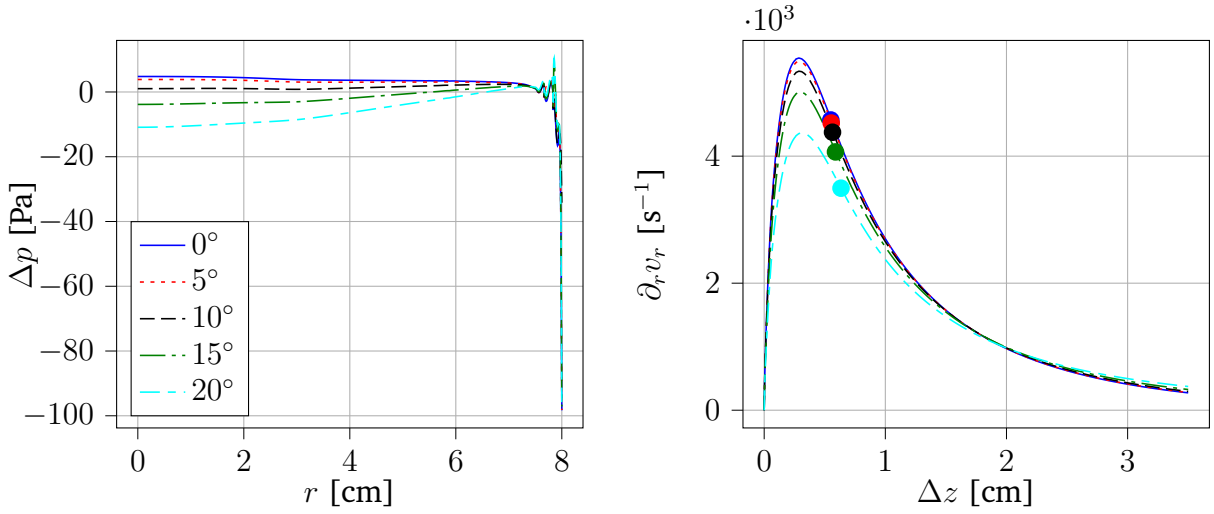

Fig. 6.47.: Gauge pressure Δp radial profile as a function of the swirl angle S at the exit of the torch and radial gradient of the radial velocity $\partial_r v_r$ along the stagnation line in front of the probe. r is the radial position, Δz is the axial position from the probe tip. The inflexion point of $\partial_r v_r$ has been marked for each regime.

Unfortunately, we did not study the formation of the recirculation bubble, as this phenomenon is unsteady. We leave it for future work.

6.3 Conclusion of the physical study

In this Chapter, we have simulated actual ICP flow conditions. We first displayed various fields for the test cases listed in Section 5.4. We showed that the flow was subsonic with quasi-constant pressure. It also presented very large temperature gradients in the near wall region. We also showed that the electric field has an impact only in the torch, where the power dissipated in the facility is concentrated in the region where the coupling between the plasma and the electric field is the largest. We also showed the recirculating nature of the flow at the inlet. We observed that no noticeable discrepancies between the probe and freestream cases exists inside the torch. The main difference occur in the chamber for the hydrodynamic field. These disparities are due to the presence of the probe which modifies pressure, streamlines and velocity fields in the jet. On the other hand, for the electric field and quantities derived from it, such as the Lorentz force or the power, the probe and freestream cases give similar results, because the electric field is almost negligible in the chamber.

Then, we assessed the effect of increasing the mass flow rate Q, background pressure p_0, total power dissipated in the facility P_{tot}, induction frequency f and swirl angle S on the electric and hydrodynamic fields. We list here the main impact of these parameters on the ICP flow field according to our simulations. The mass flow rate had mainly an impact on the hydrodynamic fields, as it influences the velocity field. Its influence can also be felt in the heat flux at the tip of the probe and the stagnation point boundary layer thickness, both of them decreasing with increasing Q. The background pressure, by impacting the density of the fluid has a huge impact on the velocity field. Combined with its influence on the transport properties of the plasma, it alters the heat repartition in the facility. A higher pressure plasma has a tendency to concentrate the heat towards the axis of symmetry, effectively increasing the heat flux at the tip of the probe. Unsurprisingly, P_{tot} brings heat to the system, participating to the elevation and repartition of temperatures and an increase of the heat flux at the probe. Indirectly, it also modifies the density of the fluid, impacting the velocity fields. This is one of the most impactful parameters. The frequency also has a great influence on the flow field, especially on the electric field generated in the plasma. In general, increasing frequency decreases the effectiveness of the heating. Finally, the swirl has almost no measurable impact, except on the pressure at the torch exit, where a large swirl can lead to large adverse pressure gradient, possibly creating a cold recirculation bubble.

We proved in this Chapter that our ICP code can easily perform parametric studies. Taking advantage of the fast convergence and ease of use of the code, we managed to study the ICP simulations for a wide range of parameters. Of course, the range of validity of our model and conclusions is limited, as we only considered an axisymmetric equilibrium steady-state ICP model without radiation. The results presented here should be validated using experimental data. These considerations are left for future work.

7

Conclusions of the thesis and future work

This work is the result of the collaboration between the von Karman Institute for Fluid Dynamics (VKI) and the University of Liège. This project started in 2020, during the author's master thesis at VKI. It was supposed to last six months, but ended up filling an entire Ph. D. project. Our work was funded by a FNRS (FRIA) fellowship. We benefited from the expertise of VKI for the physical modeling of the Plasmatron facility through Prof. Thierry Magin and the expertise in high-order solver from the ULiège team of Prof. Koen Hillewaert. The code was developed using the Unified Framework, a hybridized discontinuous Galerkin framework developed by the group of Prof. Georg May.

7.1 Conclusions

The original plan of this project was to create a solver capable of producing high-order, 3D, time accurate and possibly non (chemical and thermal) equilibrium inductively coupled plasma flow. The primary goal was to see if high-order solvers were able not only to withstand ICP simulations, but also to go far beyond what had been done by legacy solvers. It turned out that this project was far too ambitious for a single thesis. Although we did not fulfill our (very) numerous objectives, we strongly believe that this work has lead the way of future ICP simulations. But before going further, we answer the three questions asked in the introduction.

- **In addition of being precise, can a high-order solver be robust?** We answer this question with a resonant "yes"! The code that we produced was even more robust than legacy finite volume solvers. We are convinced that it is due to the monolithic approach. The idea of using this monolithic strategy came to us from previous research in the ICP simulation field by David Vanden Abeele in the early 2000, who solved the fully coupled system using a Jacobian free GMRES approach. Although those results were never published officially, David wrote in his thesis that they improved the convergence dramatically. One of the issues with this approach is that one still needs to give an approximation of the Jacobian in order to precondition the system. An analytical expression of this Jacobian, even approximated, can be cumbersome to obtain, especially with the complex chemistry at play. We took advantage of the capabilities of our code,

119

which uses automatic differentiation. This feature allows to store parameters and their derivatives with respect to the variables of the problem. The operations of additions, subtractions, *etc...* on the parameters are automatically applied to their derivatives, creating the Jacobian without having to derive it analytically nor approximate it. This approach allowed us to easily construct the Jacobian of the system and solve it monolithically.

One of the drawbacks is that Mutation++ is not equipped with automatic differentiation. Fortunately, since we were using an LTE table of states with linear interpolation, the derivatives were easy to reconstruct. However, it would be interesting to implement automatic differentiation directly in Mutation++, especially for the non-equilibrium case. One of the main arguments against a monolithic approach is their complexity of implementation and their relative rigidity. On the other hand, arguments in favor of staggered solvers is that they are easier to implement, and more flexible (one can easily use two methods for two physics *e.g.* use FEM for the electric field and HDG for the Navier-Stokes equations for ICP). Although we agree on the ease of use of the staggered solvers, they produce slow convergence for ICP applications. We also believe that the arguments against the monolithic multi-domain approach come from the fact that existing solvers are not equipped to integrate it easily. This is the same problem as parallelizing a code that was never developed to be parallelized: you have to rebuild it from the ground. However, the computational gain obtained after the parallelization of a code is rarely contested. We strongly believe that the same rationale should apply to monolithic solvers : it requires a certain effort, but once it is done, the gains are enormous. Moreover, we believe that the strong coupling in ICP requires a monolithic approach, and a dedicated solver had to be developed.

Another important point for the robustness of the solver is the design of the convective and diffusive numerical fluxes. The diffusive flux used in this work is frequently used in HDG, we did not expect any problem from this side and never had. However, we were concerned about the low-Mach AUSM convective numerical flux, since such fluxes had never been used in the framework of DG methods. Surprisingly, it worked "out-of-the box", requiring just a little adaptation for HDG. One of the drawbacks of this flux is that it is specifically designed for the low-mach flows. Out of curiosity, we tested several AUSM formulations for all Mach regimes (AUSM+up, SLAU). However, none of these solvers were as stable as the low-Mach one, meaning that a non-negligible effort has to be made in order to adapt them to HDG. These developments are vital if considering supersonic flows with real compressibility in the future.

- **Is the developed solver user-friendly?** The solver developed here gives meaningful results in only 20 minutes of computational time, starting from a crude initial solution on a laptop. This is a great improvement compared to legacy codes, that either have to run on multiple processors for 2-3 hours

if not starting from a "good" initial solution, *i.e.* profiles close to the solution of the current simulation. The pseudo-timestep method implemented is also very efficient and does not need to be monitored continuously. This allows to save a lot of computational and researchers time, as they do not have to stay next to their computer during the simulation. Moreover, we were able to perform a thorough parametric study thanks to these features. The mesh can be generated using automatic algorithms, and easily adapts to complex geometries. On the side of the programmer, new sets of equations can easily be appended to the code, thanks to the automatic differentiation, opening the path to non-equilibrium models or modification of the electric field produced by the coils. In our experience, the code is very flexible, allowing to simulate a wide variety of simulation with the same mesh and giving meaningful results. So yes, the code is user-friendly.

Although the solver is more robust and easier to use than its predecessors, it still requires parameter tuning. We primarily think about the penalization term of the diffusive flux, which has to be carefully chosen otherwise the method does not converge. Unfortunately, there is no magical formula that computes it. The mesh is also crucial in the convergence procedure. If it is not refined enough, the solver crashes. If the element size is too small, the high-accuracy solver may stall due to the capture of small scale unsteady phenomena or bad system conditioning. Since the code is high-order, it is more sensitive to instabilities, and configurations that gave a steady solution using a finite volume code might give an unsteady behaviour using HDG and never converge with the steady solver. In the end, this attests of the accuracy of the solver. Note also that specific care has to be taken in the boundary layer, where highly structured elements are required. We tested unstructured triangular elements but ended up with oscillating solution in the near wall region. We suspected that the functional space of the triangle was not rich enough to correctly capture the gradient in all directions. Anyways, the quads cured the issue. When a completely new test case needs to be simulated, the mesh and stabilization parameters of the test case have to be determined again, which, from our experience, can be a cumbersome and time consuming task. However, once these parameters are fixed, they remain valid for a large number of similar configurations. They usually need to be redetermined when the flow conditions or geometry are dramatically different from what was simulated before.

The ease of use, robustness and speed of the developed code in this thesis makes it an ideal companion for ICP experimenters. It can give valuable information in relatively short time, helping to better prepare the experiments. A striking example is the parametric study we performed in Chapter 6. The only limitation is the physics it is able to represent, which is axisymmetric plasma at equilibrium. The extensions to more general configurations is discussed in the answer to the next question.

- **Can the new solver be easily adapted to the new experiments performed in ICP facilities?** We strongly believe that the solver developed here can be extended to take into account a wide variety of physical phenomena. The problem mainly lies in its computational capabilities. Unfortunately, the HDG framework used in this thesis is not parallel and not optimized for larger computations. This is a real drawback, as we tried to run unsteady axisymmetric simulations successfully, but we could not gather enough data because the simulations were extremely slow. Another issue of ICP simulations is that detailed physics requires many equations. This increased number is felt not only at the hydrodynamic level, but also in the chemistry algorithms, which become more complex. This effect is amplified when considering 3D test cases, which require even more degrees of freedom than axisymmetric or 2D flows. When considering unsteady and turbulent behaviour, where the mesh must be sufficiently refined in order to correctly capture the physical phenomena of interest, this constraint is even more amplified. Consequently, the code must be paralleled in order to match the computational requirements. The integration of complex chemistry and thermal behaviour requires to solve many small systems of equations in order to compute the transport properties and chemical reaction rate. In order to mitigate this drawback, one could use GPU parallelization to deal with these many small computations efficiently. Unfortunately, the Mutation++ library is not yet equipped with such capabilities, and making it so is another formidable task.

  Aside from the question of computational power, the stability and accuracy of the solver are not *a priori* guaranteed for more complex flow simulations. We have discussed for instance the need of performing experiments involving shocks in the facility. However, we have not studied supersonic plasma flows, and therefore cannot make any prediction on the solver behaviour concerning shocks. In order to preserve accuracy, several solutions exists. First, at higher Mach number, the convective numerical flux has to be adapted to all speed regimes. We tested some of these solvers, but none of them were as stable as the low-Mach one. Consequently, the design of those fluxes needs to be investigated. The shocks can be stabilized by either using an entropy stable scheme, or the combination of the high-order method with the finite volume method near the shock. These latter fields of research are active in the group of Prof. Koen Hillewaert at the university of Liège (*cfr.* more specifically the work of Bilocq *et al.* [11]), and can explored for the HDG code. Capturing unsteady behaviour is also very important. We highly suspect that there exists no steady flow in ICP facility. First, our equations are time-averaged over one oscillation period of the induction current, effectively killing the effect of the oscillating electric field. Second, these suspicions come from the fact that it was impossible to obtain a steady solution when the coflow was removed from the chamber, whatever the simulation parameters. We know that steady solutions were found using finite volume solvers and no coflow, but FV is much more

dissipative than our high-order method, killing potential unsteady behaviour. Also, when running unsteady computations, the plasma jet started to oscillate. It was possible to obtain a steady state with the simple backward Euler unsteady solver after a sufficiently long simulation time and large timesteps. But as soon as the time step was decreased again or a time marching method with greater accuracy was used, the jet oscillations came back. From our experience, only the simple backward difference scheme was stable, but of course, many other temporal solver exists and should be investigated.

In short, the answer to the research question is yes, the solver can be adapted to match new experiments in the facility, but it requires additional efforts to do so. With this objective in mind, the thesis of Landry Riou, which we have partly supervised during our last Ph. D. year, has been started. Because developing a parallel code from scratch takes a non negligible amount of time, Landry is going to incorporate the results of this work in a high performance, discontinuous Galerkin multi-physics solver called ARGO. With these developments, we hope to be able to simulate more complex physics than is possible with our current solver.

As a conclusion, although we did not fulfill all the primary objective of the thesis, we produced the proof that high-order methods are advantageous in the simulation of inductively coupled plasma flow. The flexibility of the monolithic method developed here, its efficiency, the possibility to adapt to any geometric configuration and its robustness makes it the perfect candidate for future ICP computations. Moreover, it can be used easily, even by people with little experience in numerical methods, on a simple laptop. The code is also very modular, it can be adapted to new physical situations quite easily. Shortly said, we opened a new era in the simulation of ICP flows.

7.2 Future work

Although this thesis poses the basis of a new kind of ICP flow simulations, we were not able to explore more physical and geometrical features of ICP. We discuss future research directions.

The first research direction is the physical modeling of the plasma in ICP. This research can be first performed in axisymmetric configuration, then later adapted to 3D flows. We would start first with the implementation of elemental demixing in the LTE model. It allows to keep the equations relatively simple, the only difference with the classic LTE model being the addition of mass conservation equations for the elemental fractions and the diffusion of the elements. Note that the elements do not have production rates because their mass is always conserved, which greatly simplifies the computations. This relatively simple model should already yield more accurate results than classic LTE. Then, one should investigate the effect of complete

non-equilibrium. We listed many possible models in Chapter 2. Depending on the equilibrium state of the plasma, one should select a sufficiently detailed model. The radiation also has to be taken into account. In fact, radiation has an important impact on the heat transfer, but is usually neglected due to its complex modeling and huge computational cost. We believe that it should be considered in future developments, as its impact is not negligible for specific flow conditions. Efforts should also be put in the efficient computations of the transport properties and chemical reaction rate. Because the computation of these properties requires the solution of a large number of small systems, an approach using GPU could be investigated.

Another research direction is going for 3D computations. As discussed in Chapter 3, one of the main challenges is to reformulate the equation for the electric field for 3D flows. For this task, two approaches are possible. First, one could simply solve for the general electric field equation and the Laplace equation for the electric potential. This approach is exact, but computationally expensive, since 4 equations have to be solved (3 for the induced electric field, one for the electrostatic potential) in addition to the Navier Stokes system. Second, one could consider a perturbation from the axisymmetric configuration of the induced electric field and ambipolar assumption for the electrostatic one. We have not investigated these approaches, but they definitely worth the try. Another point is that 3D ICP would need a fully parallel code able to handle multiple physics. The implementation of such feature would make the study of non axisymmetric geometries possible. In particular, for the Plasmatron, one could simulate the flow inside a semi-elliptical nozzle. One could also assess the effect of the coil geometry on the flow, and emphasize 3D modes that cannot be observed with the current codes. Until now, we used not only a monolithic solver, but also a monolithic system preconditioner. When parallelizing the code, the monolithic preconditioning approach has to be abandoned. In place, multi-domain preconditioners (currently additive Schwartz ILU) are used. They allow for the efficient parallelization of the code, at the cost of a possibly greater number of iteration in order to reach convergence. The design of these multi-domain preconditioners should be thoroughly investigated in order to reduce this drawback as much as possible.

The time accurate simulations also need to be explored. This can also be done at first on an axisymmetric configuration, then on a 3D solver. As discussed above, we highly suspect that no steady ICP flow exists. The hot jet released in cold air may give rise to Kelvin-Helmholtz instabilities, that have to be correctly captured. Moreover, this unsteady behaviour may have an important impact over the flow fields and heat flux in the jet. In addition, turbulence could also have an important role in ICP facilities and should be investigated. Another point of discussion is the averaging of the equations describing ICP flows over one oscillation period of the induction current. In real conditions, the fast varying electric field may have an important impact on the plasma dynamics. Moreover, in the experimental facility, the ripple component of the generator pulse rectifier is fully transmitted to the flow. One should be able to study numerically these phenomena. Turbulence in ICP facilities may also occur at frequencies even higher than the electric oscillation period, requiring

to correctly capture the temporal variations when performing a direct numerical simulation. We also ignore the displacement currents, that can be non negligible when the induction frequency becomes large by disrupting the thermal equilibrium of the system. Taking into account this wide variety of phenomena is extremely difficult, as the system becomes very stiff. Indeed, capturing the displacement currents means capturing the speed of light, which requires a very small time step. Moreover, the ICP involves physics of very different timescales, making the system to be solved stiff (*i.e.* ill-conditioned). The accurate temporal simulation of ICP is a real challenge that need to be tackled.

Finally, we considered only subsonic computations, with a quite effective low-Mach numerical flux. As explained in the introduction of this thesis, supersonic flows are going to be studied in the Plasmatron facility. In order to be able to reproduce these results using a computational solver, a numerical flux for all speeds has to be employed. Moreover, depending on the strength of the shock encountered in the facility, shock capturing techniques may have to be implemented. The latter techniques are being explored by Maxime Borbouse (ULiège/UCLouvain) or Tobias Winter (VKI/ULiège) for high order methods. On the other hand, Landry Riou (UNSW Canberra/VKI) is currently working on the implementation of an ICP high-order code using the discontinuous Galerkin method in the software ARGO with the purpose of producing a framework able to tackle all the previous challenges. We briefly discuss the capabilities of ARGO below.

The presented list of developments for the ICP solver is far from exhaustive. We have not talked about the simulation of the plasma sheath in the near sample region for electron transpiration cooling, nor the addition of the magnetic field inside the probe in order to study the black out phenomena. One of the main ongoing work is the implementation of our solver capabilities in the ARGO high performance solver. Because ARGO is already capable of performing 3D, unsteady and turbulent high-order simulations, it is a good candidate to develop ICP solvers. That is why Landry Riou is developing a high-performance ICP solver using the latter. In particular, the code is already able to simulate material ablation. Merging the ICP with the ablation would really improve the quality of the computations, as for now the temperature profile at the torch exit obtained via an ICP code is given as input to ARGO in order to perform ablation simulations. Another topic we did not discuss was the code validation with experience. We were able to perform comparisons of our code results with actual ICP experiment. We obtained a quite good agreement, but we did not have access to a lot of data. In order to completely validate the code, one should perform a complete validation campaign.

With these considerations, we close this thesis. Although we did not venture into complex flow configurations, we nonetheless developed a completely new solver for inductively coupled plasma. By proving that ICP simulations were possible using a high-order method, and showing its robustness, ease of use and flexibility compared to legacy finite volume solvers, we have given the keys for future ICP computations.

This thesis is only the seed, from which many subsequent research in the field of ICP simulations can grow. We hope that, one day, we will be able to simulate 3D and unsteady plasma flow, for any physics, being a reference for the experimenters. But there is still much work to be done...

Bibliography

[1]Fagnani A., Helber B., Hubin 1., and Chazot 0. “In situ multi-band apparent emissivity measurements of aerospace materials in inductively coupled plasma flows”. In: *Infrared Physics & Technology* 139 (2024) (cit. on p. 12).

[2]I. Adamovich, S. Agarwal, E. Ahedo, et al. “The 2022 Plasma Roadmap: low temperature plasma science and technology”. In: *Journal of Physics D : Applied Physics* 55 (2022) (cit. on p. 3).

[3]D. N. Arnold, F. Brezzi, B. Cockburn, and L. D. Marini. “Unified Analysis of Discontinuous Galerkin Methods for Elliptic Problems.” In: *SIAM Journal of Numerical Analysis* 39.5 (2002), pp. 1749–1779 (cit. on p. 16).

[4]M. Auweter-Kurtz, H.L. Kurtz, Gordeev A.N., and Laure S. “Plasma Generators for Re-entry Simulation.” In: *Journal of Propulsion and Power* 12.6 (1996), pp. 1053–1061 (cit. on p. 11).

[5]G. I. Babat. “Electrodeless discharges and some allied problems”. In: *Journal of the Institution of Electrical Engineers - Part III: Radio and Communication Engineering* 94.17 (1947) (cit. on p. 11).

[6]S. Balay, W. Gropp, L. C. McInnes, and B. F. Smith. “PETSc, the portable, extensible toolkit for scientific computation”. In: *Argonne National Laboratory* 2.17 (1998) (cit. on p. 64).

[7]R. Balescu. *Transport processes in plasmas. Classical transport theory. vol. 1*. 1988 (cit. on p. 21).

[8]R. Balescu. *Transport processes in plasmas. Neoclassical Transport. vol. 2*. 1988 (cit. on p. 21).

[9]P. N. Baronets, A. F. Kolesnikov, S. N. Kubarev, et al. “Overequilibrium Heating of the Surface of a Heat-Shield Tile in a Subsonic Jet of Dissociated Air.” In: *Fluid Dynamics* 26.3 (1991), pp. 437–442 (cit. on p. 11).

[10]D. Bernardi, V. Colombo, E. Ghedini, and A. Mentrelli. “Three-dimensional modeling of inductively coupled plasma torches”. In: *Pure and Applied Chemistry* 77.2 (2005), pp. 359–372 (cit. on pp. 13, 14, 35).

[11]Amaury Bilocq, Maxime Borbouse, Nayan Levaux, Vincent E. Terrapon, and Koen Hillewaert. “Comparison of stabilization strategies applied to scale-resolved simulations using the discontinuous Galerkin method”. In: *Journal of Computational Physics* 539 (2025), p. 114238 (cit. on p. 122).

[12]M. I. Boulos. “Flow and Temperature Fields in the Fire-Ball of an Inductively Coupled Plasma”. In: *IEEE Transactions on Plasma Science* 4.1 (1976), pp. 28–39 (cit. on pp. 15, 34, 64).

[13]S.I. Braginskii. “Transport processes in a plasma”. In: *Reviews of Plasma Physics* 1 (1965), pp. 205–311 (cit. on p. 21).

[14]N.G. Bykova, S.A. Vasil’evskii, A.N. Gordeev, et al. “Determination of the Effective Probabilities of Catalytic Reactions on the Surfaces of Heat Shield Materials in Dissociated Carbon Dioxide Flows.” In: *Fluid Dynamics* 32.6 (1997), pp. 876–886 (cit. on p. 11).

[15]Lorenzo Capponi, Trey Oldham, Matthew Konnik, et al. “Aerothermal characterization of the Plasmatron X Wind Tunnel: Heat flux, Stagnation Pressure and Jet Unsteadiness”. In: *AIAA SciTech forum*. 2023 (cit. on p. 11).

[16]M. Capriati, A. Turchi, P.M. Congedo, and T. E. Magin. “Heat flux characterization of an under-expanded/supersonic plasma jet over a catalytic probe”. In: June 2022 (cit. on p. 14).

[17]S. Chapman and T. G. Cowling. *The mathematical theory of non-uniform gases.* Ed. by Cambridge. University Press, 1960 (cit. on p. 21).

[18]O. Chazot and B. Helber. “Plasma Wind Tunnel Testing of Electron Transpiration Cooling Concept”. In: 2017 (cit. on p. 12).

[19]O. Chazot, D. Vanden Abeele, and M. Carbonaro. “Comparison of Experimental and Numerical Results for the Dynamic Pressure in an Inductive Plasma Flow”. In: *Annals of the New York Academy of Sciences* 891 (Dec. 1999), pp. 368 –376 (cit. on p. 11).

[20]F. F. Chen. *Introduction to Plasma Physics and Controlled Fusion*. Ed. by Springer International Publisher. 2016 (cit. on p. 1).

[21]A. Cipullo. “Plasma Flow Characterisation by means of Optical Emis- sion Diagnostics”. PhD thesis. von Karman Institute, 2010 (cit. on p. 13).

[22]A. Cipullo, B. Helber, F. Panerai, L. Zeni, and O. Chazot. “Investigation of Freestream Plasma Flow Produced by Inductively Coupled Plasma Wind Tunnel”. In: *Journal of Thermophysics and Heat Transfer* 28 (2014), pp. 381–393 (cit. on p. 13).

[23]B. Cockburn and J. Gopalakrishnan. “A Characterization of Hybridized Mixed Methods for Second Order Elliptic Problems”. In: *SIAM Journal on Numerical Analysis* 42.1 (2005), pp. 283–301 (cit. on p. 17).

[24]B. Cockburn and C.W. Shu. “The Runge–Kutta Discontinuous Galerkin Method for Conservation Laws V: Multidimensional Systems”. In: *Journal of Computational Physics* 141.2 (1998), pp. 199–224 (cit. on p. 16).

[25]N. Corthouts, K. Hillewaert, T. Magin, and G. May. “A Monolithic Multi-domain Hybridized Discontinuous Galerkin Solver for Inductively Coupled Plasma Flow”. In: *Journal of Computational Physics* (2025). Accepted for publication (cit. on pp. 49, 68).

[26]S. Demange. “Absolute instabilities in heated jets”. PhD thesis. Université Libre de Bruxelles, 2021 (cit. on p. 15).

[27]S. Demange, O. Chazot, and F. Pinna. “Local analysis of absolute instability in plasma jets”. In: *Journal of Fluid Mechanics* 903 (2020) (cit. on p. 13).

[28]S. Demange, F. Pina, U. Ali Qadri, and M. Juniper. “High Fidelity Model for Self-sustained Oscillations in Heated Jets”. In: *AIAA AVIATION 2020 Forum*. AIAA (cit. on p. 13).

[29]S. Demange and F. Pinna. “On the role of thermo-transport properties in the convective/absolute transition of heated round jets”. In: *Physics of Fluids* 12 (2020) (cit. on p. 13).

[30]G. Dimarco and L. Pareschi. “Numerical methods for kinetic equations”. In: *Acta Numerica* 23 (2014), pp. 369–520 (cit. on p. 20).

[31]M. Dropmann, G. Herdrich, R. Laufer, et al. “A New Inductively Driven Plasma Generator (IPG6)—Setup and Initial Experiments”. In: *IEEE Transactions on Plasma Science* 41 (2013), pp. 804–810 (cit. on p. 11).

[32]M. Dubiner. “Spectral methods on triangles and other domains.” In: *Journal of Scinetific Computing* 6.4 (1991), pp. 345–390 (cit. on p. 54).

[33]J. Elrassi, S. Holum, L. Sombaert, et al. “Upgraded VKI Plasmatron Capabilities with Supersonic Nozzles for Extended Material Characterization Methods”. In: *Sampe Journal* 60 (2024) (cit. on p. 14).

[34]Y. Epshteyn and B. Rivière. “Estimation of penalty parameters for symmetric interior penalty Galerkin methods”. In: *Journal of Computational and Applied Mathematics* 206.2 (2007), pp. 843–872 (cit. on p. 59).

[35]A. Fagnani. “Development of Measurement Techniques and Study of the Aerothermal Response of Space Debris Materials to Atmospheric Entry Plasmas”. PhD thesis. von Karman Institute for Fluid Dynamics, October 2023, p. 141 (cit. on p. 47).

[36]A. Fagnani, B. Dias, P. Schrooyen, et al. “Investigation of Quartz Ablation in the VKI Plasmatron Facility: Comparison Between Experimental and Numerical Results”. In: *AIAA AVIATION 2021 FORUM* (cit. on p. 12).

[37]A. Fagnani, D. Le Quang Huy, B. Helber, et al. “Investigation of a Free-Stream Air Plasma Flow by Optical Emission Spectroscopy and Comparison to Magnetohydrodynamics Simulations”. In: *AIAA Scitech 2020 Forum* (cit. on p. 13).

[38]P. Fernandez, N.C. Nguyen, and J. Peraire. “The hybridized Discontinuous Galerkin method for Implicit Large-Eddy Simulation of transitional turbulent flows”. In: *Journal of Computational Physics* 336 (2017), pp. 308–329 (cit. on p. 17).

[39]D. Fries, S. Stark, J. Murray, et al. “Nitrogen thermometry in an inductively coupled plasma torch using broadband nanosecond coherent anti-Stokes Raman scattering”. In: *Applied Optics* 62 (Oct. 2023) (cit. on p. 11).

[40]Ana Gaillat, Ramon M. Barnes, Pierre Proulx, and Maher I. Boulos. “Computer modeling of enclosed inductively coupled plasma discharges”. In: *Spectrochimica Acta Part B: Atomic Spectroscopy* 50.10 (1995), pp. 1187–1205 (cit. on pp. 15, 34).

[41]I. M. Gamba, J. R. Haack, Cory D. Hauck, and J. Hu. “A Fast Spectral Method for the Boltzmann Collision Operator with General Collision Kernels”. In: *SIAM Journal on Scientific Computing* 39.4 (2017), B658–B674 (cit. on p. 20).

[42]I. M. Gamba and S. H. Tharkabhushanam. “Spectral-Lagrangian methods for collisional models of non-equilibrium statistical states”. In: *Journal of Computational Physics* 228.6 (2009), pp. 2012–2036 (cit. on p. 20).

[43]G. Gangemi, A. Laguna, M. Massot, K. Hillewaert, and T. E. Magin. “Bridging multifluid and drift-diffusion models for bounded plasmas”. In: *Physics of Plasmas* 32 (Feb. 2025) (cit. on p. 12).

[44]E.B. Georg and M. I. Yakushin. “Desintegrating in High-Enthalpy Air Stream”. In: *Inzhenemo Fizicheskii Zhumal* 32.4 (1977), pp. 581–587 (cit. on p. 11).

[45]M. Giles. “Stability Analysis of Numerical Interface Conditions in Fluid-Structure Thermal Analysis”. In: *International Journal for Numerical Methods in Fluids* 25 (2000) (cit. on p. 16).

[46]V. Giovangigli. *Multicomponent Flow Modeling*. 1999 (cit. on pp. 22, 24).

[47]V. Giovangigli, B. Graille, T. Magin, and M. Massot. “Multicomponent transport in weakly ionized mixtures”. In: *Plasma Sources Science and Technology* 19.3 (2010) (cit. on p. 27).

[48]H. Goedbloed, R. Keppens, and S. Poedts. *Magnetohydrodynamics: Of laboratory and astrophysical plasmas*. 2019, pp. 1–974 (cit. on p. 1).

[49]A.N. Gordeev, A. F. Kolesnikov, and M.I. Yakushin. “An Induction Plasma Application to Buran’s Heat Protection Tiles Ground Tests.” In: *SAMPE journal* 28.3 (1992), pp. 29–33 (cit. on p. 11).

[50]B. Graille, T. Magin, and M. Massot. “Kinetic theory of plasmas: translational energy”. In: *Mathematical Models and Methods in Applied Sciences* 19.4 (2009), 527–599 (cit. on p. 22).

[51]R. Hartmann and P. Houston. “Symmetric Interior Penalty DG Methods for the Compressible Navier–Stokes Equations I: Method Formulation”. In: *International Journal of Numerical Analysis and Modeling* 3 (Jan. 2006), pp. 1–20 (cit. on p. 59).

[52]B. Helber, C. Asma, Y. Babou, et al. “Material response characterization of a low-density carbon composite ablator in high-enthalpy plasma flows”. In: *Journal of Materials Science* 49 (2014) (cit. on p. 12).

[53]B. Helber, O. Chazot, A. Hubin, and T. Magin. “Emission Spectroscopic Boundary Layer Investigation during Ablative Material Testing in Plasmatron”. In: *Journal of Visualized Experiments* 112 (2016) (cit. on p. 12).

[54]B. Helber, B. Dias, F. Bariselli, et al. “Analysis of Meteoroid Ablation Based on Plasma Wind-tunnel Experiments, Surface Characterization, and Numerical Simulations”. In: *The Astrophysical Journal* 876.2 (2019), p. 120 (cit. on p. 12).

[55]K. Hillewaert. “Development of the Disconstinuous Galerkin Method for High-Resolution, Large Scale CFD and Acoustics in Industrial Geometries”. PhD thesis. 2013 (cit. on pp. 16, 59).

[56]S. Jaiswal, A. A. Alexeenko, and J. Hu. “A discontinuous Galerkin fast spectral method for the full Boltzmann equation with general collision kernels”. In: *Journal of Computational Physics* 378 (2019), pp. 178–208 (cit. on p. 20).

[57]T. Jang, Y. K. Seo, S. H. Sohn, and J. W. Jung. “Calculation of the off-axes magnetic field for finite-length solenoids”. In: *New Physics: Sae Mulli* 70.8 (2020), pp. 667–674 (cit. on pp. 35, 41).

[58]M. Kapper and J. L. Cambier. “Ionizing Shocks in Argon. Part 1: Collisional-Radiative Model and Steady-State Structure”. In: *Journal of Applied Physics* 109 (2011) (cit. on p. 21).

[59]M. Kapper and J. L. Cambier. “Ionizing shocks in argon. Part II: Transient and multi-dimensional effects”. In: *Journal of Applied Physics* 109 (2011) (cit. on p. 21).

[60]S. Karl, D. Fletcher, G. Degrez, T. Magin, and M. Playe. “Assessment of Radiative Transport in an Argon Plasma Flow”. In: *4th European Symposium Aerothermodynamics for Space Applications*. 2001 (cit. on p. 35).

[61]Z. Kolacinski. “Plasma contamination with electrode metal vapor jets”. In: *Plasma Chemistry and Plasma Processing* 6 (1986) (cit. on p. 9).

[62]A. F. Kolesnikov. “Conditions of simulation of stagnation point heat transfer from a high-enthalpy flow”. In: *Fluid Dynamics* 28 (1993) (cit. on p. 8).

[63]A. F. Kolesnikov. *The equations of motion of a multicomponent partially ionized two-temperature mixture of gases in an electromagnetic field with transport coefficients in higher approximations.* Tech. rep. In Russian. Institute of Mechanics, Moscow State University, 1974 (cit. on p. 21).

[64]C. H. Kruger and M. Mitchner. "Kinetic theory of two-temperature plasmas". In: *Physics of Fluids* 10.9 (1967), pp. 1953–1961 (cit. on p. 21).

[65]S. Kumar, A. Munafò, K. Stephani, D. Bodony, and M. Panesi. "Modeling three-dimensional magneto-hydrodynamic phenomena in inductively coupled plasma discharges". In: *AIAA SciTech forum*. 2024 (cit. on pp. 15, 35).

[66]V. Kumar and B. Kandasubramanian. "Advances in Ablative Composites of Carbon Based Materials: A Review". In: *Industrial & Engineering Chemistry Research* (2019) (cit. on pp. 7, 10).

[67]A. Lani, N. Villedieu, K. Bensassi, et al. "COOLFluiD: An open computational platform for multi-physics simulation and research". In: *21st AIAA Computational Fluid Dynamics Conference* (2013) (cit. on pp. 15, 79).

[68]Andrea Lani, Tiago Quintino, Dries Kimpe, et al. "Reusable Object-Oriented Solutions for Numerical Simulation of PDEs in a High Performance Environment". In: *Scientific Programming* 14.2 (2006) (cit. on p. 15).

[69]H. Le, A. Karagozian, and J. L. Cambier. "Complexity reduction of collisional-radiative kinetics for atomic plasma". In: *Physics of Plasmas* 20 (Nov. 2013) (cit. on p. 21).

[70]J. H. Lee. "Basic governing equations for the flight regimes of aeroassisted orbital transfer vehicles". In: *AIAA 19th Thermophysics Conference*. 1984 (cit. on p. 21).

[71]M. S. Liou. "A sequel to AUSM, Part II: AUSM+-up for all speeds". In: *Journal of Computational Physics* 214.1 (2006), pp. 137–170 (cit. on p. 58).

[72]M. S. Liou. "Search for a Near-Perfect Numerical Flux Scheme, Part I: AUSM+". In: *Nasa-Tm-106524* (1994) (cit. on p. 58).

[73]M. S. Liou and C. Steffen. "A New Flux Splitting Scheme". In: *Journal of Computational Physics* 23 (1993) (cit. on p. 58).

[74]D. Luís, V. Giangaspero, A. Viladegut, et al. "Effect of electron number densities on the radio signal propagation in an inductively coupled plasma facility". In: *Acta Astronautica* 212 (2023), pp. 408–423 (cit. on p. 12).

[75]T. Magin. "A Model for Inductive Plasma Wind Tunnels". PhD thesis. von Karman Institute for Fluid Dynamics, 2004, p. 141 (cit. on pp. 15, 34, 47, 58).

[76]T. Magin, L. Caillaut, A. Bourdon, and C. O. Laux. “Nonequilibrium radiative heat flux modeling for the Huygens entry probe”. In: *Journal of Geophysical Research* 111.E7 (2006) (cit. on p. 21).

[77]T. Magin and G. Degrez. “Transport algorithms for partially ionized and unmagnetized plasmas”. In: *Journal of Computational Physics* 198.2 (2004) (cit. on p. 22).

[78]T. Magin and G. Degrez. “Transport properties of partially ionized and unmagnetized plasmas”. In: *Physical Review E* 70.4 (2004) (cit. on p. 22).

[79]T. Magin, M. Panesi, A. Bourdon, R. L. Jaffe, and D. W. Schwenke. “Coarse-grain model for internal energy excitation and dissociation of molecular nitrogen”. In: *Chemical Physics* 398 (2012). Chemical Physics of Low-Temperature Plasmas (in honour of Prof Mario Capitelli), pp. 90–95 (cit. on p. 21).

[80]Axel Modave and Théophile Chaumont-Frelet. “A hybridizable discontinuous Galerkin method with characteristic variables for Helmholtz problems”. In: *Journal of Computational Physics* 493 (2023) (cit. on p. 17).

[81]J. Mostaghimi and M. I. Boulos. “Effect of frequency on local thermodynamic equilibrium conditions in an inductively coupled argon plasma at atmospheric pressure”. In: *Journal of Applied Physics* 68.6 (1990), pp. 2643–2648 (cit. on pp. 21, 34).

[82]J. Mostaghimi, P. Proulx, and M. I. Boulos. “A two-temperature model of the inductively coupled rf plasma”. In: *Journal of Applied Physics* 61.5 (1987), pp. 1753–1760 (cit. on pp. 21, 34, 36).

[83]A. Munafò, M. Panesi, and T. E. Magin. “Boltzmann rovibrational collisional coarse-grained model for internal energy excitation and dissociation in hypersonic flows”. In: *Phys. Rev. E* 89 (2 2014) (cit. on p. 21).

[84]A. Munafò, J. R. Haack, I. M. Gamba, and T. E. Magin. “A spectral-Lagrangian Boltzmann solver for a multi-energy level gas”. In: *Journal of Computational Physics* 264 (2014), pp. 152–176 (cit. on p. 20).

[85]A. Munafò, S. Kumar, and M. Panesi. “Self-consistent Modeling of Inductively Coupled Plasma Discharges”. In: Feb. 2024 (cit. on p. 16).

[86]A. Munafò and T. E. Magin. “Modeling of stagnation-line nonequilibrium flows by means of quantum based collisional models”. In: *Physics of Fluids* 26.9 (2014) (cit. on p. 21).

[87]E. Nagnibeda and E. Kustova. *Non-equilibrium reacting gas flows. Kinetic theory of transport and relaxation processes. Translated from the Russian*. Springer Berlin, Heidelberg, 2009 (cit. on p. 22).

[88]N. C. Nguyen, J. Peraire, and B. Cockburn. “An implicit high-order hybridizable discontinuous Galerkin method for linear convection-diffusion equations”. In: *Journal of Computational Physics* 228.9 (2009), pp. 3232–3254 (cit. on pp. 17, 49).

[89]N.C. Nguyen, J. Peraire, and B. Cockburn. “An implicit high-order hybridizable discontinuous Galerkin method for nonlinear convection–diffusion equations”. In: *Journal of Computational Physics* 228.23 (2009), pp. 8841–8855 (cit. on p. 17).

[90]N.C. Nguyen, J. Peraire, and B. Cockburn. “Hybridizable Discontinuous Galerkin Methods”. In: *Spectral and High Order Methods for Partial Differential Equations*. Ed. by J.S. Hestaven and Ronquist E.M. Lecture No. Springer, 2011, pp. 63–84 (cit. on pp. 17, 49).

[91]W. Owens, D. Merkel, F. Sansoz, and D. Fletcher. “Fracture Behavior of Woven Silicon Carbide Fibers Exposed to High-Temperature Nitrogen and Oxygen Plasmas”. In: *Journal of the American Ceramic Society* 98.12 (2015), pp. 4003–4009 (cit. on p. 11).

[92]W. P. Owens, J. Uhl, M. Dougherty, et al. “Development of a 30 kW inductively coupled plasma torch facility for aerospace material testing”. In: *AIAA Thermophysics Conference*. 2010 (cit. on p. 11).

[93]F. Panerai, B. Helber, I. Sakraker, et al. “Characterization of the IXV Thermal Protection System in High Enthalphy Plasma Flow”. In: *7th European Symposium on Aerothermodynamics*. 2011 (cit. on p. 12).

[94]M. Panesi, R. Jaffe, D. Schwenke, and T. Magin. “Rovibrational internal energy transfer and dissociation of N2($1\Sigma g+$)-N(4Su) system in hypersonic flows”. In: *The Journal of Chemical Physics* 138 (2013) (cit. on p. 21).

[95]C. Park. “Assessment of two-temperature kinetic model for ionizing air”. In: *Journal of Thermophysics and Heat Transfer* 3.3 (1989), pp. 233–244 (cit. on p. 21).

[96]F. Pinna. “VESTA toolkit: a Software to Compute Transition and Stability of Boundary Layers”. In: June 2013 (cit. on p. 15).

[97]W.H. Reed and T.R. Hill. *Triangular mesh methods for the neutron transport equation*. Tech. rep. Los Alamos Scientific Laboratory, 1973 (cit. on p. 16).

[98]P. Rini, D. Vanden Abeele, and G. Degrez. “Elemental demixing in inductively coupled air plasmas at high pressures”. In: *37th AIAA Thermophysics Conference* 20.1 (2004) (cit. on pp. 16, 20, 21, 35).

[99]Megh Nad Saha. *LIII. Ionization in the solar chromosphere*. Oct. 1920 (cit. on p. 1).

[100]E. Sartori. *Numerical Simulation of Chemical Reactive Flows in Inductively Coupled Plamsa Windtunnels*. Tech. rep. 2010 (cit. on p. 66).

[101]P. Schrooyen, K. Hillewaert, T. Magin, and P. Chatelain. “Fully implicit Discontinuous Galerkin solver to study surface and volume ablation competition in atmospheric entry flows”. In: *International Journal of Heat and Mass Transfer* 103 (Dec. 2016), pp. 108–124 (cit. on pp. 16, 17).

[102]J. B. Scoggins. “Development of numerical methods and study of coupled flow, radiation, and ablation phenomena for atmospheric entry”. PhD thesis. von Karman Institute for Fluid Dynamics, 2017 (cit. on p. 27).

[103]J. B. Scoggins, V. Leroy, G. Bellas-Chatzigeorgis, B. Dias, and T. Magin. “Mutation++: MUlticomponent Thermodynamic And Transport properties for IONized gases in C++”. In: *SoftwareX* 12 (2020). arXiv: 2002.01783 (cit. on pp. 28, 36, 37).

[104]H. Shiki, J. Motoki, H. Takikawa, et al. “Electrode Erosion in Pulsed Arc for Generating Air Meso-Plasma Jet under Atmospheric Pressure”. In: *Ieej Transactions on Fundamentals and Materials* 127 (Oct. 2007), pp. 567–573 (cit. on p. 9).

[105]S.T. Surzhikov. *Radiation modeling and spectral data*. Tech. rep. von Karman Institute for Fluid Dynamics, 2002 (cit. on p. 35).

[106]D. Vanden Abeele and G. Degrez. “Efficient computational model for inductive plasma flows”. In: *AIAA journal* 38.2 (2000), pp. 234–242 (cit. on pp. 15, 34, 64).

[107]D. Vanden Abeele, S. A. Vasil’evskii, A. Kolesnikov, G. Degrez, and B. Bottin. *Code-To-Code Validation of Inductive Plasma Computations*. Tech. rep. St. Genesius-Rode, Belgium: von Karman Institute for Fluid Dynamics, 1999, pp. 245–250 (cit. on pp. 47, 64).

[108]S. Venkateswaran and L. Merkle. “Analysis of preconditioning methods for the Euler and Navier-Stokes equations”. In: *30th CFD Lecture Series*. 1999 (cit. on p. 58).

[109]T. Verstraete and S. Scholl. “Stability analysis of partitioned methods for predicting conjugate heat transfer”. In: *International Journal of Heat AND Mass Transfer* 101 (2016), pp. 852–869 (cit. on p. 16).

[110]A. Viladegut, F. Panerai, O. Chazot, et al. “Design, integration and preliminary results of the IXV Catalysis experiment”. In: *CEAS Space Journal* 9 (2016) (cit. on p. 12).

[111]H. Y. Wachman, M. J. Unvesky, and J. H. McGinn. “The effects of electrode contamination on the properties of air-arc plasmas”. In: *Planetary and Space Science* 4 (1961), pp. 374–381 (cit. on p. 9).

[112]M. Woopen, A. Balan, and G. May. “A unifying computational framework for adaptive high-order finite element methods”. In: *22nd AIAA Computational Fluid Dynamics Conference*. 2015 (cit. on pp. 17, 49).

[113]M. Woopen, A. Balan, G. May, and J. Schuetz. “A Comparison of Hybridized and Standard DG Methods for Target-Based hp-Adaptive Simulation of Compressible Flow”. In: *Computers and Fluids* 98 (2014), pp. 3–16 (cit. on p. 17).

[114]M. Woopen, G. May, and J. Schütz. “Adjoint-based error estimation and mesh adaptation for hybridized discontinuous Galerkin methods”. In: *International Journal for Numerical Methods in Fluids* 76.September (2014), pp. 811–834 (cit. on p. 49).

[115]C. Zhang and I. M. Gamba. “A Conservative Discontinuous Galerkin Solver for the Space Homogeneous Boltzmann Equation for Binary Interactions”. In: *SIAM Journal on Numerical Analysis* 56.5 (2018), pp. 3040–3070 (cit. on p. 20).

[116]W. Zhang, A. Lani, and M. Panesi. “Analysis of non-equilibrium phenomena in inductively coupled plasma generators”. In: *Physics of Plasmas* 23.7 (2016) (cit. on pp. 34, 36).

List of Figures

List of Tables

A

Mesh and order dependence study

We assess the mesh size and polynomial order dependence on a realistic case. The simulation parameters are the following:

- $P = 100\,\mathrm{kW}$ (power dissipated in the facility)
- $p_0 = 10\,000\,\mathrm{Pa}$ (background pressure)
- $f = 0.37\,\mathrm{MHz}$ (induction frequency)
- $Q = 16\,\mathrm{g\ s^{-1}}$ (mass flow rate)
- $S = 20°$ (swirl angle)
- air mixture with 11 species

Two ICP configurations are studied: one with a probe and another one in freestream conditions. In both cases, a coflow equal to the inlet velocity has been added in the chamber for stabilization. The probe is hemispherical with a $50\,\mathrm{mm}$ diameter. Three meshes were used for the grid independence study: a coarse, fine and refined meshes, with increasing number of elements. We first study the effect of the order of the method on each mesh separately. Based on the results, several orders are selected depending on the quality of the provided solution. Then, a mesh refinement study is performed using the selected orders.

This procedure is performed at three specific locations:

1. Along the radial direction in the torch center (TC in Fig. A.1), at $24.3\,\mathrm{cm}$ from the torch inlet. This is the region where the heating is the strongest and the electric field is the largest. We studied there the evolution of the gauge pressure Δp, velocity in three directions v_z, v_r and v_θ, the temperature T and the real E_p^{Re} and imaginary E_p^{Im} parts of the electric field.

2. Along the radial direction, at $83.6\,\mathrm{cm}$ from the torch inlet (PF in Fig. A.1). In the case of the probe, this correspond to $\Delta z = 35\,\mathrm{mm}$ from the probe front. We studied the evolution of Δp, v_z, v_r, v_θ and T. Since the electric field is negligible in this region, it has been overlooked.

149

3. For the probe case, we study the stagnation line (STAG in Fig. A.1), extending from $\Delta z = 35\,\mathrm{mm}$ from the probe end. For this location, we studied Δp, v_z, $\partial_r v_r$ and T. v_r and v_θ are null along the center line and thus disregarded. On the other hand, we study the radial gradient of the radial velocity component $\partial_r v_r$, since its inflection point plays plays a role in the study of boundary layers. We also study $\partial_z T$ since we are also interested in the heat flux at the probe level. It is important to note that in HDG, $\partial_r v_r$ and $\partial_z T$ are unknown of the discrete problem and can be retrieved directly from the solution of the HDG equations. This is not the case for classic DG or FV methods.

The geometry of the simulated ICP torch is given in Fig. A.1, with the locations where the mesh and grid dependence study is performed.

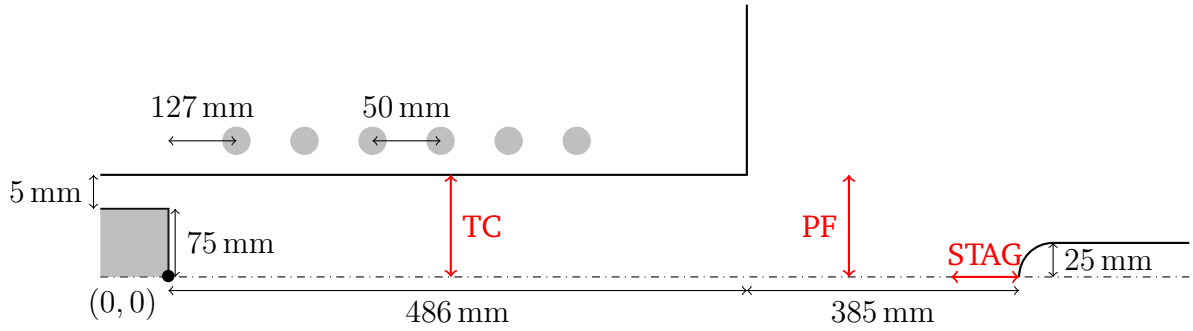

Fig. A.1.: Schematic representation of the axisymmetric Plasmatron ICP torch with a probe. The coils surrounding the facility are located at the center of the grey disks on the schematic. For the freestream case, the same schematic applies, but the probe is removed.

Profile	Start point ([m],[m])	End point ([m],[m])
Probe front	$(0.836, 0)$	$(0.836, 0.08)$
Stagnation Line	$(0.871, 0)$	$(0.836, 0)$
Torch Center	$(0.243, 0.)$	$(0.243, 0.08)$

Tab. A.1.: Start and end points of the profiles used for the mesh and order independence studies in the probe case. The point (0,0) is displayed in Fig. A.1. In the freestream case, since there is no probe, the stagnation line is not studied.

A.1 Probe configuration

The three meshes used for the probe mesh independence study are given in Fig. A.2, with the number of elements.

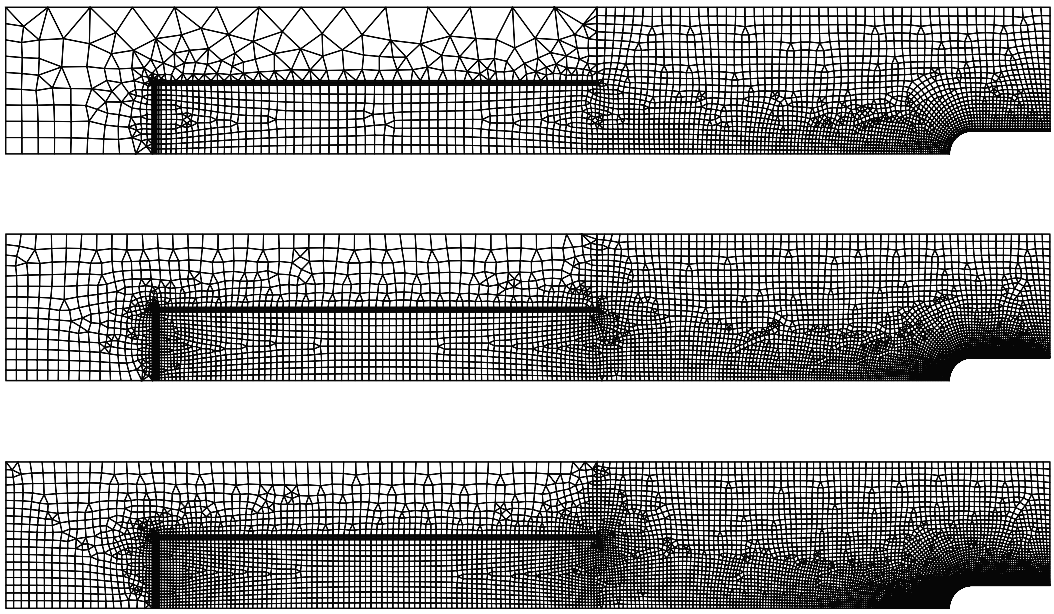

Fig. A.2.: Meshes used for the grid independence study with a probe. We call them coarse (top, 4013 elements), fine (middle, 7226 elements) and refined (bottom, 10316 elements).

Let us first discuss the solution dependence with respect to the order. First, in front of the probe (Fig. A.3 and Fig. A.4), there is a clear dependence on the order, no matter the mesh refinement. Above order 3, all variables are correctly captured. One can also see that, for the temperature field T, the profiles are well captured with a polynomial reconstruction of degree 1. Along the stagnation line (Fig. A.5 and Fig. A.6), most variables are correctly captured by polynomial reconstructions of degree 2. Once again, the temperature profile is correctly captured with degree 1. On the other hand, the radial gradient of the radial velocity $\partial_r v_r$ and axial velocity v_z are correctly captured from order 3. Finally, in the torch center (Fig. A.7 and Fig. A.8), a general remark is that a reconstruction of polynomial order 3 is necessary to capture the various profiles. No degree 1 solution is able to capture any of the fields, due to the large gradients occurring in the torch. However, degree 2 captures quite well the electric field profiles. In light of these observations, we choose polynomial reconstructions of degree 3 and 4 in order to capture correctly the variations. Finally, the mesh dependence study at $p = 4$ (Fig. A.9, A.10 and A.11) give the same result: the solution does not change with mesh refinement. Consequently, the coarsest mesh is used.

A.1.1 Dependence of the solution with respect to the order

In front of the probe

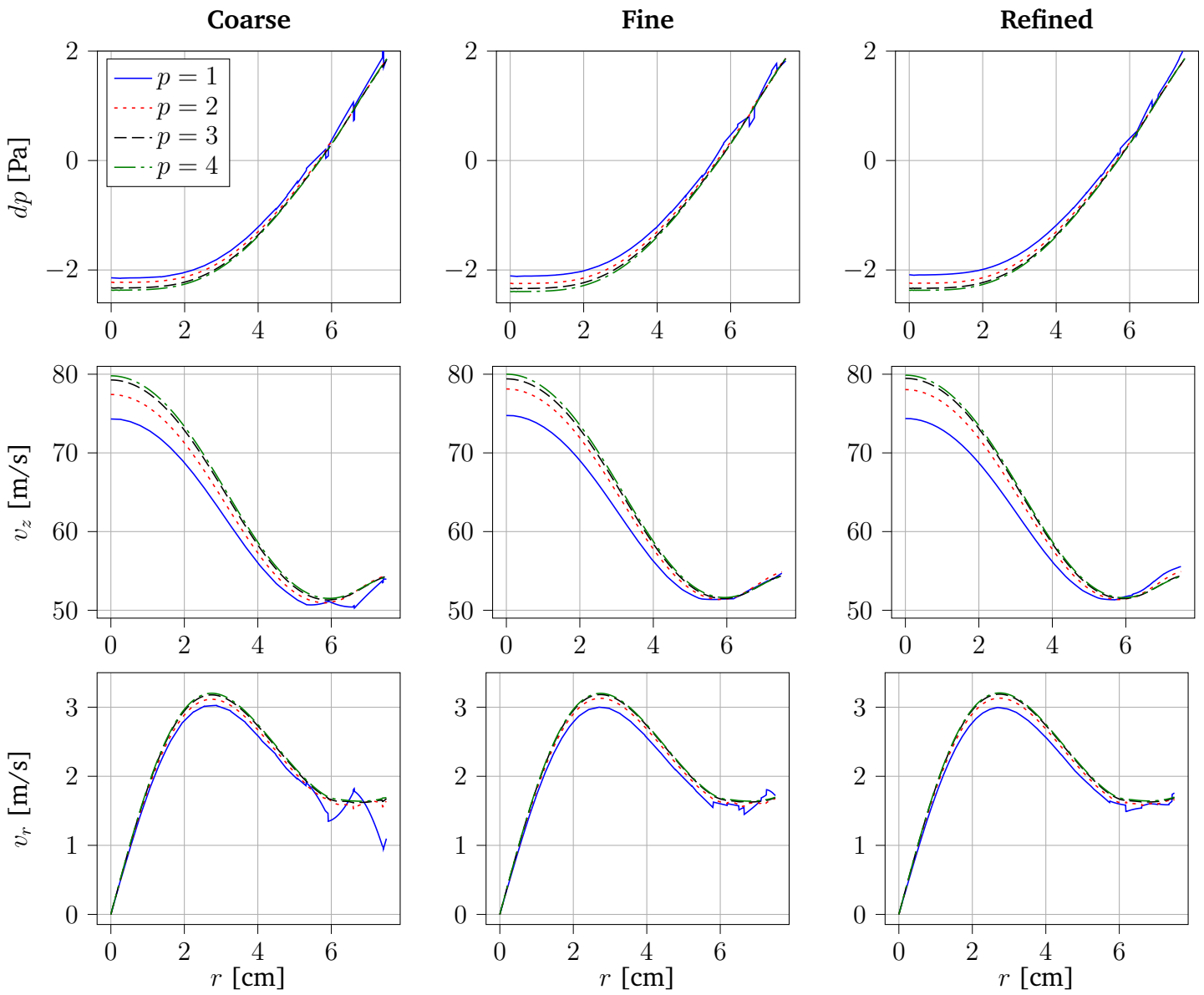

Fig. A.3.: Order independence study for the probe configuration on the coarse (left), fine (middle) and refined (right) meshes for the pressure fluctuation dp, axial v_z and radial v_r velocities at $\Delta z = 35\,\mathrm{mm}$ from the probe front. The polynomial degree of the method is p. r is the radial distance from the center line.

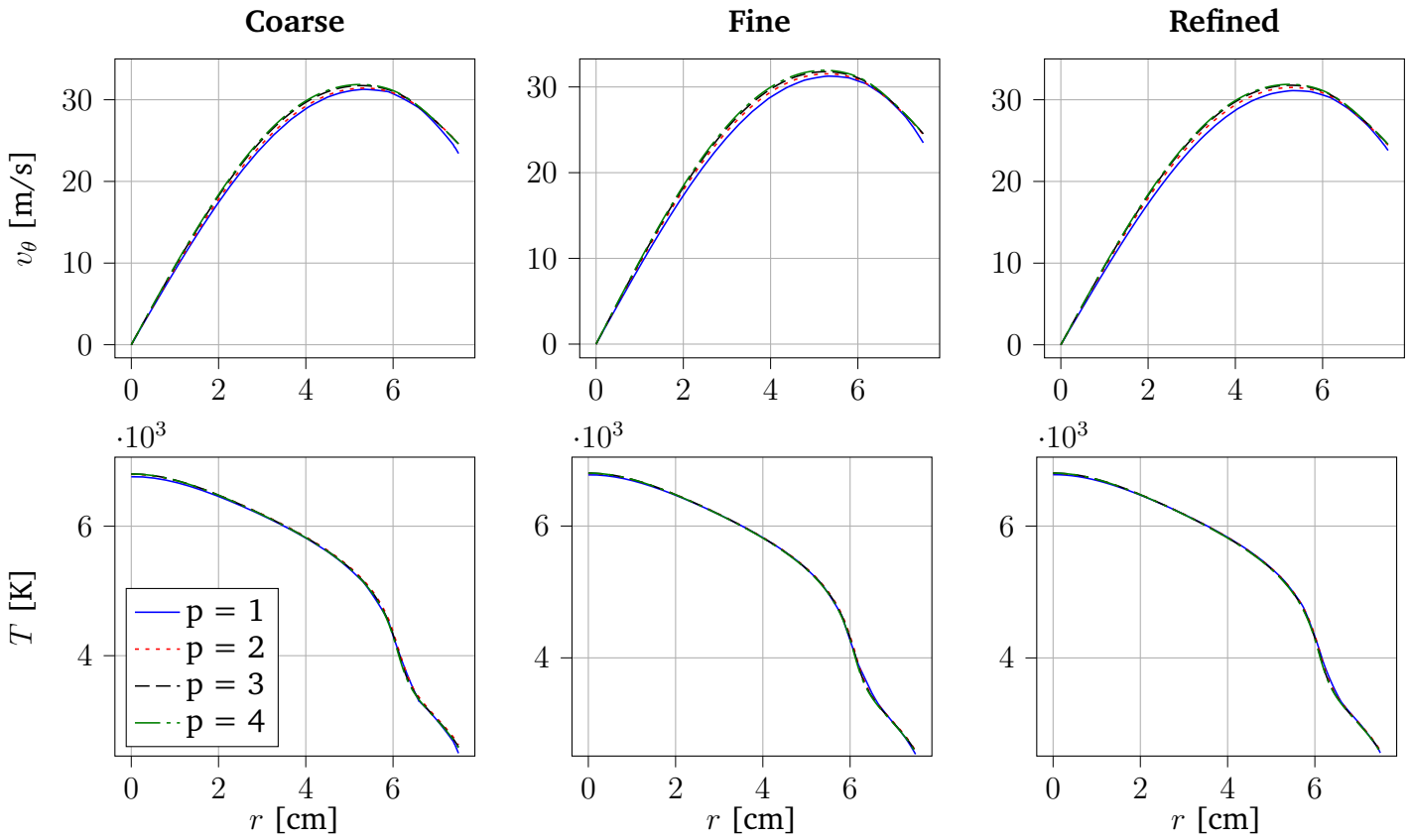

Fig. A.4.: Order independence study for the probe configuration on the coarse (left), fine (middle) and refined (right) meshes for the azimuthal velocity v_θ and temperature T at $\Delta z = 35\,\mathrm{mm}$ from the probe front. The polynomial degree of the method is p. r is the radial distance from the center line.

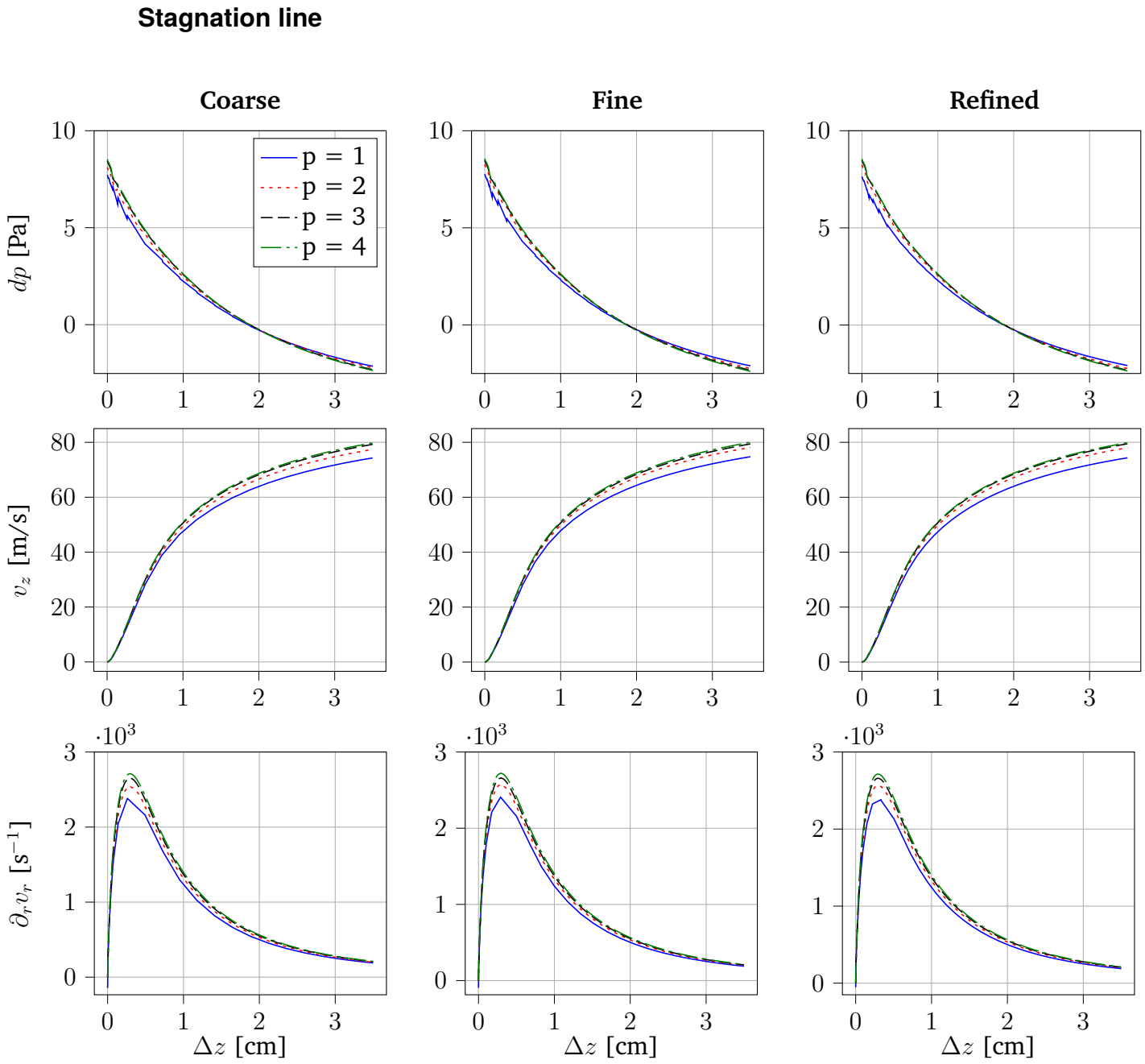

Fig. A.5.: Order independence study for the probe configuration on the coarse (left), fine (middle) and refined (right) meshes for the pressure fluctuation dp, axial v_z and radial gradient of the radial velocity $\partial_r v_r$ at $\Delta z = 35\,\mathrm{mm}$ from the probe front. The polynomial degree of the method is p. Δz is the axial distance from the probe front.

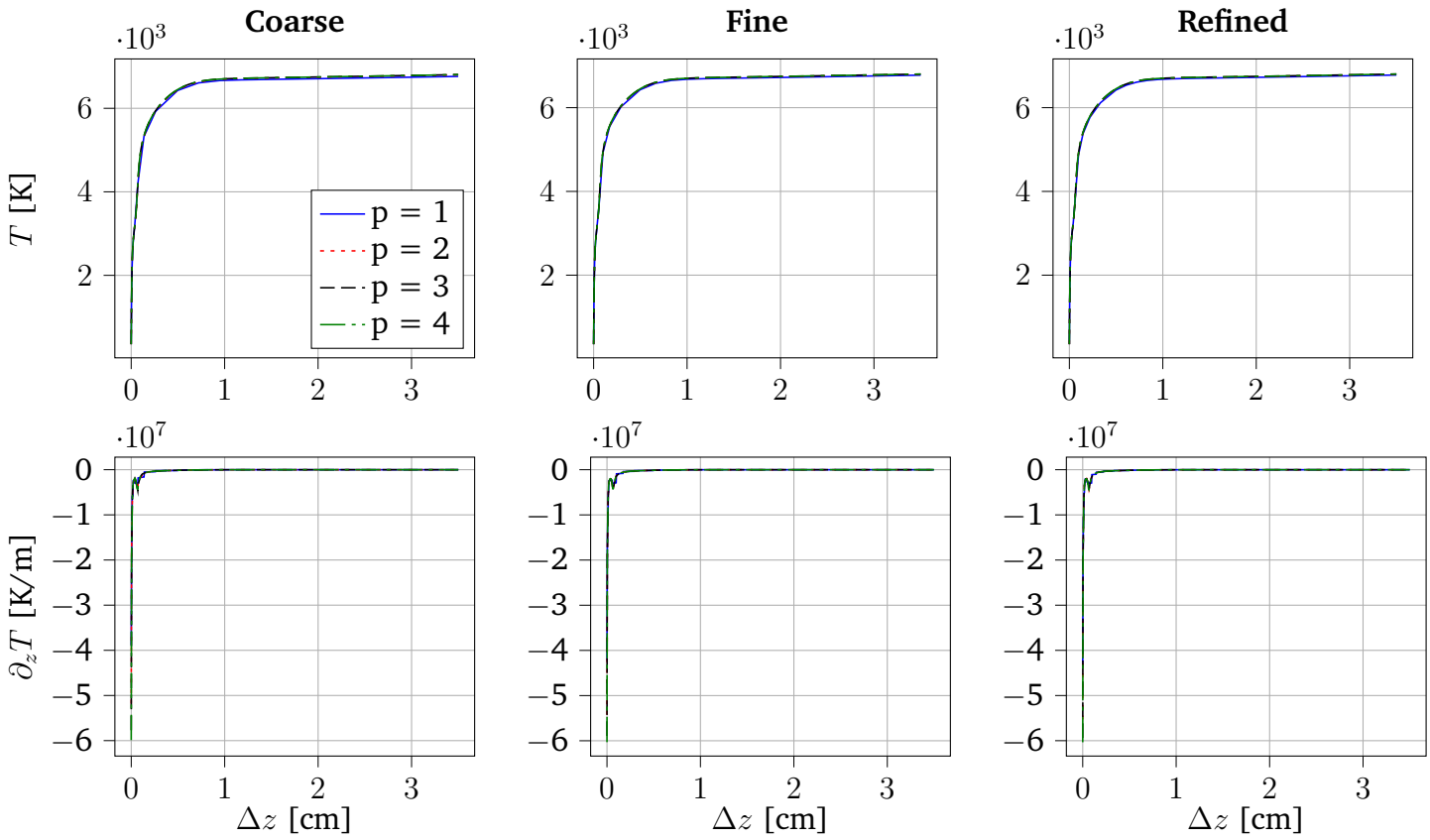

Fig. A.6.: Order independence study for the probe configuration on the coarse (left), fine (middle) and refined (right) meshes for the temperature T and axial temperature gradient $\partial_z T$ at $\Delta z = 35\,\mathrm{mm}$ from the probe front. The polynomial degree of the method is p. Δz is the axial distance from the probe front.

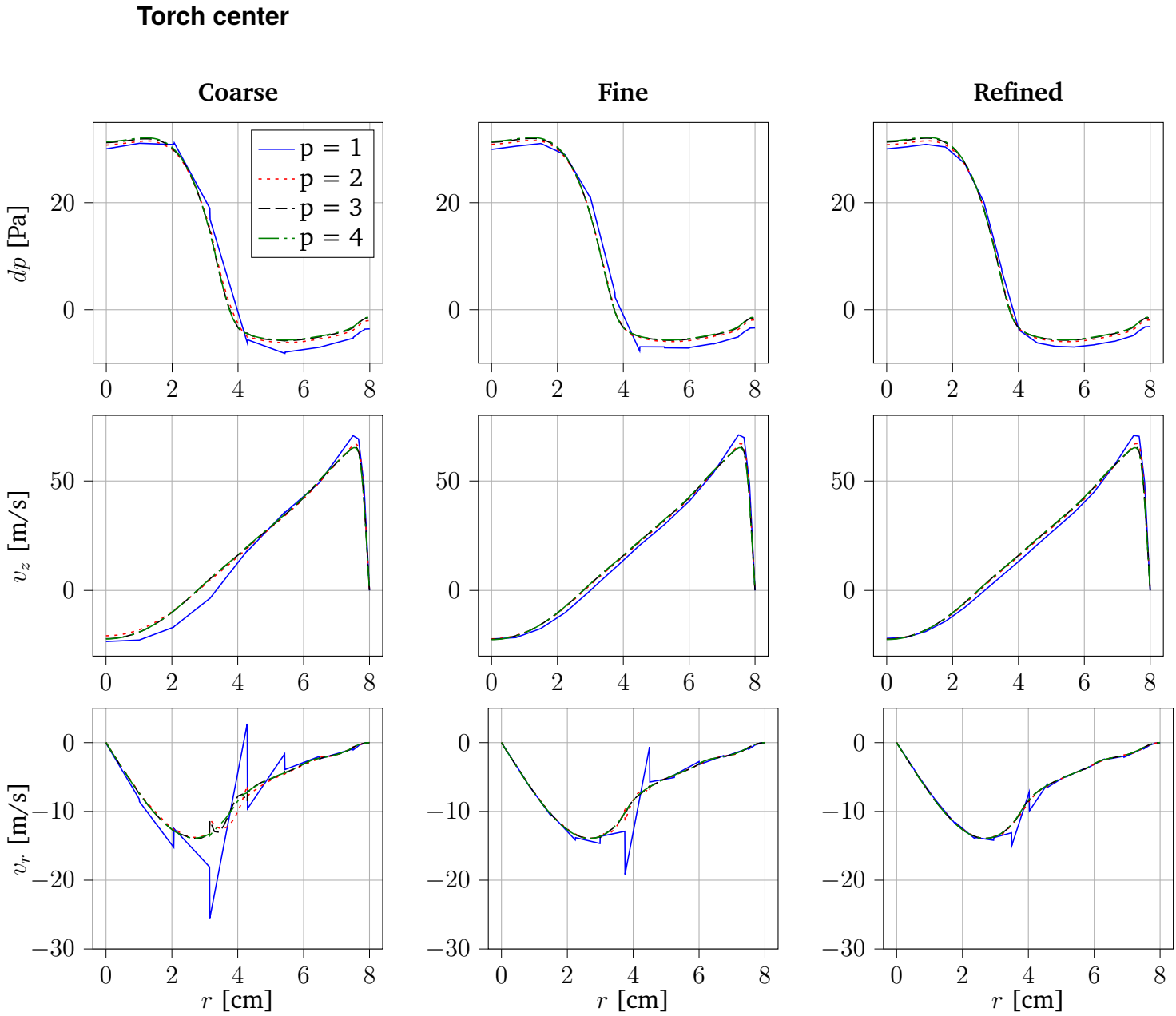

Fig. A.7.: Order independence study for the probe configuration on the coarse (left), fine (middle) and refined (right) meshes for the pressure fluctuation dp, axial v_z and radial v_r velocities in the torch center, at $24.3\,\mathrm{cm}$ from the torch inlet. The polynomial degree of the method is p. r is the radial distance from the center line.

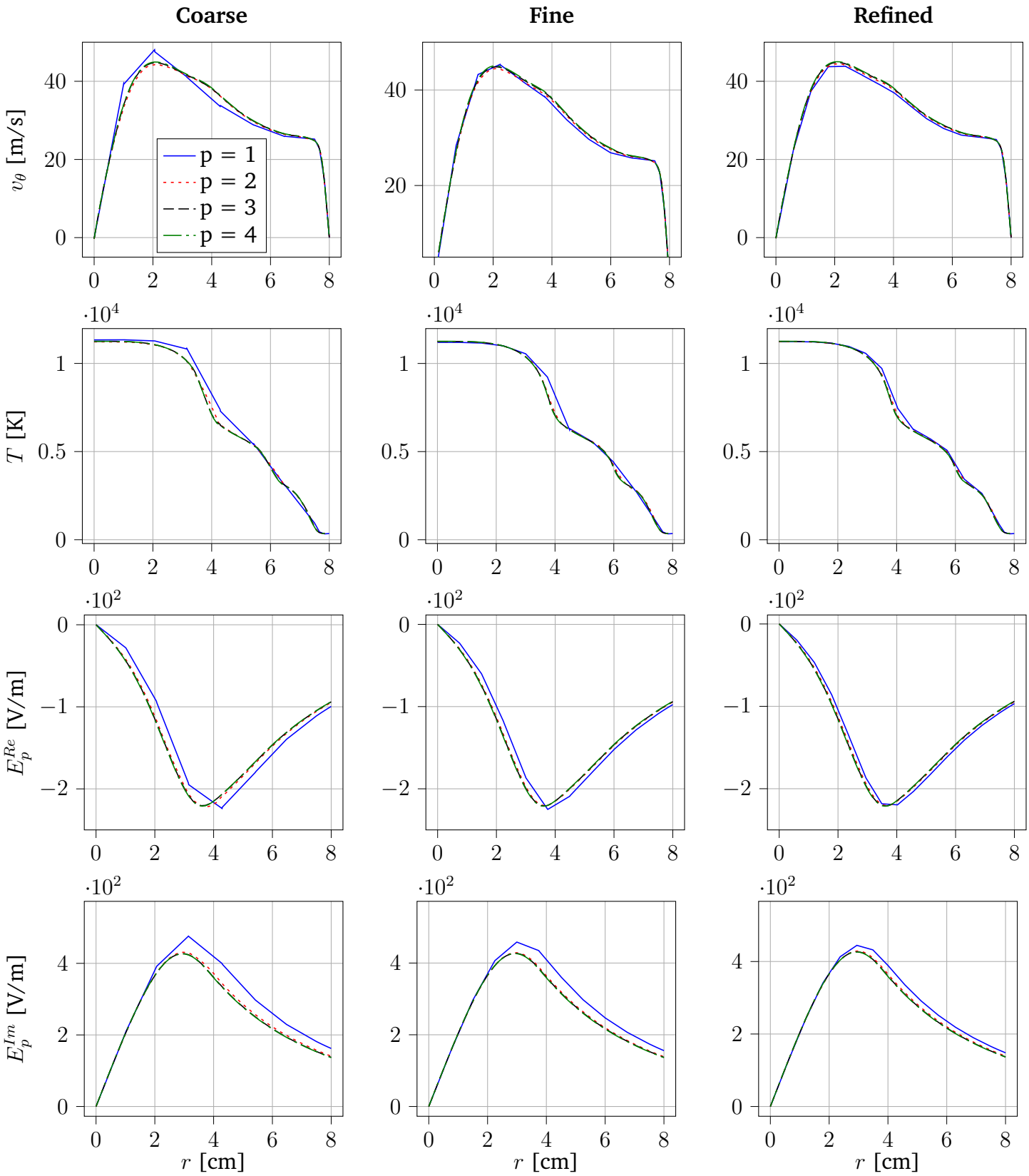

Fig. A.8.: Order independence study for the probe configuration on the coarse (left), fine (middle) and refined (right) meshes for the azimuthal velocity v_θ, temperature T and the real E_p^{Re} and imaginary E_p^{Im} parts of the plasma electric field in the torch center, at $24.3\,\mathrm{cm}$ from the torch inlet. The polynomial degree of the method is p. r is the radial distance from the center line.

A.1.2 Dependence of the solution on the mesh size

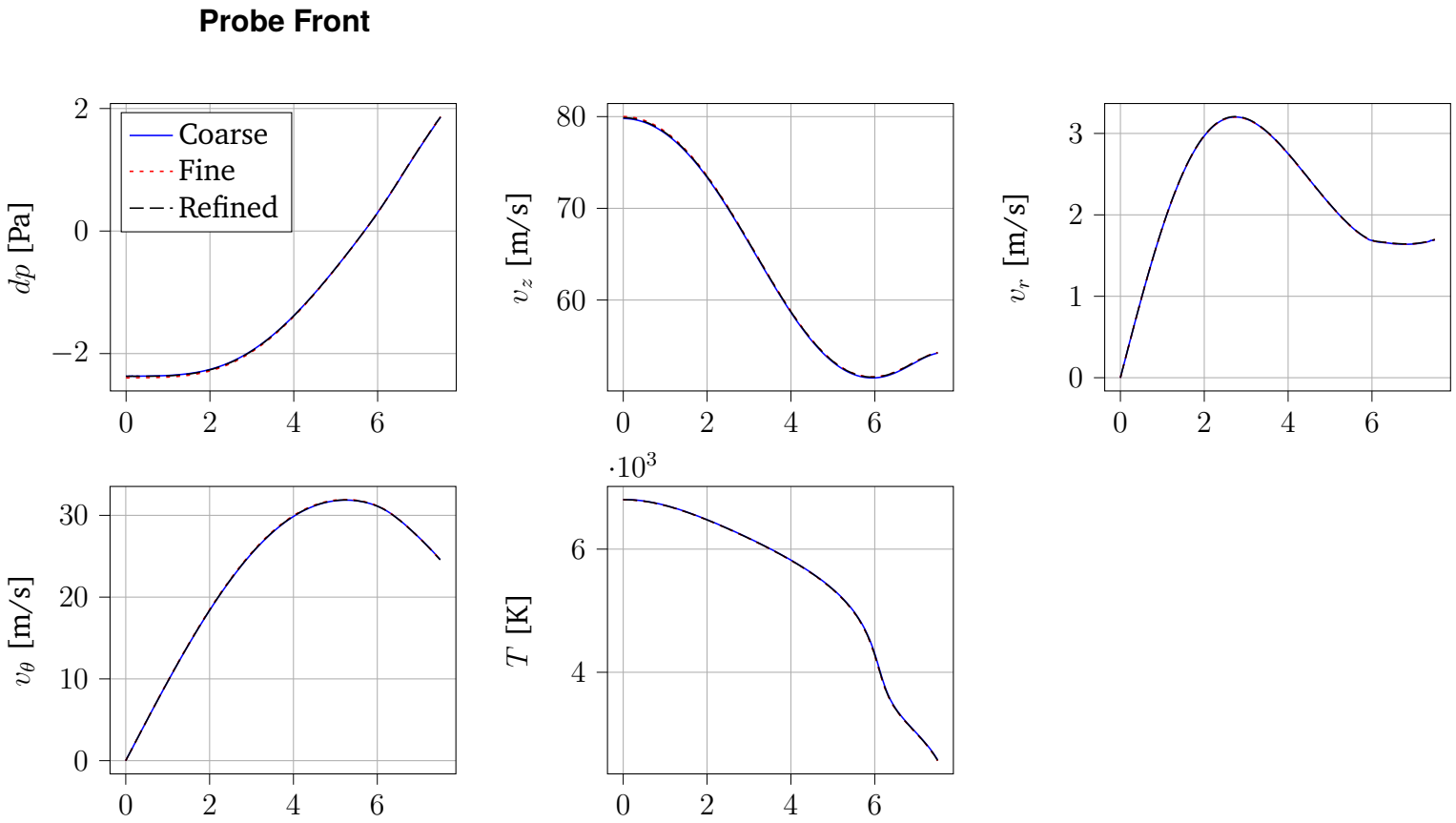

Fig. A.9.: Mesh independence study for the probe configuration on the coarse, fine and refined meshes for the pressure fluctuation dp, axial v_z, radial v_r and azimuthal v_θ velocities and temperature T at $\Delta z = 35\,\mathrm{mm}$ from the probe front. at order $p = 4$. The abscissa r ([cm]) is the radial distance from the center line.

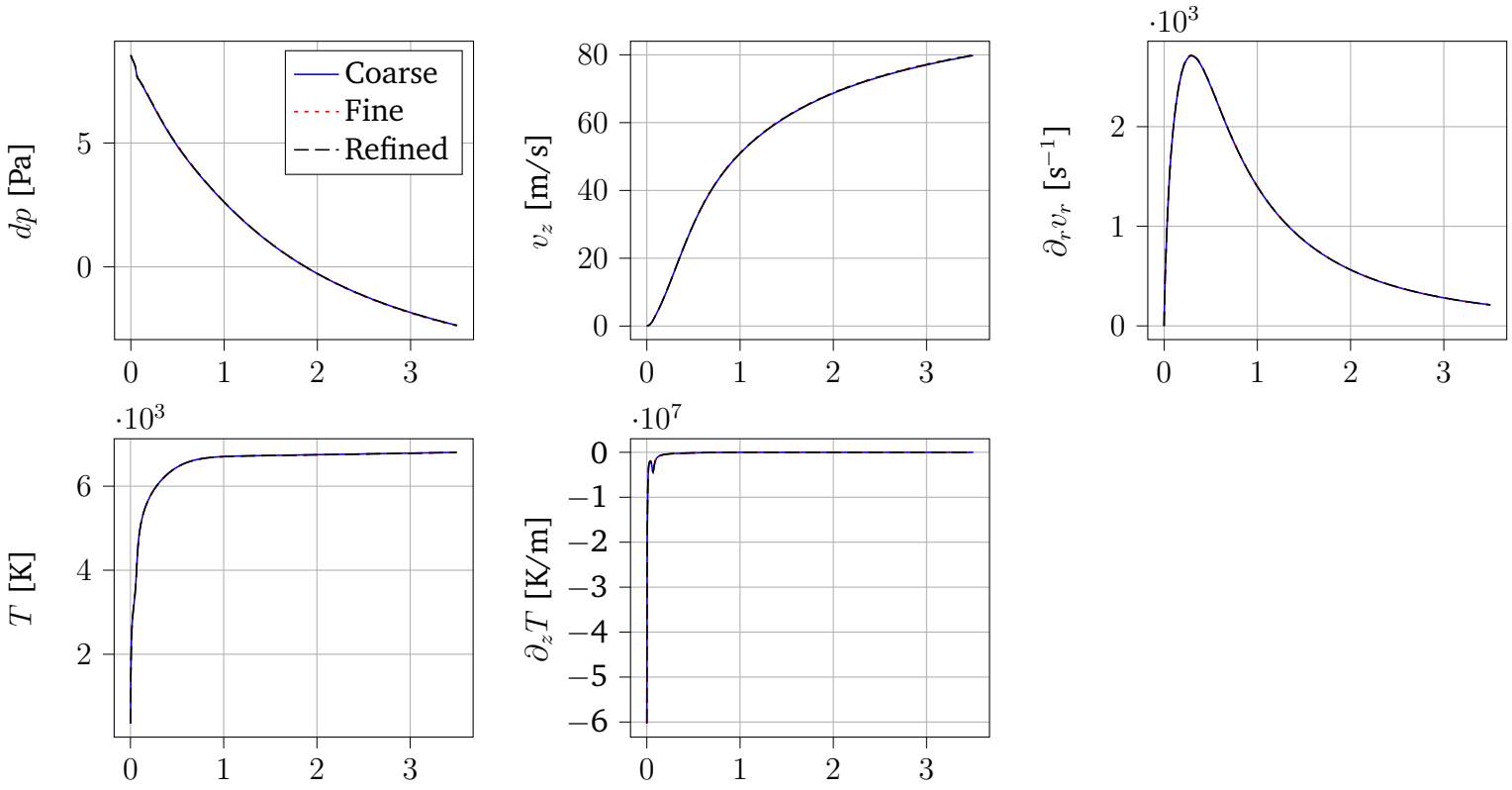

Fig. A.10.: Mesh independence study for the probe configuration on the coarse, fine and refined meshes for the pressure fluctuation dp, axial v_z and radial gradient of the radial velocity $\partial_r v_r$, temperature T and axial temperature gradient $\partial_z T$ at $\Delta z = 35\,\mathrm{mm}$ from the probe front at order $p = 4$. The abscissa Δz ([cm]) is the axial distance from the probe front.

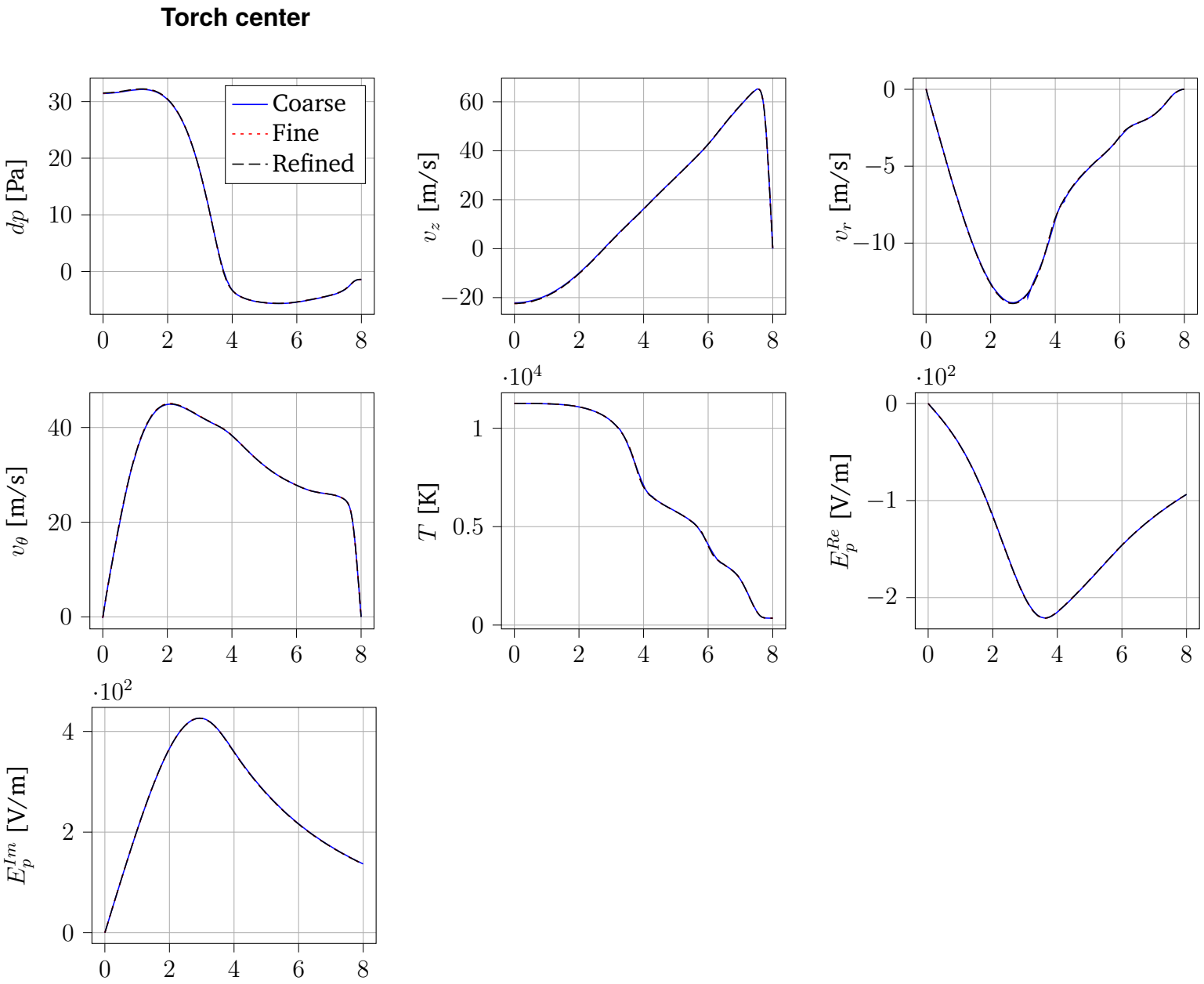

Fig. A.11.: Mesh independence study for the probe configuration on the coarse, fine and refined meshes for the pressure fluctuation dp, axial v_z, radial v_r velocities in the torch center and azimuthal velocity v_θ, temperature T and the real E_p^{Re} and imaginary E_p^{Im} parts of the plasma electric field at $24.3\,\mathrm{cm}$ from the torch inlet at order $p = 4$. The abscissa r ([cm]) is the radial distance from the center line.

A.2 Free stream configuration

The three meshes used for the free stream independence study are given in Fig. A.12. In this configuration, only the radial profiles in the center of the torch and the radial profile in the jet are studied.

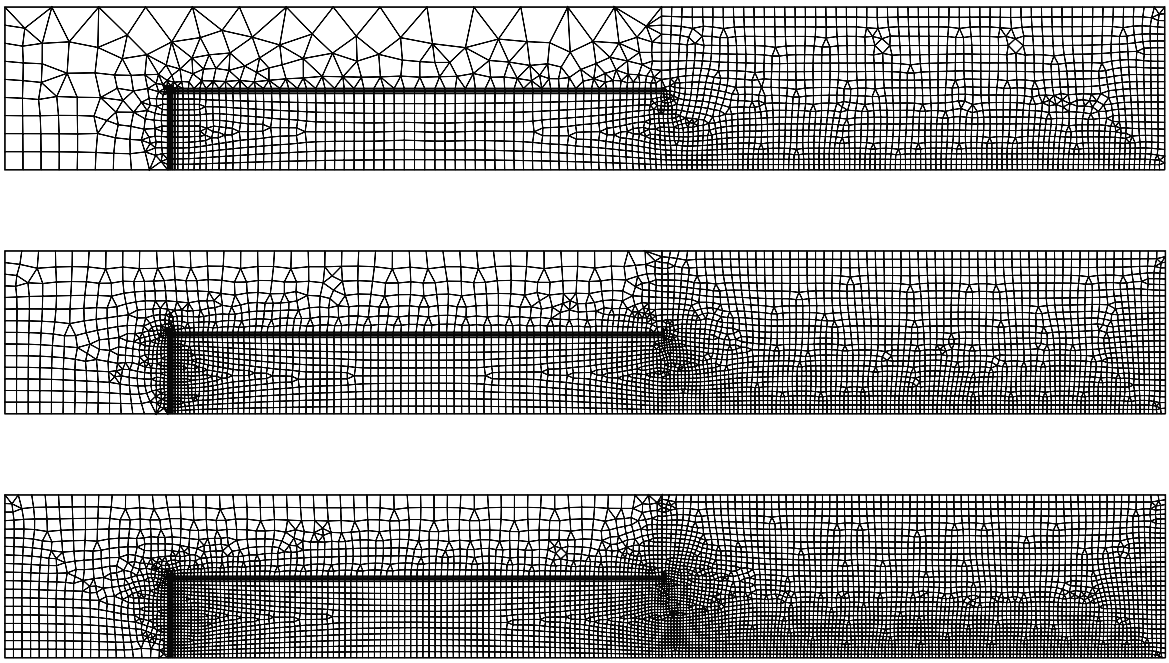

Fig. A.12.: Meshes used for the grid independence study in free stream. We call them coarse (top, 3055 elements), fine (middle, 5021 elements) and refined (bottom, 7338 elements).

Let us first discuss the solution dependence with respect to the order. First, in front of the probe (Fig. A.13 and Fig. A.14), there is a clear dependence on the order, no matter the mesh refinement. Above order 3, all variables are correctly captured. On the contrary of the probe case, the $p = 1$ is not sufficient for the temperature field, but $p = 2$ gives satisfactory results. In the torch center (Fig. A.15 and Fig. A.16), a general remark is that a reconstruction of polynomial order 3 is necessary to capture the various profiles. However, degree 2 captures quite well the electric field profiles. In light of these observations, we choose polynomial reconstructions of degree 3 and 4 in order to capture correctly the variations. Finally, the mesh dependence study at $p = 4$ (Fig. A.17 and A.18) give the same result: the solution does not change with mesh refinement. Consequently, the coarsest mesh is used.

A.2.1 Dependence of the solution with respect to the order

In the jet

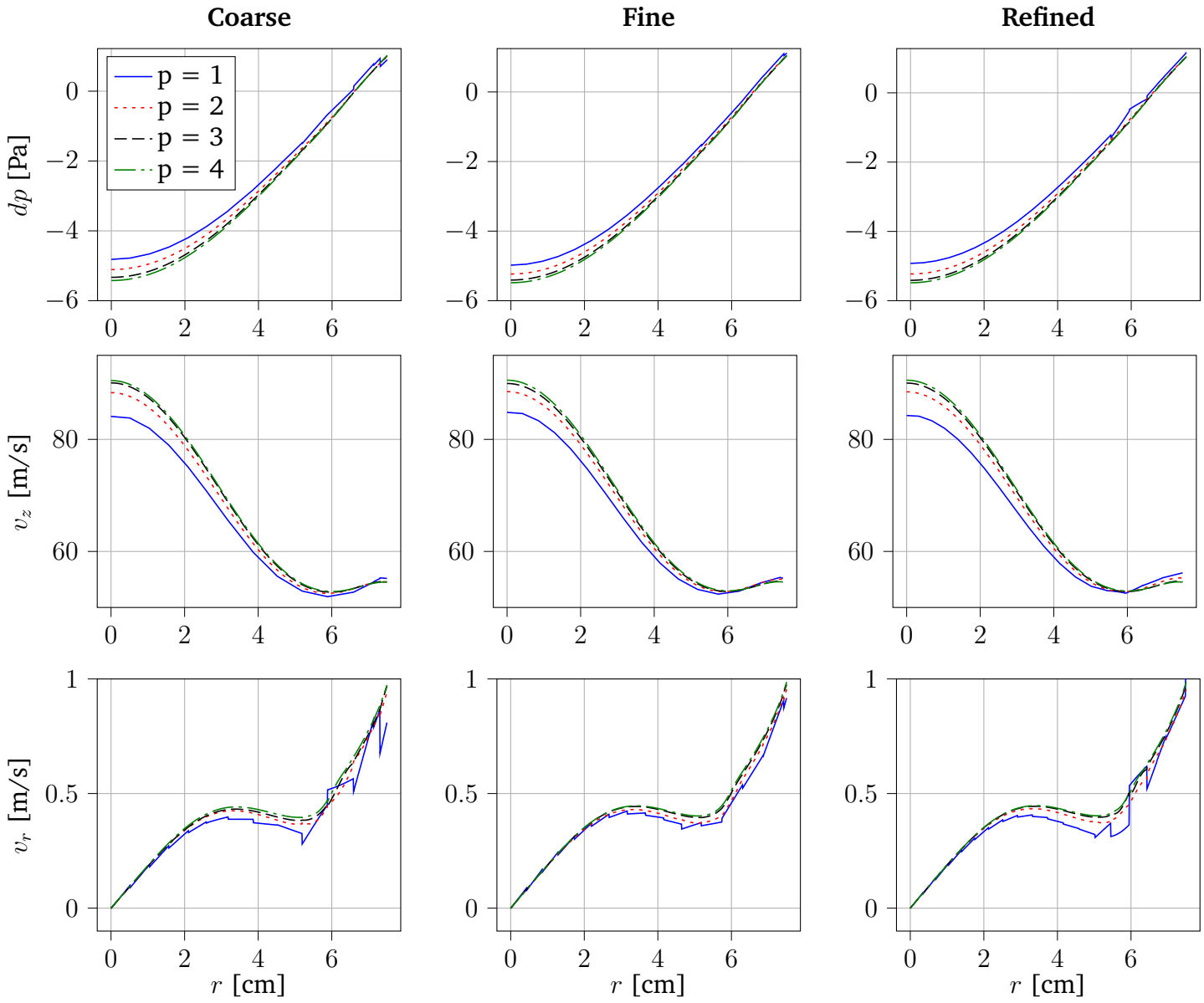

Fig. A.13.: Order independence for the free stream configuration study on the coarse (left), fine (middle) and refined (right) meshes for the pressure fluctuation dp, axial v_z and radial v_r velocities in the jet at $83.1\,\mathrm{cm}$ from the torch inlet. The polynomial degree of the method is p. The abscissa r ([cm]) is the radial distance from the center line.

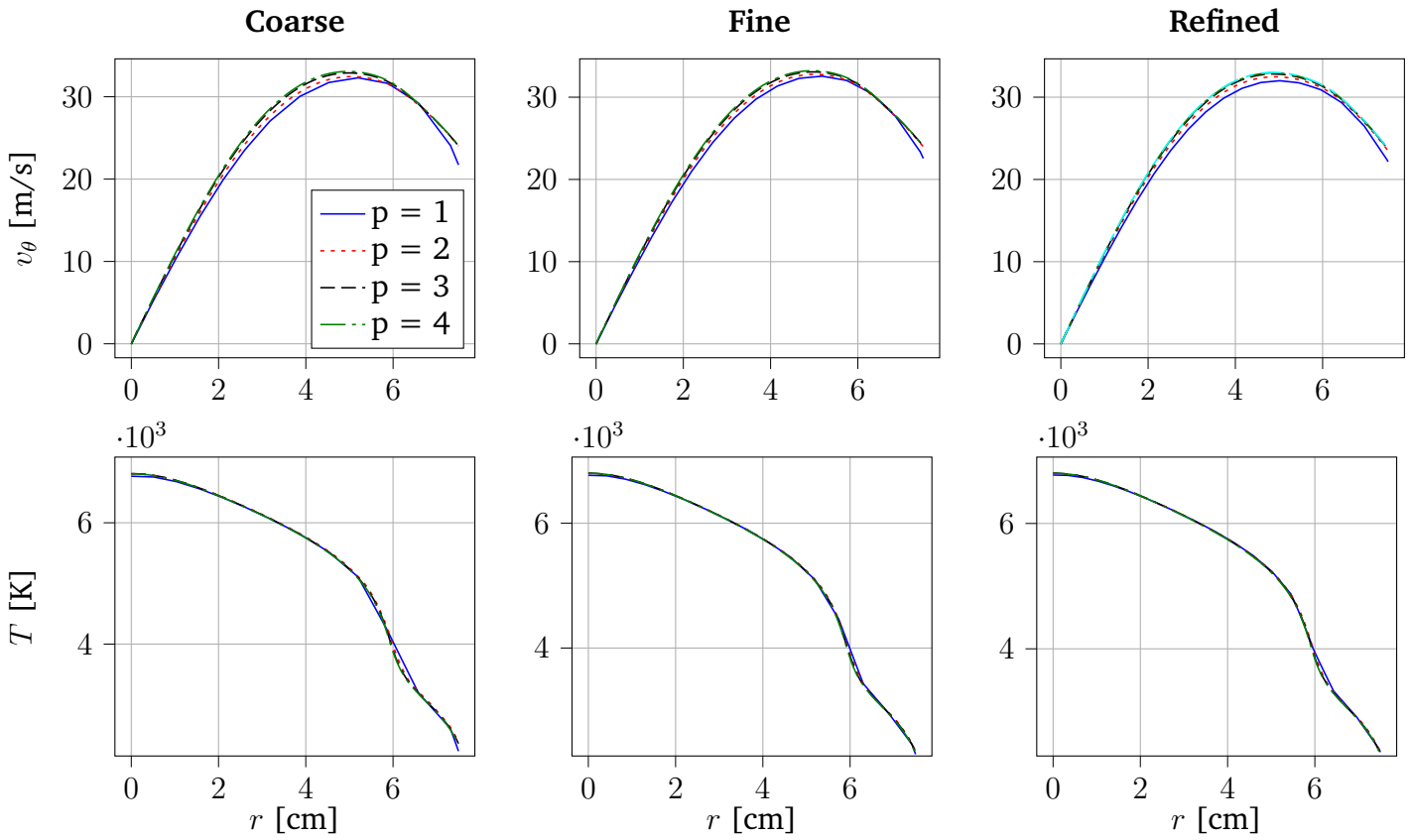

Fig. A.14.: Order independence study for the free stream configuration on the coarse (left), fine (middle) and refined (right) meshes for the azimuthal velocity v_θ and temperature T in the jet at $83.1\,\mathrm{cm}$ from the torch inlet. The polynomial degree of the method is p. The abscissa r ([cm]) is the radial distance from the center line.

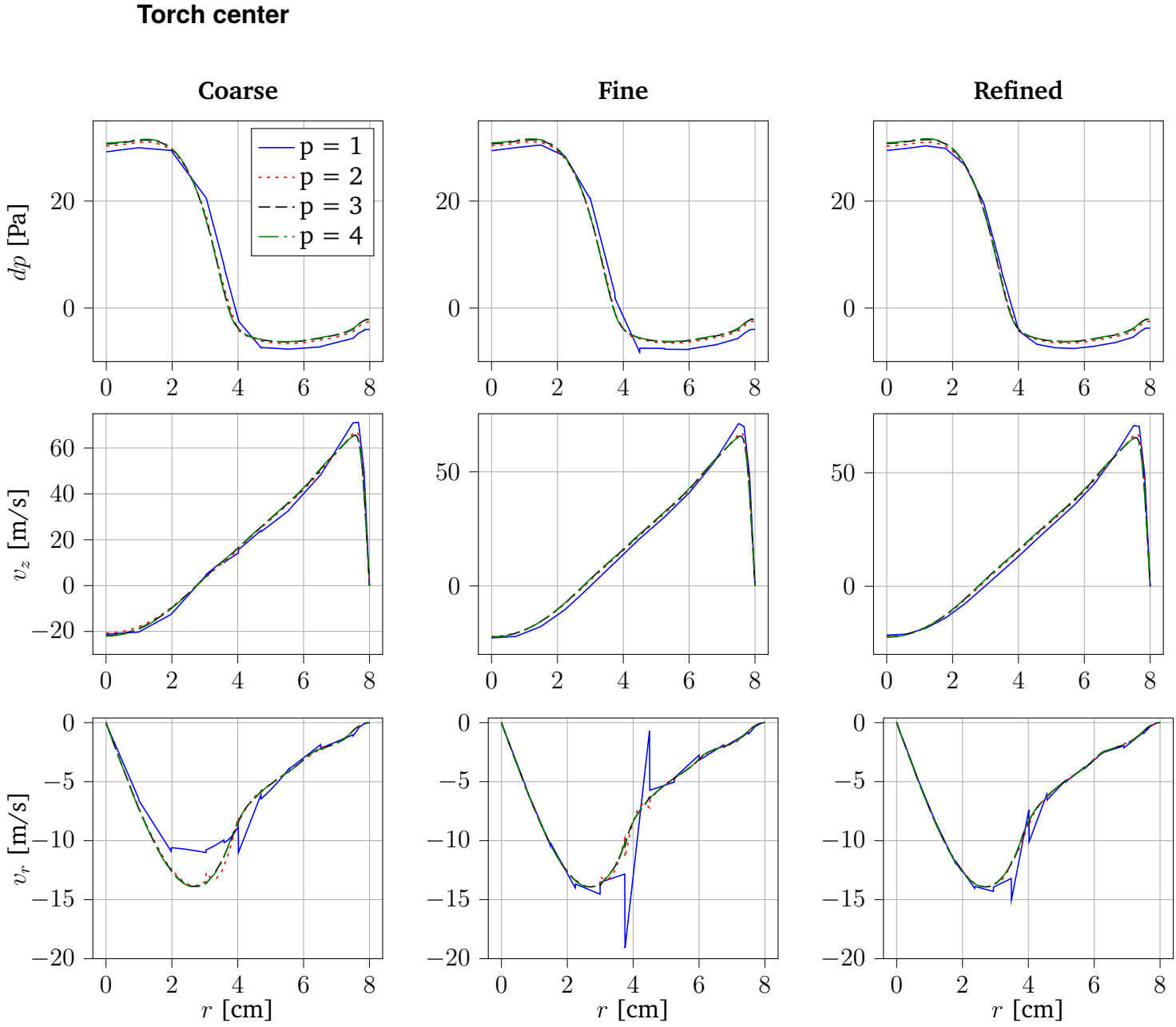

Fig. A.15.: Order independence study for the free stream configuration on the coarse (left), fine (middle) and refined (right) meshes for the pressure fluctuation dp, axial v_z and radial v_r velocities in the torch center, at $24.3\,\mathrm{cm}$ from the torch inlet. The polynomial degree of the method is p. r is the radial distance from the center line.

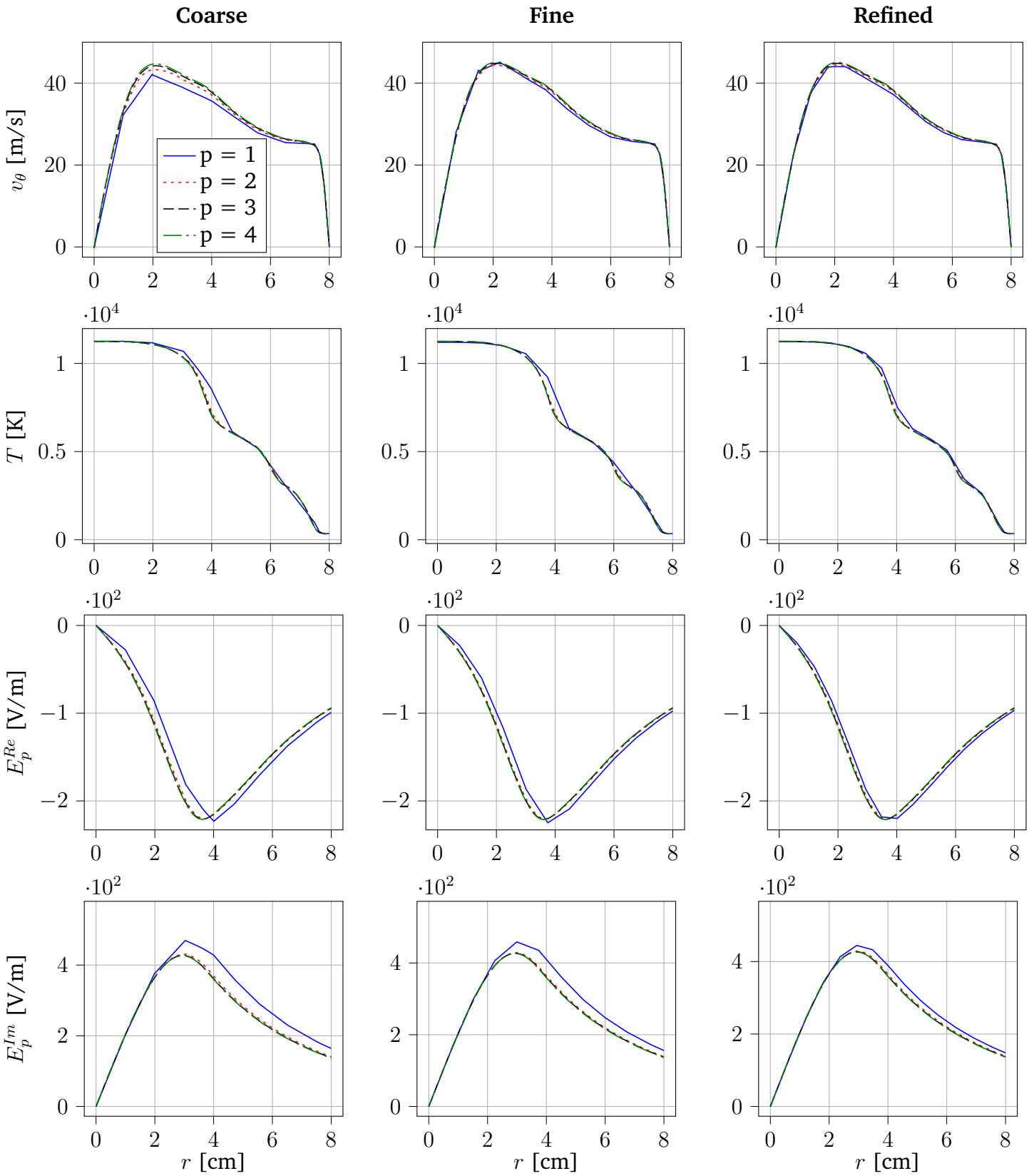

Fig. A.16.: Order independence study for the free stream configuration on the coarse (left), fine (middle) and refined (right) meshes for the azimuthal velocity v_θ, temperature T and the real E_p^{Re} and imaginary E_p^{Im} parts of the plasma electric field in the torch center, at $24.3\,\mathrm{cm}$ from the torch inlet. The polynomial degree of the method is p. r is the radial distance from the center line.

A.2.2 Dependence of the solution on the mesh size

In the jet

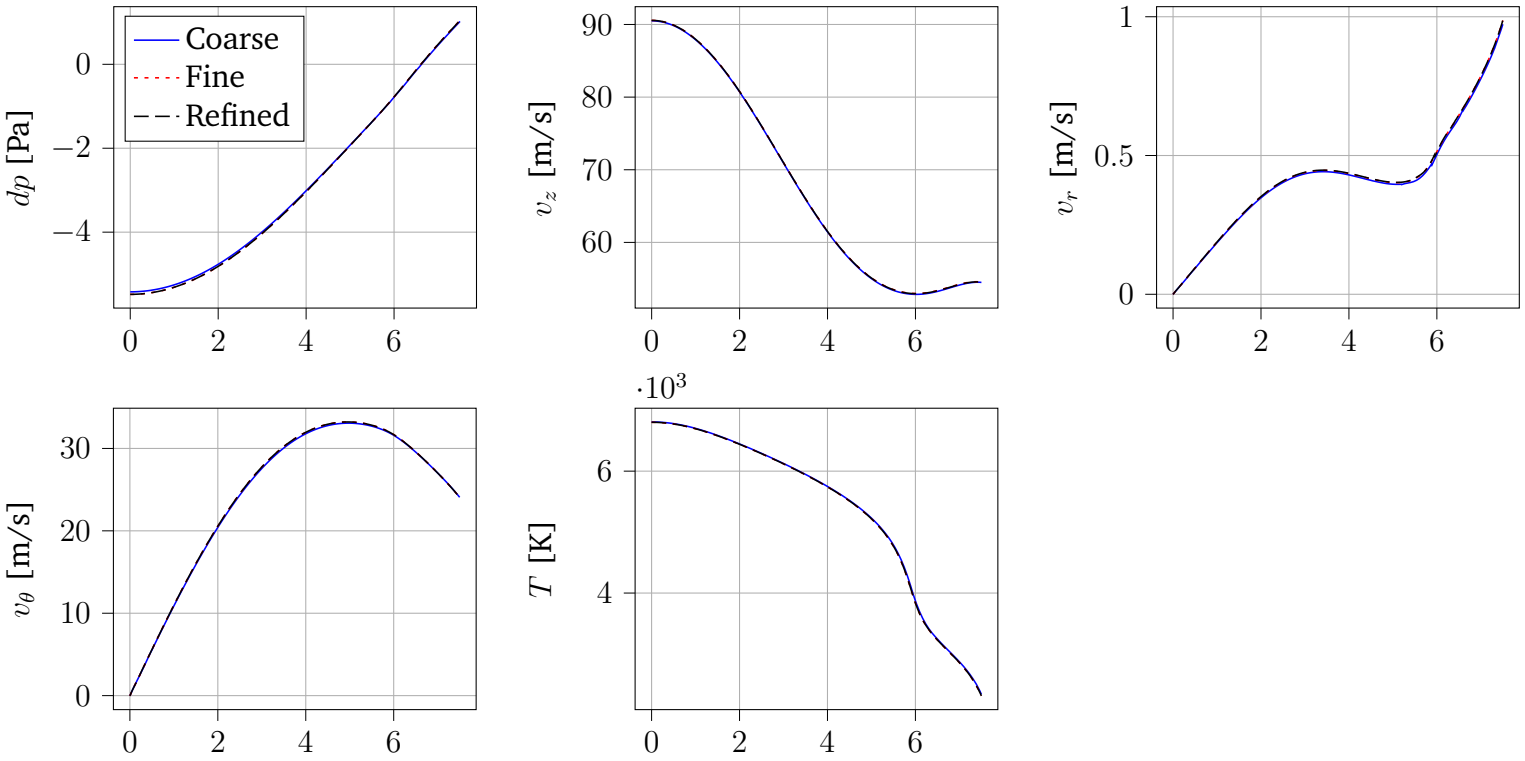

Fig. A.17.: Mesh independence study for the free stream case for the pressure fluctuation dp, axial v_z, radial v_r and azimuthal velocity v_θ and temperature T in the jet at $83.1\,\mathrm{cm}$ from the torch inlet at order $p = 4$. r ([cm]) is the radial distance from the center line.

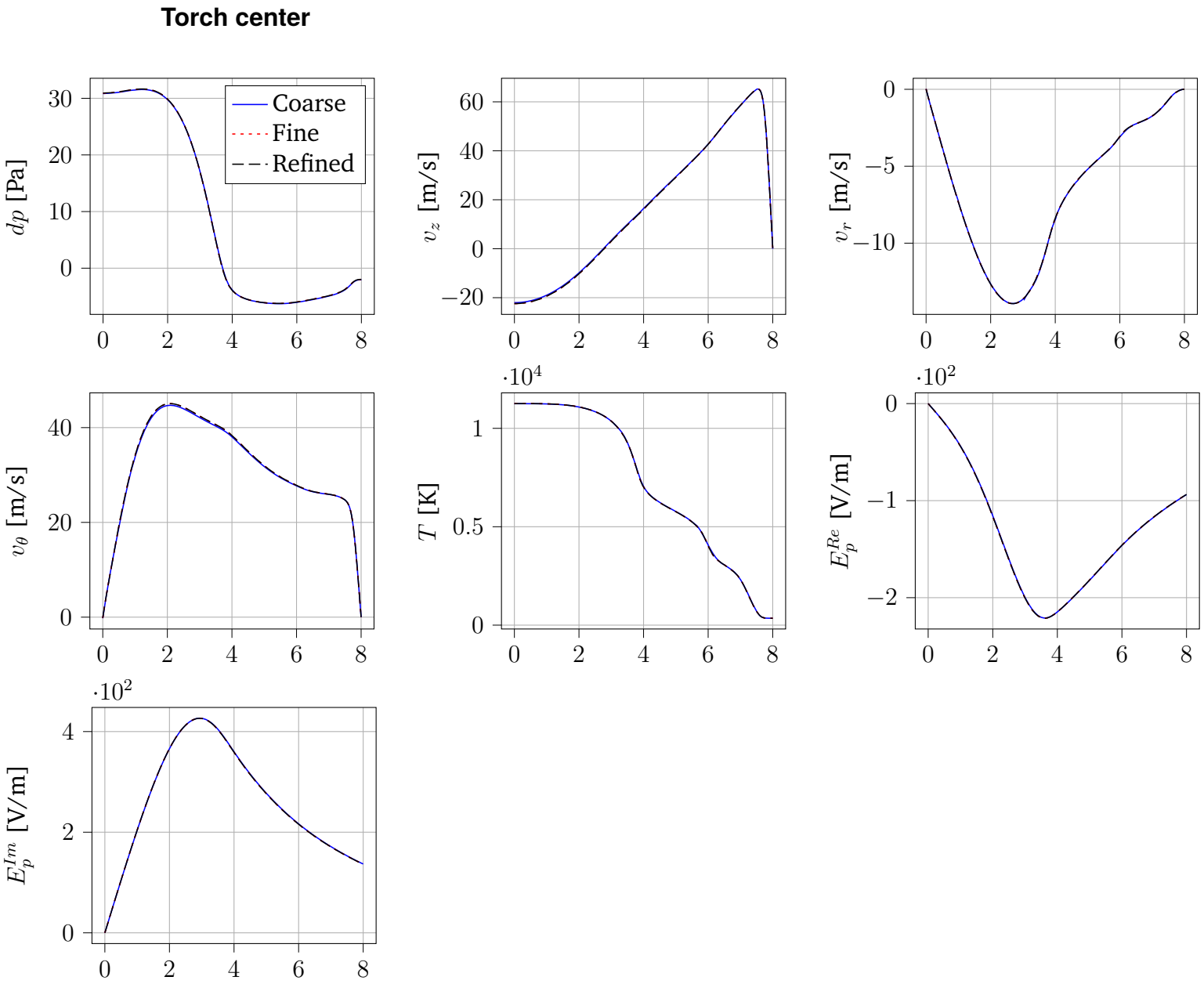

Fig. A.18.: Mesh independence study for the free stream case for the pressure fluctuation dp, axial v_z, radial v_r and azimuthal v_θ velocities, temperature T and the real E_p^{Re} and imaginary E_p^{Im} parts of the plasma electric field in the radial direction, at $24.3\,\mathrm{cm}$ from the torch inlet at order $p = 4$. r ([cm]) is the radial distance from the center line.